
The ocean's response to stochastic atmospheric forcing

A thesis submitted to the School of Environmental Sciences at
the University of East Anglia in partial fulfilment of the
requirements for the degree of Doctor of Philosophy

Shenjie Zhou

4-May-2021

© This copy of the thesis has been supplied on condition that anyone who consults it is understood to recognise that its copyright rests with the author and that use of any information derived there from must be in accordance with current UK Copyright Law. In addition, any quotation or extract must include full attribution.

Abstract

This thesis presents a series of investigations of the impact of high-frequency and small-scale atmospheric forcing on the ocean. Starting with a case study in the central Arabian Sea, a one-dimensional ocean mixed layer model is used to examine the ocean response to observed sub-daily atmospheric variability. Results show that including sub-daily atmospheric variability lowers the daily-mean sea surface temperature (SST) and damps its variability, but has little systematic effect on SST diurnal variability. This research is generalised by considering high-frequency variability via a stochastic component embedded in the atmospheric forcing and undertaking an ensemble of mixed-layer (ML) model simulations to explore the role of ML variation in generating a rectification effect on the SST. Different ML variations are engineered by tuning the solar penetration depth and comparing to a slab model where the ML depth is fixed. The SST rectification only emerges when the ML depth variation is included, and its magnitude is controlled by the background ML heat capacity that is associated with the solar penetration depth. Finally, we use a novel stochastic parameterization to represent spatially coherent mesoscale weather systems in atmospheric forcing fields. The stochastic parameterization adds high-frequency meso-scale variability to improve the ‘effective resolution’ of the atmospheric forcing fields and ‘fix’ the kinetic energy spectra. We conduct ocean model simulations with and without this realistic atmospheric forcing and find that the addition of the mesoscale forcing leads to coherent patterns of change in the SST and ML depth, which leads to statistically significant increases in

transport in the subtropical and subpolar gyres in North Atlantic and in the Atlantic Meridional Overturning Circulation (AMOC). An elevated northward heat transport across the gyre boundary, driven by the enhanced subtropical gyre, slows down the subpolar gyre after about 10 years and slightly weakens the AMOC. This thesis illustrates that the high-frequency and mesoscale atmospheric variability can not only modulate local ocean status via one-dimensional response via the influence on the surface ML depth, but also excite non-local response of the circulation patterns that potentially influences the broader-scale ocean-atmosphere feedbacks.

Access Condition and Agreement

Each deposit in UEA Digital Repository is protected by copyright and other intellectual property rights, and duplication or sale of all or part of any of the Data Collections is not permitted, except that material may be duplicated by you for your research use or for educational purposes in electronic or print form. You must obtain permission from the copyright holder, usually the author, for any other use. Exceptions only apply where a deposit may be explicitly provided under a stated licence, such as a Creative Commons licence or Open Government licence.

Electronic or print copies may not be offered, whether for sale or otherwise to anyone, unless explicitly stated under a Creative Commons or Open Government license. Unauthorised reproduction, editing or reformatting for resale purposes is explicitly prohibited (except where approved by the copyright holder themselves) and UEA reserves the right to take immediate 'take down' action on behalf of the copyright and/or rights holder if this Access condition of the UEA Digital Repository is breached. Any material in this database has been supplied on the understanding that it is copyright material and that no quotation from the material may be published without proper acknowledgement.

Contents

Abstract	iii
List of Figures	ix
List of Tables	xxiii
Acknowledgements	xxv
1 INTRODUCTION	1
1.1 Background and motivations	1
1.2 Impact of high-frequency and mesoscale atmospheric forcing on the ocean	4
1.3 Stochastic parameterization of atmospheric forcing	13
1.4 Thesis objectives	17
1.5 Thesis outline	18
2 IMPACT OF HIGH-FREQUENCY WEATHER SYSTEMS ON THE SST AND SURFACE MIXED LAYER (ML) DEPTH	21

2.1	Introduction	21
2.2	Data and Methods	23
2.2.1	Observations	23
2.2.2	Model description	24
2.2.3	Experimental design	28
2.2.4	Parameterization of cloud amount	29
2.3	Results	31
2.3.1	Fidelity in simulating SST and ML depth	31
2.3.2	Response of SST and ML depth to high-frequency weather systems	35
2.3.3	The composite analysis	37
2.3.4	Role of high-frequency wind fluctuations	40
2.4	The KC model validation	42
2.5	Summary and Conclusions	43
3	SST RESPONSE TO THE STOCHASTIC AIR-SEA HEAT FLUXES UNDER DIFFERENT SOLAR PENETRATION SCHEMES	47
3.1	Introduction	48
3.1.1	Simple stochastic climate model paradigm	50
3.1.2	Solar penetration within the upper ocean ML	54
3.2	SST response to pure white-noise air-sea heat fluxes	56
3.2.1	Methods	56

3.2.2	Spectral characteristics (variance) of stochastically-forced SST	58
3.2.3	The SST rectification excited by stochastic air-sea heat fluxes and its dependence on solar attenuation	64
3.3	Summary	79
4	OCEAN RESPONSE TO STOCHASTIC MESOSCALE WEATHER SYSTEMS	81
4.1	Introduction	81
4.2	Energy Deficiency in ERA5 wind fields	84
4.2.1	The effective Resolution of Numerical Models	84
4.2.2	Spectral Analyses of ERA5 Wind Fields	88
4.3	A Method to Improve ERA5 Wind Fields using "Cellular Automata"	91
4.3.1	Deterministic CA and Probabilistic CA rule sets	93
4.3.2	Tuning the probabilistic CA algorithm	98
4.4	Local response of the ocean to CA perturbed surface wind fields	104
4.4.1	Forcing differences	106
4.4.2	Sea Surface Temperature response in MC KPP	109
4.5	Atlantic Ocean circulation response to stochastic mesoscale weather systems	115
4.5.1	Experimental design	115
4.5.2	Model configuration	116
4.5.3	Comparison with MC-KPP experiments	120

4.5.4	Ocean circulation response to the CA perturbation	125
4.6	Summary	134
5	CONCLUSIONS AND FUTURE WORK	137
5.1	Overview of key findings	137
5.2	Connection to the motivative literatures	141
5.3	Future work	143
	Bibliography	147

List of Figures

- 1.1 A snapshot of relative vorticity ζ (s^{-1}) derived from Estimating the Circulation and Climate of the Ocean (ECCO) ocean state estimate LLC4320 simulation with the horizontal resolution of 2 km. 2

- 1.2 Composite structure of the intensive observation period (IOP) of TOGA COARE. The legends beneath the panels refer to the symbols used to represent the observational platforms in the entire COARE Domain. The large-scale domain (LSD), the outer sounding array (OSA) and the intensive flux array (IFA) are outlined. Symbols used in the figure are shown in the attached legend (reproduced in accordance to the source figure available at https://www.eol.ucar.edu/field_projects/toga-coare) 4

- 1.3 Time series of SST during the TOGA-COARE IOP from observations collected by Woods Hole Oceanographic Institute-Improved MEteorological instrumenT (WHOI-IMET) mooring, situated within the IFA region (green). Modelled SST forced by daily-mean shortwave heat flux (FHDM, black) and shortwave heat flux with diurnal cycle (FHDC, red) at the model grid point nearest to WHOI-IMET location are superimposed. A running mean FHDC SST is also shown in blue. Figure is adapted from Figure 7 in *Bernie et al. (2007)*. 5

- 1.4 True color satellite imagery derived from Moderate Resolution Imaging Spectroradiometer (MODIS) corrected reflectance products (<https://worldview.earthdata.nasa.gov/>). Upper panel shows a cyclonically rotating cloud cluster imprinted by a mesoscale polar low over Denmark Strait, east of Iceland. Lower panel depicts this fast low level jet blowing off the southern tip of Greenland, forming a patch of clear sky around the ambient region. 9
- 1.5 Four-year averages (August 1999–July 2003) of the spatial high-pass-filtered curl of the wind stress (top) and of the SST and vector-average wind stress (bottom) for the eastern tropical North Pacific (left panels) and the western North Atlantic (right panels). Figure is adapted from Figure 5 in *Chelton et al. (2004)*. 11
- 1.6 (a). Wind kinetic energy frequency spectrum derived from the wind time series collected from NDBC and PIRATA buoys (black), and from co-located ERA5 surface wind field (grey). The figure shows the averaged frequency spectra over 18 buoy locations. (b) is similar to (a) except that the comparison is made between QuikSCAT wind and ERA5 wind on wavelength domain. The wavelength spectra of the ERA5 and QuikSCAT wind are averaged over the Atlantic Ocean (60°S to 65°N). ERA5 wind kinetic energy discernibly drifts away from the observations approaching the sub-daily and higher frequency bands as well as the small-scale regimes with characteristic wavelengths less than 500 kilometres, indicating a lack of high-frequency/small-scale variability in reanalyses wind estimates. 20
- 2.1 The Arabian Sea Upper Ocean Dynamics mooring is located at 15.5°N, 61.5°E, as marked by the red circle. The location is on the climatological axis of Findlater Jet and representative of the open ocean rather than coastal water. 24

-
- 2.2 Year-long time series of (a) wind speed, (b) daily-mean net surface heat flux, (c) daily-mean SST, (d) magnitude of SST diurnal variability and (e) daily-mean ML depth. The wind speed is plotted with a coarse temporal resolution (half-daily) for clarity. The line colours show observations (grey) and simulations: CONTROL (black), WIND (red), HEAT (blue) and NO-HI (magenta). 27
- 2.3 A PWP model run over a 24 hour period with varying mixing parameterizations. It is evident that without gradient or bulk Richardson number mixing the ML is hourly defined by surface heat gain, whilst gradient mixing causes smoother profile than the bulk mixing along. Figure is adapted from *Price et al.* (1986). . . . 35
- 2.4 SST from the CONTROL (black) and the NO-HI (magenta) experiments, with daily-mean SST marked as dashed lines. The SST from an experiment forced by daily-averaged surface fluxes is shown as a brown line. 37
- 2.5 A 24-hour composite view of SST (top), ML depth (second row), and wind speed (middle) showing observations (grey), CONTROL (black) and NO-HI (magenta) experiments. The next two rows show differences in wind stress (fourth row) and net surface heat fluxes (bottom) between the CONTROL and NO-HI. The composites are for three seasons: the NE monsoon (left), the intermonsoon (middle) and the SW monsoon (right). Values of seasonal-mean differences (CONTROL - NO-HI) are shown at the top of each panel. The composite-averaged magnitude of SST diurnal variability simulated by the CONTROL and NO-HI are illustrated in the top panels. Note that different axis limits are used in different seasons for the composites of SST, ML depth and wind speed. 39

- 2.6 The 24-hour composite view of sub-daily (black) and daily-averaged (magenta) cloud cover and the difference of net surface shortwave radiation (Q_{net}^{SW}), longwave radiation (Q_{net}^{LW}), latent heat flux (Q^{LH}) and sensible heat flux (Q^{SH}) between the CONTROL and NO-HI experiments in the NE monsoon (left), intermonsoon (middle), and SW monsoon (right) seasons. Values of seasonal-mean differences (CONTROL - NO-HI) are shown on the top of each panel. Note that different axis limits are used in different seasons for the composite cloud fraction. 40
- 2.7 (a) Daily-mean SST from the CONTROL (black), NO-HI (magenta) and WIND* (green) experiments. (b) Daily-mean ML depth in the NO-HI and WIND* experiments and daily-mean SST difference (dashed) between the two experiments (WIND* - NO-HI). 42
- 2.8 Year-long time series of (a) daily-mean SST, (b) magnitude of SST diurnal variability and (c) daily-mean ML depth. The line colours show observation (grey) and the KC model simulations: CONTROL (black), WIND (red), HEAT (blue) and NO-HI (magenta). 44
- 2.9 (a) Daily-mean SST for the CONTROL (black), NO-HI (magenta) and WIND* (green) experiments. (b) Wind speed used in NO-HI and WIND* and daily-mean SST difference (dashed) between the two experiments (WIND* - NO-HI). (c) Daily-mean ML depth in the CONTROL, NO-HI and WIND* experiments. 45

- 3.1 Adapted from *Marshall and Plumb* (2008). (a) The theoretical spectrum, Eq.3.1.3, on a log-log plot. The vertical grey line indicates the frequency $\omega_c/2\pi$ where $\omega_c = \frac{\lambda}{\gamma_o}$. (b) Log-log plot of the power spectrum of atmospheric temperature at 500 mbar (black) and SST (grey) associated with the North Atlantic Oscillation, see *Czaja et al.* (2003) for details. 53
- 3.2 (a) Time series of net surface heat fluxes over 100 model days applied in all idealized experiments. (b) Power Spectral Density of the net surface heat fluxes. Little dependence of power density on the frequency shows a typical white noise spectra. 58
- 3.3 Power spectra (non-dimensional) of the stochastic air-sea heat fluxes (black) applied in the slab mode experiments and the simulated SST (grey). The white-noise-forced SST yields a red spectrum with the slope of ω^{-2} , as predicted by *Hasselmann* (1976). 59
- 3.4 (a). Time series of SST simulated by slab ocean model (black), PWP model with non-penetrative solar radiation scheme (orange) and penetrative solar radiation scheme (blue). The variabilities between the slab model SST and non-solar-penetrative PWP SST are of the same magnitude since the ML depth is mostly fixed at uppermost layer in the latter experiment. The variability in solar-penetrative PWP SST is largely damped by deeper ML. The difference and similarity on the SST variability magnitude among three experiments are further shown in (b) in form of the power spectrum. Noted that the redness of SST spectra is persistent throughout different simulations regardless of including ML adjustment and realistic solar penetration. 62

-
- 3.5 The square of magnitude of variability of sinusoidally forced SST anomalies plotted against frequencies (black circle). A fitted trend (blue line) shows that the squared variability and frequencies have a clear decaying relation with the slope equal to ω^{-2} 64
- 3.6 Adopted from *Feng et al.* (2020). Schematic plot of diurnal variation of (DV) SST (red line) and potential density profiles in the upper ocean (blue lines). During a diurnal cycle, peak SST (SST_{max}=mean SST from 1200 to 1700 LT) typically occurs in the local afternoon. The magnitude of DV SST is quantified by computing the dSST, the difference between the daytime peak and nighttime foundation SST (SST_{fn}) during a diurnal cycle. . . 66
- 3.7 Ensemble spread of 100 SST realizations forced by stochastic air-sea heat fluxes produced by slab model superimposed with the mean-forced slab SST (black) and ensemble mean of SST realizations (red). 69
- 3.8 (a). A series of sinusoidal-shaped surface forcing with same magnitude, frequency but various initial phases ranging from 0 to $\frac{3\pi}{2}$. (b). The corresponding SSTs. The sign of rectification effect on SST varies with different initial phases, indicating a strong sensitivity to the initial phases. 70
- 3.9 Scaled SST rectification effect in association to the amplitude A and phase θ_0 of the forcing. Magnitude of SST anomalies shown in colour is scaled by the maximum SST anomalies. The scaled pattern of rectified SST is not significantly affected by the choice of ω but with the actually magnitude inversely proportional to ω as indicated in Eq. 3.2.5. 72
- 3.10 Same as Figure 3.7 but for NSP PWP model. 73
- 3.11 Same as Figure 3.8 but for NSP PWP model. 75

- 3.12 Same as Figure 3.7 but for SP PWP model with the forcing amplitude at (a) 500 W/m² and (b) 5000 W/m². 77
- 3.13 Same as Figure 3.8 but for SP PWP model with the forcing amplitude at (a) 50 W/m² and (b) 500 W/m². Here we only show the sinusoidally-forced SST (red) with the initial phase $\theta_0 = -\pi$, to highlight the difference on the rectification effect caused by different magnitudes of surface forcing. Panel (a) shows that when the initial phase leads to an initial cooling for half a period and the SST negatively deviating from the reference by the most. ‘Small’ forcing amplitude drives SST to increase back up towards the reference over the second half period while SST is not warmed up enough in this case to exceed the reference SST derived from the mean-forced SST (solid black), hence there is a systematic cooling effect on SST. Panel (b) shows that if the surface forcing magnitude is large enough, SST warming can overcome the initial cooling, to ensure a systematic warming effect. 78
- 4.1 (a). *Nastrom and Gage* (1985) spectrum derived from the GASP aircraft observations (symbols) and the *Lindborg* (1999) functional fit to the MOZAIC aircraft observations, adapted from *Skamarock* (2004) Figure 1. (b). A schematic depicting the effective resolution by comparing the dependence of the model-derived spectra from the theoretical prediction, adapted from *Skamarock* (2004) Figure 10. 85
- 4.2 (a) and (b) are the spatial snapshots of the surface wind speed derived from QuikScat and ERA5 for 0800UTC on 1st of January, 2008, respectively, across Atlantic Ocean (60°S to 65°S). (c) and (d) are the corresponding relative vorticity fields. 87

- 4.3 (a) Locations of in total 18 available met-buoy stations including 8 NDBC buoys (blue circles), 9 from the PIRATA mooring array (red diamonds), and one private met buoy, SIMORC, located in Norwegian Sea (magenta stars). (b) Wavenumber spectra derived from QuikScat (black) and ERA5 wind fields (grey). The departure of the ERA5-derived spectrum is clearly shown here initiating at the length scale at 400~500 km, within the predicted intermediate range between the enstrophy inertial range and energy inertial range (e.g. *Lindborg*, 1999). (c) Frequency spectrum derived from ERA5 and collocated meteorology buoy stations. A major energy sink of ERA5 ocean winds is detected in the frequency range higher than 1 cycle per day. 92
- 4.4 Snapshots of a CA pattern evolution generated by deterministic CA rules for 2000 time steps initialized with a 4×4 block of alive cells in the middle of a 300×300 domain. The number of time steps is shown above each domain snapshot. Black colour represents the dead cells and white colour represents the alive cells. The lower panel shows the time series of CA values of the central cell. 95
- 4.5 Same as Figure 4.4 but for the probabilistic CA rule test experiment. Comparison at the bottom shows high resemblance between a developed CA pattern and observed (MODIS radiometer, true colour imagery) small-scale cloud pattern from convective events over the ocean. 97

- 4.6 (a) Frequency spectra and (b) wavenumber spectra derived from a series sensitivity of experiments to assess the effect of N_L . 6 values of N_L are selected here and the shape of spectra have shown a strong dependence on the value N_L with strong energy injection scale that drifts to small-scales and high-frequencies with the decreasing N_L . (c) Frequency spectra for different Δt_{CA} with $N_L = 1$. (d) Similar to (c) but for wavenumber spectra for different choices of ΔS_{CA} . Energy injection scale shifts downscale/high-frequency with the decrease of $\Delta S_{CA}/\Delta t_{CA}$. The difference in wavenumber spectra and frequency spectra between observations and ERA5 are plotted in grey in all panels. The ΔS_{CA} and Δt_{CA} in (a) and (b) are set to be $\frac{1}{12}^\circ$ and 1 hour, and $N_L = 1$ in (c) and (d). 99
- 4.7 (a)-(c) The probability distribution function (PDF) derived from the trial experiments on α on January 2008 for three different regions in Atlantic Ocean with the α values shown above each panel. The difference in α for different regions is small, while they all show a broadening of the PDF and a higher probability for high wind speed events in the perturbed wind field. (d) The time series of the monthly-varying α used in our CA perturbation scheme in Eq. 4.3.1 for the Atlantic Ocean domain. 102
- 4.8 Snapshots of (a) wind speed and (b) relative vorticity of ERA5 wind data after the CA perturbation applied. The example snapshots are computed from the ERA5 wind data at 0800 UTC on 1st January 2008 as in Figure 4.2. 103

- 4.9 (a) Wavenumber spectra comparison made between QuikScat (black), ERA5 (grey) and CA-perturbed ERA5 (cyan) wind fields averaged for year 2008 across the Atlantic Ocean domain. (b) Same as (a), except that it shows the frequency spectra. After perturbation, ERA5 wind fields experience improvement on the energy spectral behaviour on length scales longer than 400 km and frequency higher than 1 cycle per day. (c) The probability distribution function of the wind speed of QuikScat (black), ERA5 (grey) and perturbed ERA5 (cyan) wind. 105
- 4.10 (a) Annual-mean (year 2008) map of wind speed difference induced by probabilistic CA wind perturbation superimposed by the annual-mean background wind speed contour. (b) Same as (a), expect superimposed with annual-mean background wind direction with the northeasterlies being highlighted (0° to 90°). . . 107
- 4.11 (a) Annual-mean turbulent heat fluxes difference between perturbation and control experiments with annual-mean background wind speed contour superimposed. (b) Same as (a), but for wind stress difference. 109
- 4.12 Seasonal average of the SST response to the CA perturbation estimated over the year 2008 for (a) December, January and February (DJF), (b) March, April and May (MAM), (c) June, July and August (JJA), (d) September, October and November (SON). The 18 m isobar of the seasonal averaged control ML is superimposed to highlight the shallow ML regions. (e)-(h) are the seasonal average for the control ML depth. 111
- 4.13 Correlation between SST response and background ML depth (black), surface heat fluxes differences (red) and wind stress differences (blue) averaged as a function of latitude. 113

- 4.14 10-year mean of the difference between the COARE calculated turbulent heat fluxes and ERA5 turbulent heat fluxes from 1995-2004. A $4^\circ \times 4^\circ$ 2D Gaussian filter is applied to produce this basin-scale discrepancy: the turbulent heat fluxes calculated from ERA5 meteorological variables with the COARE algorithm tend to underestimate the turbulent heat loss (anomalous warming) in the Labrador Sea while overestimate the heat loss (anomalous cooling) across the subtropical and tropical regions. 117
- 4.15 15-year mean difference in the (a) wind speed, (b) net surface heat flux and (c) surface wind stress, between the CONTROL and PERTURB atmospheric forcing. 15-year averaged CONTROL wind speed contours are superimposed on (a) and (b), highlighting the correlation between the background wind speed and forcing differences. 15-year mean CONTROL wind stress and direction is mapped on top of surface wind stress difference denoted by white arrows. 119
- 4.16 Seasonal average of the SST response to the CA perturbation estimated over the 15-year period for (a) December, January and February, (b) March, April and May, (c) June, July and August, (d) September, October and November. SST response with magnitude smaller than 0.5°C is masked out by white colour on the map. The occurrence of large SST response, with the magnitude greater than 0.5°C , is illustrated in colours with warm colours denoting the SST increase and cold colours denoting SST decrease. The percentage the area of these large signals to the domain area are posted in the corresponding colour scales. The black contour of the seasonal averaged background ML depth from 0 to 100 m is superimposed. 123
- 4.17 Same as Figure 4.16 but for ML depth differences. 124

- 4.18 15-year mean estimate of the SST difference (PERTURB-CONTROL) (a) diagnosed from surface heat fluxes with the assumption of no ML variation, (b) computed from model output and (c) the difference between (b) and (a). 124
- 4.19 (a) The time series of CONTROL (black), PERTURB (red) and observed (grey) Florida Strait Current transport at 26.5°N. Observation is derived from the 21-year measurement of the submarine cable across the Florida Strait. Data available at https://www.aoml.noaa.gov/phod/floridacurrent/data_access.php. (b) The monthly difference of Florida Strait transport between PERTURB and CONTROL experiments. 126
- 4.20 Time series of subpolar gyre indices based on the minimum barotropic streamfunction (a) along the cross section over the Labrador Sea, (b) along the 60°N and (c) from the closed SSH contour with largest area over subpolar latitudes. Note that the absolute values of the streamfunction are plotted and larger value denotes stronger subpolar gyre. 128
- 4.21 The time series of (a) AMOC indices defined as the maximum barotropic streamfunction at 26.5°N in CONTROL (black), PERTURB (red) experiments and RAPID observation (grey). (b) The difference (PERTURB-CONTROL) in (b) AMOC index, with the positive value indicating stronger AMOC in PERTURB run. 128

- 4.22 15-year mean of (a) CONTROL wind stress curl, (b) the wind stress curl difference between PERTURB and CONTROL, smoothed by a $5^\circ \times 5^\circ$ 2D Gaussian filter. Positive value denotes the cyclonic wind stress curl. The spatial filter is applied to highlight the large-scale pattern in the wind stress curl anomaly. (c) The vertical thermocline structure averaged over 15 year period at 26.5°N , panel extends to the east of Grand Bahamas Island to illustrate the thermocline structure connection to the open ocean. (d) Basin-wide thermocline structure at 26.5°N 130
- 4.23 Time series of the difference in subpolar gyre indices (PERTURB-CONTROL) based on the minimum barotropic streamfunction (a) along the cross section over the Labrador Sea, (b) along the 60°N and (c) from the closed SSH contour with largest area over subpolar latitudes. The positive values (red bars) represent strengthened subpolar gyre in PERTURB experiment. (d) Difference of ocean heat content (OHC) ($1 \text{ ZJ} = 10^{21} \text{ J}$) in the subpolar box (40°N to 65°N , 60°W to 10°W) between PERTURB and CONTROL experiments, with positive values denoting ocean warming in PERTURB run. (e) Same as (d) but for the winter time (DJF) ML depth calculated in subpolar region, and positive values denote deeper ML in PERTURB run. 131
- 4.24 The time series of (a) the northward heat transport in CONTROL (black) and PERTURB (red) experiments, the difference (PERTURB-CONTROL) in (b) the northward heat transport and (b) accumulative heat transport at the gyre boundary at 40°N . An increased northward heat transport is found in winter 2008 and lead to an anomalous heat input into the subpolar region. 132

List of Tables

2.1	Root mean square error (<i>RMSE</i>) and mean bias deviation (<i>MBD</i>) are calculated between the observed radiative fluxes and the calculated radiative fluxes with the ‘hybrid’ and ‘longwave-only’ cloud scheme, for different clear-sky emissivity schemes as summarized by <i>Gubler et al.</i> (2012). The best combination used for net surface heat flux recalculation is the ‘hybrid’ cloud scheme and the emissivity scheme proposed by <i>Dilley and O’Brien</i> (1997).	31
2.2	Comparison of the magnitude of SST diurnal variability in observations and simulations using the PWP model and the KC model.	43
4.1	Seasonal mean average for SST difference (perturbation-control), control ML depth and surface heat fluxes difference for selected subdomains.	114
4.2	The mean SST difference and background ML depths averaged over the subtropical (10°N to 35°N, 80°W to 20°W) , the whole domain excluding Gulf Stream and the subpolar (45°N to 65°N, 60°W to 40°W) Atlantic Ocean simulated by MITgcm.	121

- 4.3 A summary of the response of ocean circulation systems (Florida Strait transport, subpolar gyre, AMOC) and the northward heat transport at the boundary gyre ($\iint vT dx dz$) to the CA perturbation. Δ = difference calculated by PERTURB - CONTROL. The statistical significance of each result is shown by the p-values for both a two-tailed *t*-test and a two-tailed binomial test, where p-values < 0.05 (95%) are considered statistically significant, and are highlighted in red. Note that the difference in subpolar gyre strength is calculated using the absolute values of the streamfunction minimum, the same as in Figure 4.23. 133

Acknowledgements

First and foremost, I would like to thank my wonderful supervisors, Xiaoming Zhai and Ian Renfrew, for their inspiration, enthusiasm, positive attitudes and patience through the four-year period of my PhD research. I am very grateful to Xiaoming for introducing me to this research topic, for countless discussions and for continuous support on my research and on my life. I thank Ian for being thoughtful and resourceful in my scientific education and for supporting me on a fantastic research cruise experience in the Iceland-Greenland Sea. Without their guidance and support, this thesis would not have been possible.

I would also like to thank a number of people who helped me along the way. I thank Qinbiao Ni, who visited Xiaoming for one year, for his generous encouragement and his great company in the office, in the gym and in the swimming pool. Thanks also go to Xiaolong Yu, for insightful discussions on the one-dimensional mixed layer model and ocean mixing, and numerous basketball advice, and more importantly for the long-lasting friendship since my master in the year 2014.

I want to give my thanks to my office mates too: Matthew Bones, Louise Biddle, Rhiannon Davies, Richard Jones, Luca Possenti, Jack Giddings, Pierre Cauchy and Stephanie Goodwin. Some of them may have only shared the office with me for a very brief time, but I am still grateful for their advice, encouragement and friendship. Special thanks to Luca Possenti for his timely jokes, pasta and beers. I also owe my special thanks to Matthew Bones who was the first person talked

to me and helped me settle down in the new office on my first day. He showed me his great passion with life and he led me to the witness of the very first pepper harvest in my life. May he rest in paradise.

Huge thanks to all my Chinese friends at UEA, my PhD would not have been as enjoyable without you, especially Ji Liu, Yuli Shan, Kan Geng, Xia Lin, Yanxin Wang, Xin Liao, Jing Wang, Juan Li. Special thanks to Ji Liu, Yuli Shan, Xia Lin and Jing Wang for their company when I visited Shan-Xi for a holiday.

Being a sports fan, basketball has been a fun motivation and stress-relief hobby for me, I would like to thank the basketball community at UEA, including everyone who has ever played with me and/or come along to my gym sessions. As a member of Norfolk Chinese Community Associate as a four-year player and a two-year coach, I would like to thank my teammates and all the opponents that I have played with. These games helped me to release my energy, have fun meeting with new people, travel around Norfolk and enjoy my life as a PhD student.

My parents, Yujing Zhou and Liping Shen, my immense thanks for their support and understanding. My pursuit on PhD would not have been possible without them. I feel very sorry that I only spent one Chinese New Year with them over the last four years. To them, I owe so much.

Above all others, I would like to express my special thanks to my wife, Yixi Zheng, for her countless tips on my presentation skills and how to be cool as a guy, for her love and self-sacrifice, and for always being there for me.

INTRODUCTION

This thesis is an effort to understand the ocean's response to stochastic variability in atmospheric forcing on a range of temporal and spatial scales. We start by describing the origin of the concept of stochastic parameterization in the atmospheric forcing, followed by some progress achieved and their importance in driving the ocean evolution and affecting the climate system.

1.1 Background and motivations

The atmosphere and ocean contain not only vigorous time-mean circulation on planetary and basin-wide scales but also high-frequency and small-scale variations associated with storms, orographic jets and convective systems in the atmosphere and mesoscale and sub-mesoscale eddies and internal waves in the ocean. One of the main characteristics of these geophysical fluids is the coexistence of motions on a vast range of spatial-temporal scales. The coupling of the motions across scales is seen in observations and has been partially reproduced in state-of-art general circulation models. A snapshot of the relative vorticity field of the surface currents derived from the Estimating the Circulation and Climate of the Ocean (ECCO) ocean state estimate LLC4320 simulation, a global ocean simulation at 2 km horizontal grid spacing (Figure 1.1), illustrates the coupling of various scales of motions in the ocean (but not exclusive to the ocean) - the coupling of sub-mesoscale filamental structures and mesoscale eddies shed from the large meanders

of the Gulf Stream current. These feature leads to questions on how motions in the ocean and atmosphere on various scales interact, and, more importantly, how the small-scale and high-frequency motions, which are numerous, ubiquitous and often energetic, affect the behaviour of the large-scale circulation and the responses of the large-scale circulation to changes in the external forcing (e.g. the atmospheric forcing to the ocean) . Answers to these questions are fundamental for improving the representation and prediction of our climate system, which is characterized by the mutual interaction of complex systems each involving entangled processes running on spatial scales from millimetres to thousands of kilometres, and temporal scales from seconds to millennia.

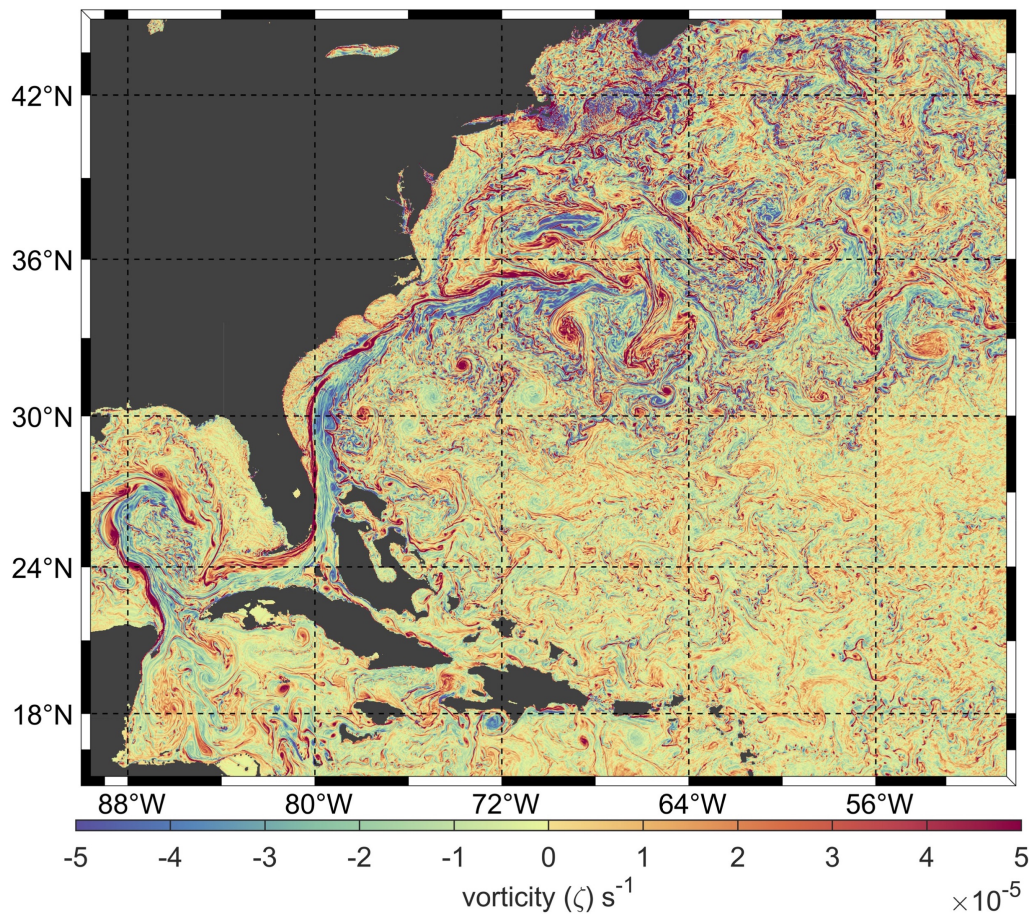


Figure 1.1: A snapshot of relative vorticity ζ (s^{-1}) derived from Estimating the Circulation and Climate of the Ocean (ECCO) ocean state estimate LLC4320 simulation with the horizontal resolution of 2 km.

Given current computer power, it is not possible to capture the whole range of

spatial and temporal scales of the ocean or atmosphere. Depending on the climate questions we pose, we have to make decisions as to what components to include in the analysis and what scales to resolve. An inevitable consequence of these decisions is that numerical schemes fail to resolve so-called sub-grid scale processes in scale-truncated models. In some cases, the slow processes active on large spatial scales are indeed those of interest. For instance, at the equilibrium state, the tropical trade winds and mid-latitude westerlies are sufficient to explain, to leading order, the formation of the subtropical gyre circulations, while the earth's rotation leads to the western boundary intensification rather than the localized small-scale turbulence. For climate predictions with coupled ocean-atmosphere models, such as those being used in the Intergovernmental Panel on Climate Changes (IPCC) assessment reports, we may want to focus on the slow dynamics of the ocean ignoring weather systems interacting with the ocean on fast time-scales of days. However, attention on the dynamics of unresolved scales are also needed to establish if they can have a significant impact on the larger scales and contribute to a reliable simulation of the slow and large-scale variables of interest. It has been clear since the very first atmospheric climate simulations that the accuracy of the large-scale flows and energy spectra is dependent upon the modelling of the sub-grid processes (*Smagorinsky, 1963*), where they found that the lateral transfer of momentum and heat by the non-linear diffusion, representing the action of motions of sub-grid scales, accounts for a significant portion of the total eddy transfer. In oceanic climate models, sub-grid interactions are even more important as baroclinic instability occurs at much smaller scales, and it is primarily responsible for the generation of mesoscale oceanic eddies (e.g. *Vallis, 2006; Ferrari and Wunsch, 2009*) but is not explicitly resolved in typical climate simulations.

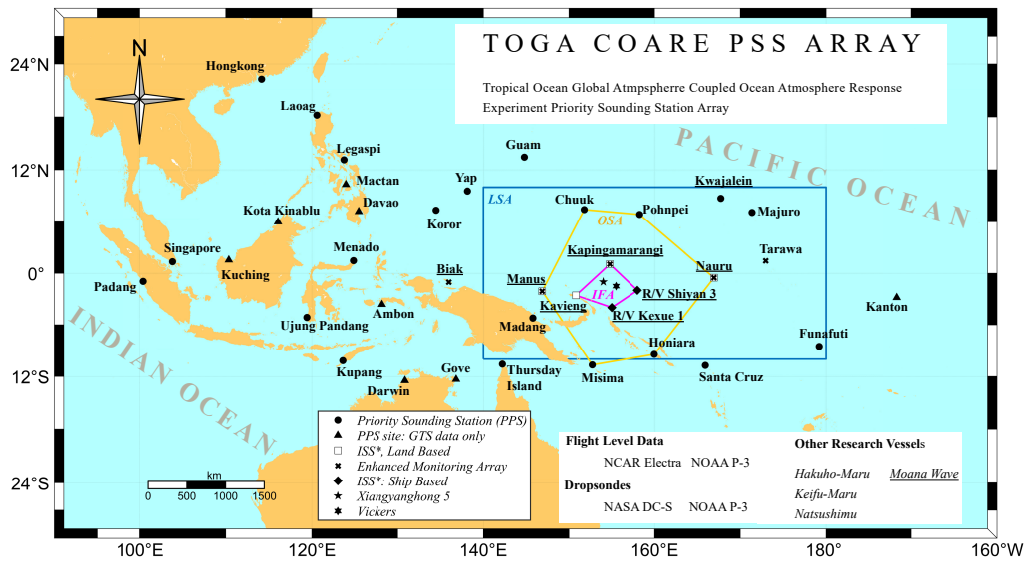


Figure 1.2: Composite structure of the intensive observation period (IOP) of TOGA COARE. The legends beneath the panels refer to the symbols used to represent the observational platforms in the entire COARE Domain. The large-scale domain (LSD), the outer sounding array (OSA) and the intensive flux array (IFA) are outlined. Symbols used in the figure are shown in the attached legend (reproduced in accordance to the source figure available at https://www.eol.ucar.edu/field_projects/toga-coare)

1.2 Impact of high-frequency and mesoscale atmospheric forcing on the ocean

Apart from the importance of intrinsic fine-scale variability in subsystems of the climate (e.g the atmosphere and ocean), the expanding volume of observations has revealed high-frequency and small-scale air-sea interaction features. These observed features are believed to have the potential to modulate the climate (sub)systems far beyond their own characteristic spatio-temporal scales via the interplays of complex non-linear feedback mechanisms. This emphasizes the urgent need of properly representing these fine-scale variation in the current generation of global climate models for a more accurate projection of future climate evolution.

High-frequency in-situ measurements of meteorological variables and co-located hydrographic variables collected in *Tropical Ocean-Global Atmosphere* (TOGA)

Coupled Ocean Atmosphere Response Experiment (COARE) highlight the importance of the high-frequency air-sea interaction in the tropical oceans on global-scale climatic variabilities over intraseasonal-to-decadal timescales (e.g. *Webster and Lukas, 1992; McPhaden et al., 1998*). The TOGA-COARE campaign consisted of a 4-month intensive observing period (IOP) (Figure 1.2) monitoring the high-frequency atmospheric/oceanic components in the western Pacific warm pool region and a large-scale mooring/buoy time series of co-located atmospheric/oceanic data as well as the air-sea exchange of heat, moisture and momentum spanning more than a decade across the tropical Pacific and Atlantic oceans. One of the key elements at the air-sea interface that has been overlooked in previous coupled climate models, SST diurnal cycle, revealed by the observations from TOGA-COARE and other parallel field campaigns, is found to impose a "rectification effect" on the tropical air-sea interaction intensity by mitigating the SST bias felt by the atmosphere in the low-coupling-frequency climate models (*Danabasoglu et al., 2006; Bernie et al., 2007, 2008*).

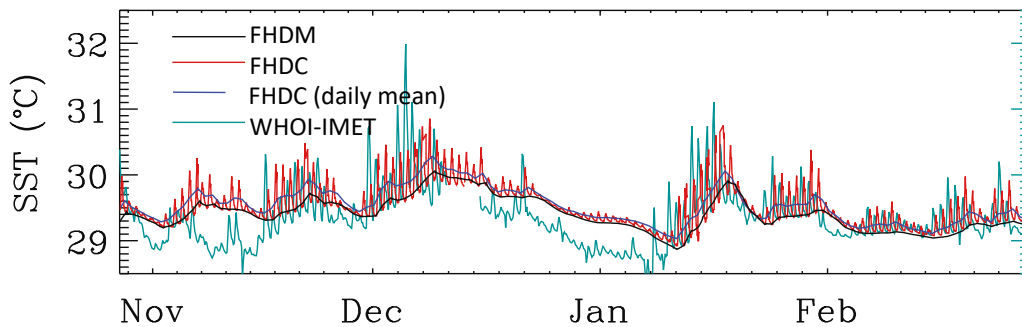


Figure 1.3: Time series of SST during the TOGA-COARE IOP from observations collected by Woods Hole Oceanographic Institute-Improved MEteorological instrument (WHOI-IMET) mooring, situated within the IFA region (green). Modelled SST forced by daily-mean shortwave heat flux (FHDM, black) and shortwave heat flux with diurnal cycle (FHDC, red) at the model grid point nearest to WHOI-IMET location are superimposed. A running mean FHDC SST is also shown in blue. Figure is adapted from Figure 7 in *Bernie et al. (2007)*.

The diurnal cycle of SST is essentially forced by the diurnal cycle in the incoming shortwave radiation associated with the sunrise and sunset over the

course a day. During the daytime warming period, heat absorbed at the sea surface drives a rapid thermal stratification and forms a thin layer of warm water. This shoaling of the surface layer leads to a rapid increase of SST during the daytime warming period as the heat capacity of the surface layer is inversely proportional to its thickness. The strength of this warming signal is mainly determined by the meteorological condition at the time when the solar radiation is large - lower wind during the daytime results in larger SST warming. As the day progresses through the afternoon, the stabilizing effects of solar radiation absorption are reduced and the surface warm layer starts to erode (deepening) due to the convective mixing caused by the loss of heat. Meanwhile, the SST decreases rapidly along with the erosion of the diurnal layer until the night time when the diurnal layer is completely removed and the mixed layer (ML) depth reaches to the point where the water below the ML is cooler. This loop repeats the following morning. The diurnal cycle of SST has demonstrated a robust rectification effect on the intraseasonal SST variability and time-mean SST in both one-way forced ocean models (e.g. *Shinoda and Hendon, 1998; Shinoda, 2005; Bernie et al., 2005, 2007*) and coupled climate models (e.g. *Danabasoglu et al., 2006; Bernie et al., 2008; Tian et al., 2016, 2018*). An example taken from *Bernie et al. (2007)* (Figure 1.3) shows the modelled SST (red) forced by observations is systematically warmer than that forced by daily-mean fluxes. The systematic warming effect of the SST diurnal cycle on the time-mean SST is more readily seen by comparing the daily-mean sub-daily-forced SST to the daily-mean SST. The diurnal cycle of SST increases the intraseasonal SST variability by a third. These increases on the long-term SST behaviour are caused by the inclusion of what is also referred as the rectification effect of SST diurnal cycle. Further studies involving general circulation models assess the rectification effect of diurnal cycle of SST and obtain improved representation of the long-term climatic modes such as Madden-Julian Oscillation (e.g. *Bernie et al., 2007, 2008*), El Niño-Southern Oscillation (ENSO) magnitude and variability (e.g. *Danabasoglu et al., 2006; Tian et al., 2016, 2018*).

Other than the diurnal cycle in SST, the high-frequency coupling of the atmosphere and ocean has played an important role in driving the ML evolution and mid-latitude SST variabilities (e.g. *Frankignoul, 1985; Frankignoul et al., 1998; Alexander and Deser, 1995; Alexander and Penland, 1996; Alexander and Scott, 2000*). For example, *Qiu et al. (2004)* carried out a one-dimensional model study over the Kuroshio Current Extension with the data collected at a buoy site situated in the Kuroshio recirculation to the south of Japan. By smoothing the surface fluxes to produce the baseline low-frequency ocean response, the SST anomalies induced by synoptic-scale atmospheric variability are computed by subtracting the baseline SST from the results. It is found that SST signals induced by the synoptic-scale heat flux forcing are mostly oscillatory with an amplitude of $\pm 1^\circ\text{C}$, while synoptic-scale wind stresses result in systematic cooling of SST by enhancing the entrainment of the colder subsurface water into the surface ML. Note that in *Qiu et al. (2004)* there is no rectification warming on SST induced by the synoptic-scale air-sea heat fluxes whereas in TOGA related studies, SST is warmed in response to the diurnal air-sea heat fluxes. This difference indicates that the SST responds differently to different high-frequency components in the air-sea fluxes and could be associated with the forcing phase and magnitudes. In the high-latitude subpolar region, the aforementioned local responses of SST and ML depth to the high-frequency atmospheric forcing can be further translated into the convective mixing and changes on the thermocline structure to affect the water mass formation and time-mean ocean circulation. *Balan Sarojini and von Storch (2009)* used an empirical model to generate fluctuations of day-to-day air-sea fluxes anomalies with constrained magnitude deviating from the climatological mean state. The relative influence of the fluctuations on the ocean circulation are assessed with an ocean general circulation model (OGCM). They found that the fluctuations of the surface fluxes lead to an increase of modelled Atlantic Meridional Overturning Circulation (AMOC) via the increased interhemispheric density field difference resulting from enhanced mixing in the subpolar North Atlantic. The impact on ocean circulation of the sensitive response of the

convective mixing in subpolar region to the high-frequency atmospheric forcing is further confirmed in other parallel works. *Holdsworth and Myers (2015)* studied the influence of high-frequency atmospheric forcing on the circulation and deep convection in the Labrador Sea by comparing model simulations with and without synoptic atmospheric phenomena. They found that in the absence of high-frequency atmospheric phenomena the AMOC is weakened by about 25%, and the average maximum ML depth in Labrador Sea decreased by more than 20%. More recently, a global-scale investigation on high-frequency atmospheric forcing is completed by *Wu et al. (2016)*. By comparing the model simulations forced by surface heat and momentum fluxes calculated from 6-hourly and monthly meteorological variables, they discovered a substantial increase (by 50%) in the wind power input into the ocean when the model is forced by 6-hourly surface fluxes (see also *Zhai et al., 2012*), along with a strengthening on the wind-driven subtropical gyre (10%-15%). The subpolar gyre associated with the enhanced deep convection events, and a resultant increase in the AMOC, implying that the high-frequency components in the atmospheric forcing play a significant role in driving the global ocean circulation and are vital for the fidelity of the paleo- and future climate projections.

As fluctuating as the high-frequency signals in the observed surface fluxes can be, these high-frequency variabilities changing over time scales from a few hours to several days are often a reflection of the transient nature of the coherent weather systems that are active over a rather local scale (1-1000km) including the mesoscale events (50-1000km) like mesoscale cyclones (e.g. hurricanes, mesoscale polar lows) and orographically-forced low-level jets (e.g. Greenland tip jet) (Figure 1.4), and even smaller convective scales fluctuations (1-50km). Before the era of satellite, the spatial structure of the aforementioned systems were usually acquired by sparse in-situ measurements such as weather stations and met buoys with the resolution restricted to scales larger than several hundreds kilometres. The availability of the satellite-borne scatterometers and radiometers opens up the possibility of the investigation of the

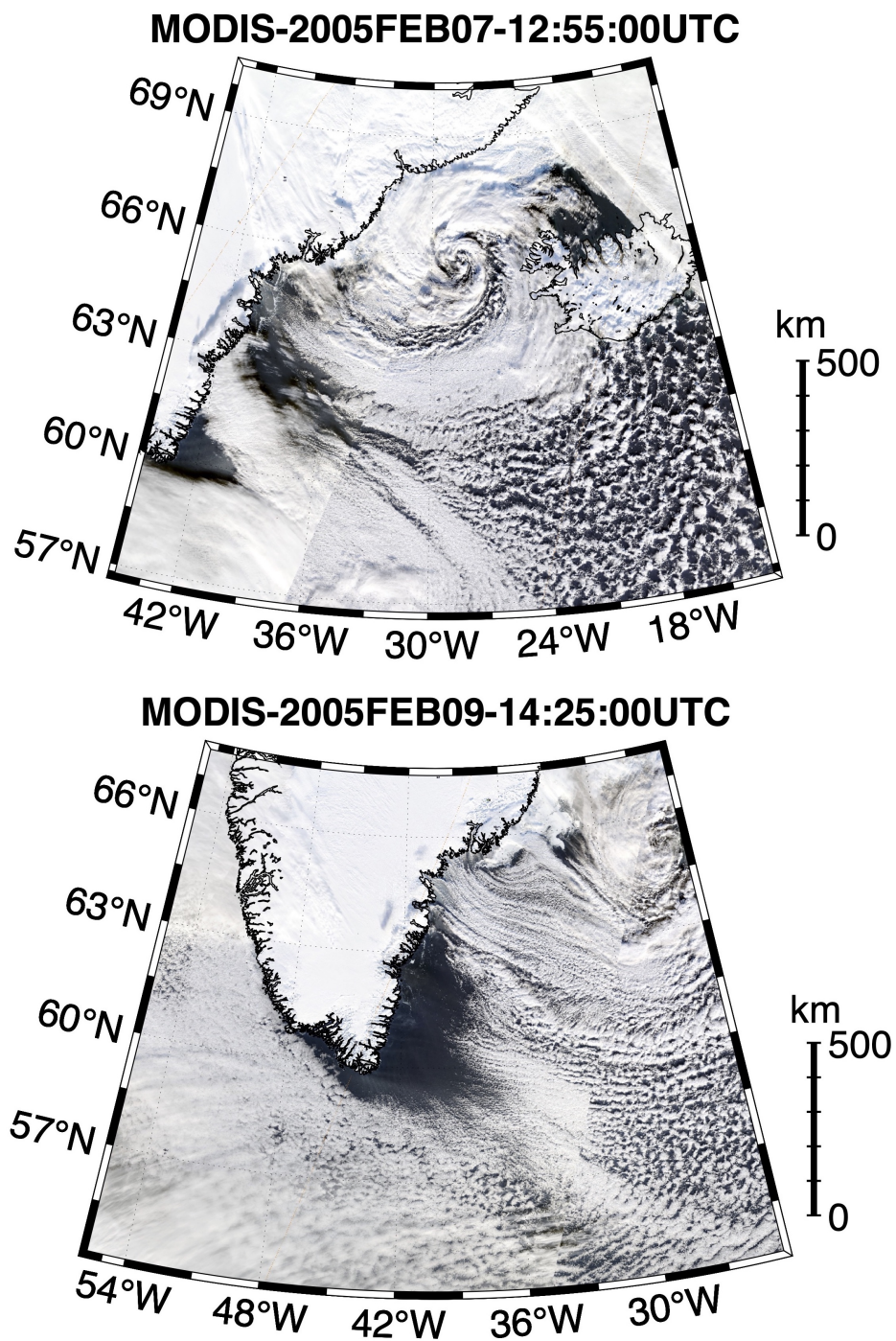


Figure 1.4: True color satellite imagery derived from Moderate Resolution Imaging Spectroradiometer (MODIS) corrected reflectance products (<https://worldview.earthdata.nasa.gov/>). Upper panel shows a cyclonically rotating cloud cluster imprinted by a mesoscale polar low over Denmark Strait, east of Iceland. Lower panel depicts this fast low level jet blowing off the southern tip of Greenland, forming a patch of clear sky around the ambient region.

ocean-atmosphere interaction on smaller scales. Since the turn of this century, the high-resolution wind measurements derived from the NASA QuikBird microwave scatterometer, so-called QuikScat scatterometer (e.g. *Chelton et al.*, 2001, 2004; *O'Neil et al.*, 2003, 2005) has revealed previously unresolved small-scale features in the ocean winds associated with interactions with the SST gradient and surface currents associated with oceanic fronts and eddies. Significant linear dependence of the wind stress divergence and wind stress curl on the downwind and crosswind SST gradient is found over regions with strong oceanic fronts and abundant eddy activities across the global ocean (Figure 1.5). Persistent small-scale structures in wind stress curl are also found to be significantly correlated with the sharp SST front structure. There are various explanations of such strong correlation between small-scale wind stress variability and mesoscale SST gradient, including vertical mixing of momentum, changes in the planetary boundary layer depth, a secondary atmospheric response due to pressure gradients within the boundary layer, and changes in cloud cover across the fronts (*Xie*, 2004; *Small et al.*, 2008; *Hogg et al.*, 2009). Although there is no single universally acknowledged mechanism for the small-scale wind variation in response to the underlying mesoscale SST structure, the feedback of such small-scale wind perturbations on the ocean circulation is non-local (e.g. *Milliff et al.*, 1996; *Spall*, 2007; *Seo et al.*, 2007; *Hogg et al.*, 2009).

The advent of high-resolution wind measurements from satellites also stimulates the effort to represent the mesoscale atmospheric variability in the coarse-resolution climate reanalyses dataset and coupled climate model for assessing ocean's response to the mesoscale atmospheric forcing. *Milliff et al.* (1998) synthesized high-wavenumber wind variability into National Centers for Environmental Prediction (NCEP) reanalyses wind fields to retain the observed wind power spectral slope derived from scatterometer measurements at all resolved wavelength. The high-wavenumber (small-scale) wind perturbation leads to enhancement of the mean atmospheric forcing compared to the NCEP

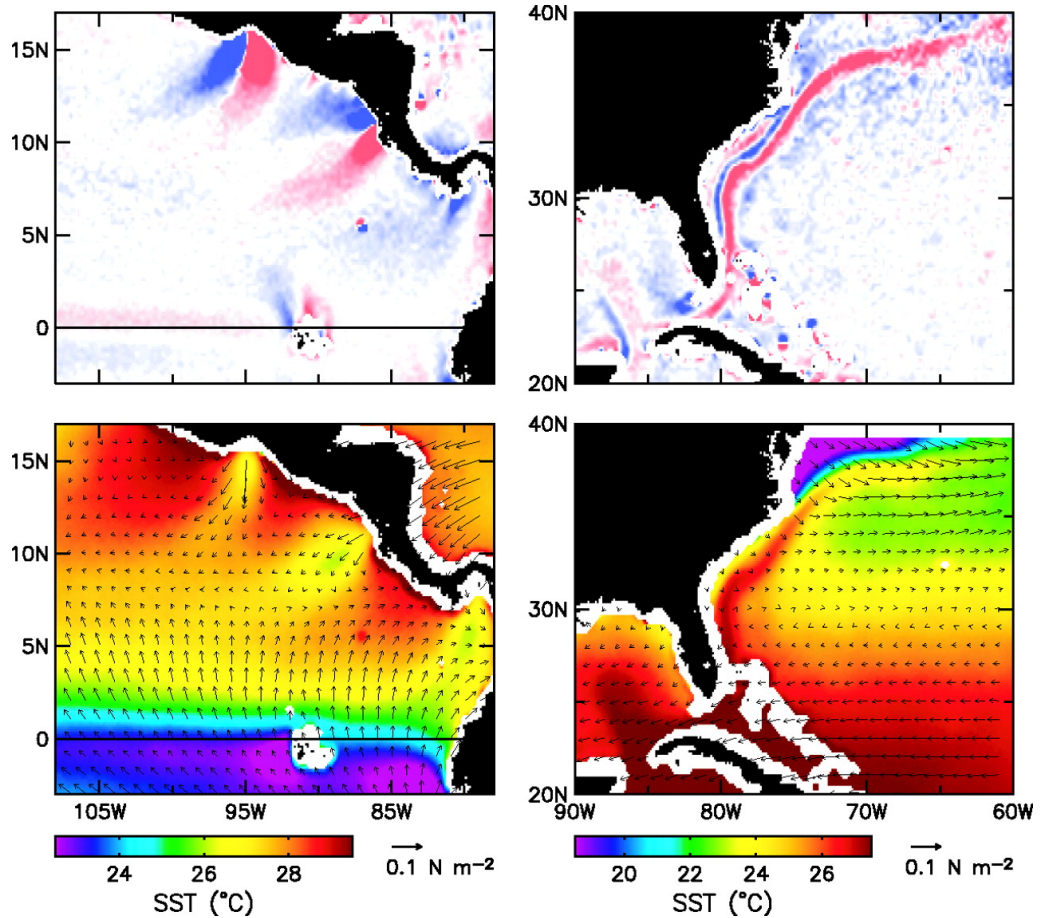


Figure 1.5: Four-year averages (August 1999–July 2003) of the spatial high-pass-filtered curl of the wind stress (top) and of the SST and vector-average wind stress (bottom) for the eastern tropical North Pacific (left panels) and the western North Atlantic (right panels). Figure is adapted from Figure 5 in *Chelton et al.* (2004).

wind, leading to a different response in the mean ocean circulation pattern. Although the ocean response of such wind perturbation is not fully reconciled due to the simplicity of the ocean circulation model used by *Milliff et al.* (1998), it implies that the ocean response to the small-scale wind perturbation is somewhat non-local and the systematic difference tends to emerge over larger-scale. With a more comprehensive OGCM, *Condrón and Renfrew* (2013) studied the impact of the mesoscale polar lows on the ocean circulation pattern, where they conducted twin experiments respectively forced by European Centre for Medium-Range Weather Forecast (ECMWF) ReAnalyses (ERA-40) wind and the same ERA40 wind with the mesoscale polar lows incorporated in from a

parameterization tuned to fit scatterometer measurements (*Condrón et al.*, 2008). By comparing the simulation of control (forced by standard ERA40 reanalysis wind) and perturbation experiments (mesoscale polar lows incorporated), they find that the polar lows drive intensified open-ocean deep convection events in the Greenland Sea, Norwegian Sea and Iceland Sea, which is mostly attributed to the excessive heat loss caused by the greater wind speed due to the mesoscale polar lows. The deep convection response further translated into a spin-up of the North Atlantic subpolar gyre (SPG) circulation, accompanied by an increase in northward heat transport. These effects of polar lows on SPG indicated that under the future climate scenarios, the predicted northward shift of mesoscale polar lows in the Nordic Seas can potentially lead to a weakened AMOC in the future. A similar technique was applied on incorporating Greenland's tip jets in reanalyses wind fields based on microwave scatterometer measurements (*Sproson et al.*, 2010). They found that the excessive heat loss and increased wind stress associated with the strengthened wind forcing from the tip jets leads to a better estimate of ML depth evolution in the Irminger Sea (*Våge et al.*, 2008), consistent with the observational evidence (*Pickart et al.*, 2003). *Hu and Meehl* (2009) assessed Atlantic hurricanes in influencing the AMOC and meridional heat transport (MHT) and found that the strengthened wind forcing and increased precipitation induced by the inclusion of hurricanes have opposite impact on AMOC and MHT and the outcome of the net effect is determined by the outcome of two competing processes. A systematic study on global-scale high-resolution operational analyses data conducted by *Jung et al.* (2014) compared the ocean circulation response to high-resolution (0.4°) and coarse-grained low-resolution (1.8°) atmospheric forcing fields and found that the high-resolution atmospheric forcing fields lead to an increase in the wind-drive gyre in the North Pacific and North Atlantic by 5-10% and an increase in AMOC by 5-10% driven by the turbulent heat flux changes in the Nordic Sea. It is therefore emphasized that the mesoscale atmospheric phenomena including the fronts, mesoscale cyclones and the topographic jets play an important role in driving the mean oceanic

circulation.

1.3 Stochastic parameterization of atmospheric forcing

As important as the high-frequency and small-scale variabilities are, incorporating them into the numerical model has always been challenging. First of all, there is always imperfection of our knowledge of the fine-scale part of the system that prevents models from explicitly resolving the small-scale and high-frequency processes. Secondly, the implementation of high-resolution and small time step simulations is computationally expensive. Instead of resolving the explicit processes over fine-scale regimes, sometimes it is more practical to estimate the effect of a collection of unresolved processes on the resolved scales in the form of certain spatial or temporal mean terms of the related properties which is referred to as the ‘bulk effect’. The mathematical representations (i.e. parameterization) of the ‘bulk effect’ on the properties over resolved scales is then implemented to help models make correct predictions. Parameterizations representing these bulk effects are referred to be *deterministic*, as they are formulated with diagnostics from the coarse-grained high-resolution (e.g. eddy-resolving) model solution, resolved-scale properties, parameters empirically determined from observations or tuned to yield numerical stability or desired physical properties. Many deterministic parameterization schemes have been used to parameterize fine-scale processes such as eddy diffusivity (e.g. *Gent and McWilliams*, 1990; *McDougall and McIntosh*, 1996; *Fox-Kemper and Menemenlis*, 2008) and surface momentum and heat exchanges between ocean and atmosphere, which are associated with the small-scale turbulence and instability within the marine-atmospheric boundary layers (e.g. *Large et al.*, 1994; *Fairall et al.*, 2003). It is noted, though, that the assumption of a ‘bulk effect’ in air-sea interaction processes is made under the context where the unresolved scales are in statistical equilibrium with the resolved scales. This equilibrium is constrained by the ‘large number law’, which is essentially

assuming the unresolved events are large enough in number within a single model grid box or within a limited period of time (e.g. *Imkeller and Monahan, 2002; Williams, 2005*) to allow certain level of predictability of the status of the grid to emerge.

However, in turbulent fluids, the above assumption does not always hold, as the unresolved processes do not necessarily follow the large number law, which renders the conventional deterministic parameterizations problematic (e.g. *Palmer, 2001; Williams, 2005*). An increase of the model resolution is ideally a solution for the unresolved processes with corresponding improvement of the knowledge of these processes. It is shown that, however, an increase of the model resolution does not necessarily eliminate the systematic errors of the model (e.g. *Palmer, 2001; Nicolis, 2004*) as the high-resolution models inevitably apply closure schemes to parameterize even smaller-scale processes which are formulated under the same principle as their low-resolution counterparts. It is conjectured that since the unresolved processes are effectively random compared to the resolved ones, they can be practically modelled by adding random noise to the models, which is referred to as a *stochastic* parameterization. Stochastic parameterization has received major success in fluid-dynamic models of homogeneous and isotropic three-dimensional turbulence, where the contribution of the small-scale turbulence to large-scale flow is controlled by the non-linear interaction of energy and enstrophy between different spatial scales and represented by a stochastic term acting in the wavenumber spectra space (*Berloff, 2005*).

The stochastic parameterizations have not just been found effective in representing the intrinsic variability of turbulent flows (e.g. atmosphere and ocean), but also been widely adapted to represent some of the fluctuating components in the external forcing, such as the atmospheric forcing of the ocean (e.g. *Frankignoul et al., 1997, 1998; Sura et al., 2001; Sura and Penland, 2002; Chhak et al., 2006; Zhai et al., 2014*), where the atmospheric forcing is formulated with some random processes because the atmospheric processes

associated with ‘weather’ systems are rapidly varying and decorrelate much faster than the forced ocean. In most of these cases, stochastic parameterizations serve as a strategy to reduce the complexity of the modelled system. The oceanic variabilities of interest have much longer timescales, from years to decades, compared to the decorrelation timescale of the atmosphere, hence the assumption of atmospheric forcing being stochastic is reasonable (*Sura and Penland, 2002*).

The effect of ‘stochastic’ weather noise on the oceanic ‘climate’ system has been an object of research since Hasselmann’s seminal paper published in 1976 (*Hasselmann, 1976*, H76 hereafter). H76 proposed a climate model where there are two distinct timescales, typically a fast one (the weather) and a slow one (the climate or the ocean), where the slow system is forced by fast scale fluctuations formulated as ‘white noise’. The climate variability predicted by this model then arises as the integrated response to a random excitation provided by the atmospheric weather. This classic theory was later applied to describe the variability of the mid-latitude sea surface temperature (SST) (e.g. *Frankignoul and Hasselmann, 1977; Frankignoul, 1985; Frankignoul et al., 1998; Sura et al., 2006; Penland and Hartten, 2014; Clement et al., 2016*), the El Niño and Southern Oscillation (ENSO) (e.g. *Penland and Sardeshmukh, 1995; Alexander and Penland, 1996; Blanke et al., 1997; Perez et al., 2005*), decadal variability of the overturning circulation (e.g. *Kwon and Frankignoul, 2012*) and interannual variability of the open ocean deep convection (e.g. *Ramstorf, 2001; Kuhlbrodt et al., 2001*).

The aforementioned studies have demonstrated attractive results produced by the assumption of stochastic atmospheric forcing in simplified conceptual models. In fact, one of the advantages of stochastic representation of unresolved variability in a climate model is to allow us to understand the underlying long-term climatic features through the stochastic reduction of multi-scale deterministic processes. These conceptual models have easy analytical tractability due to the simplified mathematical forms.

In more realistic atmosphere and ocean models, although the stochastic parameterization itself has been widely adopted to reproduce the intrinsic variabilities of flows over sub-grid scales, it is rare to apply simple stochastic parameterization of the atmospheric forcing at the air-sea interface as most of the atmospheric variabilities from daily-to-monthly timescales has been explicitly resolved and the simulated variabilities have a broader spectrum rather than the two scales as simplified in Hasselmann's theory. This does not necessarily exclude stochastic parameterization of the atmospheric forcing from the more realistic model experiments. The high-frequency and small-scale fluctuations captured in the observations of the near surface meteorological variables are always challenging for the models to properly represent, while stochastic parameterization has its advantage of obtaining some statistical consistency for the numerical simulation. For example, the near surface meteorological observations shows considerable sub-daily fluctuations but these are not always well-resolved in global-coverage reanalyses data including the newly-released ECMWF 5th generation global climate ReAnalysis (ERA5), which is numerical weather prediction (NWP) model output combined with newly available observations across a wide range of platforms. Figure 1.6 demonstrates the problematic wind kinetic energy spectrum in ERA5 wind estimate comparing to multiple averaged *in-situ* buoy time series (upper) and time-averaged scatterometer measurements (lower). Buoy measurements are documented in National Data Buoy Center (NDBC) and collected from *Prediction and Research Moored Array in the Tropical Atlantic* (PIRATA) project for year 2008. The co-located ERA5 time series are selected for comparison with buoy time series. The observed wind wavenumber spectra are derived from QuikScat sea surface wind measurements over the period of a year for comparison. Both the scatterometer measurements and ERA5 wind are sampled from the Atlantic Ocean (60°S to 65°N) area. The underestimate of the sub-daily and small-scale (<500-kilometer wavelength) wind variance illustrated in Figure 1.6 stands out and is due to under-represented high-frequency processes in NWP near sea surface. The stochastic parameterization of the

atmospheric forcing fields can be used to address these underestimated variabilities in the current generation global climate reanalyses and estimate the impact on ocean variabilities and, perhaps, their long-term trends.

1.4 Thesis objectives

There have been studies suggesting that the ocean circulation can be very sensitive to air-sea fluxes associated with unresolved weather systems such as polar lows and tip jets (e.g. *Pickart et al.*, 2003; *Condron and Renfrew*, 2013). However, a systematic study of the impact of these weather systems on global ocean circulation is still lacking. Furthermore, the underlying physical mechanisms remain unclear. *Williams* (2012) studies on the climatic impacts of stochastic air-sea fluxes associated with these weather systems and proposed the following mechanism: surface cooling destabilizes the water column and deepens the ML, whereas surface heating simply stabilizes the water column and cannot shoal the ML. The net effect of stochastic air-sea heat fluxes is therefore a deeper mixed layer and reduces SST. This conjectured mechanism, intriguing as it is, seems to be at odds with previous studies on diurnal cycle of ocean surface mixed layer, where diurnal heating/cooling is found to increase the time-mean SST because the daytime heating causes the mixed layer to shoal and reduces its heat capacity. Further study is clearly needed in order to sort out these seemingly conflicting statements about climatic impacts of stochastic air-sea fluxes. This thesis is therefore focusing on address the questions associated with 1) the conflicting results between stochastic air-sea fluxes and diurnal heat fluxes and 2) a more general unresolved mesoscale weather systems impact on ocean circulation. Chapter 2 and Chapter 3 are designed to address the first question by conducting sensitive experiments targeting the diurnal meteorological variabilities and stochastic air-sea fluxes using one-dimensional mixed layer models, where the aforementioned mechanism associated with the mixed layer response are well represented. In Chapter 2 mainly focus on

discussing the sub-daily atmospheric variabilities in meteorological variables instead of the air-sea fluxes themselves, which helps to differentiate the effects of the flux-averaging and variable-averaging on the SST. Chapter 3, on the other hand, focusing on the response of ML depth and SST to the stochastic air-sea fluxes in a more idealized experimental setup. Chapter 4 is trying to assess the response of the ocean circulation to the mesoscale weather systems in a more realistic framework using a three dimensional OGCM incorporating the direct one-dimensional response of SST and ML depth into an eddying ocean.

1.5 Thesis outline

In Chapter 2, we provide a case study focusing on assessing the impact of observed high-frequency fluctuations in the near surface meteorological variables on the SST and surface ML depth in the central Arabian Sea, taking advantage of a set of year-long high-frequency co-located meteorological and oceanic measurements. The distinct seasonality of the meteorological conditions allows a detailed evaluation of the high-frequency weather variability under different background oceanic states. The sensitivity of the oceanic variability is quantified using a one dimensional ML model and two types of forcing scenarios – observed atmospheric forcing and low-pass filtered atmospheric forcing with the cut-off frequency of one cycle per day.

In Chapter 3, we revisit the classic Hasselmann’s stochastic climate model and evaluate the SST response to the stochastic air-sea heat fluxes in terms of the variability and time-mean trend affected by simultaneous ML depth variation. Some insights are gained from a series of sensitivity experiments by alternating solar penetration schemes. The results indicate that the instantaneous response of the ocean ML may not qualitatively alter the spectral characteristics of SST response to the stochastic forcing from the slab model. The ML depth variation, however, can result in asymmetric SST response to the surface cooling and surface heating due to the change of the ML heat capacity between the ML shoaling

(surface heating) and ML deepening (surface cooling) periods. The net effect of asymmetric SST response tends to result in time-mean warming of SST compared with the SST forced by mean surface heat fluxes.

In Chapter 4, we explore the application of a stochastic parameterization of high-frequency and small-scale atmospheric forcing at the air-sea interface based on the newly-released ERA5 surface wind field. A statistical consistency with observations is achieved with the stochastic parameterization and its impact is assessed using both a one-dimensional ML model and a three-dimensional ocean general circulation model (OGCM).

In Chapter 5 we present our conclusions for the work as a whole and suggest a few avenues for future work.

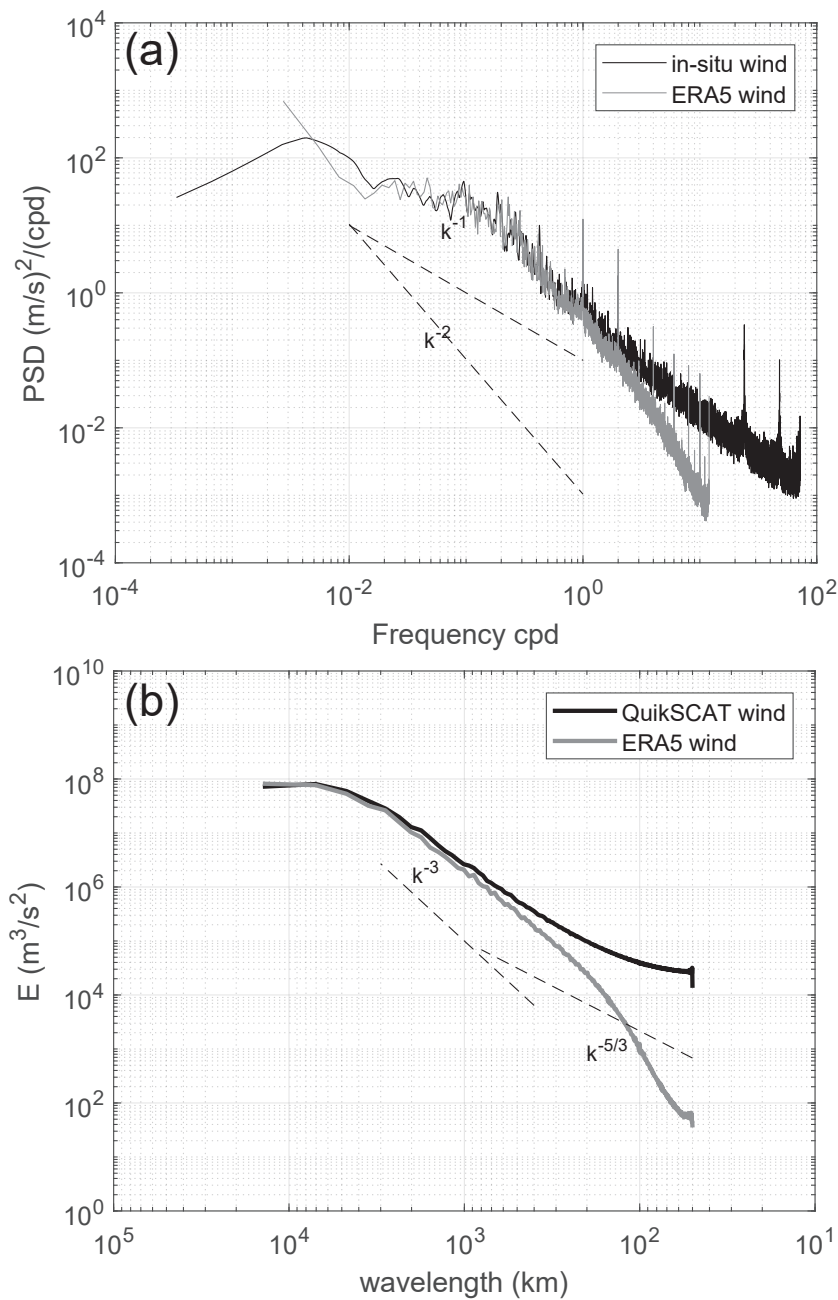


Figure 1.6: (a). Wind kinetic energy frequency spectrum derived from the wind time series collected from NDBC and PIRATA buoys (black), and from co-located ERA5 surface wind field (grey). The figure shows the averaged frequency spectra over 18 buoy locations. (b) is similar to (a) except that the comparison is made between QuikSCAT wind and ERA5 wind on wavelength domain. The wavelength spectra of the ERA5 and QuikSCAT wind are averaged over the Atlantic Ocean (60°S to 65°N). ERA5 wind kinetic energy discernibly drifts away from the observations approaching the sub-daily and higher frequency bands as well as the small-scale regimes with characteristic wavelengths less than 500 kilometres, indicating a lack of high-frequency/small-scale variability in reanalysis wind estimates.

IMPACT OF HIGH-FREQUENCY WEATHER SYSTEMS ON THE SST AND SURFACE MIXED LAYER (ML) DEPTH

The following chapter was published as paper in *Journal of Geophysical Research: Oceans* entitled with ‘The impact of high-frequency weather systems on SST and surface mixed layer in the Central Arabian Sea’ with co-authors Xiaoming Zhai and Ian Renfrew. The work is undertaken by Shenjie Zhou, all the co-authors contributed to the writing of the manuscript. It is as published with extra figures and texts that were omitted in the published paper due to space limitations. This chapter bears the focus on the high-frequency variability, in particular the sub-daily fluctuations, in the atmospheric forcing.

2.1 Introduction

Variability in air-sea fluxes on sub-daily time scales has been recognized as important in perturbing sea surface temperature (SST) and forcing changes in climate variability. For example, previous studies show that diurnal variations in solar radiation lead to a diurnal cycle in SST (e.g. *Shinoda and Hendon, 1998; Shinoda, 2005*); and this diurnal cycle in the SST causes warmer daily- and intraseasonal-mean SST, referred as the rectification effect of the SST diurnal

cycle (*Bernie et al.*, 2005). The impact of high-frequency atmospheric forcing on low-frequency SST variation can further influence long-term atmosphere-ocean phenomena such as the Madden-Julian Oscillation (e.g. *Bernie et al.*, 2007, 2008), the Intraseasonal Oscillation (e.g. *Ham et al.*, 2014; *Hu et al.*, 2015) and the El Niño-Southern Oscillation (ENSO) (e.g. *Danabasoglu et al.*, 2006; *Terray et al.*, 2012).

Most modelling studies that examine the impact of atmospheric forcing on sub-daily time scales have done so by filtering the surface turbulent and radiative fluxes. Few studies have filtered the meteorological variables. Owing to the non-linear dependence of air-sea fluxes on meteorological variables, high-frequency fluctuations in meteorological variables such as surface wind and air temperature not only cause air-sea fluxes to vary at high frequencies but also contribute significantly toward the low-frequency and time-mean air-sea momentum and energy fluxes (e.g. *Zhai et al.*, 2012; *Gulev and Belyaev*, 2012; *Zhai and Wunsch*, 2013). Therefore, for the purpose of assessing the impact of weather systems on the ocean, filtering the meteorological variables, rather than air-sea fluxes, is the appropriate approach. A number of recent studies have investigated the impact of mesoscale and synoptic-scale weather systems on the ocean and found that the presence of weather systems (e.g. polar lows, topographic jets) strongly enhances heat loss in the subpolar North Atlantic, which leads to intense deep convection in convective areas (*Våge et al.*, 2008; *Condrón et al.*, 2008), spinning-up the gyre circulation and strengthening the meridional overturning circulation (*Condrón and Renfrew*, 2013; *Jung et al.*, 2014; *Holdsworth and Myers*, 2015; *Wu et al.*, 2016). However, there have been few studies focusing on the composite impact of weather systems on sub-daily time scales on the upper ocean, particularly at low latitudes, with the exception of specific studies on the impacts of tropical cyclones on the upper ocean (e.g. *Bender et al.*, 1993; *Price et al.*, 2008; *Dare and McBride*, 2011).

In this study, we use one-dimensional mixed-layer models to investigate the impact of weather systems on sub-daily time scales on the SSTs and ML depth

in a monsoon-dominated tropical sea, the central Arabian Sea, taking advantage of the comprehensive observational data available at this site (*Weller et al.*, 1998). In particular, we compare model simulations forced by sub-hourly sampled meteorological variables, including surface wind, air temperature, humidity and cloud amount, to simulations forced by variables that have been filtered. Additional sensitivity experiments are also conducted to pin down the key meteorological variable(s) and their impacts on sub-daily time scales in the central Arabian Sea.

2.2 Data and Methods

2.2.1 Observations

Our meteorological observations are year-long (Oct 16, 1994 - Oct 19, 1995) time series of surface 10-meter zonal and meridional wind velocities, air and sea surface temperatures, relative humidity, barometric air pressure, downwelling shortwave and longwave radiation and precipitation rate recorded every 7.5 minutes by a moored meteorological measurement package deployed off the Omani coast (15.5°N, 61.5°E; Figure 2.1) in the central Arabian Sea. Co-located subsurface oceanic instruments attached on the mooring reached down to 300 meters, and recorded temperature, salinity and current velocities every 15 minutes. The atmospheric conditions at this site are dominated by three seasons (see Figure 2.2a and b): the northeast (NE) monsoon season (November, 1994 - mid February, 1995) is characterized by moderate, cold and dry northeasterly wind forcing, and oceanic heat loss; the intermonsoon season (mid February, 1995 - mid June, 1995) is dominated by weak wind events, allowing oceanic heat gain; and the southwest (SW) monsoon season (mid June, 1995 - mid September, 1995) features a strong southwesterly wind burst associated with the Findlater Jet (*Findlater*, 1977) blowing diagonally across the Arabian Sea, and summertime oceanic heat gain. A detailed introduction of this dataset is covered

in *Weller et al.* (1998), which confirms that the atmospheric conditions from 1994 to 1995 are generally typical for this site.

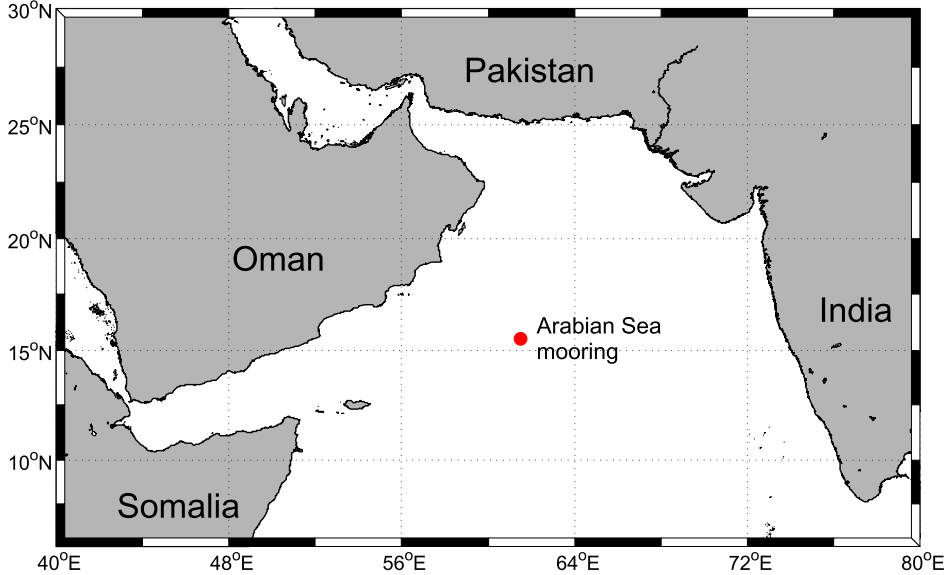


Figure 2.1: The Arabian Sea Upper Ocean Dynamics mooring is located at 15.5°N, 61.5°E, as marked by the red circle. The location is on the climatological axis of Findlater Jet and representative of the open ocean rather than coastal water.

2.2.2 Model description

The main simulations shown in this chapter are conducted with the one-dimensional Price-Weller-Pinkel (PWP) model developed by *Price et al.* (1986). The PWP model is prescribed with surface buoyancy fluxes and wind stress, as such modelled ocean reflects pure passive response to the surface forcing. In the model, mixing processes are attributed to two turbulent energy sources: the static instability introduced by surface buoyancy loss and the shear instability generated by the vertical shear of the current at the base of ML due to surface wind stress. The net surface heat flux is composed by sensible and latent heat fluxes (turbulent heat fluxes), net longwave radiation and net shortwave radiation. The turbulent heat flux and longwave radiation are only applied on the surface layer, while the shortwave radiation penetrates over the water column with a double exponential dependence to the depth (*Krause,*

1972), as expressed in Eq.2.2.1,

$$I(z) = I(0)[I_1 e^{(\frac{-z}{\lambda_1})} + I_2 e^{(\frac{-z}{\lambda_2})}]. \quad (2.2.1)$$

The subscripts ‘1’ and ‘2’ refer to the fraction (%) of shortwave and longwave components of the insolation, with the value of 0.6 and 0.4 respectively in PWP model. $I(z)$ denotes the solar absorption below the depth z . The absorption of solar layer between depth z and $z+\Delta z$ equals to

$$I(z) - I(z + \Delta z). \quad (2.2.2)$$

In the case of fairly clear, mid-ocean water (type IA) (*Jerlov*, 1976), which we assume holds for the measurement in the central Arabian Sea site,

$$\begin{aligned} I_1 &= 0.62 & \lambda_1 &= 0.6m \\ I_2 &= 1 - 0.62 & \lambda_2 &= 20m, \end{aligned} \quad (2.2.3)$$

and thus about half of the solar radiation is absorbed within the uppermost meter of the water column. The remaining shortwave component of the insolation is absorbed with an extinction scale of 20 m. For each time step, after the surface heat and freshwater flux being applied on temperature, salinity and density profiles, the model starts to remove the static instability by executing a free convection subroutine in order to satisfy the static stability criterion, ensuring the vertical density gradient is positive throughout the water column, i.e.

$$\frac{\partial \rho}{\partial z} \leq 0. \quad (2.2.4)$$

Starting from the uppermost layer, all the variables above certain depth where the density gradient is negative (statically unstable) would be completely mixed by replacing the vertical average between the depth and the surface. This routine iterates through all the layers til the entire water column is statically stable.

The wind mixing is parameterized by running the density profile through two criteria, ML stability and shear flow stability (Eq. 2.2.5). The ML stability simulates the ML entrainment by the relaxation of the bulk Richardson number (R_{i_B}) over the whole ML and the shear flow stability simulates the effects of the local mixing caused by the vertical of the current velocity by relaxation of the gradient Richardson number (R_{i_G}) over the adjacent layers at the base of ML. These two processes are essentially the wind-mixing processes in the sense that the velocity which appears in the Richardson numbers is entirely wind driven, and both processes would be inactive if the wind vanished.

$$\begin{aligned}
 R_{i_B} &= \frac{gh\Delta\sigma}{\sigma(\Delta V)^2} \geq 0.65, \\
 R_{i_G} &= \frac{g\frac{\Delta\sigma}{\Delta z}}{\sigma\frac{(\Delta V)^2}{(\Delta z)^2}} \geq 0.25.
 \end{aligned}
 \tag{2.2.5}$$

The R_{i_B} parameterizes the bulk mixing effect of the ML entrainment forced by the surface wind stress by taking the ratio of the density gradient and vertical current shear at the base of the ML depth. The entrainment to the ML depth is switched on when the R_{i_B} is smaller than 0.65 (*Price et al.*, 1978), a value determined from the laboratory experiments. The R_{i_G} calculates the ratio between the square of buoyancy frequency (or Brunt-Väisälä frequency). The gradient Richardson number is calculated for all the adjacent layers within the stratified part of water defined by the bulk mixing process. The sequenced partially mixing is activated between the layer with the smallest R_{i_G} and the layer just beneath when the smallest R_{i_G} is less than 0.25. The critical gradient Richardson number is set to be 0.25 based on laboratory experiments (*Miles*, 1961; *Howard*, 1961). The effect of bulk mixing and gradient mixing has been discussed in *Price et al.* (1986) (Figure 2.3) that the bulk mixing can clearly identify the depth of the base of ML, but the thermocline structure shown on the temperature profiles are unrealistically sharp. The inclusion of gradient mixing causes a smoothing of such abrupt transition between the ML and level below to acquire a reasonable thermocline structure.

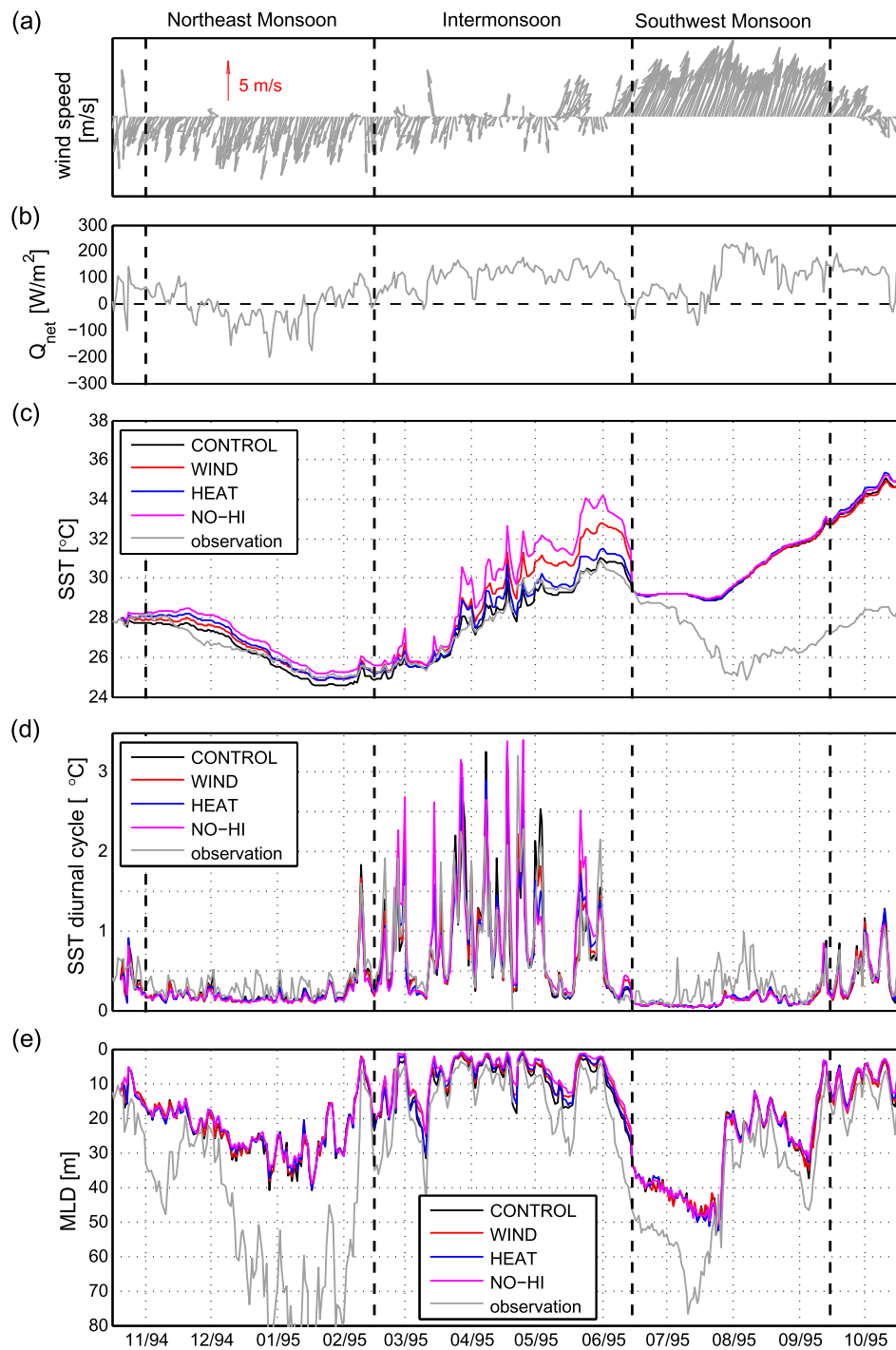


Figure 2.2: Year-long time series of (a) wind speed, (b) daily-mean net surface heat flux, (c) daily-mean SST, (d) magnitude of SST diurnal variability and (e) daily-mean ML depth. The wind speed is plotted with a coarse temporal resolution (half-daily) for clarity. The line colours show observations (grey) and simulations: CONTROL (black), WIND (red), HEAT (blue) and NO-HI (magenta).

2.2.3 Experimental design

We first conduct a control simulation (CONTROL) forced by air-sea fluxes calculated from the observed atmospheric variables at their original 7.5-min temporal resolution, using the COARE 3.0 bulk flux formulae (*Fairall et al.*, 2003),

$$\begin{aligned}
 Q_{net}^{SW} &= Q^{SW}(1 - \alpha), \\
 Q_{net}^{LW} &= Q^{LW} - \varepsilon_{atm}\sigma(T_S)^4, \\
 Q^{LH} &= \rho_{air}C_eL_e|\mathbf{U}|(q_{air} - q_{sat}), \\
 Q^{SH} &= \rho_{air}C_hc_p|\mathbf{U}|(T_{air} - T_S), \\
 Q_{net} &= Q_{net}^{SW} + Q_{net}^{LW} + Q^{LH} + Q^{SH}, \\
 \tau &= \rho_{air}C_d|\mathbf{U}|\mathbf{U},
 \end{aligned} \tag{2.2.6}$$

where Q_{net}^{SW} and Q_{net}^{LW} are the net shortwave and longwave radiation at sea surface, Q^{LH} and Q^{SH} are the latent and sensible heat fluxes, α is the albedo, C_e and C_h are the transfer coefficients for moisture and heat respectively, c_p is the heat capacity of the dry air, L_e is the latent heat of vaporisation, T_{air} and T_S are the observed surface air temperature and sea surface temperature, q_{air} and q_{sat} are the observed specific humidity and saturated humidity at T_S and P (barometric pressure), C_d is the drag coefficient and \mathbf{U} is the 10-m wind velocity. The effect of including surface ocean currents in the bulk formulae on turbulent air-sea momentum and heat fluxes is not considered here due to the lack of surface current measurements. It is noted the temperature and humidity gradient is evaluated by subtracting ocean related values from sea surface meteorological variables, therefore positive value for the heat flux components indicates that the ocean is gaining heat and vice versa.

To isolate and quantify the influence of high-frequency atmospheric variability, we conduct three additional experiments. The WIND experiment is the same as CONTROL except that the surface turbulent and radiative heat fluxes are

calculated from daily-averaged (24-hour running mean) meteorological variables. The HEAT experiment is the same as CONTROL except that the surface wind stresses are calculated from daily-averaged winds. The NO-HI experiment is forced from both surface heat fluxes and wind stresses calculated with daily-average meteorological variables. In each experiment, the model is reinitialized at the beginning of each season as defined in section 2.1, which allows us to estimate the impact of the high-frequency atmospheric forcing under different meteorological conditions without being interfered by any potential model drift from the previous season. An alternative one-dimensional turbulence closure Kantha-Clayson (KC) model (*Kantha and Clayson, 1994*) has also been run with identical forcing and experimental design and it shows qualitatively the same results (see section).

2.2.4 Parameterization of cloud amount

The cloud amount (C) is not directly observed, yet it plays a crucial role in regulating the downwelling shortwave and longwave radiation. In previous studies of weather's impact on the ocean (e.g. *Condron and Renfrew, 2013; Wu et al., 2016*), perturbing the cloud amount has not been considered. Here its role on the radiative fluxes is examined. To determine the effect of high-frequency (sub-daily time scale) cloud variability on surface radiative heat fluxes, C has to be determined. To do so, we use parameterizations of C based on empirical relationships between cloudiness and downwelling radiation.

Firstly, C can be calculated from the observed shortwave radiation (Q^{SW}) and the (theoretical) clear-sky shortwave radiation (Q_{clr}^{SW}) according to *Reed (1977)*:

$$\frac{Q^{SW}}{Q_{clr}^{SW}} = 1 - 0.62C + 0.0019(90 - Z), \quad (2.2.7)$$

where C is the fraction of cloud cover and Z is the solar zenith angle in degrees. The clear-sky shortwave radiation determination is based on *ASCE-EWRI (2005)*.

Secondly, cloud cover also affects the downwelling longwave radiation according to *Zillman* (1972):

$$Q^{LW} = Q_{clr}^{LW} + 0.96C\sigma T_{air}^4(1 - 9.2 \times 10^{-6}T_{air}^2), \quad (2.2.8)$$

where Q^{LW} is the observed downwelling longwave radiation, Q_{clr}^{LW} is the clear-sky downwelling longwave radiation, T_{air} is the air temperature in Kelvin and $\sigma = 5.67 \times 10^{-8} \text{Wm}^{-2}\text{K}^{-4}$ is the Stefan-Boltzmann coefficient. The clear-sky longwave radiation can be determined following:

$$Q_{clr}^{LW} = \varepsilon_{atm}\sigma T_{air}^4, \quad (2.2.9)$$

where ε_{atm} is the clear-sky emissivity which depends on water vapor pressure and air temperature.

During the day, C can be derived via (2.2.7) or (2.2.8), while during the night C can only be derived from (2.2.8). As such, two possible ways to determine C are tested: a) the ‘longwave-only’ C ; b) the ‘hybrid’ C derived using (2.2.7) during the day and (2.2.8) during the night. Table 2.1 shows the root mean square errors (RMSE) between the observed radiative heat fluxes and those calculated with either ‘hybrid’ or ‘longwave-only’ cloud scheme involved. In our study, the ‘hybrid’ scheme is used to recalculate the radiative fluxes since on average RMSE associated with the ‘hybrid’ scheme is only about one-third of that associated with the ‘longwave-only’ scheme. In addition, twelve parameterization schemes for ε_{atm} summarized in *Gubler et al.* (2012) were tested and the scheme proposed by *Dilley and O’Brien* (1997) was chosen since it provides the best fit in calculated net radiative fluxes compared to the observations (Table 2.1). With this parameterization of C , the sub-daily cloud variability owing to weather systems can then be filtered out in sensitivity experiments such as WIND and NO-HI. It is worth pointing out that the diurnal solar forcing remains unaltered in all the experiments since it is a consequence of the Earth’s rotation, rather than weather phenomena. Consequently, the above

approach enables us to filter out all the meteorological signals associated with high-frequency weather systems without disrupting the solar cycle.

ε_{atm} scheme	'hybrid' vs. obs.		'lw-only' vs. obs.	
	<i>RMSE</i>	<i>MBD</i>	<i>RMSE</i>	<i>MBD</i>
<i>Maykut and Church</i> (1973)	31.74	-14.02	112.37	-58.04
<i>Ångström</i> (1915)	25.98	-3.30	78.15	-19.08
<i>Brunt</i> (1932)	26.75	6.20	71.60	15.94
<i>Swinbank</i> (1963)	25.40	1.48	66.78	-2.58
<i>Idso and Jackson</i> (1969)	25.77	3.88	64.90	4.95
<i>Brutsaert</i> (1975)	29.59	13.44	77.37	30.45
<i>Konzelmann et al.</i> (1994)	27.37	9.14	68.43	19.44
<i>Satterlund</i> (1979)	27.77	9.92	69.05	20.02
<i>Idso</i> (1981)	48.91	38.77	118.96	69.62
<i>Iziomon et al.</i> (2003)	25.72	2.39	68.10	5.19
<i>Prata</i> (1996)	28.32	11.12	72.88	25.20
<i>Dilley and O'Brien</i> (1997)	25.35	-0.52	68.20	-5.11

Table 2.1: Root mean square error (*RMSE*) and mean bias deviation (*MBD*) are calculated between the observed radiative fluxes and the calculated radiative fluxes with the 'hybrid' and 'longwave-only' cloud scheme, for different clear-sky emissivity schemes as summarized by *Gubler et al.* (2012). The best combination used for net surface heat flux recalculation is the 'hybrid' cloud scheme and the emissivity scheme proposed by *Dilley and O'Brien* (1997).

2.3 Results

2.3.1 Fidelity in simulating SST and ML depth

The PWP model only simulates the local response of oceanic properties to the surface heat and momentum fluxes without accounting for the lateral advection of heat. In this section, the results of the CONTROL experiment are compared with the observation to evaluate the suitability of the PWP model and address the relative importance of the horizontal processes in three different seasons. The interpretation of the results follows the separation of three seasons as marked by

the vertical dashed lines in Figure 2.2.

Daily mean

Figure 2.2c shows the daily-mean SST (black) simulated in CONTROL agrees reasonably well with the observed daily-mean SST (grey) during the NE monsoon and intermonsoon seasons while the CONTROL SST gradually drifts away from the observations at the onset of the SW monsoon season. Although there are some discrepancies between the CONTROL and observed daily-mean ML depth, the PWP model reproduces the overall seasonal trend of ML depth found in the observations — deep ML in the monsoon seasons and much shallower ML in the intermonsoon season (Figure 2.2e).

In the NE monsoon season, the agreement between the CONTROL daily-mean SST and observed daily-mean SST suggests that the horizontal processes play a minor role in setting the SST evolution during this season. The CONTROL daily-mean ML deepens corresponding to the daily heat loss at the sea surface (Figure 2.2b) throughout December and January and shoals in response to the net surface heat gain and weaker wind events towards the mid-February (Figure 2.2a,b), agreeing with the general trend of observed daily-mean ML depth. However, the observed daily-mean ML depth also shows a rapid deepening-shoaling-deepening trend from early November to late December, resulting from the changes in the thermocline structure caused by the passage of a pair of eddies at the mooring site as confirmed by concurrent altimetric SSH imagery (*Fischer et al.*, 2002). An additional heat budget analysis conducted by *Fischer et al.* (2002) suggests that the horizontal heat advection is near-zero within the ML, which explains the agreement between the one-dimensionally forced SST and the observed SST in the NE monsoon season. Their heat budget analysis also shows a strong horizontal heat flux below the ML from November to early December due primarily to the variations in the thermocline thickness associated with the mesoscale eddies (*Fischer*, 2000).

In the intermonsoon season, the simulated daily-mean SST and ML depth both agree well with the observations, indicating that the upper ocean variability during this time period is primarily surface-driven. A heat and salt budget analysis based on the observations (Figure 12 and Figure 13 in *Weller et al.* (2002)) demonstrate a one-dimensional balance during the intermonsoon season and confirm that horizontal processes have little effect on the intermonsoon SST and ML depth evolution.

In the SW monsoon season, the drift of simulated SST is coincident in time with a reported cool filament (*Fischer et al.*, 2002) developed from the Omani coast and transported offshore towards the mooring site. Influenced by this horizontal input of thermal variability, the observed daily-mean SST is much lower than that simulated by the PWP model (where the SST is only locally-driven). Although the daily-mean SST in the SW monsoon season is strongly affected by horizontal processes, a better agreement on the daily-mean ML depth between simulation and observation (Figure 2.2e) suggests that the prevailing strong southwesterlies throughout the whole season is the primary local mechanism for the ML deepening and entrainment (*Weller et al.*, 2002), and the strong surface heat gain during mid-July (Figure 2.2b) is responsible for the ML shoaling in both the observation and the simulation, while horizontal processes are not as significant in regulating the ML development as those in the NE monsoon season.

Sub-daily variability

On sub-daily time scales, the PWP model performs well in reproducing the magnitude of SST diurnal variability as shown in Figure 2.2d. The observed SST diurnal variability (grey) is pronounced in the intermonsoon season (0.71°C on average) and relatively weaker in both monsoon seasons (0.26°C in the NE monsoon season, 0.21°C in the SW monsoon season). This significant seasonal dependence of the magnitude of SST variability in the observations is reproduced in the CONTROL experiment (black), which is primarily

determined by the distinct seasonal meteorological conditions in terms of the strength of the surface heating and the wind-driven mixing (e.g. *Bernie et al.*, 2007). In particular, the surface heating forces the formation of a thin warm layer of a small heat capacity in the surface ocean during the daytime heating period, which leads to a rapid increase of the SST. The wind forcing, on the other hand, acts to inhibit the heating-driven stratification by inducing shear instability at the base of ML and the consequent mixing and entrainment processes suppress the increase of the SST during the day. The weaker SST diurnal variability in both monsoon seasons is mostly attributed to the strong monsoonal winds prevailing throughout the whole season, while the weak surface heating during the daytime also contributes to smaller SST diurnal oscillations in the NE monsoon season. For the intermonsoon season, strong solar heating and relatively calm winds are in favour of a greater SST diurnal cycle. It is noted that both the PWP model and the KC model predict the magnitude of SST diurnal variability in the SW monsoon season to be around 0.1°C , while in observation the value exceeds 0.5°C from July to mid-August (Figure 2.2d and Figure 2.8b). The underestimated SST diurnal variability is likely due to the lack of horizontal processes in the PWP model.

Comparisons with the observations show that the PWP model has skills to simulate the daily-mean SST and ML depth, and the SST diurnal variability for most of the year. Results from the CONTROL experiment suggest that, at the Arabian Sea mooring site, the ML heat budget is mostly controlled by the one-dimensional heat exchanges at both the air-sea interface and the base of the ML with the exception of some drift during the SW monsoon season. Nevertheless, the horizontal heat fluxes seems to affect the ML dynamic much less and the main drivers of the ML variability in the SW monsoon season, i.e. strong wind-driven shear instability and strong surface buoyancy-driven restratification, are well represented in the model. Despite some limitations in the SW monsoon season, overall the one-dimensional model set up provides an reasonably good simulation of SST and ML depth at our study site and is

sufficiently good to warrant investigating a series of sensitivity simulations with varied atmospheric forcing.

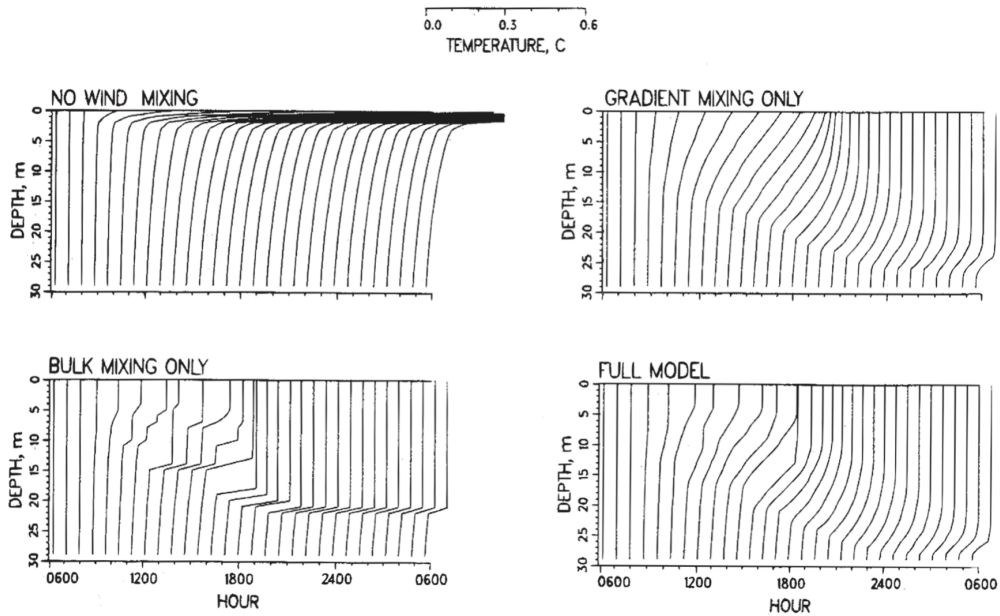


Figure 2.3: A PWP model run over a 24 hour period with varying mixing parameterizations. It is evident that without gradient or bulk Richardson number mixing the ML is hourly defined by surface heat gain ,whilst gradient mixing causes smoother profile than the bulk mixing along. Figure is adapted from *Price et al.* (1986).

2.3.2 Response of SST and ML depth to high-frequency weather systems

Figure 2.2 shows the SSTs and ML depths simulated by the four experiments. Comparing the results of the CONTROL (black) and the NO-HI (magenta) experiments suggests that including high-frequency weather systems in the atmospheric forcing systematically deepens the ML and significantly lowers the SST. On average, including high-frequency weather systems deepens the ML depth by 1.3 m and lowers the SST by 0.8°C in the CONTROL simulation compared to the NO-HI simulation. Particularly, the high-frequency weather systems lower the daily-mean SST more significantly in the intermonsoon season. Averaging over the entire season, the SST is lowered by 1.7°C in

CONTROL compared to NO-HI, due to the inclusion of high-frequency variability in the atmospheric forcing. Furthermore, high-frequency (sub-daily) weather systems also damp the low-frequency (daily-mean) SST variability. For example, the standard deviation of daily-mean SST in the intermonsoon season is considerably weaker in the CONTROL experiment ($1.9\text{ }^{\circ}\text{C}$, close to $1.86\text{ }^{\circ}\text{C}$ in observation) than that in the NO-HI experiment ($2.9\text{ }^{\circ}\text{C}$). Results from WIND (red) and HEAT (blue) further show that high-frequency weather systems lower the daily-mean SST via their effect on turbulent momentum and heat fluxes, although their effect on turbulent heat fluxes appears to have a greater impact on the daily-mean SST (Figure 2.2c).

The difference between the approach of averaging meteorological variables used in the present study and the approach of averaging surface fluxes used in previous studies (e.g. *Shinoda and Hendon*, 1998; *Shinoda*, 2005; *Bernie et al.*, 2005) is highlighted in Figure 2.4 for a 6-week period in the intermonsoon season. Averaging surface fluxes eliminates the diurnal cycle in SST and lowers the daily-mean SST by up to $0.85\text{ }^{\circ}\text{C}$ ($0.2\text{ }^{\circ}\text{C}$ on average) due to the absence of the rectification effect of a thin warm surface layer formed during the day. In contrast, averaging meteorological variables is found to increase the daily-mean SST by as much as $3.7\text{ }^{\circ}\text{C}$ while still maintaining the diurnal cycle of SST. The total difference in SST between forcing with averaged meteorological variables and averaged fluxes is up to $4\text{ }^{\circ}\text{C}$.

As shown in Figure 2.2 (see also Table 2.2), although high-frequency weather systems significantly lower the daily-mean SST, they have little systematic effect on the magnitude of the SST diurnal variability at our study site (Figure 2.2d). Both the magnitude of the SST diurnal variability and its seasonal dependence are similar in the four experiments and resemble the observation. The non-systematically affected SST diurnal variability is likely to be attributed to the randomly distributed high-frequency cloud and wind over a 24-hour composite window (see following section).

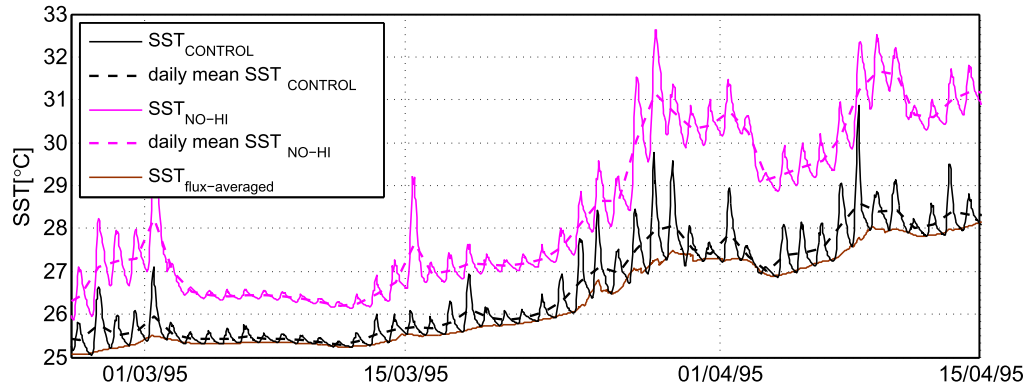


Figure 2.4: SST from the CONTROL (black) and the NO-HI (magenta) experiments, with daily-mean SST marked as dashed lines. The SST from an experiment forced by daily-averaged surface fluxes is shown as a brown line.

2.3.3 The composite analysis

Our model results have shown that the high-frequency atmospheric forcing lowers the SST and deepens the ML depth (Figure 2.2c-e) much more significantly in the intermonsoon season than the monsoon seasons. To further examine this seasonal dependence of the response of upper ocean SST and ML depth to the high-frequency weather systems, we construct 24-hour composites of surface fluxes, wind speed, SST and ML depth for experiments CONTROL and NO-HI and the observations for each season (Figure 2.5).

Two main factors contribute to the much greater difference in SST between the CONTROL and the NO-HI experiments seen in the intermonsoon season (-1.83°C on seasonal average) (Figure 2.5) than monsoon seasons (-0.71°C in the NE monsoon season and -0.11°C in the SW monsoon season). First, including high-frequency weather systems leads to a greater increase in wind speed (0.31 m/s) and surface heat loss in the intermonsoon season (-13.27 W/m^2 in total with -9.53 W/m^2 contributed by wind-related turbulent fluxes) compared to the other two seasons. This is mainly because that we are taking the vector average for the wind, where the wind components are daily averaged before being passed to wind speed computation. In the intermonsoon winds fluctuate more (blowing in different directions) than monsoonal winds which mostly blow in the uniform

direction (NE monsoon blows southwestward and SW monsoon blows northeastward, see also Figure 2.2a) and therefore the intermonsoon wind components tend to cancel out each other when the daily mean is applied and leads to more significant wind speed decrease when daily-averaged wind component is used. Further analysis shows that the difference in net surface heat flux between CONTROL and NO-HI are explained mostly by the difference in turbulent heat flux owing to high-frequency wind fluctuations, with the difference in radiative heat flux owing to high-frequency cloud variability making only a small contribution (Figure 2.6).

Second, the background ML depth modulates the SST response to the high-frequency atmospheric forcing seasonally due to its seasonal variation. As shown in Figure 2.2e, both the observed and model-simulated ML is much shallower in the intermonsoon season (typically 15 m in observation) than in monsoon seasons (40–50 m in observation). The effect of seasonally dependent ML depth in modulating the impact of high-frequency weather systems is more readily seen by comparing the results from WIND and NO-HI. In both experiments, the impact of high-frequency weather systems on surface heat fluxes is excluded, i.e., without the first contributing factor. While the wind stress differences between WIND and NO-HI are comparable among all three seasons (~ 0.005 N/m²; see also Figure 2.5), the cooling effect on the SST is much greater in the intermonsoon season (Figure 2.2c), because the shallower surface ML in the intermonsoon season, via its smaller heat capacity, amplifies the cooling effect induced by the stronger shear instability and enhanced entrainment by including the high-frequency wind fluctuations.

The composite analysis also provides a closer look at the impact of high-frequency weather systems on the SST diurnal variability. Our results show that high-frequency cloud variability (Figure 2.6) and high-frequency wind variability (Figure 2.5) at the study site has no clear and significant diurnal cycle except for in wind speed during the NE monsoon season, which is a modest 0.4 m/s. As such, filtering out high-frequency cloud and wind variability

does not significantly alter the diurnal cycles of solar radiation and wind-induced vertical mixing and entrainment. Consequently, high-frequency weather systems are found to have little systematic effect on the magnitude of the SST diurnal variability at this site.

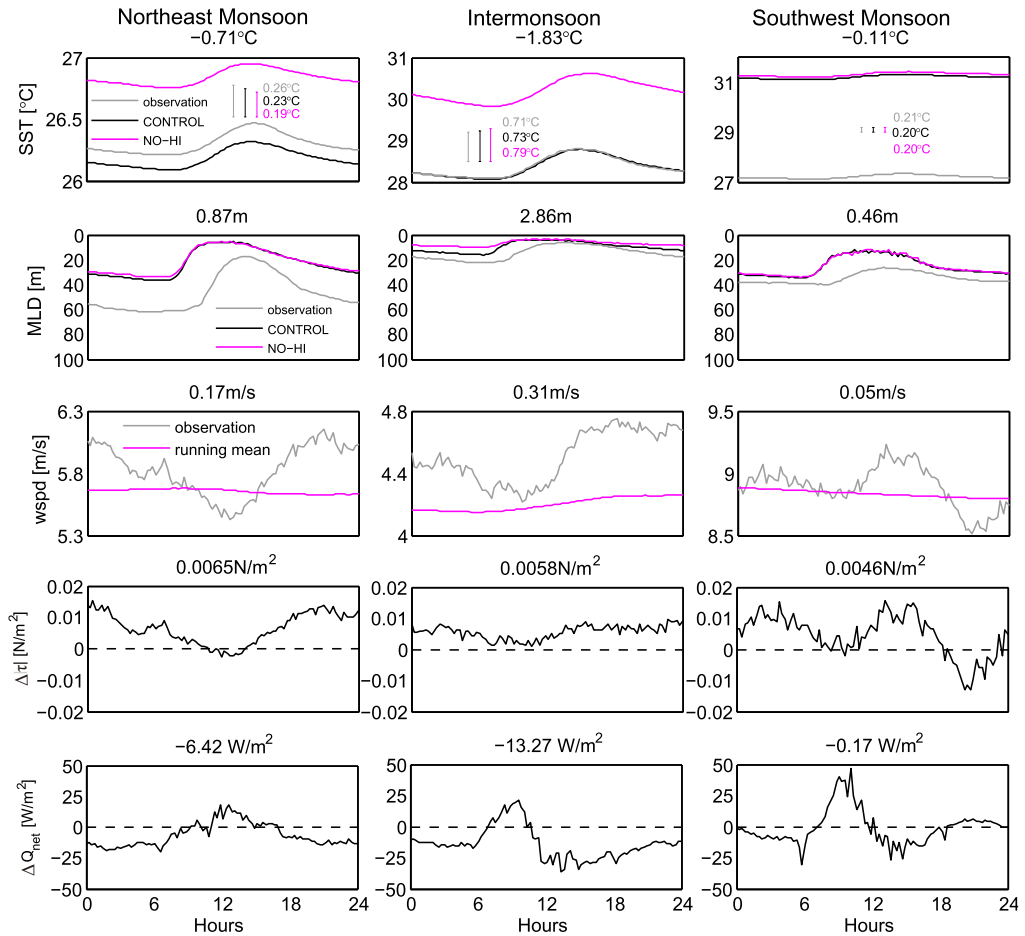


Figure 2.5: A 24-hour composite view of SST (top), ML depth (second row), and wind speed (middle) showing observations (grey), CONTROL (black) and NO-HI (magenta) experiments. The next two rows show differences in wind stress (fourth row) and net surface heat fluxes (bottom) between the CONTROL and NO-HI. The composites are for three seasons: the NE monsoon (left), the intermonsoon (middle) and the SW monsoon (right). Values of seasonal-mean differences (CONTROL - NO-HI) are shown at the top of each panel. The composite-averaged magnitude of SST diurnal variability simulated by the CONTROL and NO-HI are illustrated in the top panels. Note that different axis limits are used in different seasons for the composites of SST, ML depth and wind speed.

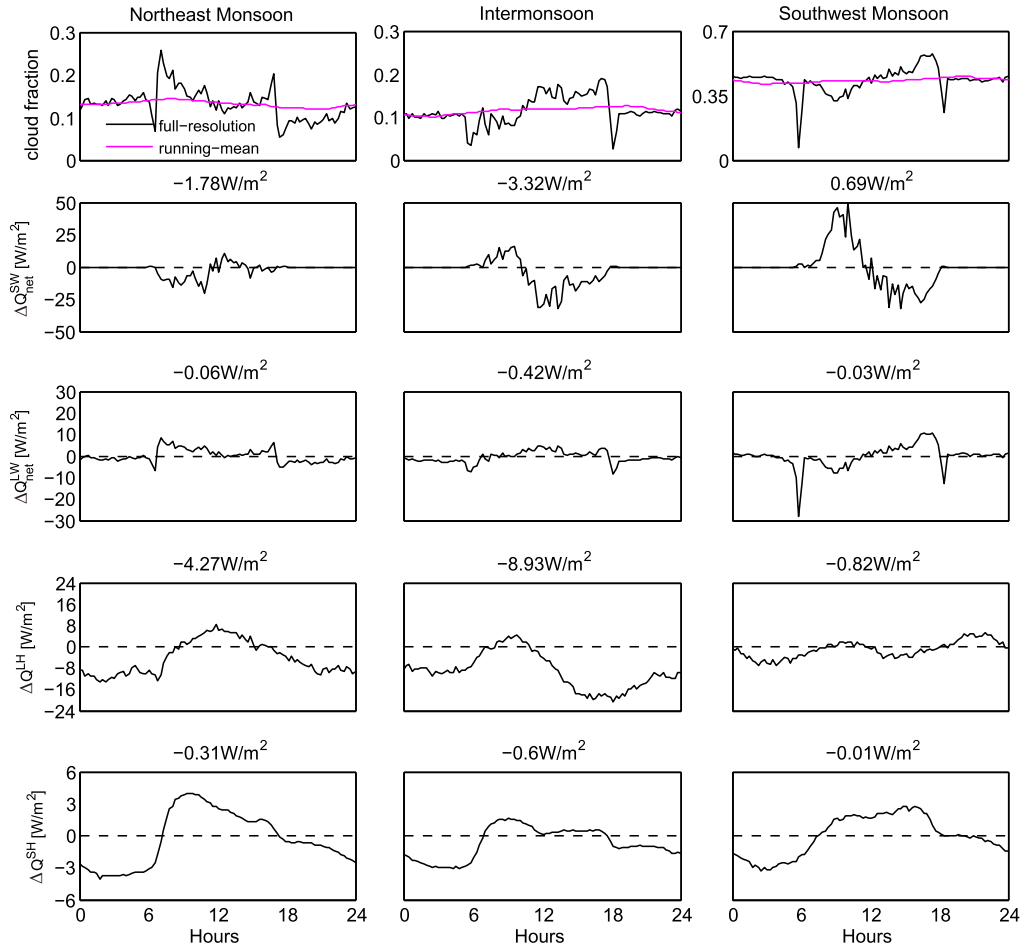


Figure 2.6: The 24-hour composite view of sub-daily (black) and daily-averaged (magenta) cloud cover and the difference of net surface shortwave radiation (Q_{net}^{SW}), longwave radiation (Q_{net}^{LW}), latent heat flux (Q^{LH}) and sensible heat flux (Q^{SH}) between the CONTROL and NO-HI experiments in the NE monsoon (left), intermonsoon (middle), and SW monsoon (right) seasons. Values of seasonal-mean differences (CONTROL - NO-HI) are shown on the top of each panel. Note that different axis limits are used in different seasons for the composite cloud fraction.

2.3.4 Role of high-frequency wind fluctuations

The bulk flux formulae (Eq.2.2.6) shows that the surface winds (\mathbf{U}) are involved not only in the wind stress but also in the turbulent heat fluxes calculations. The impact of the high-frequency wind gusts on the turbulent heat fluxes is shown in the composite analysis, which suggests that the wind-related turbulent heat fluxes are the major contribution to the difference in the net surface heat fluxes between the CONTROL (high-frequency) and the NO-HI (low-frequency) experiments.

To investigate the net effect of high-frequency wind fluctuations on modulating the SST evolution and ML depth, an extra experiment WIND* is conducted. The WIND* experiment is forced by the surface heat fluxes and wind stress that calculated from the observed high-frequency wind and other daily-mean variables (e.g. air temperature, SST, barometric pressure etc.) Therefore the observed difference in the results between WIND* and CONTROL are only caused by the high-frequency variabilities in these daily filtered variables. In other words, if there is not much difference between WIND* and CONTROL, then it suggests that the high-frequency wind variabilities are capable of exciting most of the variabilities in the ocean response. The simulated SST evolves closely along the CONTROL simulations (Figure 2.7a) as expected, since the high-frequency wind explains most of the high-frequency variability in the atmospheric forcing via both the momentum and turbulent heat fluxes. The increased turbulent heat loss and enhanced wind-driven shear instability caused by including high-frequency wind variability lead to cooler SST and deeper the ML depth in the WIND* experiment in comparison with the NO-HI experiment. Our results also show that the magnitude of the SST difference between WIND* and NO-HI is tightly linked to the background ML depth on a day-to-day time scale during the intermonsoon season when the ML depth is shallow (Figure 2.7b). Similar to the mechanism of ML seasonal regulation on the SST difference between NO-HI and CONTROL as discussed in the previous section, during the intermonsoon season, most of the variability of ML thermal anomalies induced by enhanced entrainment and turbulent heat loss are reflected on the SST field due to the smaller heat capacity of shallower ML depth. Such linkage between SST difference and ML variability is absent in both the monsoon seasons, as the heat anomalies are evenly distributed over a deeper ML in the model and thus the thermal variability reflected on the SST field is largely damped.

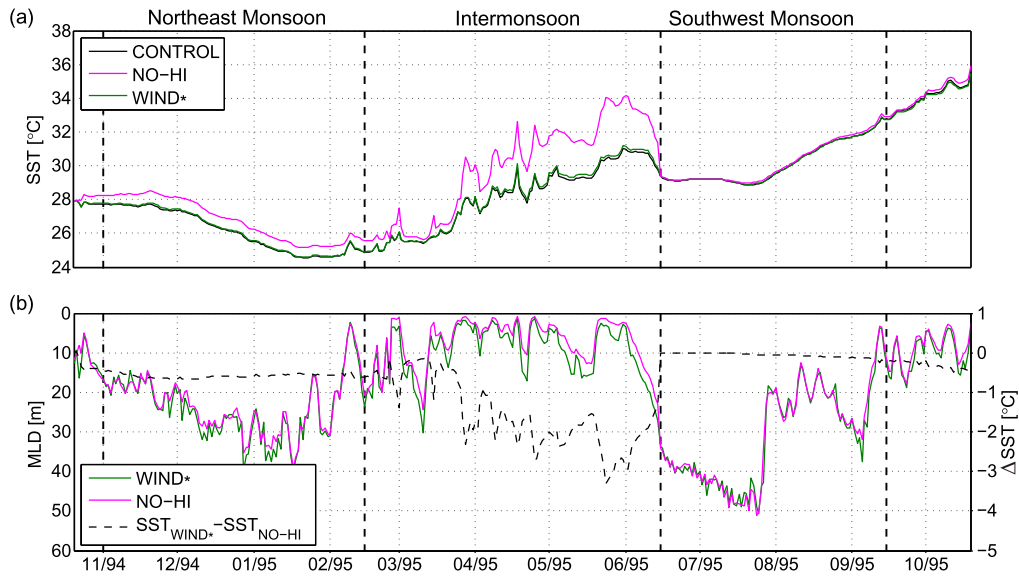


Figure 2.7: (a) Daily-mean SST from the CONTROL (black), NO-HI (magenta) and WIND* (green) experiments. (b) Daily-mean ML depth in the NO-HI and WIND* experiments and daily-mean SST difference (dashed) between the two experiments (WIND* - NO-HI).

2.4 The KC model validation

As an alternative to the PWP model, we repeated our simulations with a turbulence closure model, the Kantha-Clayson (KC) model (*Kantha and Clayson, 1994*). The results are broadly similar to those from the PWP model (see Figure 2.8 and 2.9). The KC model has captured the major role played by high-frequency weather systems – deepening the ML, lowering the low-frequency SST and damping its variability, without systematically altering the SST diurnal variability. By comparing the simulated SST, the magnitude of SST diurnal variability and the ML depth between KC and PWP simulations, it is concluded that the mixing process is enhanced in the KC model. In the KC model, the simulated SST is somehow lower than observations in the NE monsoon season, and the drift between model simulation and observations takes place at the onset of southwesterly burst as we find in PWP predictions. The simulated ML depth in CONTROL is generally deeper than that in PWP by 18 m on average. The ML depth in the KC model reaches down to 50 m in the intermonsoon season and nearly 100 m in the SW monsoon season. The magnitude of the SST

diurnal variability is also smaller than the PWP (Table 2.2). All these comparisons indicate that the mixing processes parameterized in KC model is stronger than that in PWP model. Despite of the difference in the strength of vertical mixing, it is robust that the high-frequency wind variability is the major contribution to the changes of air-sea heat and momentum fluxes due to the high-frequency weather systems at this site. The response of SST to high-frequency weather systems in the KC model is not as closely correlated to the background ML depth on daily time scale during the intermonsoon season as that found in the PWP model since the high-frequency variability in SSTs are damped by the deeper ML depth in the KC simulations. The seasonal correspondence between the ML depth and either SST response or the magnitude of SST diurnal variability still exists. The broad agreement between results from the KC model and PWP model lends confidence on the robustness of the findings of this study.

Integration	Magnitude of diurnal variability in SST (°C)			
	Mean	Max	Min	STD
	PWP/KC	PWP/KC	PWP/KC	PWP/KC
CONTROL	0.44/0.52	3.33/2.30	0.04/0.11	0.53/0.42
WIND	0.43/0.51	3.35/2.44	0.04/0.09	0.51/0.45
HEAT	0.43/0.50	3.33/2.28	0.04/0.10	0.50/0.41
NO-HI	0.45/0.45	3.40/2.42	0.04/0.07	0.57/0.41
Observation	0.54	2.29	0.04	0.59

Table 2.2: Comparison of the magnitude of SST diurnal variability in observations and simulations using the PWP model and the KC model.

2.5 Summary and Conclusions

We have investigated the impact of high-frequency (sub-daily time scale) weather systems on SST and ML depth using the one-dimensional PWP model and an observational dataset collected in the central Arabian Sea. By comparing model simulations that include, partially include, and exclude atmospheric

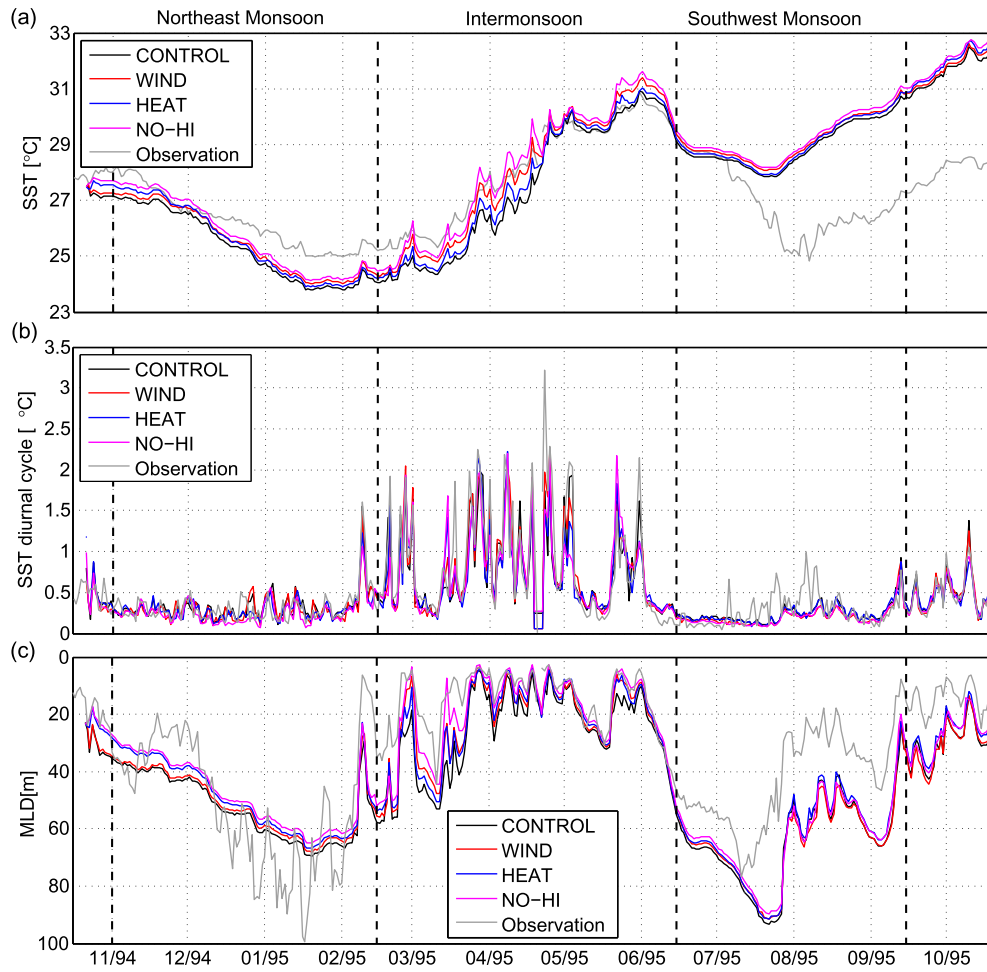


Figure 2.8: Year-long time series of (a) daily-mean SST, (b) magnitude of SST diurnal variability and (c) daily-mean ML depth. The line colours show observation (grey) and the KC model simulations: CONTROL (black), WIND (red), HEAT (blue) and NO-HI (magenta).

forcing associated with high-frequency weather systems, we find:

- High-frequency weather systems lower the daily-mean SST by 0.8°C on average (and as much as 3.7°C) and damp its variability, but have little systematic effect on the diurnal variability of SST. This is in sharp contrast to the effect of diurnal air-sea fluxes which act to increase the daily-mean SST via a rectification effect of a thin warm surface layer formed during the day. The difference in the SST between filtering the meteorological variables and filtering the fluxes was up to 4°C in the central Arabian Sea.

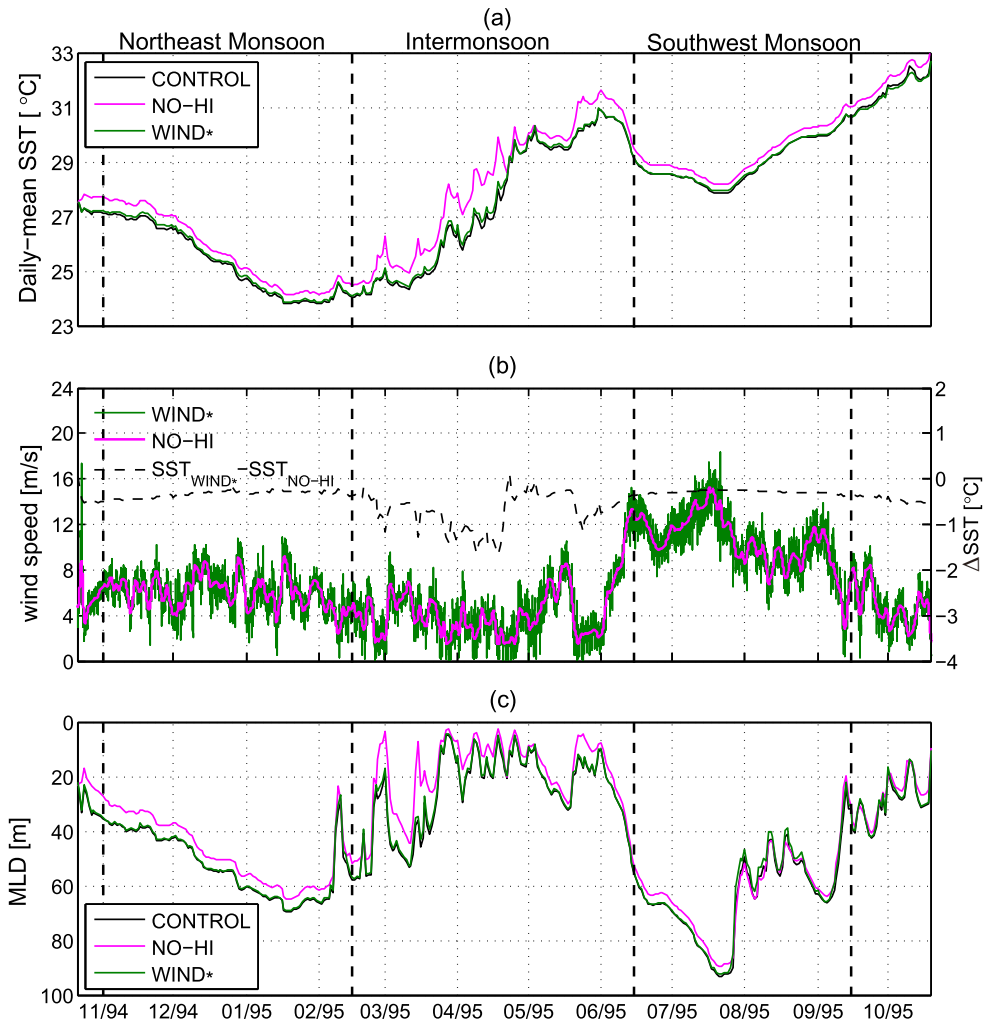


Figure 2.9: (a) Daily-mean SST for the CONTROL (black), NO-HI (magenta) and WIND* (green) experiments. (b) Wind speed used in NO-HI and WIND* and daily-mean SST difference (dashed) between the two experiments (WIND* - NO-HI). (c) Daily-mean ML depth in the CONTROL, NO-HI and WIND* experiments.

- The magnitude of the SST's response to high-frequency weather systems is strongly regulated by the background ML depth on daily-to-seasonal time scales. There is a greater response in SST during the intermonsoon season, when the ML depth is shallow, compared to the response in the monsoon seasons. Implicitly our results show an interesting link across timescales. High-frequency meteorological forcing impacts the ML depth, while low-frequency (seasonal) changes in the ML depth dictate the magnitude of the SST response.

- High-frequency weather systems impact the SST and surface ML at this site primarily through fluctuations in the wind field via their influence of the wind stress and turbulent heat flux. The seasonal feature of the wind fluctuations (intermonsoon winds blowing unevenly while monsoon winds blowing uniformly in direction) results in greater wind speed changes in the intermonsoon season caused by the daily averaging of the winds, and thus leads to greater air-sea fluxes changes, which contributes to the greater responses of SST and ML depth.
- The shallower ML depth in the intermonsoon season is tightly connected with the less intensified wind characterized by rich fluctuations and the moderate surface heating condition. The fact that the fluctuating wind forces a shallower ML depth and averaging on the fluctuating wind causing greater wind speed reduction and hence difference in the surface heat fluxes are both contributing to a more pronounced SST difference seen between the CONTROL and NO-HI experiments.

The work presented in this chapter illustrates a distinct seasonal cycle in the oceanic response to high-frequency weather systems under different monsoonal forcings over a typical year in the central Arabian Sea. The generic set up of our experiments suggests our findings are likely to be applicable to other tropical seas with similar monsoon-dominated atmospheric conditions. We also demonstrated that in the one-dimensional framework, oceanic response is sensitive to the high-frequency atmospheric forcing. The systematic impact of the sub-daily weather systems is small in magnitude but likely to be accumulated if it is neglected in the long-term climatic simulations. How exactly the three dimensional ocean is responding the such subtle variability and how this one-dimensional mechanism can be translated into the three dimensional ocean now becomes a more intriguing question to answer.

SST RESPONSE TO THE STOCHASTIC AIR-SEA HEAT FLUXES UNDER DIFFERENT SOLAR PENETRATION SCHEMES

A more general question is posed in this chapter, that is, how does the ocean respond to pure stochastic atmospheric forcing? The question is inspired by the results from the previous chapter and it is also an extended exploration of a simple stochastic climate model firstly proposed by *Hasselmann* (1976), where this rather simplified conceptual model grasped some fundamental features of the oceanic response to the atmospheric forcing in the observations. *Hasselmann* (1976) discussed this interesting link across time scales between the ocean response and atmospheric forcing, where the forcing is forged as a pure white noise to mimic the unpredicted, fast-evolving weather system relative to the long-term climatic/oceanic evolution. We further assess the noise-induced rectification effect on the long-term trend and the role played by the varying ML depth in this simplified systems, and found that the varying ML hardly changes the spectral behaviour of the SST response but it is crucial for the magnitude of the long-term SST evolution trend. The word ‘rectification’ in this chapter is generalized as the difference between the time-mean of SST forced by stochastic surface fluxes and SST forced by the time-mean fluxes of the same stochastic time series. Although it is also termed as ‘noise-induced drift’ in some literatures, the difference assessed here is believed to be generated by high-frequency variabilities represented as

stochastic components in the forcing fields, as such, a ‘rectification’ on the SST driven by time-mean forcing fields where these variabilities are absent.

3.1 Introduction

The spectra of climatic time series are characterized by three important features: continuity, redness and presence of multiple peaks (*Mitchell, 1976*). The existence of multiple peaks indicates that deterministic processes are responsible for their generation. For example, there are climate variabilities pronounced at preferred timescales due to the internal oscillations of the climate system such as the ENSO or the Atlantic Quasi- (e.g. *Deser and Blackmon, 1993; Dima et al., 2001*) and Multi- (*Dima and Lohmann, 2007*) decadal Variability. The repetitive and cyclical external forcing from diurnal and annual cycles of solar radiation due to Earth’s rotation and revolution, respectively, to the astronomical Milankovitch cycles can drive peaks on the climatic variance at specific time scales.

In contrast to the climate variability resulting from the deterministic processes, the high-frequency fluctuations especially for the atmospheric system can result from the random forcing (e.g. the evolution of weather system). These high-frequency variability can be translated into the long-term variance of the system via the accumulative responses and non-linear feedbacks. In the previous chapter, the sub-daily time-scale fluctuations in the meteorological fields are shown to significantly modulate the seasonal-to-intraseasonal SST and ML depth variability under a one-dimensional framework. Particularly, the wind fluctuation tends to act as the prominent factor in regulating the low-frequency variability of upper ocean relative to the other meteorological components such as air temperature, humidity and cloud via its involvement in determining both the exchanges of turbulent heat flux and momentum flux at the air-sea interface.

This link across time scales between the rapidly developed atmosphere interacting with slowly-evolving ocean in the climate systems has been discussed widely in

climate literature, and was firstly depicted in the articles by *Hasselmann* (1976) and *Frankignoul and Hasselmann* (1977) (hereafter H76, FH77). They proposed a conceptual framework to understand the nature of SST variability via a simple stochastic climate model, arguing that the ocean-ML temperature anomalies are the results of the integration of the stochastic atmospheric heat fluxes forcing, which should be an autoregressive process of the first order (AR1). These random variabilities can be associated with, for example, the high-frequency fluctuations in the atmospheric circulation with a decorrelation timescale within a week or two (*Deser et al.*, 2010). The growth rate of the SST variability is suppressed by a negative linear damping term representing the turbulent heat fluxes and longwave radiative fluxes adjustment to the SST anomalies. Substantial progress has been made in understanding the extratropical thermal coupling mechanisms and damping effect induced by the air-sea fluxes adjustment (e.g. *Frankignoul*, 1985; *Alexander and Penland*, 1996; *Barsugli and Battisti*, 1998; *Frankignoul et al.*, 1998) based on the fundamental work laid down by H76 and FH77.

While the assumption of the stochastic heat fluxes are found to be effective in reproducing some of the mid-latitude SST anomalies as observed, much of these discussions have been primarily statistical in nature and often the influence on the mean SST or its time dependence on the evolution of stochastically induced variability has been ignored. In many previous studies, the coherence between the stochastic forcing and the ocean response has been examined. However, different phenomena can yield the same spectra and coherence often obscuring the dynamics of the systems (*Chhak et al.*, 2006), such as the ML variation (e.g. *Alexander and Penland*, 1996). As presented in the previous chapter, the evidence shows that the high-frequency variabilities in air-sea fluxes and meteorological fields can systematically regulate the surface ML thermodynamics. Can we extend what we learned from the rectification effect on the upper ocean from either the SST diurnal cycle or the high-frequency wind variability to a stochastically-forced ocean? In other words, does the stochastic air-sea fluxes generate any systematic effect on the SST and upper

ocean ML depth evolution in light of our expectations from the canonical diurnal cycle of the air-sea fluxes? In this chapter, we show that the stochastic air-sea heat fluxes tend to excite this ‘rectification’ effect in the time-mean SST field in a similar fashion to that illustrated in other investigation on the high-frequency SST variabilities (e.g. *Shinoda and Hendon*, 1998; *Shinoda*, 2005; *Bernie et al.*, 2005, 2007, 2008; *Kawai and Wada*, 2007; *Guemas et al.*, 2011), using a one-dimensional ML model. This one-dimensional response usually tends to be worn off due to the advective processes instantaneously and the excited variabilities of the response mostly cancel off between the opposite phases of the surface forcing when the average is taken over a short period, while the systematic net effect from the stochastic air-sea interaction can emerge over a longer time period of evolution from the accumulation of the residual left from the compensation between phases due to the asymmetric SST responses and the amplification from the non-linear internal feedbacks in more sophisticated models with more degrees of freedom (e.g. *Williams*, 2012).

3.1.1 Simple stochastic climate model paradigm

H76 proposed a simple stochastic climate model paradigm where slow changes of the climate were interpreted as the integral response to continuous random excitation by short timescale ‘weather’ disturbances. This idea that the slowly responding components such as ice sheets, oceans, or vegetation acting as integrator of the random input from the fast evolving weather components is analogous to the interaction between heavy particles and ensemble of light particles in the framework of ‘Brownian motion’. Such integration of the random input is known as an autoregressive process of the first order (AR1). Unlike the ‘Brownian motion’ where the internal stabilizing mechanisms are absent, H76 model included a negative linear feedback term in the forcing driving an asymptotically stationary response of the slow subsystem, which otherwise tends to grow infinitely with time.

FH77 presented a prompt application of H76 theory to investigate the variability of the mid-latitude SST in response to random atmospheric forcing simulated by a quasi-geostrophic (QG) barotropic atmospheric model by incorporating a white noise time series into forcing terms. The stochastic atmosphere model is coupled to a fixed slab ocean model and the system is damped by a linear negative air-sea feedback acting as the enhanced loss/gain of heat to/from the atmosphere resulting from the anomalously warm/cold SST. The simulated SST anomalies showed similar spectral characteristics as the observed SST anomalies: SST variances decrease with the frequency within one year timescales and then independent of frequency over the longer timescales as the damping term confines the SST anomalies growth over time. FH77 model demonstrates a case of how the thermal inertial introduced by ocean's ML smooths out the high-frequency variabilities of SST to yield a slow response, i.e. a 'reddened' spectrum.

FH77 model is more readily seen by considering a ML energy balance model (*Marshall and Plumb, 2008*),

$$\gamma_o \frac{dT}{dt} = -\lambda T + Q_{net} \quad (3.1.1)$$

where $\gamma_o = \rho_{ref} c_\omega h$ (i.e., density \times specific heat \times depth, with units of $\text{J K}^{-1} \text{m}^{-2}$), $\lambda = 15 \text{ W m}^{-2} \text{K}^{-1}$ (obtained from observations) is the damping rate of the SST anomalies T due to the turbulent heat exchange across the air-sea interface, Q_{net} is the net air-sea heat flux. In mid-to-high-latitude region, changes of SST is strongly forced by the passing of storms through their modulation of the surface winds, air temperature, humidity, hence the air-sea fluxes Q_{net} . The variability of surface heat fluxes caused by these short-period atmospheric systems are then treated as random noise relative to the slowly responding ocean. In Eq. 3.1.1, we set $Q_{net} = \hat{Q}_\omega e^{i\omega t}$, where \hat{Q}_ω is the amplitude of the stochastic component of the air-sea flux at frequency ω associated with the atmospheric eddies (*Marshall and Plumb, 2008*). For 'white noise' processes, one has a \hat{Q}_ω independent of ω . Similarly, the response of SST is given by $T = \hat{T}_\omega e^{i\omega t}$. According to Eq. 3.1.1,

the amplitude of SST anomalies is derived as the function of \hat{Q}_ω and ω ,

$$\hat{T}_\omega = \frac{\hat{Q}_\omega}{\gamma_o(\frac{\lambda}{\gamma_o} + i\omega)}. \quad (3.1.2)$$

Hence the spectrum of SST anomalies in response to the stochastic ‘weather’ noise yields

$$\hat{T}_\omega \hat{T}_\omega^* = \left(\frac{\hat{Q}_\omega}{\gamma_o}\right)^2 \frac{1}{\omega^2 + (\frac{\lambda}{\gamma_o})^2}, \quad (3.1.3)$$

where the \hat{T}_ω^* is the complex conjugate of \hat{T}_ω .

In Eq. 3.1.3, $\omega_c = \lambda/\gamma_o$ defines a critical frequency depending on the heat capacity of the ocean ML (h) and the strength of air-sea coupling (λ). The variability of the temperature response over higher frequencies ($\omega > \omega_c$) decays rapidly with frequency with the slope of -2 on the logarithmic scale, while the response levels out over the lower frequencies ($\omega < \omega_c$) as evident from the grey curve in Figure 3.1a. In comparison, Figure 3.1b shows the observed temperature spectra of the atmosphere and of SST, where the SST spectrum is much redder than atmospheric temperature, somewhat consistent with ω^{-2} dependence predicted by Eq.3.1.3. In the case of absence of negative feedback, Eq.3.1.3 reduces to

$$\hat{T}_\omega^2 = \left(\frac{\hat{Q}_\omega}{\gamma_o}\right)^2 \frac{1}{\omega^2}, \quad (3.1.4)$$

known as the non-stationary state of climatic response in FH77 model. The SST anomalies variance in this case increases at low frequencies ($\hat{T}_0^2 \rightarrow \infty$) without the limit of stabilising internal feedback mechanism (e.g. Figure 3 in FH77).

Although Hasselmann’s theory rationalizes part of the observed mid-latitude SST variability with reddened spectrum yielding the ω^{-2} dependence under the forcing of a ‘white’ atmospheric spectrum, it is not quite clear how this stochastic atmospheric variability influences the time-mean ocean evolution. The problem does not stand out in Hasselmann’s original model since the ‘ocean’ is treated as a fixed-depth plate. It was also noted in later studies that an AR1 process cannot explain the re-emergence effect of wintertime SST

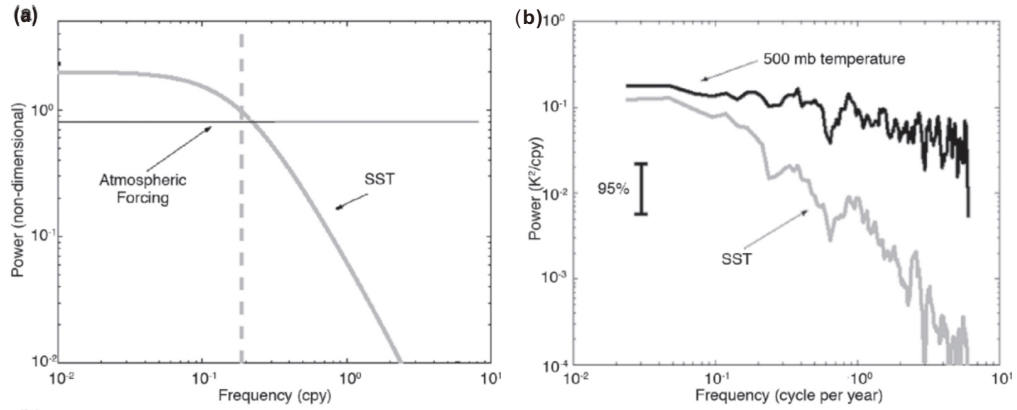


Figure 3.1: Adapted from *Marshall and Plumb* (2008). (a) The theoretical spectrum, Eq.3.1.3, on a log-log plot. The vertical grey line indicates the frequency $\omega_c/2\pi$ where $\omega_c = \frac{\lambda}{\gamma_o}$. (b) Log-log plot of the power spectrum of atmospheric temperature at 500 mbar (black) and SST (grey) associated with the North Atlantic Oscillation, see *Czaja et al.* (2003) for details.

anomalies in the following fall and winter observed in the most extratropical region (e.g. *Alexander and Deser*, 1995; *Dommenget and Latif*, 2002, 2008; *Fraedrich et al.*, 2004) where the ML variation is vital.

Based on H76 stochastic climate model, here we introduce two elements from the realistic world – the ML response and the solar absorption through the water column. The adjustment of the ML in the ocean model is a fundamental process associated with the upper ocean dynamic and thermodynamic characteristics. It defines the upper ocean heat capacity and modifies the sensitivity of the SST in response to the surface forcing. It has been recognized that the variation of ML is important for regulating the SST variability over time, for example, the high-frequency induced rectification on long-term SST development (e.g. *Williams*, 2012; *Zhou et al.*, 2018). The solar penetration, on the other hand, redistributes the upper ocean heat and effectively modifies the ML response towards the surface heat fluxes. The penetration depth or the attenuation intensity of the solar radiation throughout the water column is important in setting the upper ocean heat capacity and hence a crucial determinant of the response of the SST and of the temporal scale of SST variability (e.g. *Frankignoul*, 1985; *Deser et al.*, 2003).

3.1.2 Solar penetration within the upper ocean ML

The incoming solar irradiance is the main energy source in the ocean heat budget, and hence strongly impacts the oceanic thermal structure. Shortwave radiation absorbed by the ocean is attenuated exponentially with depth. The attenuation depth (e-folding depth) depends on the wavelength and biogenic components of the water. Traditionally, the water types are classified Jerlov I, IA, IB, II and III (*Jerlov, 1976*) based on their spectral optical attenuation depth. The shortwave attenuation depth in open oceans is about 20-30 m, and it decreases with increasing water turbidity, particularly in coastal regions.

One-dimensional ML modelling studies have long illustrated the importance of solar transmission on SST and ML depth evolution. For example, *Denman (1973)* introduced an attenuation coefficient for downward solar irradiance in Kraus-Turner model to investigate the time-dependent behaviour of the upper ocean to varying meteorological inputs. The model was sensitive not only to the rate of production of energy for mixing, but also to the rate of absorption with depth of the solar radiation. *Lewis et al. (1983)* explored the effect of phytoplankton on solar radiation absorption in the upper layer of the open ocean, suggesting that certain vertical distribution of chlorophyll augments vertical mixing and deepens the ML. *Sui et al. (1997)* demonstrated that the intraseasonal variability of SST is sensitive to the solar attenuation depth in Topical Ocean-Global Atmosphere (TOGA) Coupled Ocean-Atmosphere Response Experiment (COARE) domain. *Shinoda (2005)* further discussed the sensitivity of SST diurnal cycle and intraseasonal variability to the different components of solar radiation under the framework of a double-exponential function where the visible light is approximately separated into red and blue components. It was concluded that the SST diurnal cycle is sensitive to the extinction depth of the red light component while the intraseasonal is closely connected to the blue light penetration. The impact of the red light absorption on SST diurnal cycle can further translated into the intraseasonal variability via

the rectification effect induced by SST diurnal cycle. The sub-surface warming due to the solar penetration is a key factor involved in the generations of SST seasonal variability, hence improves the predictability skills of SST (e.g. *Rochford et al.*, 2001) and has significant implications in affecting the climate variation during the warming seasons (e.g. *Hosoda et al.*, 2015).

In OGCMs, studies have reported that the influence of the solar penetration parameterization was manifested counter-intuitively due to the secondary response of the advective heat transport associated with the tropical circulation systems to the changes of solar penetration scheme. *Murtugudde et al.* (2002) studied the solar penetration on the upper tropical ocean circulation with an OGCM by comparing experiments with ocean colour-based solar penetration depth and the control experiment with fixed solar penetration depth. It is found that with a realistic solar penetration scheme, the excess sub-surface warming produces a warmer SST compared to the control experiment. They argued that the sub-surface warming due to the penetration of solar radiation actually leads to a weaker surface current divergence, hence the processes of upwelling and entrainment are inhibited which are key for the cool SST anomalies in the equatorial oceans. Similarly, *Sweeney et al.* (2005) also obtained a warmer equatorial oceans in their sensitivity experiments even though the solar penetration leads to an overall deeper oceanic ML depth. They attributed the slowdown of surface pole-ward currents to a deeper ML depth on and off the equator caused by deeper solar penetration.

In summary, in a local forcing-dominated region, a shallower solar penetration depth associated with higher surface chlorophyll concentration is in favour of trapping heat within the surface layer, contributing to warmer SST and shallower ML depth. Deeper solar penetration is corresponding to relatively clear water bodies and the solar radiation is distributed over a deeper water column, leading to insufficient SST warming and deeper ML depth. While over the equatorial regions, the secondary response of the current systems to the changes of solar penetration depth could overcompensate the one-dimensional

thermodynamic response. It is noted that, though, most of these studies invoke time-mean surface heat fluxes to force the ocean model or couples the ocean model with deterministic atmosphere models to assess the behaviours of upper ocean, few has considered how stochastic variabilities in air-sea heat fluxes caused by transient processes such as the cloud blocking or wind fluctuations alter the oceanic response under different solar penetration schemes. In this chapter, this question is explored with a series of idealized experiments using one-dimensional PWP model. Prescribed white-noise time series is imposed to the model acting as the air-sea heat fluxes to understand firstly how the ocean is thermodynamically responding to the pure surface noise in terms of power spectral characteristics (e.g. H76 and FH77), and secondly what the impacts of the stochastic atmospheric variabilities are on the long-term evolution by assessing whether there is any integral effect of noise-induced rectification.

The rest of the chapter is organized as follows. In section 3.2, we demonstrate the spectral characteristics and the trend of evolution of the SST response to the pure white-noise surface heat fluxes using a one-dimensional ML model, assessing the role played by ML depth adjustment and the solar attenuation in affecting the SST response. Results from the idealized experiments show a strong sensitivity of the SST evolution to the solar penetration depth. Summary is included in section 3.3.

3.2 SST response to pure white-noise air-sea heat fluxes

3.2.1 Methods

Three ML models are used here to represent three types of ML approximations involved in the wide range of ocean model studies: slab ocean model, one-dimensional ML PWP model without solar penetration and PWP model

with standard solar penetration scheme.

In the slab model, the ML depth is fixed and the solar radiation is uniformly absorbed within the ML depth. The slab ocean model is essentially a zero-dimension model running at each grid point and represents an approximation of the well-mixed ocean ML. The applications of slab model usually take the advantage of its simplification and efficient computation to perform very long integration allowing exploration on the climate variability over longer time scales (e.g. H76) or the coupled systems where only the interaction between atmosphere and ocean ML is of interest (e.g. *Clement et al.*, 2016). In our case, the simplified slab model is meant for reproducing the SST variability predicted by Hasselmann's theory as the base line where ocean thermodynamics involved is tuned to the most simplified state. Then we introduce two elements, the variation of ML and solar penetration, into the model for further comparisons.

As described in previous chapter, the one-dimensional PWP model computes the ML depth and SST via three criteria: the static stability, ML stability (bulk Richardson number) and shear flow stability (gradient Richardson number) (more details in Chapter 2 and *Price et al.* (1986)). Here we switch off the freshwater fluxes and momentum fluxes and the only determinant of the ML depth is the static stability associated with the surface heat fluxes. We further vary the solar penetration scheme by turning it on and off to assess the influence of solar attenuation on the ML depth adjustment and the SST evolutions. With the solar penetration switched off, the solar radiation is completely absorbed within the uppermost layer.

The air-sea heat fluxes in idealized experiments are composed by the stochastic solar radiation and constant non-solar heat fluxes. The solar radiation is taken as a pure white noise time series (Figure 3.2) with rich variability on sub-daily timescales. The magnitude of the solar radiation is uniformly distributed from 0 to 1000 W/m^2 , i.e., $Q_{sw} \sim U(0, 1000)$. The time-mean Q_{sw} is 500 W/m^2 , balanced

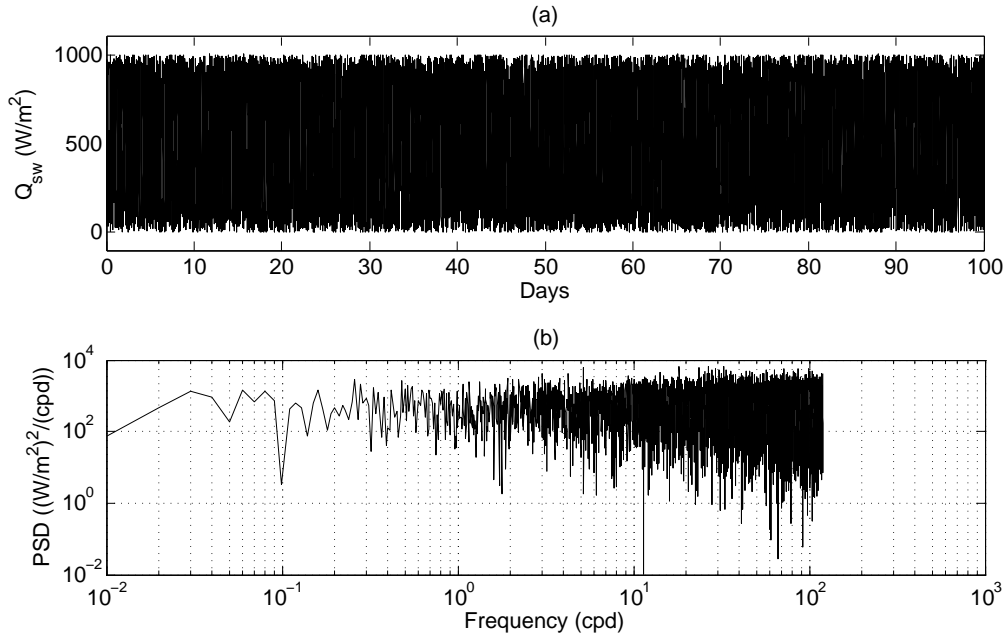


Figure 3.2: (a) Time series of net surface heat fluxes over 100 model days applied in all idealized experiments. (b) Power Spectral Density of the net surface heat fluxes. Little dependence of power density on the frequency shows a typical white noise spectra.

with the constant non-solar heat loss, $Q_{out} = -500W/m^2$. So the total time-mean net surface heat fluxes is zero for all three models. The model is integrated at every 360 seconds. No extra fluxes are applied at the bottom boundary of the ocean in all three model experiments and the temperature is freely evolving with the deep solar penetration at the bottom.

3.2.2 Spectral characteristics (variance) of stochastically-forced SST

a. Slab model

The heat exchange and temperature evolution in the stochastically-forced slab ocean model is governed by

$$\frac{\partial T}{\partial t} = \frac{Q_{sw} + Q_{out}}{\gamma_0}, \quad (3.2.1)$$

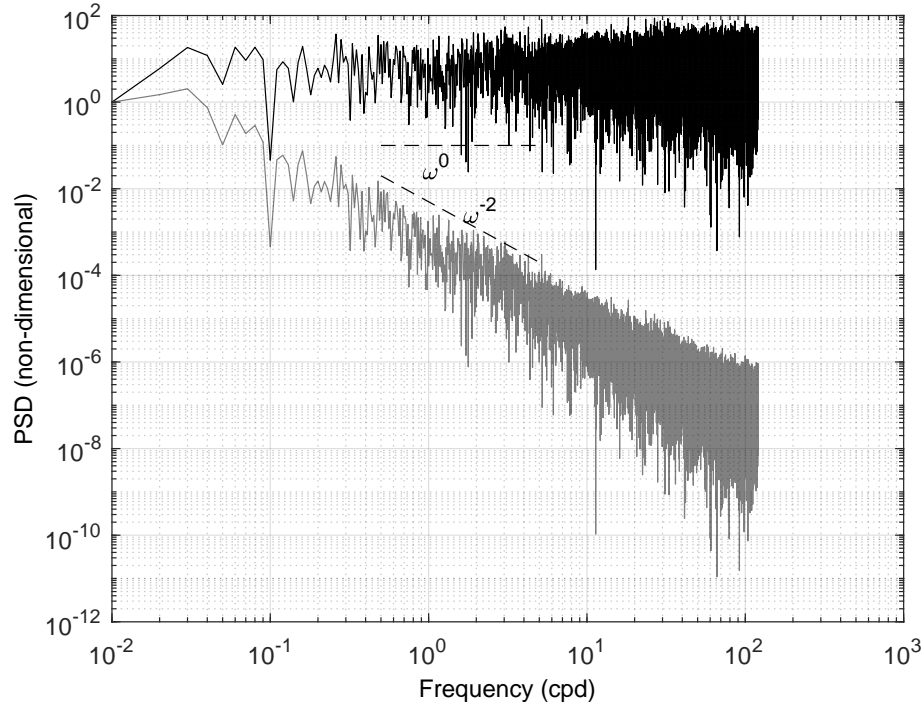


Figure 3.3: Power spectra (non-dimensional) of the stochastic air-sea heat fluxes (black) applied in the slab mode experiments and the simulated SST (grey). The white-noise-forced SST yields a red spectrum with the slope of ω^{-2} , as predicted by *Hasselmann* (1976).

where $\gamma_0 = \rho C_p h$ is constant. The stochastically-forced slab ocean model with fixed ML depth is essentially a time integration of a stochastic time series. The ML depth in slab model is the thickness of the vertical model grid size (1 m). The spectral characteristic of the SST in slab model is consistent with that predicted by *Hasselmann's* theory, yielding a reddening of spectrum with a ω^{-2} slope at the frequency domain. The SST spectra in Figure 3.3 shows no flattening toward the low-frequency bands due to the lack of damping effect $-\frac{\lambda}{\gamma_0}T$ (see Eq. 3.1.1) coming from the air-sea heat fluxes adjustment to the modelled SST. The slab model experiment here depicts the uncouple regime of the simple stochastic climate model.

b. Non-Solar-Penetrative (NSP) PWP model

In the NSP PWP model, the solar radiation is completely absorbed within the uppermost layer. The base of ML remains at the depth uppermost layer when the surface temperature is higher (more buoyant) than the layers beneath. The ML deepens (the convective mixing is triggered) only if the temperature of the uppermost layer is lower than the layers underneath due to the surface heat loss. Here we set the ML depth in the slab model the same as the thickness of the uppermost layer used in PWP model, so the non-solar-penetrative (NSP) PWP model is essentially the same as the slab model during the period when uppermost layer is gaining heat and warmer than water below. This feature of NSP PWP model leads to similar magnitude of the SST increase (Figure 3.4a) and SST variance (Figure 3.4b) in comparison with the slab model SST. A ω^{-2} dependence of the power density spectrum on the frequency is found in NSP experiment, indicating that including the ML depth adjustment to the surface buoyancy forcing does not qualitatively alter the spectral characteristics of the SST response to the stochastic surface heat fluxes except for an overall power shift in accordance to the thermal inertia determined by the ML depth.

c. Solar-Penetrative (SP) PWP model

In solar-penetrative (SP) PWP model, solar absorption through the ocean water subjects to the solar attenuation with depth parameterized by a double-exponential dependence. *Paulson and Simpson (1977)* fitted the double exponential equation to solar transmission profiles in accordance to the Jerlov water type classifications and obtained a set of extinction coefficients for each water type,

$$I(z) = r_1 \times e^{-\frac{z}{\lambda_1}} + r_2 \times e^{-\frac{z}{\lambda_2}}. \quad (3.2.2)$$

$I(z)$ is the radiant flux density on the ocean surface primarily due to the downward solar irradiance. The double-exponential equation approximately separates the

radiation absorbed by the ocean into two parts, red spectral components and the blue spectrum components. The coefficient $r_1 = 0.6$ denotes the fraction of red end of spectrum and $r_2 = 0.4$ refers to the fraction of blue end of spectrum of the visible light. $\lambda_1 = 0.6$ m and $\lambda_2 = 20$ m are standard extinction coefficients for IA Jerlov water type which is representative for the open ocean water. Subscripts 1 and 2 respectively refer to the scale of the attenuation length of the red and blue components through the water column. Whereas more complex parameterization of the solar transmission profiles can be obtained by a multi-wavelengths function with the extinction coefficients derived from the surface chlorophyll concentrations (e.g. *Morel and Maritorena, 2001*), it is beyond our intention to refine the solar penetration parameterization in idealized experiments.

The solar penetration acts to dilute the solar absorption density at the surface layer and redistributes the solar irradiance exponentially in the vertical and leads to some different SST behaviour from the NSP PWP mode when the exact same forcing is applied. The first effect is that the magnitude of SST increase is much smaller as the solar heat absorbed at the uppermost layer is reduced by nearly half (depending on the attenuation coefficient) compared to that in NSP PWP. Secondly, the convective mixing much more frequently triggered than the NSP PWP because of a constantly heat loss (turbulent heat loss + outgoing longwave radiation) that only applied at the uppermost layer and a sub-surface warming from the solar penetration. These two processes collectively work against the solar absorption in the uppermost layer and make it more difficulty to achieve an overall stratification in the SP PWP model even when the net surface heat flux across the air-sea interface is positive toward the ocean. Overall, the solar penetration in SP PWP leads to an broadly deeper ML depth (Figure 3.4b), and a much more damped magnitude of SST variability (Figure 3.4a) and variance level (Figure 3.4c) comparing to the slab model SST and NSP SST.

Figure 3.4c shows that despite of the realistic ML response to the surface heat forcing under the influence of solar penetration, the SP SST spectrum (blue line in Figure 3.4c) yields Hasselmann's prediction well and can also be regarded as

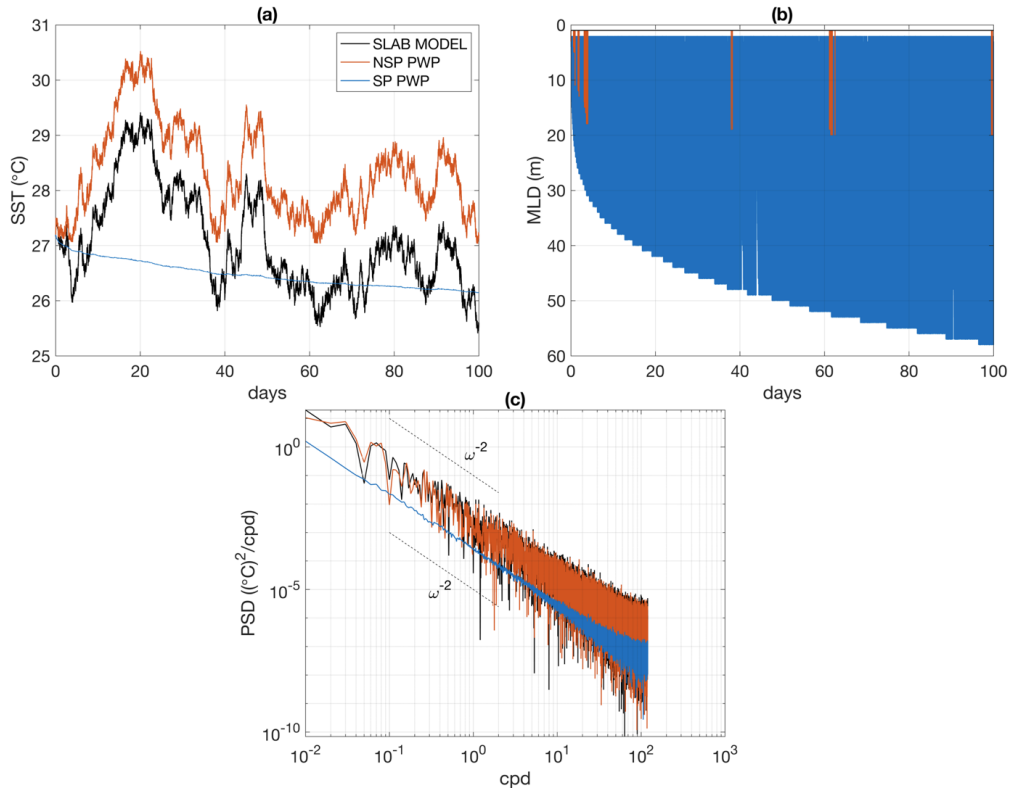


Figure 3.4: (a). Time series of SST simulated by slab ocean model (black), PWP model with non-penetrative solar radiation scheme (orange) and penetrative solar radiation scheme (blue). The variabilities between the slab model SST and non-solar-penetrative PWP SST are of the same magnitude since the ML depth is mostly fixed at uppermost layer in the latter experiment. The variability in solar-penetrative PWP SST is largely damped by deeper ML. The difference and similarity on the SST variability magnitude among three experiments are further shown in (b) in form of the power spectrum. Noted that the redness of SST spectra is persistent throughout different simulations regardless of including ML adjustment and realistic solar penetration.

an integration of surface noise only with the magnitude modulated by the time-varying ML depth. The consistency of the red spectrum of SST among three experiments indicates that the response of the ML to the stochastic air-sea heat fluxes also yields a white noise spectrum or at least has no significant correlation with the air-sea heat fluxes, maintaining the white-noise nature of the forcing term $\frac{Q_{sw}}{H}$ in NSP and SP experiments. This conjecture is supported by model results and observations (e.g. *Alexander and Penland, 1996; Frankignoul et al., 1998*).

The red spectrum of the mid-latitude SST anomalies has been found in several

in-situ mooring observations over various mid-latitude ocean weather stations (OSWs) (e.g. *Alexander and Penland, 1996*) and theoretically supported by Hasselmann's stochastic climate model, although some SST observation indicated extra spectral peak embedded in a red-noise spectrum at various time scales such as associated diurnal cycle or the annual SST anomalies re-emergence. The explanation on the red spectrum of SST variability primarily is stemmed from the integration of AR1 process that is used to approximate fast-evolving weather systems. Although the red spectrum of SST variability is mathematically sound, it not always clearly interpreted physically. Here we present an attempt to attribute the variance level at different frequency bands to the single-frequency atmospheric forcing derived from decomposing the stochastic heat flux (Q_{net} on the right hand side of Eq. 3.1.1) on frequency domain. We first to create a series of nineteen sinusoidal signals with different periods varying from 750 seconds to 1000 days. We then test the response of SST to the corresponding single frequency forcing with the one-dimensional PWP model. Figure 3.5 shows the variances of the simulated SST anomalies as a function of the forcing frequency. The variance of the SST decreases with the frequencies at a slope of ω^{-2} , consistent with what is predicted by H76 and FH77 theory. Considering the largely linear relation between ML temperature and surface heat fluxes in a simple one-dimensional ML model, the greater variance of SST in response to a low-frequency heat flux oscillation is mainly resulted from a longer period of integration of the monotonic heating and cooling from the atmosphere and vice versa. This explanation provides a new perspective of understanding the predominating 'red spectrum' embedded in the large volume of ocean and atmospheric observational dataset which tend to be referred simply as 'yielding' red spectra without a clear physical interpretation.

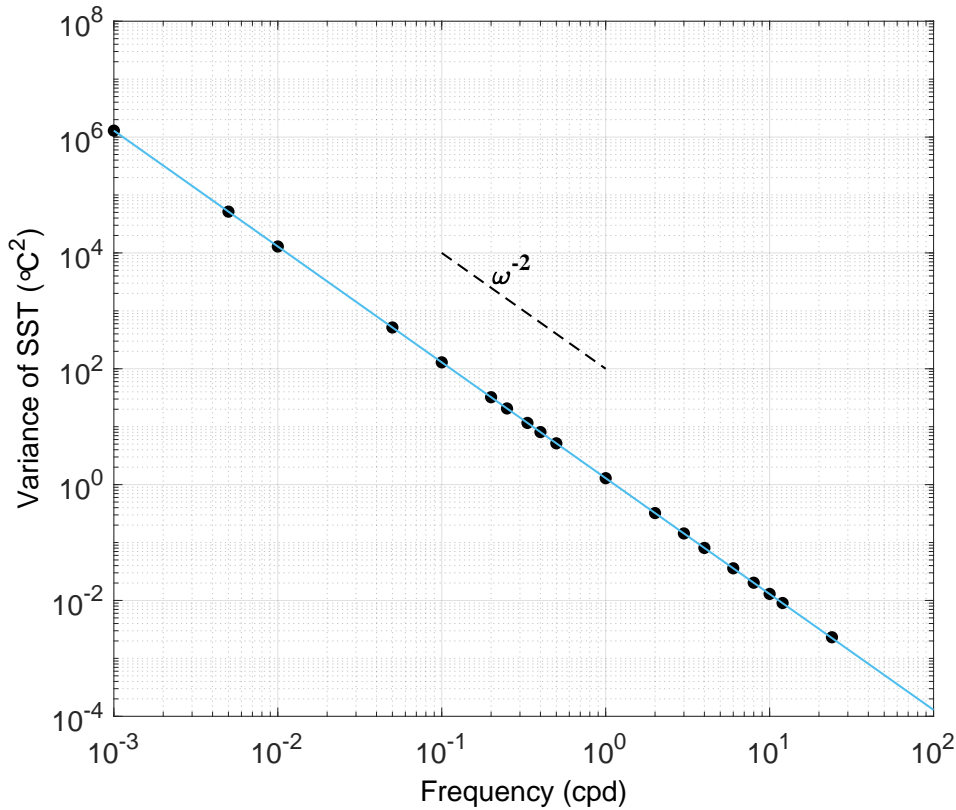


Figure 3.5: The square of magnitude of variability of sinusoidally forced SST anomalies plotted against frequencies (black circle). A fitted trend (blue line) shows that the squared variability and frequencies have a clear decaying relation with the slope equal to ω^{-2} .

3.2.3 The SST rectification excited by stochastic air-sea heat fluxes and its dependence on solar attenuation

Since the Tropical Ocean-Global Atmosphere Coupled Ocean-Atmosphere Response Experiment (TOGA-COARE) project, there has been a growing appreciation on the importance of the high-frequency properties exchanges between the atmosphere and ocean in the coupled climate system. A large volume of studies have pointed out that the inclusion of SST diurnal cycle significantly improve the reproduction of the intraseasonal variability of the SST (e.g. *Shinoda and Hendon, 1998; Shinoda, 2005; Bernie et al., 2005*) and ocean-atmosphere phenomena such as MJO (MJO) (e.g. *Bernie et al., 2007, 2008*) and inter-annual variability of the ENSO (e.g. *Tian et al., 2018*).

One of the basic effects of the SST diurnal cycle on the long-term SST variability is the systematically-positive rectification effect as illustrated in Figure 3.6. During the night, the heat loss to the atmosphere at the surface leads to enhanced mixing and the ML reaches to its greatest depth right before sunrise. Meanwhile, as the ML deepens, its heat content is mixed downward, hence the SST decreases. It is noted that during the night cooling period, the magnitude of SST decrease are damped by the deeper ML. At the onset of daytime, the positive downward solar radiation causes a rapid shoaling of the ML depth that amplifies the warming of the surface as the absorbed heat is distributed over a shallower layer. In the period of sunset, the stabilizing effect of the solar heat fluxes weakens and the stratification below the ML depth is slowly eroded. The ML deepens and SST drops again. The turbulent mixing intensifies during the night and stratification built up during the day is then more or less eroded, depending on the intensity of the non-solar heat fluxes and the surface wind stress. The diurnal variation of the ML depth in response to the atmospheric, in particular the solar radiation, induces an asymmetric ocean thermal inertia over the course of a day, leading to an asymmetric SST response to cooling and heating, and therefore a warming rectification in comparison to the SST forced by daily fluxes where such asymmetric response is absent.

The diurnal variation of SST has nicely illustrated that the SST response to the surface heat fluxes are asymmetric during the warming and cooling periods due to the variation of the surface ML depth. Here, we conjecture that such mechanism should still hold for the stochastic forcing condition. Essentially, the stochastic surface fluxes are composed by randomly distributed warming and cooling spikes over time which has been regarded as a statistically sound representation of the fluctuations in the air-sea heat fluxes caused by the transient weather systems. Intuitively, the ML depth variation in response to the stochastic fluxes should demonstrate same nature as that to the diurnal fluxes, i.e. shoaling for the surface warming and deepening for the surface cooling, which would eventually result in a similar asymmetric SST response. Unlike the diurnal variation, however, such

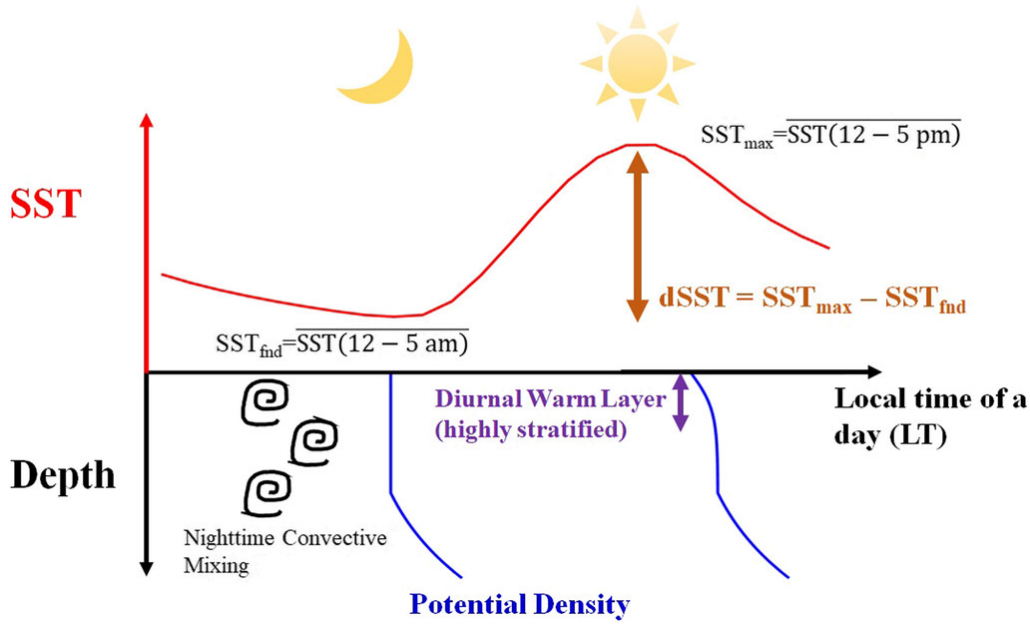


Figure 3.6: Adopted from *Feng et al. (2020)*. Schematic plot of diurnal variation of (DV) SST (red line) and potential density profiles in the upper ocean (blue lines). During a diurnal cycle, peak SST ($SST_{\max} = \text{mean SST from 1200 to 1700 LT}$) typically occurs in the local afternoon. The magnitude of DV SST is quantified by computing the $dSST$, the difference between the daytime peak and nighttime foundation SST (SST_{fnd}) during a diurnal cycle.

asymmetry of SST response does not necessarily occurs regularly within the exact same time window, which makes the actual time-mean SST estimate hard to be predicted.

The stochastic climate model paradigm proposed by H76 and FH77 has been widely adopted as the null hypothesis of the SST variability in middle and high latitudes where random atmospheric forcing is a good approximation (*Deser et al., 2010*). It is noted though, the simple stochastic climate model consists of a stochastically-varied atmosphere and slab ocean with fixed ML depth. Such simplification on the ML thermodynamics can lose some basic elements of the upper ocean adjustment to the stochastic atmospheric variability. Previous studies have reported that the noise-induced rectification can significantly modulate the mean climate state (e.g. *Sardeshmukh et al., 2003; Balan Sarojini and von Storch, 2009*) and the accumulation of such noise-induced deviation can potentially reach a tipping point initiating a noise-induced transition between

different climate equilibrium scenarios (e.g. *Wang et al.*, 1999). Although the reported rectification is produced by models with more higher degree of complexity compared to our one-dimensional mixed layer models. In order to test whether the variation of ML depth alone in the mixed layer model could excite SST rectification forced by the stochastic surface fluxes via the ML modulation, as we speculated above, a few idealized experiments are designed with a simple slab model and PWP one-dimensional ML model to assess the difference in the SST response affected by different ML thermodynamics. Here, we show that in a linear system, the stochastic perturbations in the air-sea heat fluxes tends to introduce aforementioned rectification effect on time-mean SST in a passively-forced ocean model. Such SST response to the stochastic surface heat fluxes is of close relation to the ML depth variation, which can be effectively altered by tuning the solar penetration depth that controlling the heat content vertical distribution contributed by the solar radiation.

Three models – slab model, NSP PWP and SP PWP model – are used to assess the response of SST to the stochastic surface heat fluxes under different solar penetration scenarios. The surface forcing is constructed in the same way as what we applied in the previous idealized experiments (as see in Figure 3.2) — the surface heat forcing is composed by solar radiation which is a uniformly distributed white-noise time series, ranging from 0 to 1000 W/m² with a 500 W/m² time mean, and a constant non-solar (i.e. net longwave radiation and turbulent heat fluxes) heat loss component with -500 W/m² to compensate the surface solar radiation. The wind stress is zero so that the SST responses simulated here are purely buoyancy-driven. It is foreseeable that the inclusion of wind stress (either fluctuations or mean) will contribute to the deepening of ML and damping the SST variability induced by the stochastic variabilities in the heat forcing. For each model, we repeatedly construct the surface forcing with the randomly generated solar radiation for 100 times to achieve an ensemble of 100 realizations of SST. The size of ensemble is chosen to guarantee that the resultant SST response demonstrates a representative behaviour and the experiment is computationally

efficient enough to be easily duplicated. We then investigate the behaviour of the SST response by calculating the ensemble mean of the SST realizations for each model experiment and comparing with the SST forced by the time-mean heat fluxes. The difference between the ensemble-mean SST and the SST forced by the time-mean flux (mean-forced SST hereafter) is referred to the rectification effect induced by the stochastic surface heat forcing.

a. Slab model

The SST produced by slab model is the time integration of the ratio between surface heat fluxes and prescribed ML depth. In stochastically-forced situation, the trend and variability of resultant SST is completely induced by the surface forcing without any ML variation imprinted on it. No significant difference is detected between the ensemble mean of 100 SST realizations and the SST produced with the time-mean surface forcing (i.e. a constant 500 W/m^2 solar radiation and -500 W/m^2 non-solar heat loss) as shown in Figure 3.7.

The characteristics of slab model SST ensemble spread are more readily explained by considering a series of SST realizations forced by sinusoidal-shaped surface heat forcing with varied initial phases (Figure 3.8a). Such experimental design intends to sub-sample the sinusoidal components that compose the random noise and meanwhile preserve the key features of SST response which can be interpreted physically and mathematically with much more clarified examples. The sub-sampled sinusoidal components of random surface heat forcing time series has a form as follows,

$$Q_{net} = A \sin(\omega t + \theta_0), \quad (3.2.3)$$

where A is the magnitude of the forcing, ω and θ define the forcing frequency and initial phase respectively. In the slab model, the tendency of SST follows Eq. 3.2.1, and the temporal evolution of SST is obtained by taking the integral of Eq.

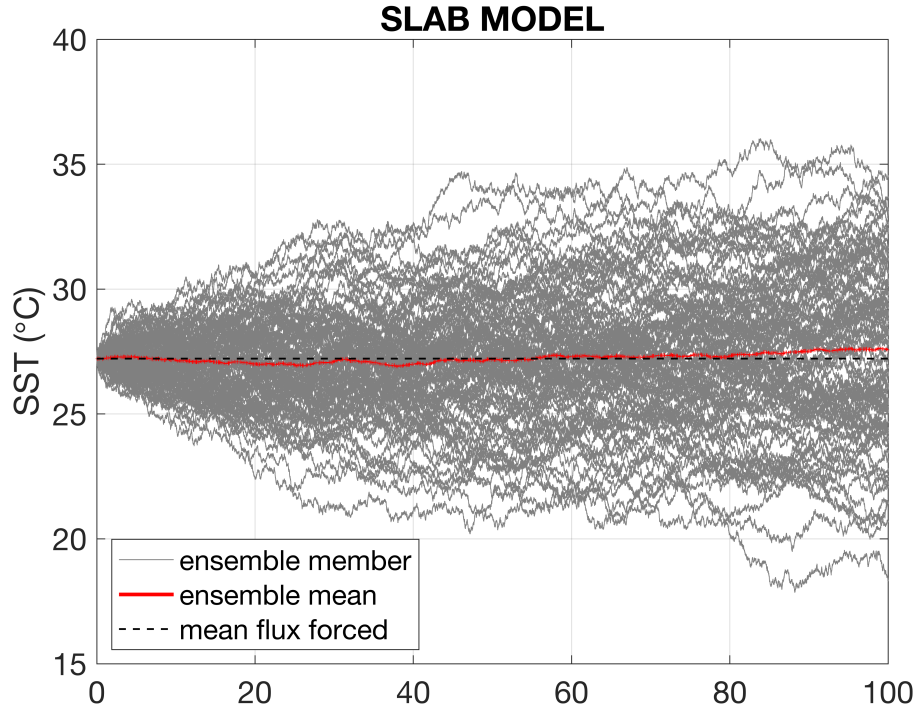


Figure 3.7: Ensemble spread of 100 SST realizations forced by stochastic air-sea heat fluxes produced by slab model superimposed with the mean-forced slab SST (black) and ensemble mean of SST realizations (red).

3.2.1 over time period t ,

$$\begin{aligned}
 T(t) &= T(0) + \int_0^t \frac{A \sin(\omega\tau + \theta_0)}{\gamma_0} d\tau \\
 &= T_0 + \frac{-A \cos(\omega\tau + \theta_0)}{\omega\gamma_0} \Big|_0^t \\
 &= T_0 + \frac{A \cos(\theta_0)}{\omega\gamma_0} + \frac{-A \cos(\omega t + \theta_0)}{\omega\gamma_0}.
 \end{aligned} \tag{3.2.4}$$

If we take the time average over the completed period corresponding to the forcing frequency (i.e. $t = \frac{2n\pi}{\omega}$, $n = 1, 2, 3, \dots$), the time-mean SST can be estimated as,

$$\bar{T} = T_0 + \frac{A \cos(\theta_0)}{\omega\gamma_0}. \tag{3.2.5}$$

The rectification effect of SST in slab model for the single realization SST is then determined by three parameters of the surface forcing — A (amplitude), ω (frequency) and θ_0 (initial phase). Figure 3.9 demonstrates the relationship

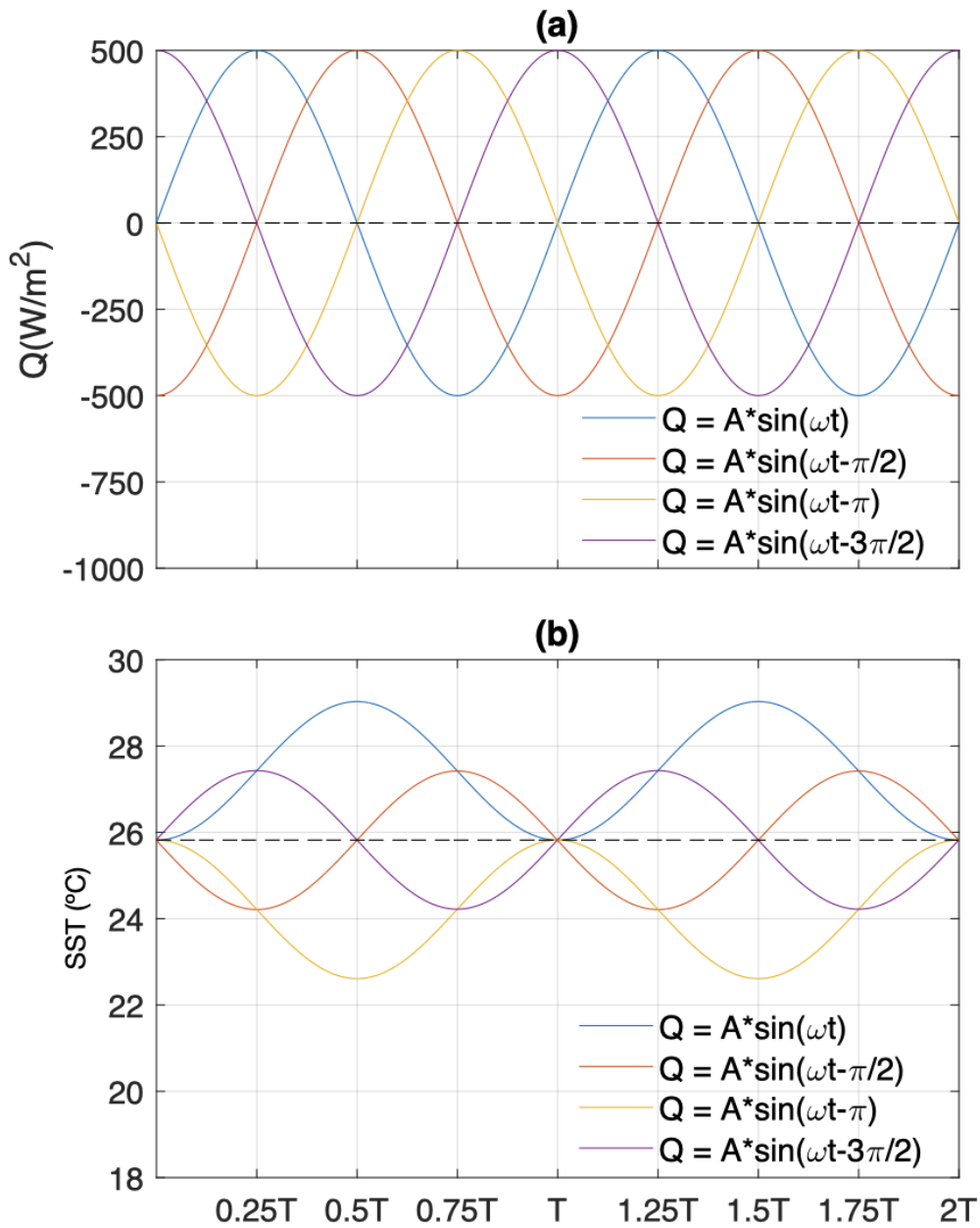


Figure 3.8: (a). A series of sinusoidal-shaped surface forcing with same magnitude, frequency but various initial phases ranging from 0 to $\frac{3\pi}{2}$. (b). The corresponding SSTs. The sign of rectification effect on SST varies with different initial phases, indicating a strong sensitivity to the initial phases.

between the rectified SST and A and θ_0 . The magnitude of SST anomalies shown in Figure 3.9 is scaled by the maximum SST anomalies to highlight the relative magnitude of the SST anomalies to the A and θ_0 . It is noted that the ω is also important for the resultant magnitude of SST anomalies (Eq. 3.2.5) but it does not effectively alter the pattern of the this scaled SST rectification pattern. In slab

model, the combination of a small ω and large A contributes to large magnitude of SST variability induced by the surface forcing because smaller frequency is equivalent to a longer warming/cooling period while the larger forcing magnitude means stronger surface forcing (Figure 3.9). Meanwhile, it is clearly shown in Figure 3.8b and Figure 3.9 that θ_0 is the key parameter that determines the rectification effect on SST in the slab model. Specifically, when the initial phase is 0, SST is initially forced by this half period of warming which acts to build up a warming signal on SST and later on cooling simply removes that warming signals and brings SST back to the reference state, leading to a positively rectified SST. Similarly, when the initial phase is $-\pi$, a half period of surface cooling causes SST to decrease and the warming afterwards tunes up the SST to the reference state, leading to a negatively rectified SST. In summary, the sinusoidal experiments show that in the slab model, the direction of the rectification effect on SST has a strong dependence on the initial phases associated with the timing and longevity of the cooling and warming anomalies in the surface forcing. Overall the positive and negative rectification associated with different initial phases tends to cancel out each other since the SST equally responds to the cooling and warming anomalies without any ML depth modulation, resulting in a net-zero SST rectification in the sense of the ensemble mean.

b. NSP PWP model

Although NSP PWP has shown qualitatively the same SST spectral characteristics with the slab model SST, the inclusion of ML depth adjustment has caused a totally different ensemble SST spread from the slab model as expected. The SST realizations produced by NSP PWP are plotted in Figure 3.10 with the same colour-coded SST ensemble members, ensemble mean and reference SST as in Figure 3.7. In NSP PWP, the ensemble SST always evolves above the reference SST and the ensemble mean is clearly warmer than the reference SST. This is because that in NSP PWP model, the ML depth deepens in response to the negative buoyancy fluxes due to the surface cooling, while it

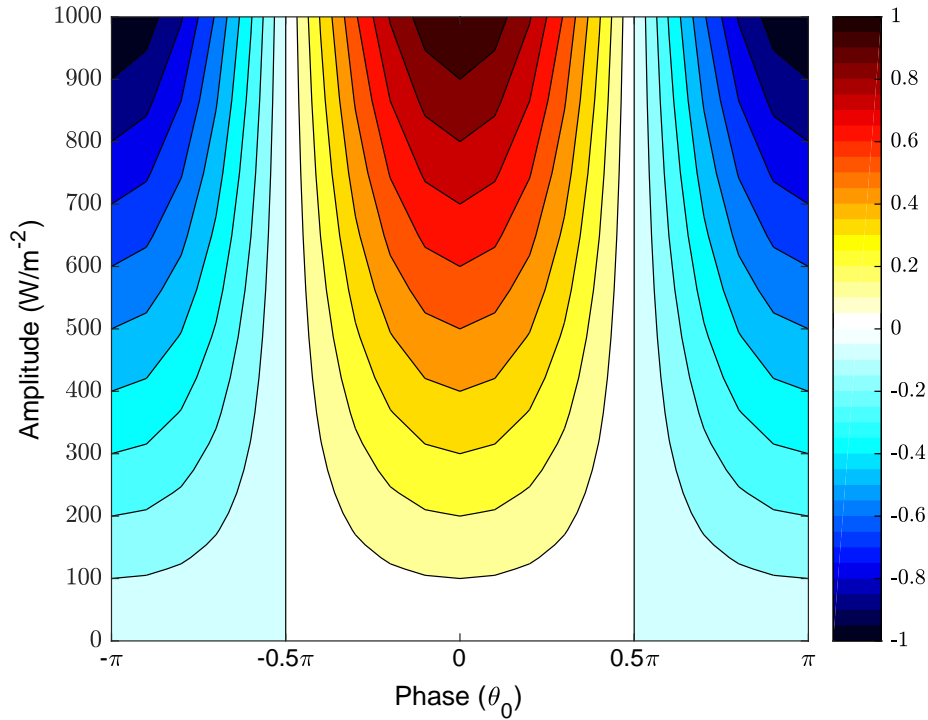


Figure 3.9: Scaled SST rectification effect in association to the amplitude A and phase θ_0 of the forcing. Magnitude of SST anomalies shown in colour is scaled by the maximum SST anomalies. The scaled pattern of rectified SST is not significantly affected by the choice of ω but with the actual magnitude inversely proportional to ω as indicated in Eq. 3.2.5.

bounces back to the surface when the solar heating is greater than the non-solar heat loss since all the solar radiation has been applied at the uppermost layer. In other words, when the uppermost layer is heated, the SST drastically increased due to the shallow ML depth while when the uppermost layer is cooled, the SST slowly decrease since the heat loss is distributed over a deeper ML and the SST variation is then largely damped. This asymmetry of SST response to the surface warming and cooling anomalies due to the adjustment of ML depth leads to the overall positively rectified SST.

The systematic rectification effect in stochastically-forced SST ensemble can be understood with the sinusoidally-forced experiments. As shown in Figure 3.11b, regardless of the difference within the initial stage associated with the forcing initial phases, the resultant SSTs have almost the same amount of positive rectification in relative to the reference SST. This weak initial phase dependence

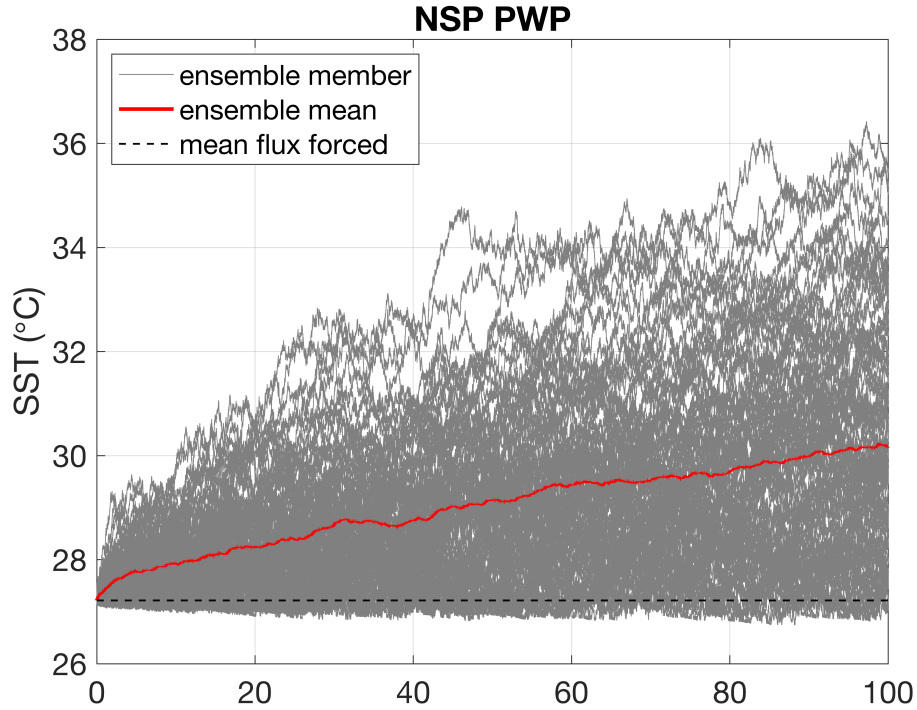


Figure 3.10: Same as Figure 3.7 but for NSP PWP model.

of the SST rectification can be again mathematically interpreted. The temporal evolution of SST in NSP PWP model can be approximately expressed as follow,

if $\theta_0 \in [-\pi, 0)$,

$$T(t) = \begin{cases} T(0) + \int_0^t \frac{A \sin(\omega\tau + \theta_0)}{\gamma_1} d\tau, & 0 < t < -\frac{\theta_0}{\omega}, \\ T(0) + \int_0^{-\frac{\theta_0}{\omega}} \frac{A \sin(\omega\tau + \theta_0)}{\gamma_1} d\tau + \int_{-\frac{\theta_0}{\omega}}^t \frac{A \sin(\omega\tau + \theta_0)}{\gamma_2} d\tau, & t \geq -\frac{\theta_0}{\omega}, \end{cases}$$

if $\theta_0 \in [-2\pi, -\pi)$,

$$T(t) = \begin{cases} T(0) + \int_0^t \frac{A \sin(\omega\tau + \theta_0)}{\gamma_2} d\tau, & 0 < t < -\frac{2(\pi + \theta_0)}{\omega}, \\ T(0) + \int_0^{-\frac{2(\pi + \theta_0)}{\omega}} \frac{A \sin(\omega\tau + \theta_0)}{\gamma_2} d\tau + \int_{-\frac{2(\pi + \theta_0)}{\omega}}^t \frac{A \sin(\omega\tau + \theta_0)}{\gamma_1} d\tau, & -\frac{2(\pi + \theta_0)}{\omega} \leq t < -\frac{\theta_0}{\omega}, \\ T(0) + \int_0^{-\frac{2(\pi + \theta_0)}{\omega}} \frac{A \sin(\omega\tau + \theta_0)}{\gamma_2} d\tau + \int_{-\frac{2(\pi + \theta_0)}{\omega}}^{-\frac{\theta_0}{\omega}} \frac{A \sin(\omega\tau + \theta_0)}{\gamma_1} d\tau \\ + \int_{-\frac{\theta_0}{\omega}}^t \frac{A \sin(\omega\tau + \theta_0)}{\gamma_2} d\tau, & t \geq -\frac{\theta_0}{\omega}, \end{cases} \quad (3.2.6)$$

where $\gamma_1 = \rho_w C_p h_1$, $\gamma_2 = \rho_w C_p h_2$. Here we assume that the ML depth is deep enough during the cooling period and is approximately expressed as a constant value ($h_1 \gg 1$ m), while the ML depth is constantly 1m during the warming period ($h_2 = 1$ m). And the rectification effect on SST can be determined by estimating the difference between reference SST $T(0)$ and time-mean SST $\bar{T}(t)$ over the period of $t = \frac{2n\pi}{\omega}$, ($n = 1, 2, 3, \dots$),

$$\bar{T}(t) - T(0) = \begin{cases} \frac{A \sin(\theta_0) - A\theta_0}{2n\pi\omega\gamma_1} + \frac{A\theta_0 - A \sin(\theta_0)}{2n\pi\omega\gamma_2} + \frac{A \cos(\theta_0) - A}{\omega\gamma_1} + \frac{A}{\omega\gamma_2}, & \theta_0 \in [-\pi, 0), \\ \frac{A[\sin(\theta_0) + \theta_0] - 2A \cos(\theta_0)(\pi + \theta_0)}{2n\pi\omega\gamma_2} + \frac{2A \cos(\theta_0)(\pi + \theta_0) - A[\sin(\theta_0) + \theta_0]}{2n\pi\omega\gamma_1} \\ + \frac{A \cos(\theta_0) - A}{\omega\gamma_1} + \frac{A}{\omega\gamma_2}, & \theta_0 \in [-2\pi, -\pi). \end{cases} \quad (3.2.7)$$

The underlined terms in Eq. 3.2.7 does not varies with the averaging period, while the rest of the equation vanishes if the averaging period is long enough (i.e. $n \rightarrow +\infty$), and hence the rectification effect on SST in NSP PWP model is reduced to,

$$\frac{A \cos(\theta_0) - A}{\omega\gamma_1} + \frac{A}{\omega\gamma_2}. \quad (3.2.8)$$

Considering $\gamma_1 \gg \gamma_2$, the magnitude of rectification effect on SST is large determined by term $\frac{A}{\omega\gamma_2}$, with weak correlation to the initial phase θ_0 mostly damped by the deeper ML depth adjusted to the surface cooling. Meanwhile the SST is overwhelmingly heated up over a shallow ML depth during the warming period, hindering the difference on SST initial cooling associated with the different initial phases in the forcing, leading to a small dependence on initial phases. For the stochastically-forced scenario, ML adjustment acts in the same way to damp the cooling and magnify the warming on SST in response to the stochastically-fluctuating air-sea heat fluxes and hence the stochastic variability in the air-sea heat fluxes contribute to a systematically positive SST rectification.

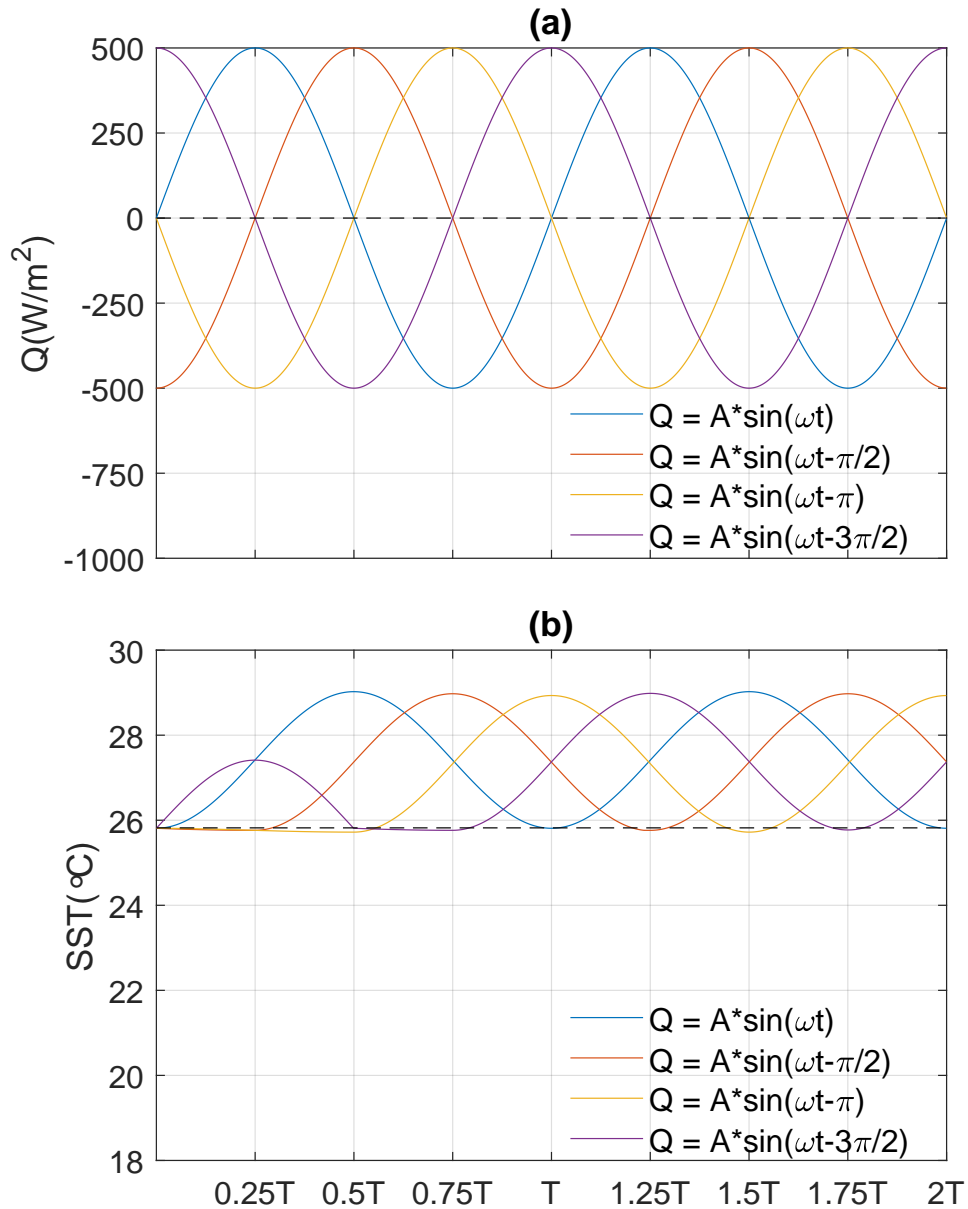


Figure 3.11: Same as Figure 3.8 but for NSP PWP model.

c. SP PWP model

In SP PWP model, the solar radiation is allowed to penetrate through the water column, diluting the solar absorption at the uppermost layer and distributing the solar irradiance exponentially along the depth. The ML depth again evolves with the air-sea heat fluxes — it deepens in response to the ML heat loss and acts to damp the cooling signals on SST while shoals to enlarge the warming signals. The existence of the asymmetric modulation from ML depth is

intuitively expected to produce similar SST ensemble spread to the NSP PWP model (Figure 3.10) with a systematically positive rectification induced by the stochastic surface forcing. However, SSTs simulated in the first ensemble experiment with SP PWP model (Figure 3.12a) behave similarly to the slab model SST, that is, the ensemble SST equally distributed above and below the reference SST and no significant difference detected between the ensemble-mean SST and the reference SST. This odd behaviour of SST led us to assess other possible parameters that determines the SST rectification effect. We tuned up the amplitude of the surface forcing from 500 W/m^2 to an unrealistic 5000 W/m^2 and repeated the ensemble experiments with SP PWP model, and the resultant SST spread is shown in Figure 3.12b. When the amplitude of the surface forcing is large, the positive rectification effect emerges on the SST under the work done by the asymmetric ML depth modulation. In spite of the false amplitude, there is such potential for noise-induced positive SST rectification.

It is understandable that the amplitude plays a crucial role in SP PWP model in terms of determining the SST rectification effect. When the solar radiation is penetrative, a substantial amount of solar heat ($\sim 50\%$) is penetrated into the layers below the uppermost layer while the non-solar heat loss is complete applied at the surface. The sub-surface warming and surface heat loss creates this near surface thermal inversion and is in favour of strengthening the mixing through which the cold deep water intrudes into the ML and cools down the SST. This process is manifested when the amplitude of the surface forcing is small (Figure 3.13a), where the solar radiation is not sufficient to warm up the ML and overcome the cooling deviation from the reference state during the initial cooling period associated with the initial phase. The sign of the rectification effect of a SST realization forced by single-frequency forcing in small amplitude case then largely depends on initial phases, and thus a net-zero ensemble-mean SST rectification, resembling the SST behaviour in the slab ocean model. When the warming on the SST is large enough to persistently overcome the initial cooling deviation (Figure 3.13b), SST ensemble members are systematically warmer than the reference due

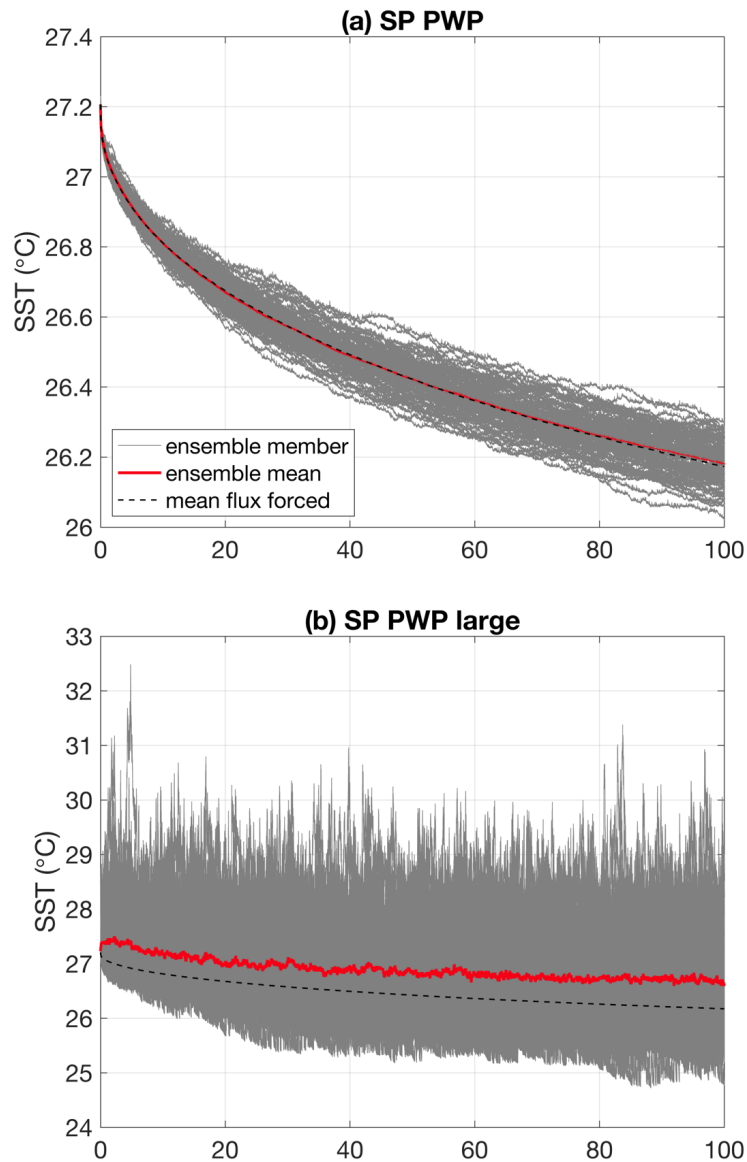


Figure 3.12: Same as Figure 3.7 but for SP PWP model with the forcing amplitude at (a) 500 W/m^2 and (b) 5000 W/m^2 .

to the asymmetric ML modulation. It is also noted that the rectification effect in our experiments are calculated as the difference between ensemble-mean SST and mean-forced SST and the same for the sinusoidally-forced experiments. One can always find that the SST oscillation in sinusoidally-forced scenario can produce a positive rectification effect in SP PWP model regardless of the forcing amplitude if the initial cooling effect is considered in the time-mean forcing (dashed line in Figure 3.13). The dashed line in Figure 3.13 denotes the SST forced by the heat fluxes starting with the initial heat loss and followed by the constant time-mean

value.

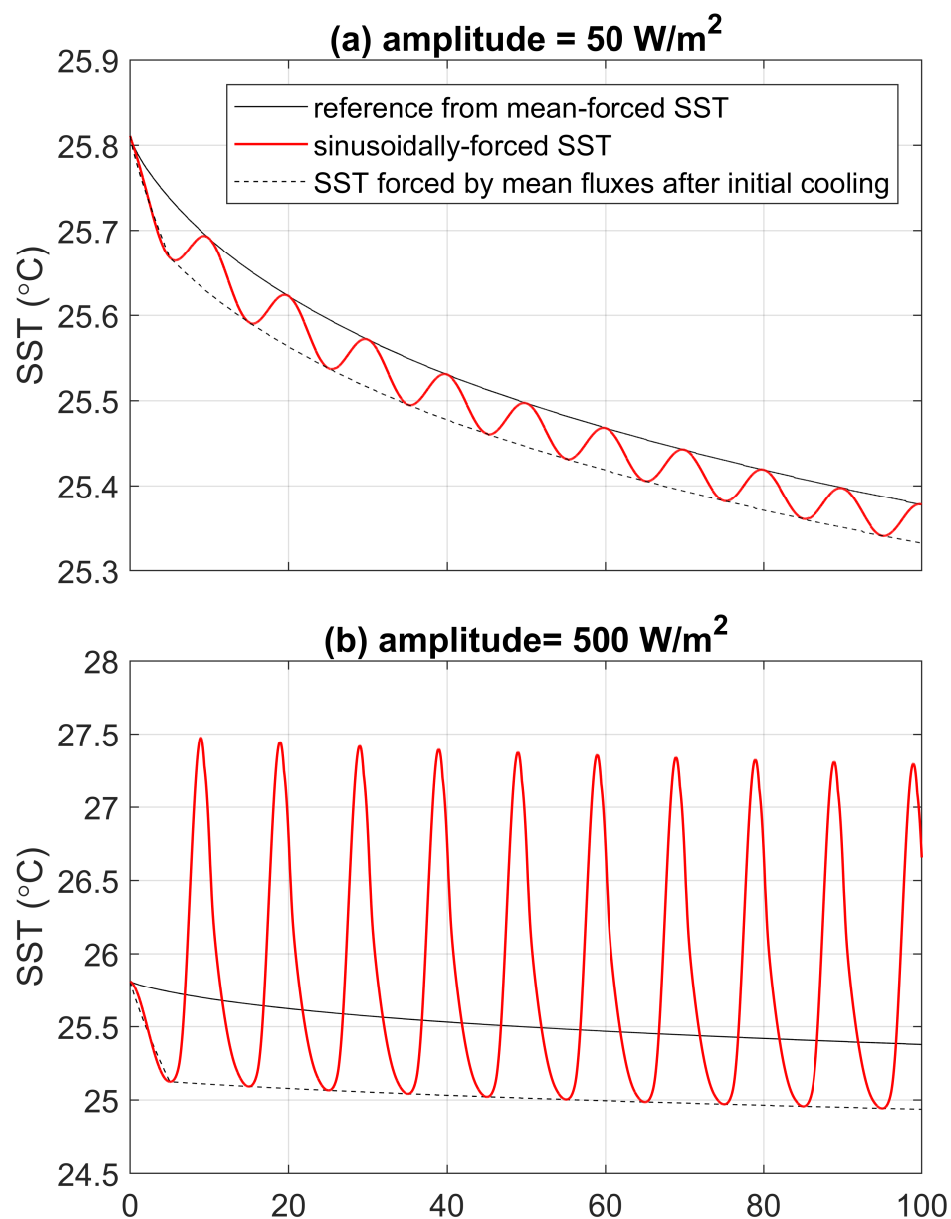


Figure 3.13: Same as Figure 3.8 but for SP PWP model with the forcing amplitude at (a) 50 W/m² and (b) 500 W/m². Here we only show the sinusoidally-forced SST (red) with the initial phase $\theta_0 = -\pi$, to highlight the difference on the rectification effect caused by different magnitudes of surface forcing. Panel (a) shows that when the initial phase leads to an initial cooling for half a period and the SST negatively deviating from the reference by the most. ‘Small’ forcing amplitude drives SST to increase back up towards the reference over the second half period while SST is not warmed up enough in this case to exceed the reference SST derived from the mean-forced SST (solid black), hence there is a systematic cooling effect on SST. Panel (b) shows that if the surface forcing magnitude is large enough, SST warming can overcome the initial cooling, to ensure a systematic warming effect.

3.3 Summary

In this chapter, a series of idealized experiments are designed to investigate the SST's response to the stochastic air-sea heat fluxes under the different solar penetration schemes which is equivalent to the different ML depth thermodynamics.

The interests on the stochastic air-sea heat fluxes are raised by the seminal papers of H76 and FH77 who argued that the ocean's response to the fast changing atmosphere can be simplified as an integral result of highly-fluctuated random atmospheric noise. This hypothesis is statistically sound and has been proved by numerous observations and model works. Even though Hasselmann's stochastic climate model managed to explain some of the spectral characteristics of observed oceanic variables, this model does not include any active ML adjustment to the surface forcing. One of the main concern is to assess the role played by the variation in ML depth by forcing three models — slab model with fixed ML, a non-solar-penetrative (NSP) PWP ML model and solar-penetrative (SP) PWP model with a pure white-noise air-sea heat fluxes time series. We managed to reproduce this red SST spectrum response across models (Figure 3.4), reassuring that Hasselmann's theory does not qualitatively affected by inclusion and exclusion of the time-varying ML depth. This universal red SST spectrum is further interpreted with a set of sinusoidally-forced experiments with different forcing frequency (Figure 3.5) and we argued that the large SST variance at lower frequency band is in association with a longer warming/cooling period when the surface heat fluxes variability is effectively accumulated on SST fields.

However, the shape of the power spectrum does not necessarily reveal all the processes at work on the temporal-spatial domain that affect the time-mean trend and variability of SST. Intuitively, the ML adjustment should be in favour of a warmer time-mean SST under the stochastic heat forcing via the asymmetric ML modulation on the heat capacity within the ML depth in comparison with

the mean-forced reference SST. We conducted the experiments with the same three models and we found that the stochastic variability in the air-sea heat fluxes has this potential to induce the positive SST rectification (Figure 3.10 and Figure 3.12b) as we would expect from our conjecture, while the SP PWP experiments indicate that only the heat fluxes with unrealistically large variability can effectively lead to such positive rectification since the SST is not as effectively warmed as it is in NSP PWP due to this extra convective mixing caused by the thermally static instability between the uppermost layer (uppermost layer solar absorption compensated by non-solar heat loss) and the layer just beneath (sub-surface warming from solar penetration).

OCEAN RESPONSE TO STOCHASTIC MESOSCALE WEATHER SYSTEMS

4.1 Introduction

The air-sea interface is of great importance to the ocean and atmosphere. Winds blowing across the sea surface are the primary forcing mechanism for driving the ocean circulation. Winds also determine the rate of evaporative and sensible heat changes at the sea surface, which balances the radiative heating from the incoming solar irradiance and net radiative loss from the longwave radiation. On the other hand, the water vapour released into the air condenses into cloud and precipitation and the associated release of latent heat contributes to driving the atmospheric circulation. The coupled interaction between the ocean and the atmosphere is therefore key to understanding both the oceanic and atmospheric circulations and is therefore critically important for weather forecasting and determining the roles of the ocean and atmosphere in climate variability. Before the turn of this century, the space-time variability of winds over the ocean was mostly based on reports from ships of opportunity. The sparse distribution of these observations restricted the resolution to scales larger than several hundred kilometres, while large areas outside of standard ship routes were seldom sampled.

For a long time, it has been recognized that, outside the tropics, the ocean-atmosphere thermodynamic interaction at large scales can be interpreted

as the ocean passively responding to wind-induced latent and sensible heat flux (e.g. *Hasselmann, 1976; Frankignoul, 1985; Barsugli and Battisti, 1998*). An increase in the volume of satellite-borne microwave radar scatterometers and microwave radiometers that could estimate global wind and SST at high spatial resolution has opened up the possibility of investigating ocean-atmosphere interactions on smaller scales. It has been revealed that the ocean-atmosphere interaction is fundamentally different on oceanic mesoscales of 10s-100s km. As scatterometry provides far more extensive geographical and temporal coverage and higher spatial resolution of ocean vector winds than are obtained by any other means, it pushes our knowledge on atmosphere-ocean interaction towards higher-wavenumber scales. However, the temporal fluctuations of the fine-scale structures reported by scatterometer are difficult to accurately resolve as the surface wind measurement derived from scatterometer snapshots are not measured simultaneously. It has been long recognized that a wind forcing with a smoothing period longer than 2~3 days does not suffice to excite large-scale, barotropic Rossby waves which are the major contributors to the kinetic energy below the surface Ekman layer (e.g. *Large et al., 1991*). High-frequency atmospheric forcing associated with orographic jets and mesoscale polar lows has also been recognized to be critical for determining the strength, frequency and location of the high-latitude deep convection events in various model studies (e.g. *Pickart et al., 2003; Condron and Renfrew, 2013; Holdsworth and Myers, 2015*).

Data assimilation techniques have been developed to combine the advantage of the continuous coverage of numerical models in time and space and the realistic visions revealed by a variety of observational platforms including satellite measurements and in-situ measurements (i.e. ships, met-buoys, land-based stations etc.) to produce reanalyses products that are in fine-resolution and high-frequency regimes to produce a continuous and globally-covered surface wind estimate under the context of a dynamic constraint confined by the numerical models. Limited by the model capability, such reanalyses data

commonly experience a less accurate representation of the observed small-scale variability. It is documented that the 10-m winds from National Center for Environmental Prediction (NCEP) and European Centre for Medium-Range Weather Forecast (ECMWF) global numerical weather prediction models considerably underestimate the wind variability on scales smaller than 1000 km compared with that derived from QuikScat scatterometer measurements even though both of these reanalyses have assimilated QuikScat observations (*Chelton et al.*, 2006). Efforts have been made to synthesize the scatterometer like mesoscale wind features (i.e. mesoscale polar lows, hurricanes and orographic jets) in the reanalyses data to attribute the impact of these systems on the ocean circulation (e.g. *Milliff et al.*, 1996, 1998; *Condron et al.*, 2008; *Hu and Meehl*, 2009; *Sproson et al.*, 2010; *Condron and Renfrew*, 2013). Furthermore, more attribution studies are completed by manipulating the resolution of the atmospheric forcing on temporal and spatial domains to isolate the effect of high-frequency and mesoscale features (e.g. *Jung et al.*, 2014; *Holdsworth and Myers*, 2015; *Wu et al.*, 2016). It is broadly agreed that the mesoscale weather systems reflected by the mesoscale and high-frequency features in the wind are able to stimulate a series of non-local circulation responses over longer time scales, by either altering the wind-drive gyre circulation in the mid-latitude North Atlantic or triggering extensive open ocean convection in the North Atlantic subpolar region.

Our evaluation of the newly released ERA5 climatic reanalysis dataset has indicated a consistent atmospheric energy deficiency, as identified in its predecessors in comparison with the QuikScat measurements, even though a much better accuracy is obtained in this latest wind fields (e.g. *Hoffmann et al.*, 2019). The rest of this chapter is organized as follows. In Section 4.2, we provide an overview of the ERA5 dataset and identify the energy deficiency in 10-m ocean winds. In Section 4.3, we present a novel approach to introduce a realistic amount of small-scale wind forcing to improve the distribution of reanalyses wind energy in space and time. We conducted sensitivity experiments

using perturbed wind fields in comparison with the original ERA5 wind fields to understand local oceanic response to the additional perturbation in Section 4.4 using an one-dimensional ocean ML model. We then look at the impact in a fully three-dimensional state-of-art OGCM in Section 4.5. A brief summary is provided in Section 4.6.

4.2 Energy Deficiency in ERA5 wind fields

4.2.1 The effective Resolution of Numerical Models

The atmospheric kinetic energy spectra in the free troposphere and lower stratosphere possess a robust and remarkable universality. Results from an observational analysis of kinetic energy spectra, produced in a seminal study by *Nastrom and Gage* (1985) using the Global Atmospheric Sampling Program (GASP) dataset, are shown here in Figure 4.1. The spectrum in Figure 4.1 illustrates the large-scale k^{-3} dependence of the atmospheric kinetic energy spectrum (enstrophy inertial range), along with a transition to a $k^{-5/3}$ dependence found in the mesoscale and smaller scales (energy inertial range), where k denotes the wavenumber. Also depicted in Figure 4.1 is the result of an analysis of the Measurement of Ozone and Water Vapor by Airbus In-Service Aircraft (MOZAIC) aircraft observations by *Lindborg* (1999). Making use of the structure functions, Lindborg produced a simple functional fit to the MOZAIC kinetic energy spectrum that results in a remarkably close fit to the GASP kinetic energy spectrum. Additionally, similar results have been reported for kinetic energy spectra analyses of aircraft data by *Cho et al.* (1999a,b) for Pacific Exploratory Missions (PEM) Tropics flights. The results have shown only a small dependence on latitude, season, or altitude (*Nastrom and Gage*, 1985; *Cho et al.*, 1999a,b).

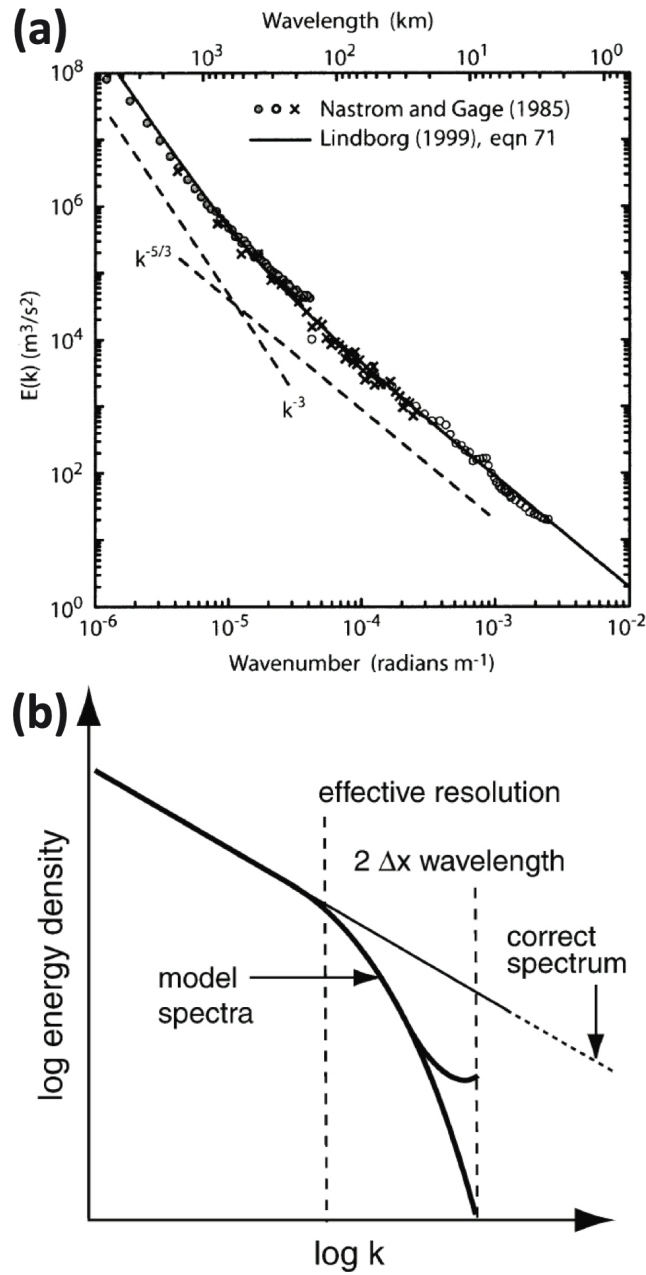


Figure 4.1: (a). *Nastrom and Gage* (1985) spectrum derived from the GASP aircraft observations (symbols) and the *Lindborg* (1999) functional fit to the MOZAIC aircraft observations, adapted from *Skamarock* (2004) Figure 1. (b). A schematic depicting the effective resolution by comparing the dependence of the model-derived spectra from the theoretical prediction, adapted from *Skamarock* (2004) Figure 10.

The explanation for the large-scale k^{-3} dependence of the kinetic energy spectrum (between length scales of ~ 4000 km to ~ 500 km) has arisen from applications of 2D turbulence theory (e.g. *Kraichnan*, 1967; *Charney*, 1971), which predicts a

downscale (forward) enstrophy (mean-square vorticity) cascade with a constant enstrophy flux and no energy flux within the range. The explanation for the $k^{-5/3}$ dependence has been controversial and two explanations for the mesoscale behaviour of spectra have been put forward. One hypothesis posits the input of energy from small scales by processes such as convection or other sources and an upscale (inverse) transfer of a small portion of this energy, with the resulting $k^{-5/3}$ spectrum predicted by 2D turbulence theory (e.g. *Gage, 1979*). The other hypothesis suggests that the mesoscale spectrum is dominated by internal gravity waves (*Dewan, 1979; VanZandt, 1982*).

The $k^{-5/3}$ dependence of the mesoscale spectra suggests that the small scale motions are energetic and can potentially feed energy upscale to flatten the spectral slope at length scales smaller than the intermediate region of wavelengths from 500 to 1000 km. While in numerical models, these small-scale features are not properly resolved due to limitations of the model's spatial and temporal resolution, the propagation of model errors, and the uncertainties induced by initializing and verifying forecasts at small scales because of lack of mesoscale data (*Skamarock, 2004*). The inadequate representation of small-scale features then leads to an energy deficiency within the energy inertial range characterized by a theoretical $k^{-5/3}$ dependence of the energy spectrum. The departure of the model derived energy spectra from observations defines the effective resolution of the model (*Skamarock, 2004*). The model is regarded as capable of accurately resolving features at this effective resolution (Figure 4.1b). By comparing Weather Research and Forecast (WRF) model simulations with different spatial resolutions at 22 km, 10 km and 4 km with the *Lindborg (1999)* function fit spectra, *Skamarock (2004)* found that the effective resolution to be about $7 \times \Delta x$, where the Δx is the grid resolution. Although the factor of the effective resolution relative to the model resolution does vary between different models associated with model diffusion schemes (e.g. *Lean and Clark, 2003; Hamilton et al., 2008*). *Skamarock (2004)* also found that a reduction of the energy dissipation rate in the WRF model would lead to increased energy at the smaller

scales and better spectral tails, while further reduction would result in unrealistic arising of energy spectrum. In summary, a spectral analysis of the kinetic energy of wind field can be used to determine the effective resolution of a model or reanalyses product by pinpointing the spatial scale where the spectral slope departs from these k^{-3} or $k^{-5/3}$ relations.

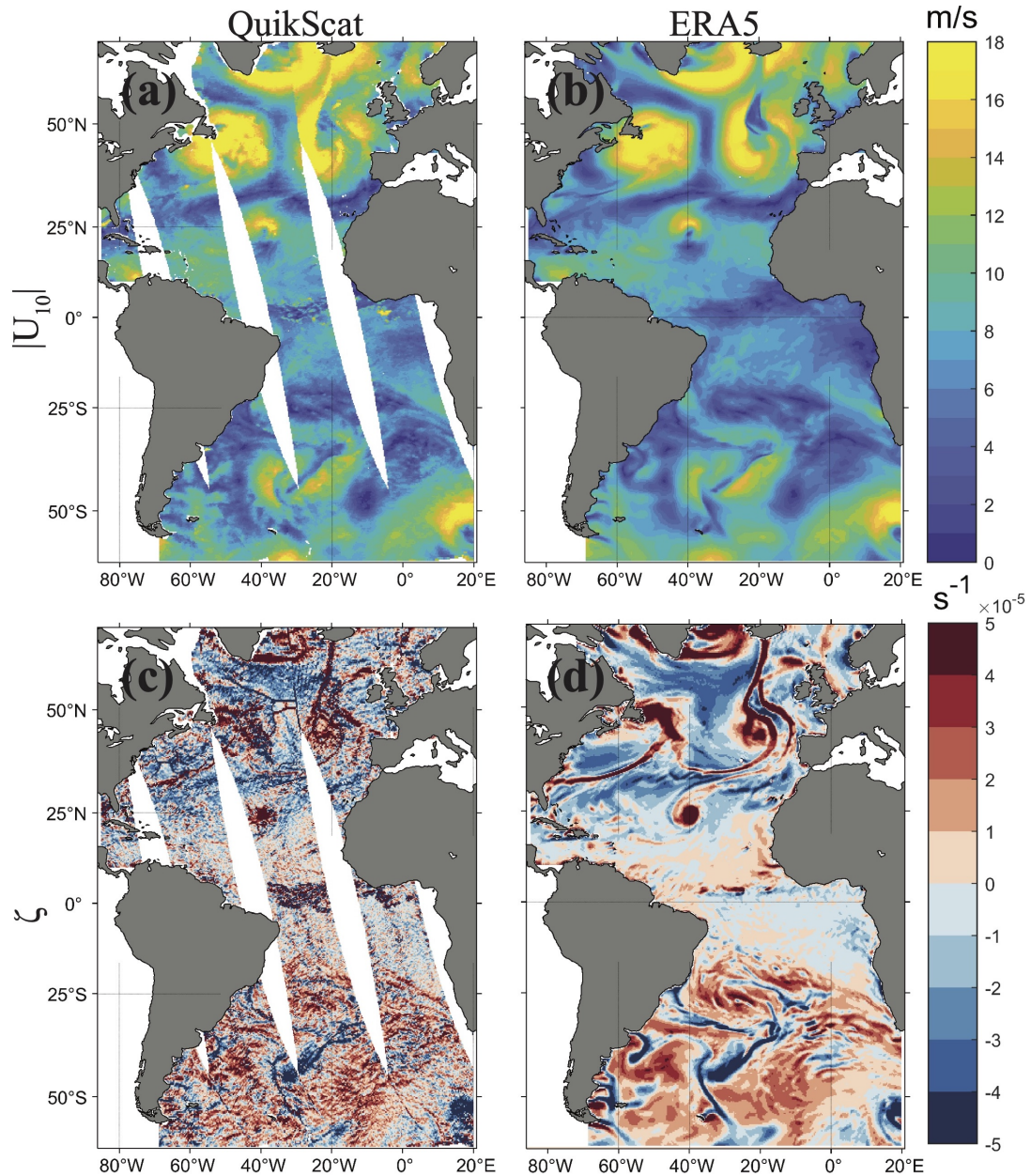


Figure 4.2: (a) and (b) are the spatial snapshots of the surface wind speed derived from QuikScat and ERA5 for 0800UTC on 1st of January, 2008, respectively, across Atlantic Ocean (60°S to 65°S). (c) and (d) are the corresponding relative vorticity fields.

4.2.2 Spectral Analyses of ERA5 Wind Fields

In this study, we evaluate the representation of small-scale feature in the newly released ERA5 wind fields. As ERA5 will be widely used within the climate community for climatic evolution interpretation for at least 10 or so years, it is of great interest to understand how well ERA5 resolves critical mesoscale and smaller-scale atmospheric features. Here, our region of focus is the Atlantic Ocean from $60^{\circ}\text{S}\sim 65^{\circ}\text{N}$. Figure 4.2 compares the surface wind speed and relative vorticity computed with QuikScat scatterometer measurements and ERA5 output on 1st January 2008. The spatial maps compare well on large scales – as one would expect since ERA5 assimilates QuikScat winds. However, the ERA5 wind and vorticity fields are generally smoother than those observed by scatterometer. One distinct difference is concentrated in the tropical regions (0° , 40°W - 0°) where QuikScat captures a strong meridional shear of sea surface winds whereas this feature is much weaker and smaller in reanalyses fields. The vorticity field clearly reveals a major lack of small structures (spatial variabilities) in ERA5 across the whole selected domain.

Following on what has been established by *Skamarock* (2004) and other previous evaluation work on operational analyses datasets such as NCEP and ECMWF (e.g *Chelton et al.*, 2006), we have conducted a wavenumber spectral analysis to assess the representation of small-scale features by ERA5 as a measure to understand how well the Integrated Forecast System (IFS) model used to produce the reanalysis fields deals with the small-scale energy sink. The wavenumber spectral analysis is performed over the Atlantic Ocean domain (Figure 4.2 and Figure 4.3a) and the comparison is made between the QuikScat and ERA5 wind measured from 1st January to 31st December, 2008.

The wavenumber spectral analysis is performed using a discrete Fourier transform (DFT) method based on spatially detrended wind fields within the selected domain of the Atlantic Ocean (Figure 4.3a) following the method proposed by *Errico* (1985). The linear large-scale trend of a $N \times M$ wind field

$a_{i,j}$ is removed as follows:

1. First, for each j , determine the slope

$$s_j = \frac{a_{N,j} - a_{1,j}}{N - 1}; \quad (4.2.1)$$

2. Next, for each i, j pair, remove the trend in the i direction to yield

$$a'_{i,j} = a_{i,j} - \frac{1}{2}(2i - N - 1)s_j; \quad (4.2.2)$$

3. Repeat steps 1 and 2 with the roles of i and j reversed, with $a'_{i,j}$ replacing $a_{i,j}$, M replacing N , and obtain the new detrended field $a''_{i,j}$ (in place of $a'_{i,j}$ in step 2). The $a''_{i,j}$ are actually independent of the order in which the trends are removed. The results are periodic, i.e.,

$$a''_{i,1} = a''_{i,M}, \quad (4.2.3)$$

for all i , and

$$a''_{1,j} = a''_{N,j}, \quad (4.2.4)$$

for all j .

The detrending is applied as the spectral analysis is performed over a limited area, where those planetary-scale atmospheric phenomena exhibit an aperiodic structure with large trends across the domain (*Denis et al.*, 2002). A standard periodic Fourier transform on regional domains would result in the aliasing of large-scale variance into shorter scales.

The spatially-detrended wind map is then passed to the DFT to generate the wavenumber spectra. It is noted that the wavenumber spectra displayed in Figure 4.3b and for the rest of the chapter are computed along the meridian lines to be assured that the DFT takes a sufficient sample of long enough continuously-measured wind by QuikScat swath to cover the large spatial scales

and to illustrate a full range of observed wavenumber spectra. The wavenumber spectrum is then averaged over the selected wind samples within each wavenumber bins. The size of the wavenumber bin is determined by uniformly dividing the range between the minimum and maximum length scales by the number of the grid points along the meridional direction covered by the domain. For year 2008, about 10,000,000 samples (sample size > 60) from the QuikScat scatterometer are selected for the wavenumber spectrum calculation. The wavenumber spectrum of ERA5 wind is formulated in the same way described above. It is clearly revealed by Figure 4.3b that the ERA5 surface wind kinetic energy is damped and departs from the observed spectra derived from QuikScat measurements at a length scale of 400~500 km, the intermediate range where the enstrophy inertial range and energy inertial range merge together. This implies that ERA5 has an effective resolution of about 400 to 500 km.

Another aspect of this model-derived energy sink issue that tends to get overlooked is that a lack of small spatial scale energy is likely to result in a deficiency at high-frequency temporal scales considering the typically large velocities of small-scale disturbances (e.g. orographic jets and outburst of wind extremes such as polar lows, secondary frontal cyclones, mesoscale convective systems and squall lines in tropical regions) are only active for a short period of time varying from several hours to several days. To address the frequency spectrum discrepancies, we compare the ERA5 wind frequency spectra with that derived from the buoy time series. In total 18 buoys situated in the Atlantic Ocean are selected for the comparison for year 2008, with 9 from the Prediction and Research moored Array in the Tropical Atlantic (PIRATA) monitoring programme, 8 from National Data Buoy Center (NDBC) and one private met buoy SIMORC located in the Norwegian Sea (Figure 4.3a). The ERA5 wind are sampled at the nearest grid point to these met buoys. Both the observed and ERA5 frequency spectra are averaged over the 18 locations. By comparing the frequency spectra, we are able to identify an underestimation in high-frequency wind variance within frequencies higher than one cycle per day (Figure 4.3c).

The spectral analysis shown in Figure 4.3b,c indicates that the processes that are imperfectly represented in ERA5 wind fields are temporal-spatially coherent and the differences in both wavelength and frequency domains are not negligible. Considering ERA5 wind data have relatively high temporal (hourly) and spatial (31 km) resolution compared to other global reanalysis dataset, the energy deficiency shown by our spectral analysis is likely to be representative of all global reanalysis products.

4.3 A Method to Improve ERA5 Wind Fields using "Cellular Automata"

The previous section has demonstrated that ERA5 reanalysis underestimates the wind kinetic energy at small scales (<500 km) and high-frequencies (sub-daily scales), which may have a significant impact on the ocean. It is conceived that one of the pathways (apart from explicitly resolving small-scale processes in a deterministic way) to improve representation of the small-scale features in operational weather and climate models is to parameterize their ensemble effects. This can be done by introducing a suitably contrived near-grid-scale stochastic forcing function to inject energy back into the model as a mimic of convective-scale processes such as deep convection and orographical disturbances (e.g. *Palmer et al.*, 2005; *Shutts*, 2005). Following this approach, we test the conjecture that the energy deficiency in ERA5 is the results of insufficient energy input from the sub-grid-scale processes by introducing a kinetic energy backscatter scheme called Cellular Automata Stochastic Backscatter Scheme (CASBS) (e.g. *Shutts*, 2005).

The cellular automata (CA) method uses a discrete model that generates patterns with coherent structures over a number of discrete grid cells in space and time. The pattern is generated via assigning and altering the value of grid cells using rules associated with the state of the neighbouring cells at the

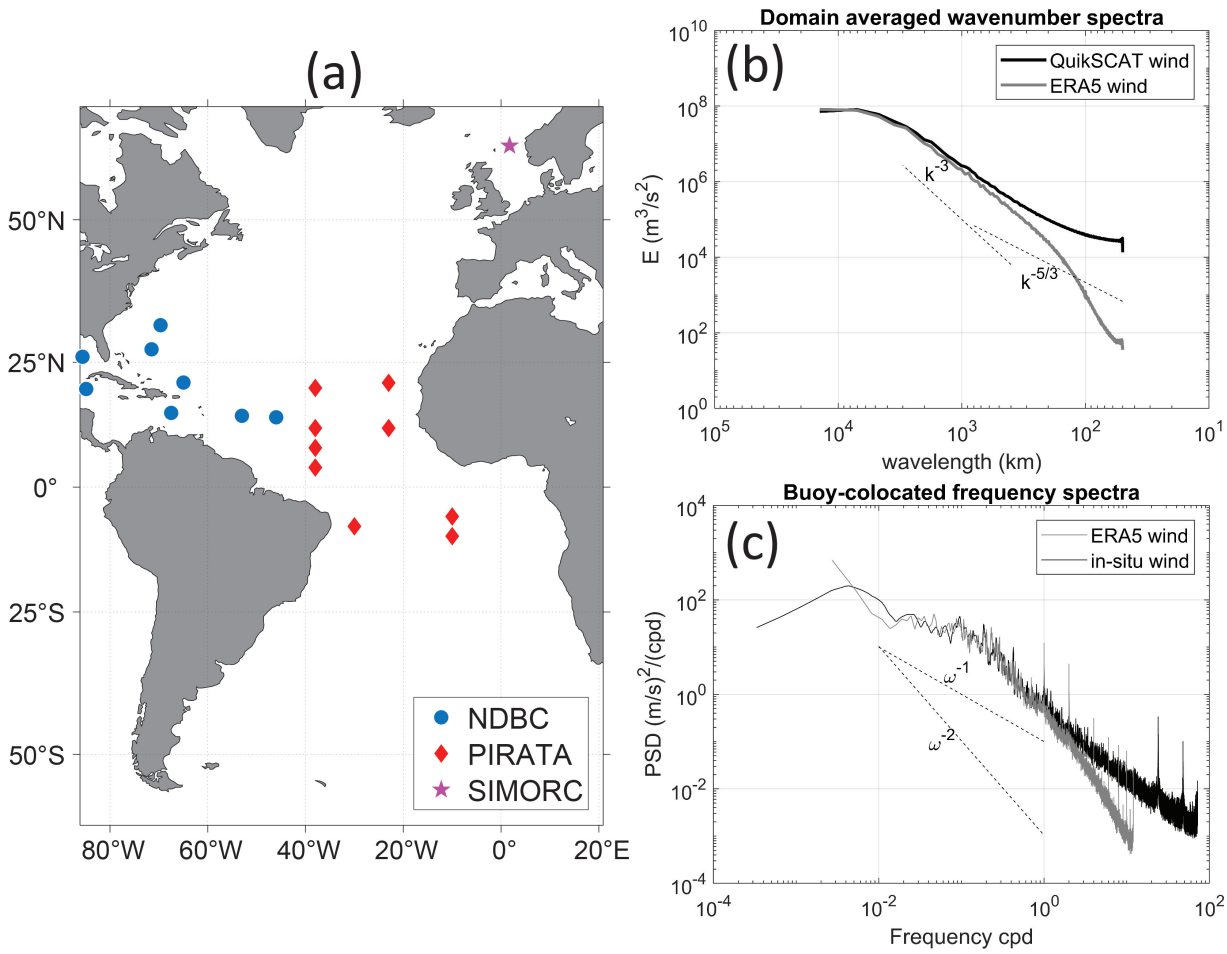


Figure 4.3: (a) Locations of in total 18 available met-buoy stations including 8 NDBC buoys (blue circles), 9 from the PIRATA mooring array (red diamonds), and one private met buoy, SIMORC, located in Norwegian Sea (magenta stars). (b) Wavenumber spectra derived from QuikScat (black) and ERA5 wind fields (grey). The departure of the ERA5-derived spectrum is clearly shown here initiating at the length scale at 400~500 km, within the predicted intermediate range between the enstrophy inertial range and energy inertial range (e.g. Lindborg, 1999). (c) Frequency spectrum derived from ERA5 and collocated meteorology buoy stations. A major energy sink of ERA5 ocean winds is detected in the frequency range higher than 1 cycle per day.

concurrent and earlier times. The CA algorithm was firstly introduced to the atmospheric modelling community by Palmer (1997), where it was envisaged to be able to parameterize the sub-grid-scale atmosphere disturbances associated with convection and orography. It has the potential to be coupled to various model diagnostics such as the convective available potential energy, which drives the atmosphere deep convection events related to the convective cloud clustering and precipitation patterns (Bengtsson et al., 2013). Shutts (2005) incorporated a

CA algorithm into the kinetic energy backscatter scheme in the ECMWF ensemble forecast system by applying the CA generated perturbation as a streamfunction forcing field to parameterize the energy dissipation rate raised from the orography information, deep convection and numerical errors. *Berner et al.* (2008) implemented the CA energy backscatter scheme in the ECMWF coupled ocean-atmosphere model and found an improved performance in reducing the model uncertainty and probabilistic skill of seasonal forecasts due primarily to the energy injected by CA at the near-grid scales being backscattered non-linearly to larger scales. *Bengtsson et al.* (2013) reported that a CA algorithm could be used to perturb the updraught mass flux equation to improve the stochastic nature of atmospheric deep convection. Although the CA scheme is mostly used for sub-grid scale process parameterization, the fact that temporal fluctuations of the CA perturbation can improve the frequency spectrum of the simulated motions is overlooked in general. Here we show that CA algorithm can improve the ERA5 wind fields comparing to observed behaviours of wind energy in both wavelength and frequency domains.

4.3.1 Deterministic CA and Probabilistic CA rule sets

A cellular automata, CA, describes the local evolution of discrete states of a grid cell, according to a set of rules involving the states of the neighbouring grid cells at the previous time step. The rules generate self-organization of cells and complex patterns on spatial scales larger than one grid cell. For applications in atmospheric modelling, this method has the advantage of generating coherent perturbation pattern over a wide range of spatial scales. Originally, the rules of CA follow the automata of ‘Conway’s Game of Life’ (GOL, *Martin*, 1970), and are deterministic with the evolution of the generated pattern being fully predictable. The rules are summarized in *Shutts* (2004) and usually take 3 steps to determine the state of each grid point at each iteration. Before the iteration starts, the rules define two states for each grid cells: alive or dead. At the initial state, all the grid cells take the integer value of 0 and some of them are randomly assigned with

the same value (larger than 0), called the number of life (N_L). These cells are then regarded as alive cells. For a regular grid with a 3×3 array of cells where the central cell is surrounded by 8 neighbouring cells, the rules take the following steps:

1. When a dead grid cell is surrounded by exactly 2 or 3 alive cells, then at the next time step the dead cell becomes alive and is assigned with the N_L .
2. When an alive grid cell is surrounded by exactly 3, 4 or 5 alive cells, it remains the same state at the next step by keeping whatever value it holds for the current step;
3. when an alive grid cell is surrounded by a different number of alive cells, it decreases the assigned number of life by 1 for the next time step until the value equals zero and it is regarded as a dead grid cell.

The value of a grid can be constrained to between -1 to 1 after scaling and a mean-removal is applied over the domain. Three key parameters in the CA algorithm collectively control the spatial and temporal characteristics of the generated CA pattern: (1) the number of life N_L assigned to the grid cells initially which determines the length of the memory of the alive cells throughout the development of the CA pattern; (2) CA grid size ΔS_{CA} , together with the N_L , defines the smallest spatial scales the CA algorithm can simulate ($\sim \Delta S_{CA} \times N_L$); (3) CA time step Δt_{CA} together with the N_L defines the shortest time scales of a CA pattern ($\sim \Delta t_{CA} \times N_L$). It should be noted that ΔS_{CA} and Δt_{CA} should be selected to be compatible with the targeted products, for example, in practice, the size of the CA grid is typically smaller than the model resolution in order to resolve sub-grid variabilities. Note the CA grid size and time step does not alter the behaviour of the original CA pattern, but they are vital for the products that need to be perturbed.

We conducted a test run using deterministic CA rules on a 300×300 grid point domain, initializing the algorithm with a 4×4 block of alive cells in the centre of

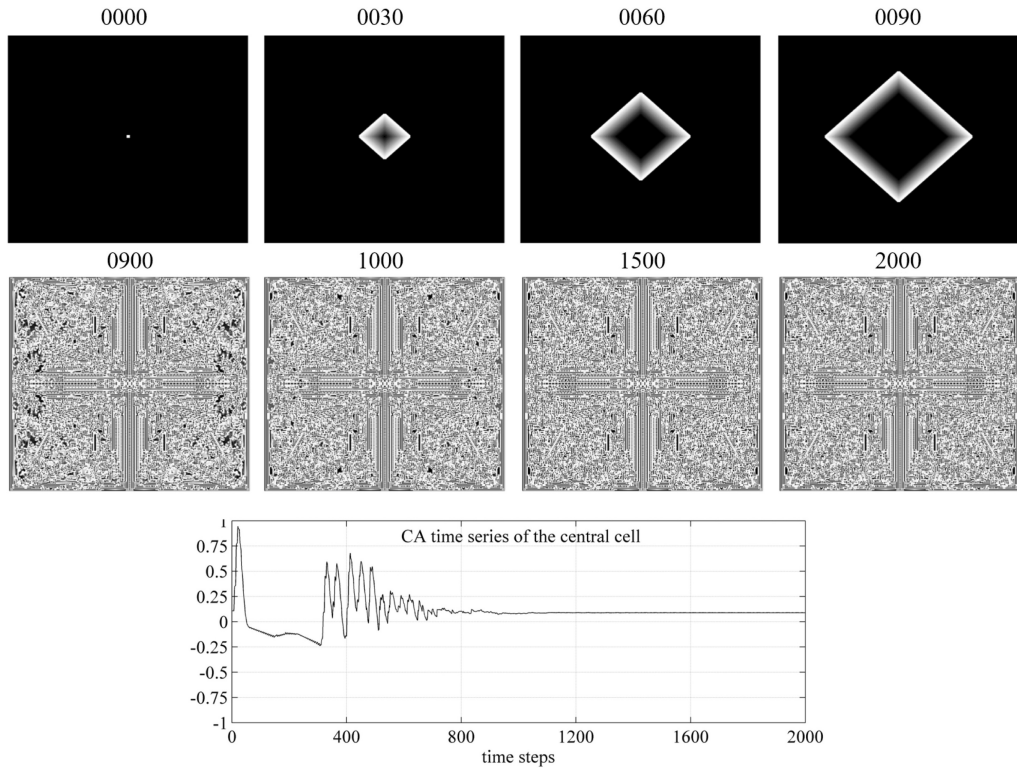


Figure 4.4: Snapshots of a CA pattern evolution generated by deterministic CA rules for 2000 time steps initialized with a 4×4 block of alive cells in the middle of a 300×300 domain. The number of time steps is shown above each domain snapshot. Black colour represents the dead cells and white colour represents the alive cells. The lower panel shows the time series of CA values of the central cell.

the domain. The N_L is set to be 32 for a long enough memory of pattern growth. The snapshots in Figure 4.4 show a rectangular deterministic CA pattern in the first few hundred steps and piled-up alive cells filling the whole domain with little evolution between consecutive time steps after 900 time steps. The time series of scaled CA values at the central grid cell shows that the CA pattern ceases to evolve after about 900 time steps due to the overwhelming generation of alive cells. From time step 10 to 300, the lack of fluctuations at the centre of the domain is consistent with the expanding square-shaped pattern at the early stage of the computation. This particular issue is actually dependent on the initial condition and it is likely to diminish when the N_L is randomly prescribed to multiple cells at the first place.

In our study, we follow the philosophy taken by *Bengtsson et al.* (2013) and explore probabilistic CA rules to include some stochasticity in the generated pattern for

a more physical appearance of the sub-grid variability than that shown in Figure 4.4. In practice, we define threshold values of the probability for the ‘birth’ and ‘decay’ of a living cell, mainly to balance the unfavoured ‘decay’ events that we see in the deterministic CA rules. Specifically, our probabilistic CA rules take the following steps:

1. When a dead grid cell is surrounded by exact 2 or 3 alive cells, then at the next time step there is a 75% chance that the dead cell becomes alive and is assigned with the N_L .
2. When an alive grid cell is surrounded by exact 3, 4 or 5 alive cells, it remains the same state at the next step by keeping whatever value it holds for the current step;
3. When an alive grid cell is surrounded by any other number of alive cells, there is a 95% chance that it decreases the assigned number of life by 1 for the next time step until the value equals zero and it is regarded as a dead grid cell.

The probability is implemented by using a random number generator to uniformly select a number between 0 and 1. The chance that a value returned by the generator is less than 0.75 is 75%, likewise the chance for the value less than 0.95 is 95%. As stated above, for these probabilistic CA rules we set 75% to the ‘birth’ events and 95% to the ‘decay’ events. In other words, the altered rules are not just introducing stochasticity to the generated pattern, but also trying to suppress the growing rate of the alive cells (see Figure 4.4) by allowing more free space for the pattern development throughout the time. Figure 4.5 shows that these probabilistic rule additions add some randomness into the pattern evolution which is propagated and manifested through time. The resultant pattern is different in each independent experiment even with exactly the same initial condition and same rules due to the induced randomness. The probabilistic CA pattern depicted in Figure 4.5 is more ‘organic’ looking and resembles the observed patterns of small-scale convective cells seen commonly

over ocean (e.g. *Stevens et al.*, 2020) (see also Figure 4.5 bottom panels). CA value of single grid cell evolves continuously throughout time with the ‘birth’ and ‘decay’ rate in balance to avoid all-alive (as shown in Figure 4.4) or all-dead situations.

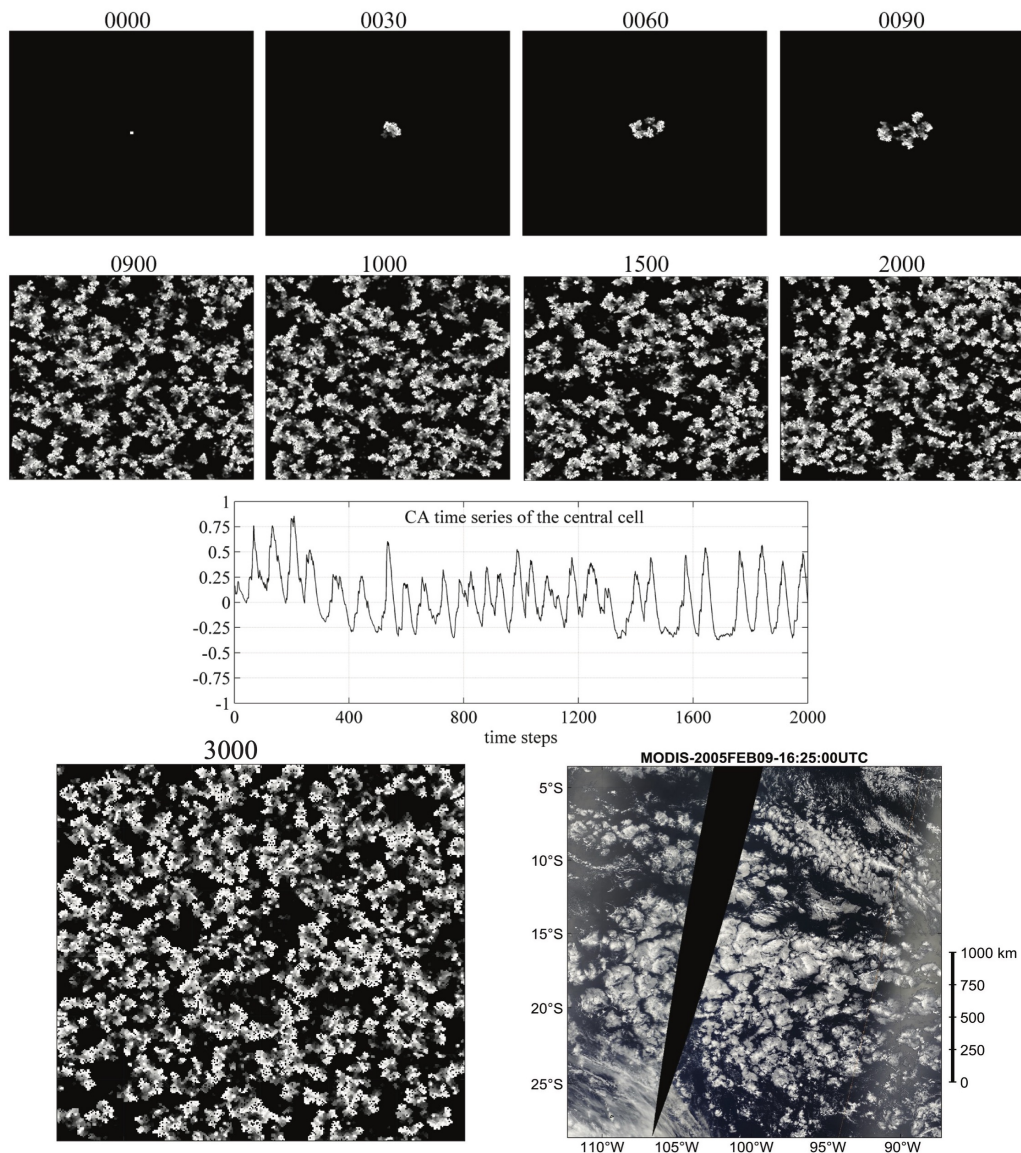


Figure 4.5: Same as Figure 4.4 but for the probabilistic CA rule test experiment. Comparison at the bottom shows high resemblance between a developed CA pattern and observed (MODIS radiometer, true colour imagery) small-scale cloud pattern from convective events over the ocean.

4.3.2 Tuning the probabilistic CA algorithm

Within the CA algorithm, the temporal and spatial characteristics are not only sensitive to the deterministic and probabilistic rules but also controlled by a small set of parameters. As we mentioned early, the value of N_L implicitly determines the length of the single CA grid cell memory over time and heavily affects the spatial span of a self-organized structure. It is intuitive that a larger N_L leads to a broader spread of a spatially coherent structure that is longer-lasting. These relationships can be translated into physical domain of space and time by combining the N_L with a specified grid size ΔS_{CA} and length of each time step Δt_{CA} of the CA algorithm. As mentioned in the previous section, ΔS_{CA} and Δt_{CA} do not necessarily have to be the grid size and the time step of the atmospheric model (e.g. the ECMWF Integrated Forecast System, the model used to generate ERA5 data), rather ΔS_{CA} and Δt_{CA} can be set independently to achieve other parameterization constraints.

We directly apply the CA generated pattern diagnostically onto ERA5 wind fields which we have available every 1 hour. The perturbation scheme we adopt is similar to that used in *Shutts* (2005), and it is mathematically expressed as follow,

$$\begin{aligned} u_{CA} &= u_{era5} + \sigma_{|U_{10}|} \times \alpha(month) \times CA(N_L, \Delta S_{CA}, \Delta t_{CA}), \\ v_{CA} &= v_{era5} + \sigma_{|U_{10}|} \times \alpha(month) \times CA(N_L, \Delta S_{CA}, \Delta t_{CA}). \end{aligned} \quad (4.3.1)$$

In this scheme, the same perturbation term is added onto the zonal (u_{era5}) and meridional (v_{era5}) wind velocities with its magnitude constrained by the spatial wind speed standard deviation $\sigma_{|U_{10}|}$ and a tunable non-dimensional coefficient α . The perturbation hence introduces more small-scale variabilities on the wind directions and the wind vorticity field which is potentially missed by the lack of small-scale wind fluctuations in ERA5 wind data (Figure 4.2c, d). The N_L of the CA perturbation is 1, the CA grid size ΔS_{CA} is $\frac{1}{12}^\circ$ (one third of the ERA5 horizontal spacing), the CA time step is the same as ERA5 wind field, which is 1 hour. The actual smallest length scale resolvable by the ERA5 data is around

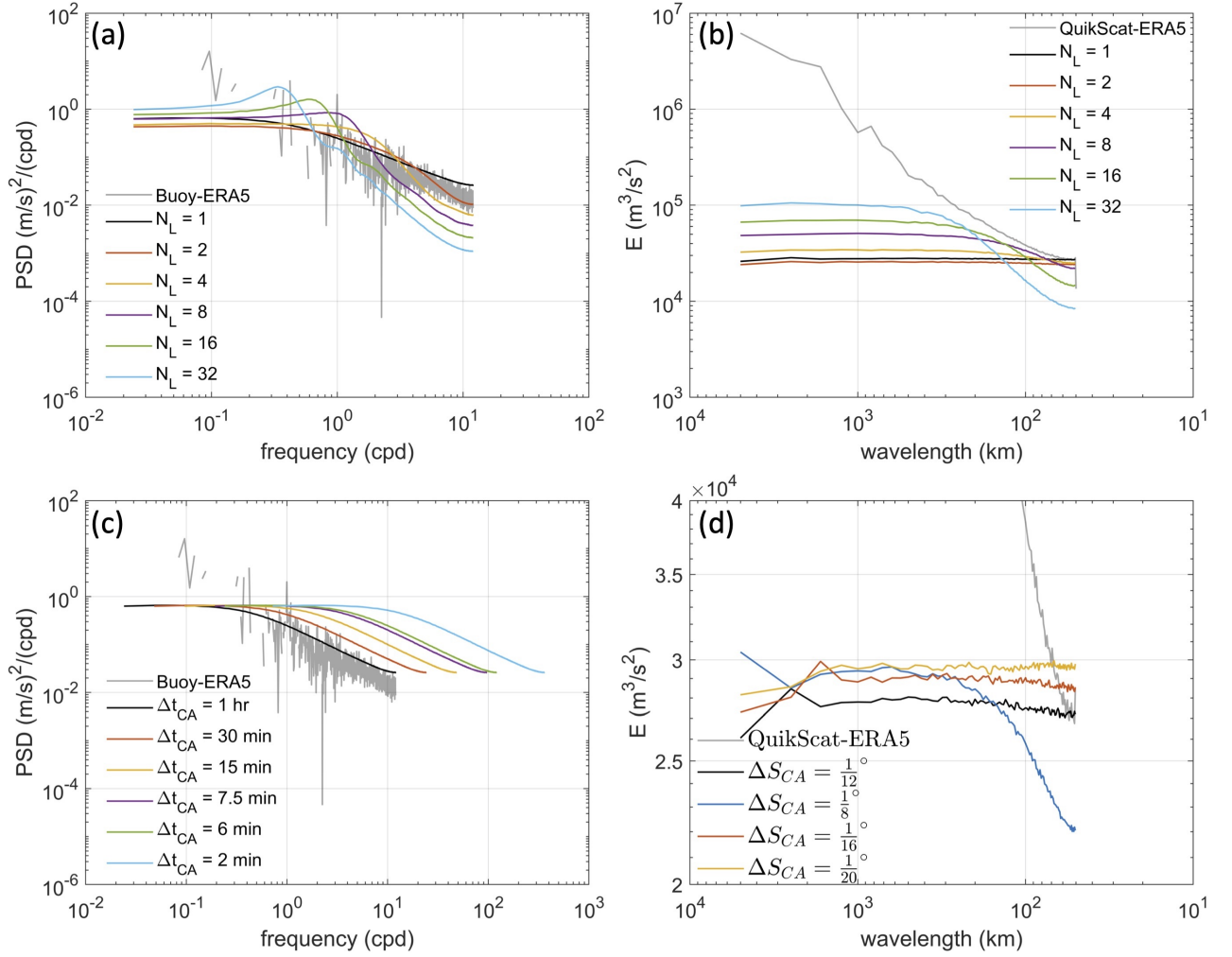


Figure 4.6: (a) Frequency spectra and (b) wavenumber spectra derived from a series sensitivity of experiments to assess the effect of N_L . 6 values of N_L are selected here and the shape of spectra have shown a strong dependence on the value N_L with strong energy injection scale that drifts to small-scales and high-frequencies with the decreasing N_L . (c) Frequency spectra for different Δt_{CA} with $N_L = 1$. (d) Similar to (c) but for wavenumber spectra for different choices of ΔS_{CA} . Energy injection scale shifts downscale/high-frequency with the decrease of $\Delta S_{CA}/\Delta t_{CA}$. The difference in wavenumber spectra and frequency spectra between observations and ERA5 are plotted in grey in all panels. The ΔS_{CA} and Δt_{CA} in (a) and (b) are set to be $\frac{1}{12}^\circ$ and 1 hour, and $N_L = 1$ in (c) and (d).

31 km while we downloaded the data on a longitude-latitude grid with horizontal resolution of $\frac{1}{4}^\circ$. The α is a constant value for the entire domain but varies for each month. The magnitude of α varies between 0.4 to 0.5 with little seasonality. The choice of the parameters are evaluated below.

We adjust ΔS_{CA} , Δt_{CA} and N_L for an optimal performance of the CA perturbed

wind in fitting with the observation in the spectral analysis. Figure 4.6 illustrates the frequency power spectrum density and wavenumber kinetic energy diagrams with different choice of N_L , ΔS_{CA} and Δt_{CA} . Figure 4.6a shows that the a spectral peak inevitably emerges on the frequency spectra, with the corresponding time scale of the peaks shifting toward longer time scales with the increase of N_L , but there is no such peak when N_L takes 1. The frequency spectrum when N_L takes 1 shows a good agreement with the discrepancies between the ERA5 and buoy measurements derived from those in Figure 4.3b. The wavenumber spectra of the CA pattern for different N_L are plotted in Figure 4.6b. It shows that the CA spectrum with N_L equals 1 suitably compensates the wind energy spectra difference between the QuikScat and ERA5 at the smallest scale (~ 40 km), while other N_L values do not produce the same effect. CA spectra of other N_L values tend to shift the energy input to larger scales. It seems that larger N_L leads to a better match with the spectral discrepancies between QuikScat and ERA5, while these larger-scale energy input is likely to induce spurious mesoscale features of the length scales comparable to those systems have been well-resolved in ERA5 (Figure 4.2) and damage the coherent structure of these systems. Therefore we set the N_L as 1 to remove the unwanted frequency spectrum peaks which are absent in observations as illustrated in Figure 4.3c.

The choice of Δt_{CA} and ΔS_{CA} are determined by comparing the energy improvement over the targeted time and length scales. Figure 4.6c and Figure 4.6d compare the performance of CA frequency spectra and wavenumber spectra for different time step and grid size values with the N_L equals to 1. Clearly, the CA algorithm tends to inject more energy into higher frequencies for smaller Δt_{CA} and to smaller wavelength for smaller ΔS_{CA} . Figure 4.6c shows that CA perturbations with Δt_{CA} smaller than 1 hour tend to overestimate the high-frequency variabilities comparing to the actual discrepancies. Furthermore, the CA perturbation is aiming for improving the high-frequency processes that have been resolved in ERA5 field instead of resolve the high-frequency variabilities that are totally missed in the ERA5 field, which is also unlikely to

achieve. Therefore, the Δt_{CA} is set to be 1 hour. Figure 4.6d suggests that $\frac{1}{12}^\circ$ for ΔS_{CA} is probably the largest grid size to generate the effective CA perturbation as even a slight increase of the grid size (e.g. $\frac{1}{8}^\circ$) would lead to an upscale energy shift. Although ΔS_{CA} smaller than $\frac{1}{12}^\circ$ demonstrates quite similar shape and magnitude of the energy input (Figure 4.6c), it costs longer computational time for CA to develop. As such, we set $\frac{1}{12}^\circ$ for ΔS for its relative efficiency. As a result, the CA perturbation can improve the frequency spectra of the ERA5 wind and mitigate the lack of small-scale variabilities. We are also cautious in using the CA algorithm to improve the ERA5 wind field between 100-500 km scale where most mesoscale weather systems resides. As is noted, the CA perturbation does not fully recover the energy spectrum over the whole mesoscale bandwidth as see in Figure 4.6b and Figure 4.6d. The design of the CA perturbation does not specifically take information of any observed mesoscale systems or any comparisons between observation and ERA5 on each single weather systems. Therefore, tuning up the spatial resolution of CA grid to lift up the mesoscale wind energy would induces spurious mesoscale systems that does not exist in observation as the CA perturbation is filled up in the spatial domain isotopically (Figure 4.5). Here the CA perturbation at the smallest scales can be safe to regard as an estimate of 'error' or 'uncertainty' of the ERA5 products which can be assumed as random and non-systematic.

The non-dimensional coefficient α links to the magnitude of CA perturbation and is tuned to optimise the agreement between the perturbed wavenumber spectra and observations. The α is firstly assumed to be a function of longitude, latitude and time as the wavenumber spectra difference between QuikScat and ERA5 winds is expected to have regional variations. We first selected 7 regions across the Atlantic Ocean and conducted a test experiments for one month with other CA parameters take the value as mentioned above. The α values determined for different regions have demonstrated little difference (Figure 4.7a-c). A noticeable PDF broadening and a higher probability in high wind speed events are detected for different regions, which is generally underestimated

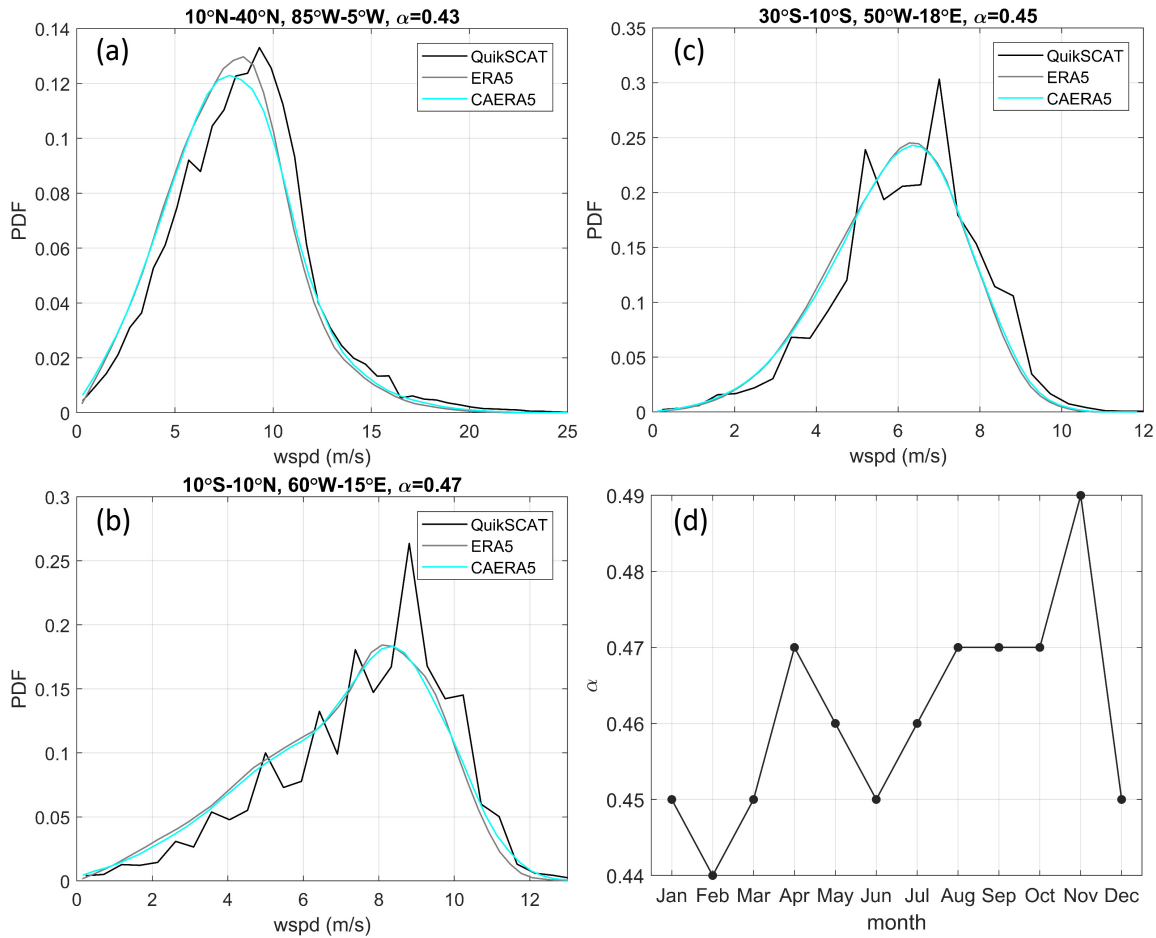


Figure 4.7: (a)-(c) The probability distribution function (PDF) derived from the trial experiments on α on January 2008 for three different regions in Atlantic Ocean with the α values shown above each panel. The difference in α for different regions is small, while they all show a broadening of the PDF and a higher probability for high wind speed events in the perturbed wind field. (d) The time series of the monthly-varying α used in our CA perturbation scheme in Eq. 4.3.1 for the Atlantic Ocean domain.

in original ERA5 wind data. This result also reflects that the CA perturbation is able to reproduce some of the outburst of wind extremes that are observed in the QuikScat data. Therefore a single value for α is applied to the entire domain. Another reason for the spatially-uniform α is that different α values result in problematic discontinuity at the boundary between two regions on the perturbed wind fields. The α is then re-evaluated for each month to make sure an optimized wavenumber spectra for different seasons. The monthly time scale is also chosen to avoid any high-frequency fluctuations induced by α itself. The final version of α is a time series containing 12 values for each month applied

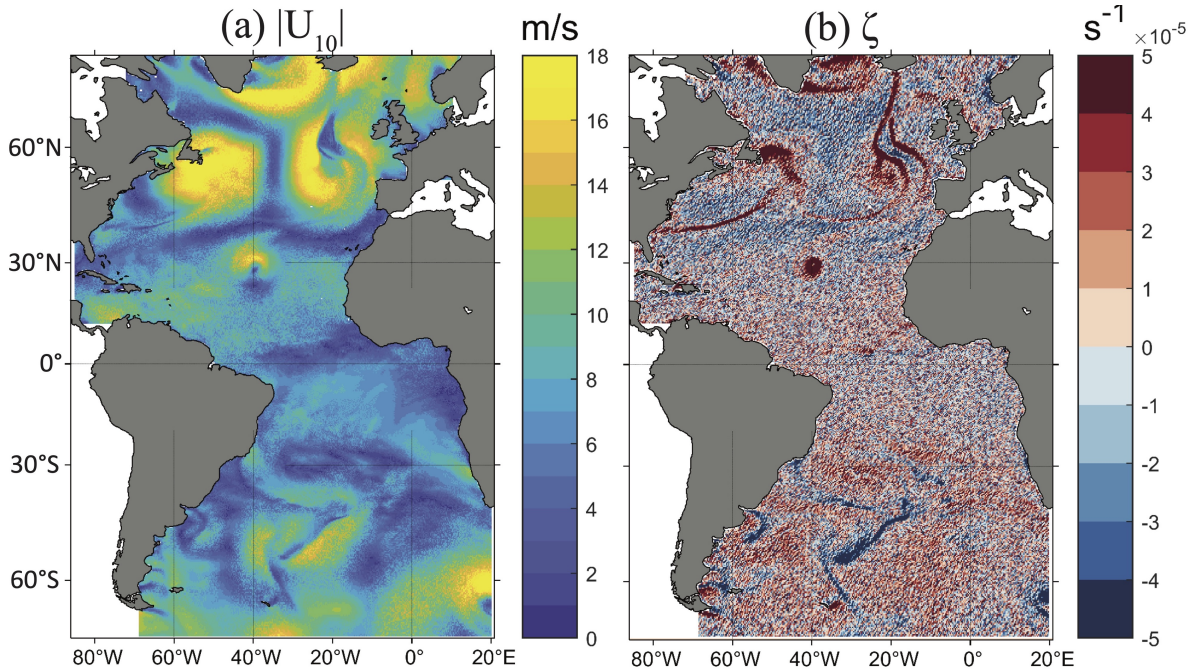


Figure 4.8: Snapshots of (a) wind speed and (b) relative vorticity of ERA5 wind data after the CA perturbation applied. The example snapshots are computed from the ERA5 wind data at 0800 UTC on 1st January 2008 as in Figure 4.2.

over the whole domain. The magnitude of α varies from 0.4 to 0.5 and demonstrates little regular seasonality (Figure 4.7d).

The spatial maps in Figure 4.8 depict the wind speed and relative vorticity fields after the CA perturbation has been added, i.e. u_{CA} and v_{CA} in Eq. 4.3.1. The example snapshots are taken from 1st of January 2008 (see Figure 4.2). Of course the CA perturbation does not resolve the exact mesoscale structures as observed in QuikScat (Figure 4.2a,d) because the CA evolves independently from either the observations or the reanalysis fields. But it does enhance the small-scale wind variability in a noisier and patchier sense across the entire domain that resembles the QuikScat observations (e.g. the vorticity). Regions with less organized wind variability differences between ERA5 and QuikScat in the first place (i.e. high-latitude and mid-latitude regions) benefits more from the CA perturbation while over the tropical regions, the organized mesoscale convection events captured by QuikScat are mostly missed from the ERA5 fields and our CA scheme is not capable of reproducing that 100 km scale variability. Looking for an improved match in a snapshot wind field is naive and does result

in disappointment in the CA method. Nevertheless, in this study, we focus on demonstrating the potential of the CA perturbation as a ‘spectra fixer’ of ERA5 wind fields and focus on the improved wind spectra as shown in Figure 4.9. Our domain-averaged wavelength spectra have shown that the CA perturbation has significantly improved the energy underestimation on the length scale from 40km to 400 km (Figure 4.9a), and the spectral ‘gap’ in the small-scales has been filled by the CA perturbation. The frequency spectra averaged over 18 buoy sites after the CA perturbation have also demonstrated an improvement on resolving the wind variance on the sub-daily time scales (Figure 4.9b) from 1 to 10 cpd, which has been conventionally overlooked in other stochastic perturbation studies. The results in Figure 4.9 confirm that the CA perturbation can effectively improve the ERA5 wind spectra to fit the observations over the small-scales and high-frequency scales at the same time. The CA perturbation also results a slightly broader spread of the perturbed wind speed probability distribution function with an overall increased probability in high wind speed events (e.g. wind speed >15 m/s) events which tend to be underestimated in ERA5 wind fields comparing to observations (Figure 4.9c), which confirms our choice of a single α value for the entire domain.

4.4 Local response of the ocean to CA perturbed surface wind fields

The perturbation experiments on surface wind fields suggest that the probabilistic CA algorithm can be used as a spectra fixer to improve the underestimated small-scale and high-frequency wind variability in ERA5 reanalysis output. It is then of interest to assess the perturbation from a different perspective by investigating the oceanic response to such a perturbation. To understand the impact of the CA wind perturbation on the ocean, we first use a Multi-Column K-Profile Parameterization (MC-KPP) ocean ML model (*Large et al., 1994; Klingaman et al., 2011*) to investigate the

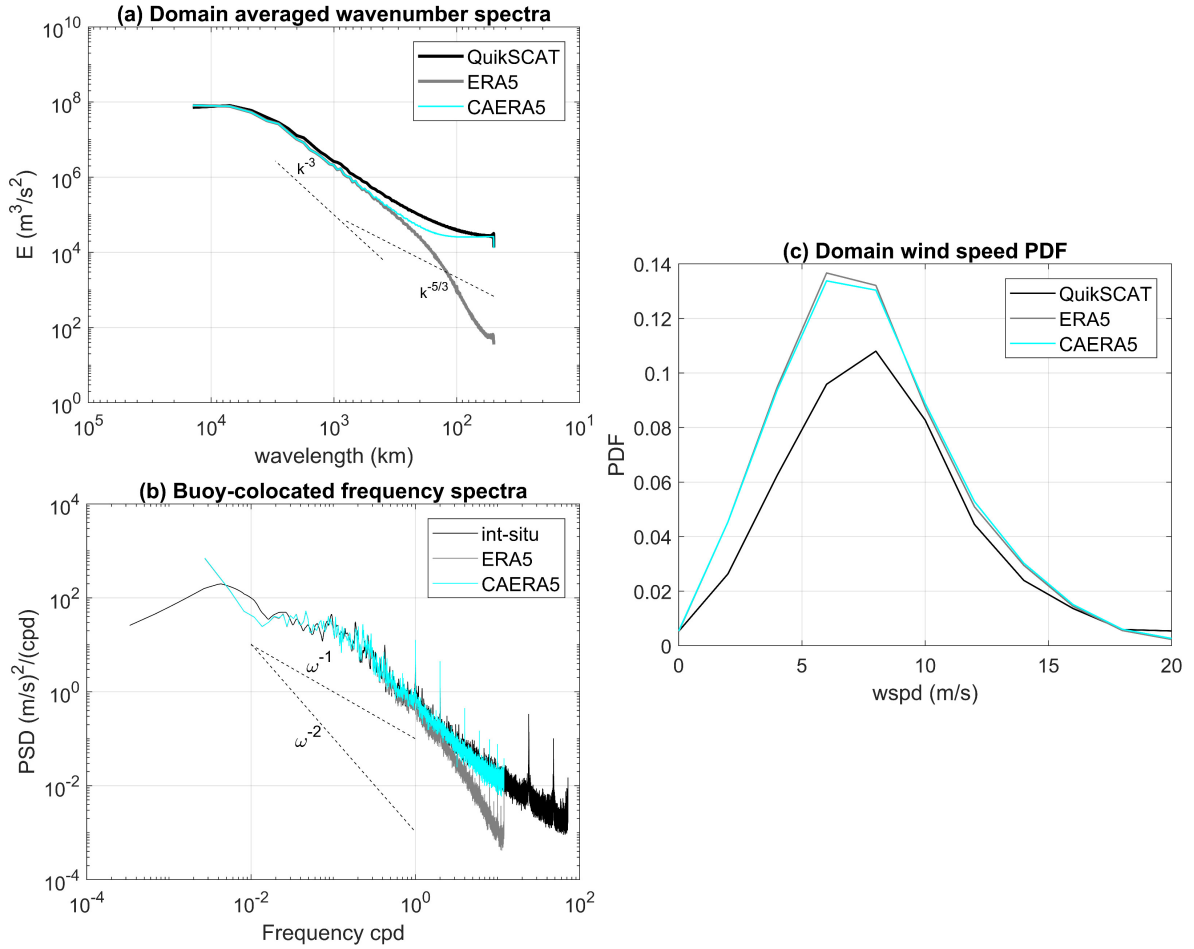


Figure 4.9: (a) Wavenumber spectra comparison made between QuikScat (black), ERA5 (grey) and CA-perturbed ERA5 (cyan) wind fields averaged for year 2008 across the Atlantic Ocean domain. (b) Same as (a), except that it shows the frequency spectra. After perturbation, ERA5 wind fields experience improvement on the energy spectral behaviour on length scales longer than 400 km and frequency higher than 1 cycle per day. (c) The probability distribution function of the wind speed of QuikScat (black), ERA5 (grey) and perturbed ERA5 (cyan) wind.

impact of the improved local air-sea interactions. We designed two experiments: (1) a control simulation driven by the ERA5 surface meteorological fields including the wind velocities, surface air temperature, sea surface temperature, barometric pressure and downward radiative heat fluxes (both shortwave and longwave) and (2) a perturbation experiment forced with the same suite of variables except with the wind velocities being replaced with the CA-perturbed wind velocities, i.e. (u_{CA}, v_{CA}) in Eq. 4.3.1). The fluxes in both experiments are computed with the COARE 3.0 bulk flux formula (Fairall *et al.*, 2003) from the

above bulk meteorological variables.

4.4.1 Forcing differences

The wind speed difference caused by the CA perturbation fluctuations on the wind velocities is the main driver in the forcing differences between the control and sensitivity experiments. This is consistent with our findings of Chapter 2, where the vector rather than the scalar difference were crucial (*Zhai, 2013; Zhou et al., 2018*). Recall that the perturbation pattern is generated independently from observations and background ERA5 wind fields. The CA perturbation applies directly to the wind velocities, which then propagates through the quadratic relation between wind velocities and wind speed magnitude toward the wind speed fields, the turbulent heat fluxes, via their linear dependence on wind speed, and the wind stress via its quadratic dependence on wind speed.

We find that the impact of the CA perturbation on the wind speed field is dependent on the background wind speed and wind direction as illustrated by Figure 4.10, where the annual-mean wind speed differences computed from the two experiments are illustrated along with the annual-mean background wind speed contours (Figure 4.10a) and annual-mean background wind direction contours (Figure 4.10b) for the year 2008. The perturbation causes an averaged annual-mean wind speed increase of only 0.07 m/s, while locally the increase can be up to 1.6 m/s. The maximum wind speed increase is derived from the hourly instead of the time-mean difference, hence the value exceeds the scale shown in Figure 4.10. It is found that overall the wind speed is enhanced due to the perturbation with greater enhancement of wind speed emerging in the region experiencing relative weak wind forcing, such as over the tropical Atlantic Ocean. Meanwhile, a slight damping effect is detected on the wind speed difference map across the subtropical North Atlantic basin, adjacent to the region with greater wind speed enhancement. Looking at the overlaid annual-mean wind direction contour suggests that the subtropical North

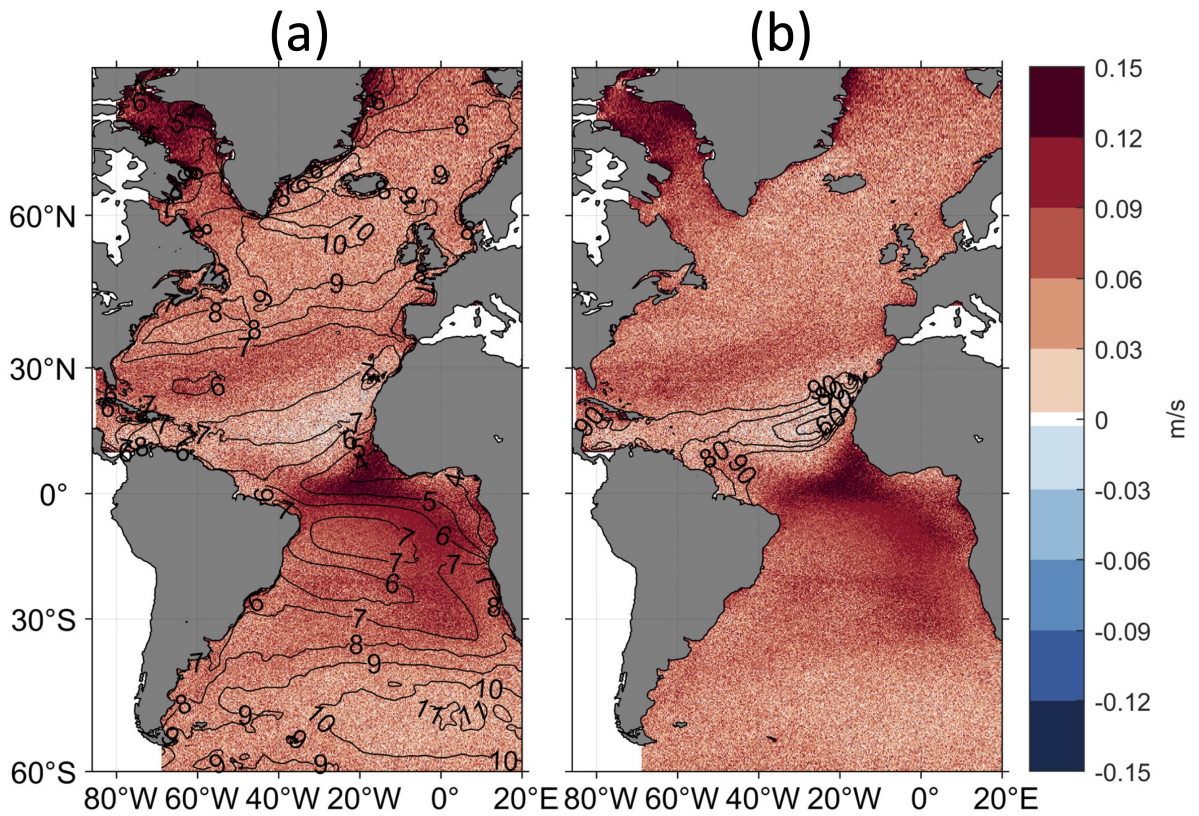


Figure 4.10: (a) Annual-mean (year 2008) map of wind speed difference induced by probabilistic CA wind perturbation superimposed by the annual-mean background wind speed contour. (b) Same as (a), expect superimposed with annual-mean background wind direction with the northeasterlies being highlighted (0° to 90°).

Atlantic is prevailed by northeasterly winds (with wind direction ranging from 0° to 90°), in which case the zonal and meridional velocity components share the same sign and are affected by CA perturbation in the same direction according to the perturbation scheme (Eq. 4.3.1). Therefore the damping effect of the of CA perturbation on both components is double-counted and manifested on the wind speed when the CA perturbation is acting to decrease the magnitude of both velocity components. The wind speed difference is averaged at 0.07 m/s, while the ERA5 wind speed is typically of 1 to 2 orders of magnitude greater than the wind speed difference. The wind speed difference caused by the CA perturbation is therefore a minor contribution.

The wind speed differences are further translated into differences in the surface heat fluxes and wind stress. The surface turbulent heat flux is linearly dependent

on the wind speed hence the heat flux difference is proportional to the wind speed difference. This relation leads to greatly enhanced heat loss from ocean to the atmosphere over the tropical Atlantic ocean owing to greater wind speed increase (Figure 4.11a). Overall the annual-mean turbulent heat loss is enhanced by 1.22 W/m^2 averaged over the whole domain, while locally the instantaneous heat loss can reach up to 20.74 W/m^2 (both values are derived from the area away from sea ice) in the east tropical Atlantic. The annual-mean turbulent flux perturbation is two orders of magnitude less than the control mean flux (-104.02 W/m^2). In other words, the heat flux perturbation from the CA algorithm is also a very minor contribution.

The quadratic dependence between the wind speed and wind stress leads to the fact that the wind stress difference is controlled by both the wind speed differences and the background wind speed but more dominated by the background wind speed because of the much greater magnitude. Therefore, greater wind stress enhancement is located in the tropical easterlies region and mid-to-high latitudes in both hemispheres (Figure 4.11b) where there is a prevailing strong background wind ($>7 \text{ m/s}$). The domain averaged annual-mean wind stress enhancement is 0.003 N/m^2 , with localized maximum instantaneous enhancement of 0.4 N/m^2 at the mid-latitude of north Atlantic, where the prevailing westerlies are situated. Again, the wind stress difference is two orders of magnitude lower than the mean control estimate, confirming the minor contribution from the CA perturbation.

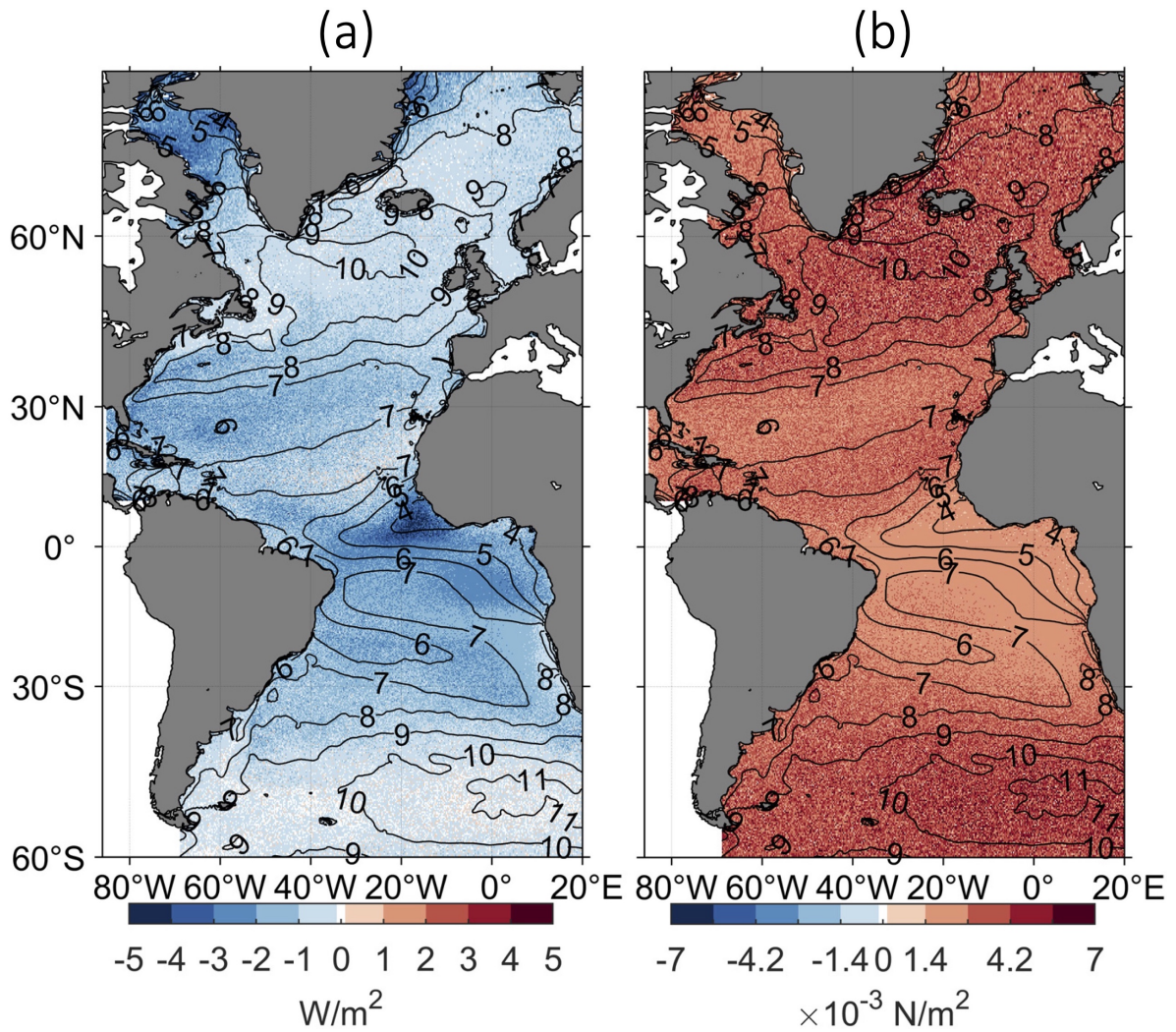


Figure 4.11: (a) Annual-mean turbulent heat fluxes difference between perturbation and control experiments with annual-mean background wind speed contour superimposed. (b) Same as (a), but for wind stress difference.

4.4.2 Sea Surface Temperature response in MC KPP

The MC-KPP ocean ML model is adapted from the KPP model and coded to run a group of single-column simulations over a geographic region in parallel. The KPP assumes that the turbulent mixing is dominated by the vertical turbulent fluxes of temperature, salinity and momentum. It diagnoses the oceanic surface boundary layer (ML) using a local Richardson number scheme (bulk ML scheme), Monin-Obukhov similarity theory and the Ekman layer depth computed from surface wind stress. The KPP model allows properties to vary within the ML via a specified vertical shape function and parameterizes the non-local transport

associated with advective mixing processes such as oceanic eddies, independent from the vertical gradient of mixing quantities (*Large et al.*, 1994).

The original MC-KPP code was designed to be coupled to a dynamic atmospheric model both regionally and globally, while it faces a minor issue of taking into account the local ocean bathymetry information. Ignoring this factor leads to the ocean water column unrealistically mixing through the seabed. A three-dimensional land sea mask is generated using the bathymetry data derived from temperature and salinity of World Ocean Atlas 2018 (WOA18) to make sure the simulated mixing process is constrained by the maximum ocean depth at each grid point. The model is initialized with WOA18 monthly climatology temperature and salinity profiles. Both control and perturbation experiments are run for a month, then reinitialized for the next month and are run for 12 months for the year 2008. In total 12 months of control experiments and 12 months of perturbation experiments are created. Note that the model outputs of MC-KPP are mapped onto a $\frac{1}{4} \times \frac{1}{4}^\circ$ grid (Figure 4.12), identical to the ERA5 data, because there is actually no horizontal dimensions associated with each model column.

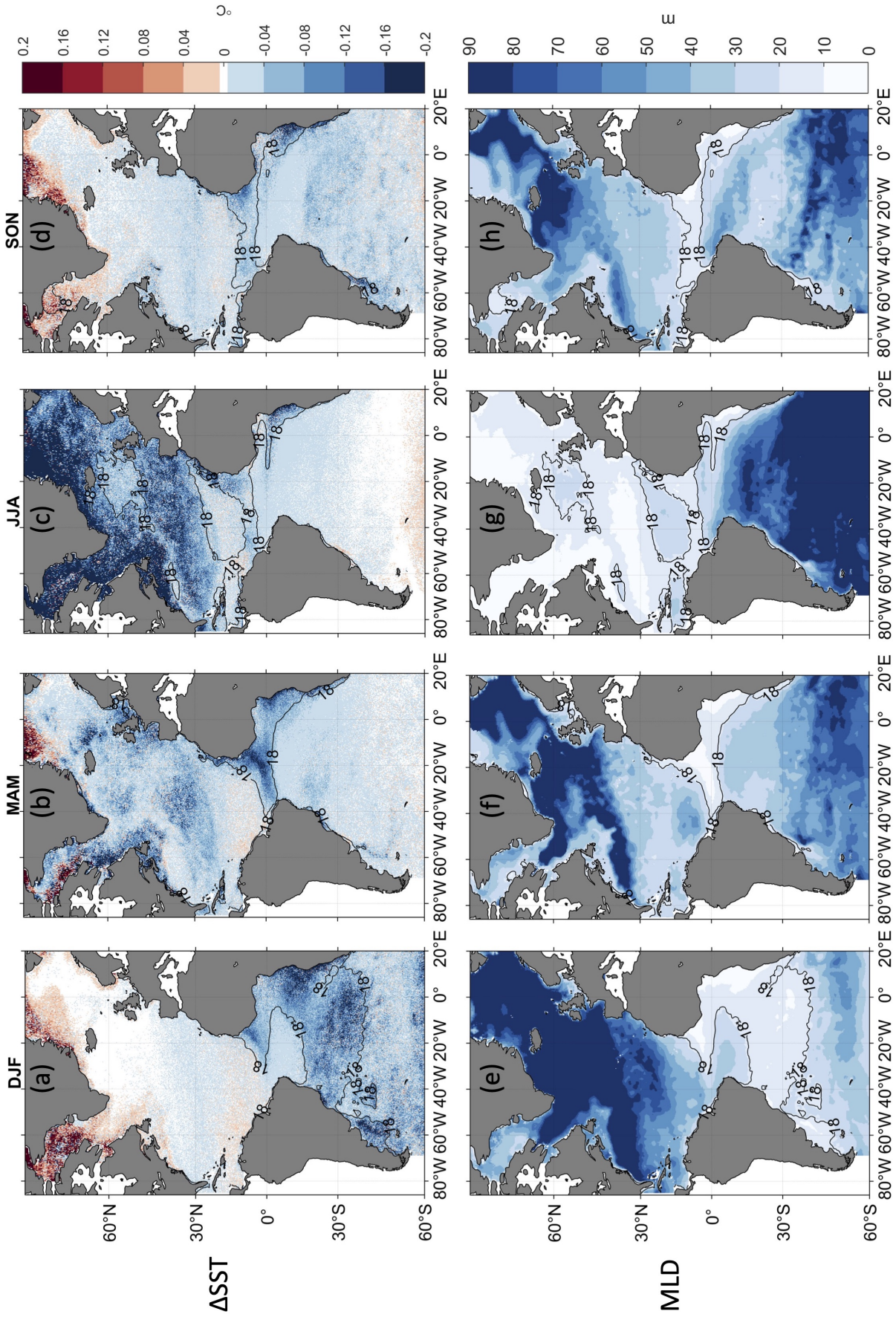


Figure 4.12: Seasonal average of the SST response to the CA perturbation estimated over the year 2008 for (a) December, January and February (DJF), (b) March, April and May (MAM), (c) June, July and August (JJA), (d) September, October and November (SON). The 18 m isobar of the seasonal averaged control ML is superimposed to highlight the shallow ML regions. (e)-(h) are the seasonal average for the control ML depth.

The upper ocean response to the CA wind perturbation is first investigated via seasonal differences computed from the control and perturbation experiments. The difference is calculated by subtracting control SST from perturbation SST to reveal the response to the wind perturbations. The top panels in Figure 4.12 depict the seasonal variation of SST response to the CA perturbation from boreal winter to autumn for the year 2008. The SST across the entire domain decreases due to the heat loss in the perturbation experiments, except for the high-latitude northern North Atlantic out of the boreal summer time (Figure 4.12a, b and d) where the initial temperature profiles are characterized by an unstable thermal structure maintained by haline stratification due to the effect of sea ice formation. In addition, the SST response demonstrates considerable seasonal variation, with greater surface cooling in the summer time for both hemispheres and surface cooling throughout the year over the tropical Atlantic (Table 4.1). The seasonal nature of the strong SST response is largely dictated by the seasonal variation of background ML depth, that significantly alters the ML heat capacity. In both hemispheres, the generally shallower ML in summer leads to smaller surface heat capacity, hence a greater SST response for a similar amount of heat flux. In boreal summer, the SST cools by 0.1°C across the North Atlantic, with some local areas in northern North Atlantic characterized by a cooling of over 1°C . Similarly, in boreal winter, there is significant cooling in the subtropical South Atlantic, locally over 1°C , where the ML depth are confined to less than 20 m.

Figure 4.13 illustrates the correlation between the SST response and other parameters mentioned earlier: the ML depth, surface heat loss enhancement and wind stress enhancement. The correlation between SST response and ML depth is large over most latitudes, as suggested by the seasonal mean spatial map (Figure 4.12e-h), except for in the tropical ocean where ML depth is constantly shallower with the magnitude varying around 25 m (see Table 4.1) due to the constant surface heat gain. The variability of the SST response over the tropical Atlantic is moderately correlated to the ML depth and covarying closely with the surface heat flux changes comparing to other latitudes with a correlation

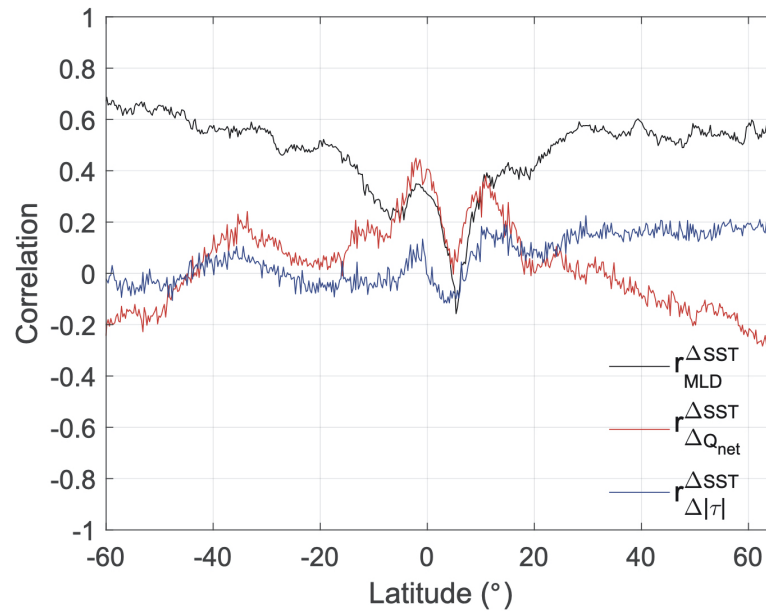


Figure 4.13: Correlation between SST response and background ML depth (black), surface heat fluxes differences (red) and wind stress differences (blue) averaged as a function of latitude.

coefficient of up to 0.5 shown by the peaks at 0° and 10°N . In the tropical Atlantic, solar radiation and relative calm atmosphere force a shallower tropical ML. The largely enhanced surface heat loss over the tropical seas is therefore well-imprinted on the SST response pattern. The wind stress enhancement is indeed one of the factors resulting in enhanced vertical mixing, but it plays a lesser role in setting the SST response pattern (little correlation with the SST response) due primarily to the relative small magnitude of wind stress difference.

It is noted that over the high-latitude North Atlantic the enhanced mixing leads to SST warming in the water column, while a fingerprint of sea ice formation in the initial profile reflects a bias during the surface heat fluxes calculation using bulk formula and the way these heat fluxes are prescribed to the KPP model. Firstly, the sea ice coverage is assimilated into the WOA18 temperature and salinity profiles, and the bulk flux formula takes the warmer SST under the sea ice to compute the turbulent heat fluxes without considering the presence of sea ice. Secondly, the MC-KPP model applies the overestimated turbulent heat loss directly on the temperature profile without taking into account the effect of sea

ice blocking this heat loss. It is noted that there is no SST increase in the boreal summer in the northern North Atlantic during the ice-free period, which confirms our interpretation of this sea ice issue.

The control and perturbation experiments conducted using the MC-KPP ocean ML model clearly demonstrate a systematic sea surface cooling across the domain with a noticeable seasonal cycle in the enhanced SST cooling for difference regions which is remarkably in phase with the seasonal variation of background ML depth and locally correlated to the enhanced surface heat loss at low-latitudes. The improved wind variability over the small-scale and high-frequency regimes induced by the CA perturbation systematically causes a SST difference with the magnitude around 0.1°C basin-wide and 1°C locally in the South and North subtropical Atlantic during the summer season of both hemispheres. These systematic changes in SST and the difference in the atmospheric forcing fields, driven by the mesoscale wind perturbations, are likely have an impact on the ocean circulation.

$\Delta\text{SST}(^{\circ}\text{C})$	DJF	MAM	JJA	SON
10°N to 60°N	-0.073	-0.040	-0.017	-0.027
10°S to 10°N	-0.058	-0.077	-0.047	-0.057
60°S to 10°S	-0.013	-0.029	-0.089	-0.035
<hr/>				
$\text{MLD}_{control}$ (m)				
10°N to 60°N	24.46	35.75	75.24	51.31
10°S to 10°N	26.01	24.26	29.24	26.07
60°S to 10°S	103.75	75.55	17.75	32.84
<hr/>				
ΔQ_{net} (W/m^2)				
10°N to 60°N	-1.18	-1.54	-1.20	-0.99
10°S to 10°N	-1.97	-2.49	-1.91	-2.01
60°S to 10°S	-1.23	-1.16	-1.06	-1.44

Table 4.1: Seasonal mean average for SST difference (perturbation-control), control ML depth and surface heat fluxes difference for selected subdomains.

4.5 Atlantic Ocean circulation response to stochastic mesoscale weather systems

4.5.1 Experimental design

The CA generated wind perturbations applied to the zonal and meridional wind velocities consist primarily of coherent small-scale and high-frequency structures (Figure 4.5 bottom panels), with little large-scale organized signals. The resultant differences in wind speed, surface heat fluxes and wind stress, however, reveal some self-organized large-scale patterns with preferred strong heat loss over low latitudes and stronger wind stress enhancement over mid-to-high latitudes, as a result of the distribution of the background wind field. This large-scale difference in the atmospheric forcing is likely to trigger a large-scale ocean circulation response. Previous studies have explored the ocean's response to surface wind perturbations either in an ad-hoc manner by synthesizing observed small-scale patterns explicitly in the forcing fields (e.g. *Hu and Meehl, 2009; Sproson et al., 2010; Condron et al., 2008; Condron and Renfrew, 2013*) or by altering the resolution of the atmospheric forcing in both spatial and temporal dimensions to isolate the effect of resolved mesoscale or high-frequency atmospheric variabilities (*Jung et al., 2014; Holdsworth and Myers, 2015; Wu et al., 2016*). It has generally been found that including high-frequency mesoscale atmospheric systems leads to a strengthening of either the gyre circulation via the intensified surface wind forcing (*Stommel, 1948*), or an increase in the MOC strength via enhanced heat loss at high-latitudes (*Marshall and Schott, 1999*). The enhanced turbulent heat loss and wind stress brought about by the CA perturbation shares some similarities to the effects caused by the mesoscale and high-frequency atmospheric variabilities documented in previous studies. It is of interest now to examine how the ocean circulation responds to the CA perturbation and whether the CA generated perturbation leads to any qualitatively different ocean circulation behaviours than found in previous

studies.

4.5.2 Model configuration

To fully understand the ocean response to the CA perturbation of the surface wind fields, we employed the Massachusetts Institute of Technology general circulation model (MITgcm) (*Marshall et al., 1997*) to conduct twin experiments under the same forcing scenarios as in the MC-KPP experiments, namely a control simulation forced with ERA5 winds and a perturbation simulation forced with CA-perturbed ERA5 wind. We now focus on the ocean dynamics in the North Atlantic basin with our MITgcm domain extending from 14°S to 74°N and from 100°W to 20°E with a horizontal resolution of $\frac{1}{10}^\circ \times \frac{1}{10}^\circ$. The model configuration is identical to that used in *Zhai and Marshall (2013)*, except that there are in total 50 geopotential levels, whose thickness increases with depth, ranging from 1.5 m at the surface to 213 m at the bottom (compared to 33 levels in *Zhai and Marshall (2013)*). The finer vertical resolution near the surface is designed to better resolve the magnitude and variability of the SST response to the atmospheric forcing (g.e. *Bernie et al., 2005; Zhou et al., 2018*). The model topography is generated from the National Geophysical Data Center (NGDC) Earth TOPOgraphy 5 minute grid (ETOPO5) 5' Gridded Elevations/Bathymetry for World. A linear drag coefficient of 1.1×10^3 is used to calculate the bottom stress. The horizontal tracer mixing is dealt with using biharmonic operators with a background diffusivity of $10^{10} \text{ m}^4/\text{s}$. The momentum is mixed in the horizontal using a scale-selective biharmonic operator with a Smagorinsky-like viscosity (*Griffies and Hallberg, 2000*). A restoring boundary condition is applied to restore the temperature and salinity near the boundary to the monthly mean climatology derived from the Ocean Model Intercomparison Project (OMIP) model output with a time scale of 3 days. Sea ice is not represented in our model configuration.

The model was first spun up for 23 years at $\frac{1}{5}^\circ$ resolution, forced by the

climatological monthly mean forcing obtained from National Centers for Environmental Prediction-National Centers for Atmospheric Research (NCEP-NCAR) reanalysis (*Kalnay et al.*, 1996), and is then run for another 30 years at $\frac{1}{10}^\circ$ resolution. A further spin-up run is conducted for 5 years with atmospheric forcing derived from the ERA5 meteorological fields from 1995 to 1999, allowing the model to adjust to the new ERA5 forcing. The SST and sea surface salinity (SSS) are restored to OMIP climatology at a time scale of 3 months to avoid unrealistic model drifting.

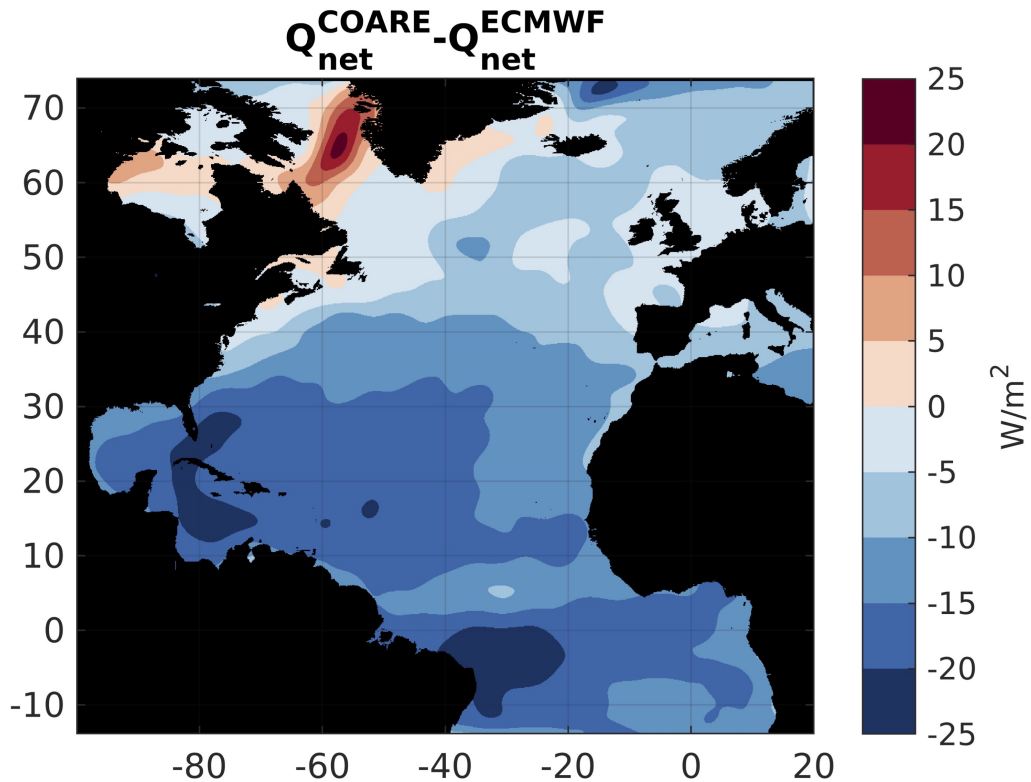


Figure 4.14: 10-year mean of the difference between the COARE calculated turbulent heat fluxes and ERA5 turbulent heat fluxes from 1995-2004. A $4^\circ \times 4^\circ$ 2D Gaussian filter is applied to produce this basin-scale discrepancy: the turbulent heat fluxes calculated from ERA5 meteorological variables with the COARE algorithm tend to underestimate the turbulent heat loss (anomalous warming) in the Labrador Sea while overestimate the heat loss (anomalous cooling) across the subtropical and tropical regions.

A pair of 15-year twin experiments (2000-2014) are conducted where the model is forced by two sets of atmospheric forcing (CONTROL and PERTURB hereafter) formulated in an identical way as in the MC-KPP experiments. For

both experiments, the atmospheric forcing is calculated using COARE3.0 bulk formula from ERA5 meteorological variables, and the PERTURB has the CA perturbation added into the wind components. The CA perturbation parameters are also set to be the same as in the MC-KPP experiments. The CA pattern is generated within the same geographic domain as the ocean model with a grid size of $\frac{1}{12}^\circ$, which is about one third of the horizontal resolution of ERA5 data. The CA perturbation time step is 1 hour which is the same as ERA5 wind data time resolution, meaning that the perturbation is added to the ERA5 wind fields every hour. The number of life N_L is set to be 1 to avoid an unrealistic frequency peak in the perturbed wind field (Figure 4.6a). An annually repeating α , the coefficient constraining the CA perturbation magnitude, is applied here for the multi-year perturbation because although the non-dimensional coefficient α varies monthly, it demonstrates little interannual dependence.

A few modifications are made for the generation of the atmospheric forcing fields, to eliminate the bias induced by using off-line bulk flux forcing. As we mentioned in the previous section, sea ice information is absent from the off-line turbulent heat flux calculation. Here, we crudely parameterize turbulent heat fluxes under sea ice by multiplying the open-ocean fraction inferred from ERA5 sea ice concentration data with the CONTROL and PERTURB turbulent fluxes. The inclusion of sea-ice information avoids unrealistic heat loss from the ocean at high-latitudes North Atlantic. Another modification is applied to mitigate the difference between heat fluxes calculated using the COARE bulk formula and those output directly from the ECMWF-IFS for ERA5. This difference leads to anomalous subpolar warming and subtropical cooling as shown by the monthly composite average difference between the CONTROL and ECMWF turbulent heat fluxes over 1995 to 2004 in Figure 4.14. Note this composite monthly difference map is smoothed by a $4^\circ \times 4^\circ$ Gaussian 2D low-passed filter to bring out large-scale differences. This anomalous surface flux pattern leads to a drift in the ocean state over time in the CONTROL run, purely from the bulk flux methodology. To eradicate this drift, the filtered heat flux difference (Figure

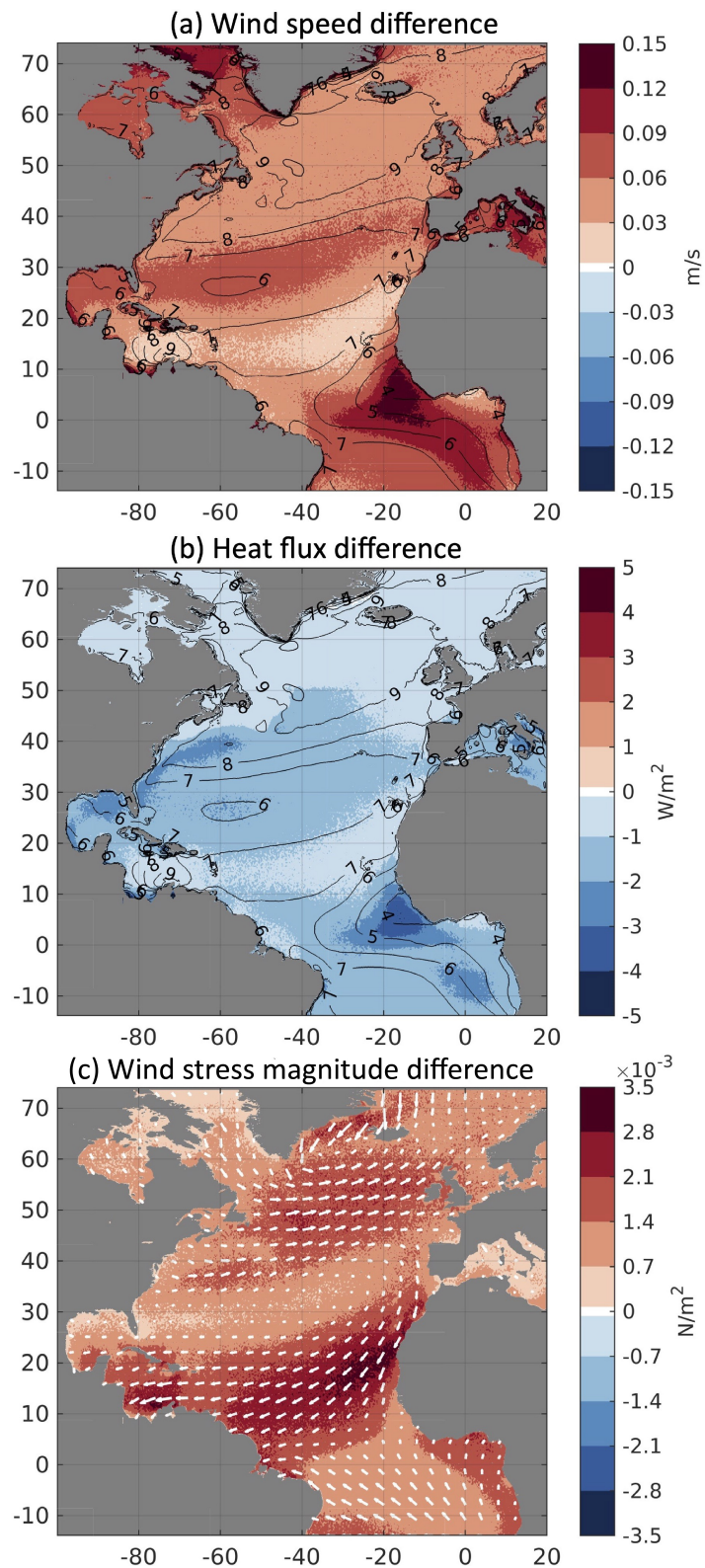


Figure 4.15: 15-year mean difference in the (a) wind speed, (b) net surface heat flux and (c) surface wind stress, between the CONTROL and PERTURB atmospheric forcing. 15-year averaged CONTROL wind speed contours are superimposed on (a) and (b), highlighting the correlation between the background wind speed and forcing differences. 15-year mean CONTROL wind stress and direction is mapped on top of surface wind stress difference denoted by white arrows.

4.14) is subtracted from both the CONTROL and PERTURB forcing fields.

4.5.3 Comparison with MC-KPP experiments

The difference in the atmospheric forcing caused by the CA perturbation has been discussed in section 4.4 for the 1-year MC-KPP experiment. An even smoother large-scale signature emerges in the atmospheric forcing differences after they are averaged over the longer 15-year period (Figure 4.15). As before, the CA perturbation tends to enhance the surface wind speed which, in turn, leads to enhanced surface heat loss and wind stress. The greater wind speed increase, again, lies in regions of weaker background wind such as the Inter Tropic Convergence Zone (ITCZ) and the centre of subtropical gyre, leading to a greater heat loss difference in these regions. The wind stress field, on the other hand, bears more intensification over the regions characterized by stronger background wind such as the tropical easterlies and mid-latitude prevailing westerlies. The overall magnitude of heat flux difference spanning the 15-year period varies from -5 to 0 W/m^2 between the PERTURB and CONTROL. This is close to the estimate made in a recent study by *Gavrikov et al. (2020)*, who found a similar magnitude in the turbulent heat flux difference between their high-resolution (14 km horizontal spacing) down-scaled atmospheric circulation model output over the North Atlantic and its low-resolution counterpart (77 km horizontal spacing). The typical magnitude of the wind stress intensification varies from 0.001 to 0.003 N/m^2 . Furthermore, the turbulent heat flux difference over the Gulf Stream region becomes more pronounced due to greater surface temperature and humidity gradients (see also Figure 5 in *Gavrikov et al. (2020)*), which is less clear in one-year difference shown in Figure 4.11. Note that the difference in surface heat loss over the Labrador Sea and Nordic Sea is much smaller than that shown in Figure 4.11a, due primarily to the inclusion of sea ice information that leads to a much weaker dependence of turbulent heat fluxes to wind speed changes in both CONTROL and PERTURB forcing.

Mean Δ SST($^{\circ}$ C)	DJF	MAM	JJA	SON	00-14
45 $^{\circ}$ N to 65 $^{\circ}$ N	-0.07	-0.10	-0.25	-0.17	-0.15
Domain (-GS)	-0.31	-0.33	-0.39	-0.37	-0.35
10 $^{\circ}$ N to 35 $^{\circ}$ N	-0.46	-0.47	-0.57	-0.56	-0.52
<hr/>					
MLD _{CONTROL} (m)					
45 $^{\circ}$ N to 65 $^{\circ}$ N	1050.80	805.81	28.97	258.20	535.94
Domain (-GS)	302.80	227.07	33.29	88.66	162.96
10 $^{\circ}$ N to 35 $^{\circ}$ N	141.24	98.99	34.96	56.09	82.82

Table 4.2: The mean SST difference and background ML depths averaged over the subtropical (10 $^{\circ}$ N to 35 $^{\circ}$ N, 80 $^{\circ}$ W to 20 $^{\circ}$ W) , the whole domain excluding Gulf Stream and the subpolar (45 $^{\circ}$ N to 65 $^{\circ}$ N, 60 $^{\circ}$ W to 40 $^{\circ}$ W) Atlantic Ocean simulated by MITgcm.

The SST response to the CA perturbation simulated by the MC-KPP model reveals an overall SST cooling across the domain as a result of the increased surface heat loss and wind stress intensification, with the magnitude, spatial distribution and seasonality of SST cooling being strongly regulated by the background ML depth (Figure 4.12). We find a similar SST response simulated by the MITgcm, which tends to occur more frequently in the subtropical and tropical regions in the boreal summer where the background stratification is strong, i.e. a shallower surface ML depth and a strong vertical temperature or density shear (Figure 4.16). Specifically, averaging over 15 years for each season, the SST decreases significantly by 0.5 $^{\circ}$ C over about 35% of the model domain in the boreal summer (JJA) and autumn (SON) seasons, while this number drops to 10% in winter (DJF) and spring (SON). The magnitude of the SST response listed in Table 4.2 shows a consistent seasonality that is also revealed by the spatial SST difference map, with the most pronounced SST decrease in JJA and SON. The basin-averaged SST response is somehow larger in the MITgcm than that in MC-KPP experiments, with a domain averaged SST decrease of 0.35 $^{\circ}$ C averaged over 15-year period (Table 4.2) and a maximum instantaneous SST decrease of up to 3.6 $^{\circ}$ C in the tropical east Atlantic Ocean. The large SST response pattern highlighted in Figure 4.16 is smoother and spreads over a

broader area compared to that simulated in MC-KPP (Figure 4.12a-d). This is likely to be the result of lateral mixing and advection in the MITgcm, whereas there is no communication between the one-dimensional columns in MC-KPP.

Figure 4.17 depicts the seasonal variation of ML depth response. It is found that the most significant ML deepening is happening in the mid-to-high latitude region where the background stratification tends to be weaker comparing to the lower latitudes. Averaging over 15-years for each season, the ML depth deepens over 200 m during the DJF and MAM season. Little difference is found during the summer months (JJA) across the domain during which period the stratification is strong and the ML structure is less sensitive to the differences in the surface fluxes induced by the CA perturbation. Figure 4.18a shows a further diagnosis on the SST changes purely computed from the surface heat fluxes difference and CONTROL ML depth. Figure 4.18c plots the difference between model output SST difference (Figure 4.18b) and the diagnosed SST difference, indicating that the SST changes in the open ocean are partially contributed by the surface heat fluxes anomalies while other sources of SST decrease can be attributed to the entrainment of cold water from underneath the ML base. This is more readily seen in the region where the ML deepening is pronounced (i.e. the mid-to-high latitude between $30^{\circ}N$ and $50^{\circ}N$). It is noted that in the tropical eastern Atlantic, diagnosed SST changes is stronger than simulated SST difference. This does not necessarily mean that the entrainment brings warmer water from below but more likely a results of advective processes acting to smooth out the strong lateral temperature gradient in the 3D models. However, the advective processes is hard to quantify here to completely disentangle the partition of the heat budget contribution from the surface heat loss, entrainment. Nevertheless, the broad spatial distribution of SST response and ML depth response is consistent with the strength of the background stratification, although the advective processes might be contributing or diminishing the difference, but the net effect emerges from the comparison between the model outputs suggests that the one-dimensional response is dominating most of the open ocean SST and ML depth responses.

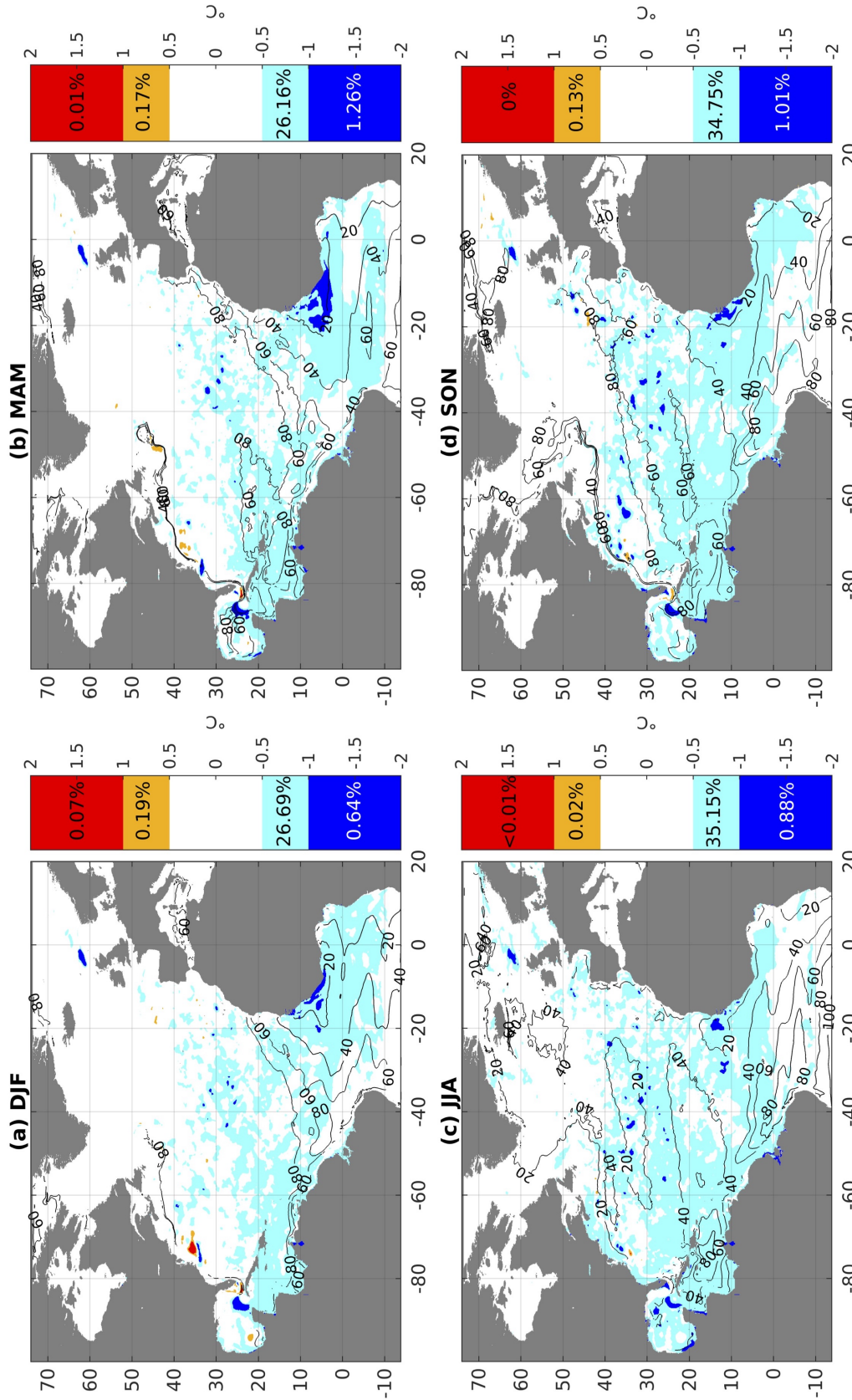


Figure 4.16: Seasonal average of the SST response to the CA perturbation estimated over the 15-year period for (a) December, January and February, (b) March, April and May, (c) June, July and August, (d) September, October and November. SST response with magnitude smaller than 0.5°C is masked out by white colour on the map. The occurrence of large SST response, with the magnitude greater than 0.5°C , is illustrated in colours with warm colours denoting the SST increase and cold colours denoting SST decrease. The percentage of the area of these large signals to the domain area are posted in the corresponding colour scales. The black contour of the seasonal averaged background ML depth from 0 to 100 m is superimposed.

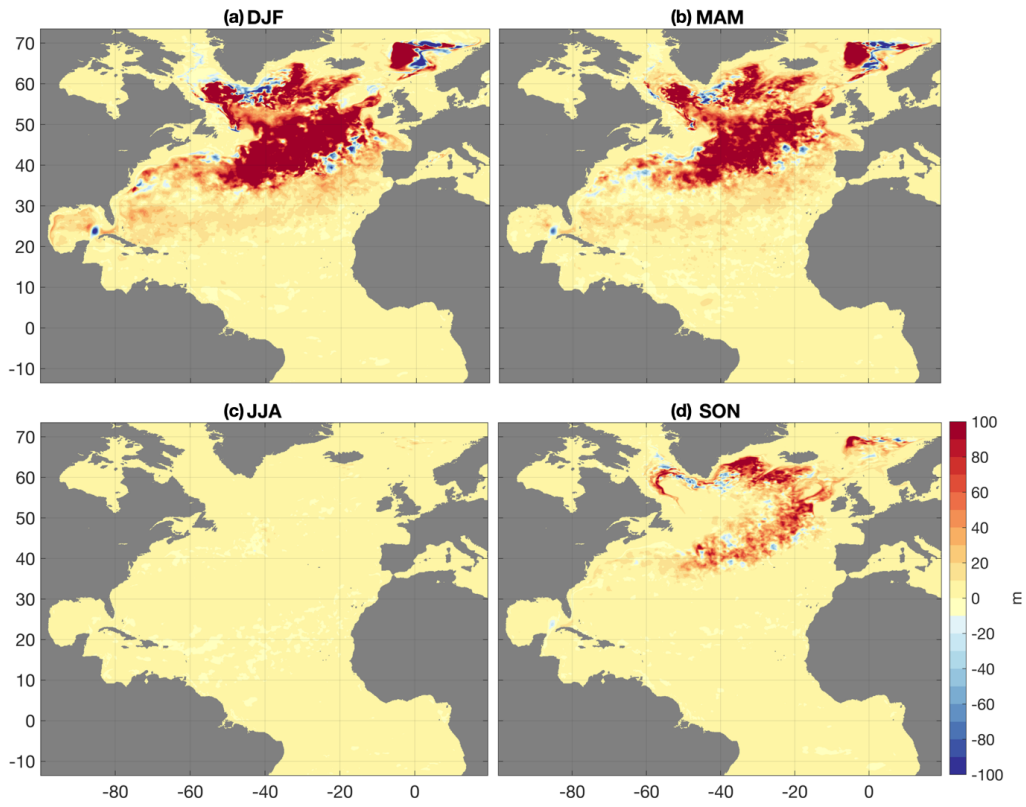


Figure 4.17: Same as Figure 4.16 but for ML depth differences.

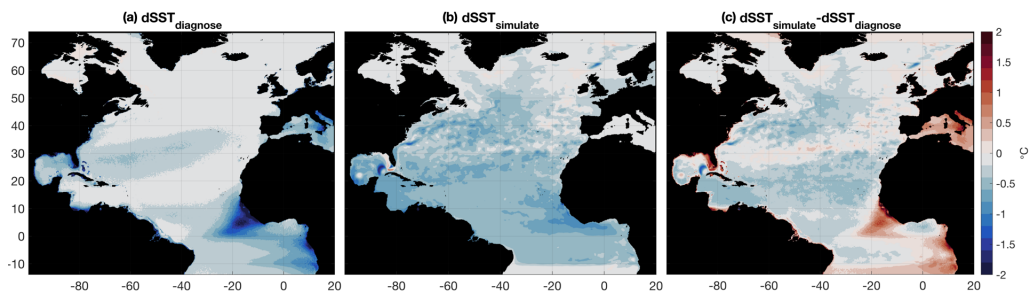


Figure 4.18: 15-year mean estimate of the SST difference (PERTURB-CONTROL) (a) diagnosed from surface heat fluxes with the assumption of no ML variation, (b) computed from model output and (c) the difference between (b) and (a).

4.5.4 Ocean circulation response to the CA perturbation

Here we mainly focus on the changes of the horizontal gyre circulations in the North Atlantic and also the AMOC. By comparing the volume transport and heat content changes, we find an inter-gyre interaction driven by the CA perturbation that results in a non-monotonic signal in the response of these large-scale circulation systems during the twin experiments period. We first examine the trends in the simulations and compare to volume transport observations. Then secondly look at the differences between the twin experiments in detail.

A. The trend and variability

The North Atlantic subtropical gyre circulation is predominantly wind-driven and its strength is well imprinted on the northward volume transport within the narrow western boundary region. Here we compare the model-simulated volume transport across the Florida Strait at 26.5°N with that inferred from submarine cable measurements (*Baringer and Larsen, 2001; Rayner et al., 2011*). Figure 4.19a shows that the model broadly captures the interannual variability of the Florida Strait transport with the mean transport of CONTROL Florida Strait current, 26.9 ± 3.2 Sv ($1 \text{ Sv} = 10^6 \text{ m}^3/\text{s}$) in CONTROL, about 4 Sv smaller than the observation, which is 31.6 ± 2.4 Sv. The CONTROL Florida Strait transport increases during the simulation, becoming comparable to the observed transport around 2009. The mean transport of the CONTROL experiment estimated from 2010 to 2014 is 29.8 ± 2.0 Sv, which is closer to 32.0 ± 2.4 Sv observed for that period. The underestimation on the time-mean Florida Strait transport could be associated with model spin-up issue due to the switch of atmospheric forcing from NCEP to ERA5. The transport estimated from the PERTURB experiment demonstrates a smaller difference with the observation with a mean transport of 28.8 ± 3.3 Sv throughout the modelling period. The PERTURB Florida Strait transport also becomes more comparable with the observation since 2009 with the

mean transport of 31.3 ± 2.4 Sv for 2010-2014.

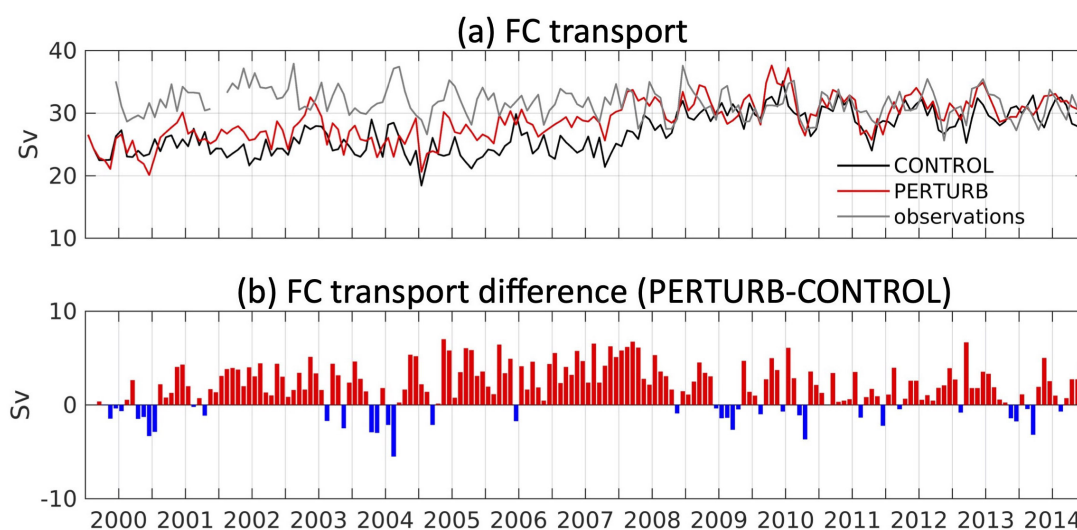


Figure 4.19: (a) The time series of CONTROL (black), PERTURB (red) and observed (grey) Florida Strait Current transport at 26.5°N . Observation is derived from the 21-year measurement of the submarine cable across the Florida Strait. Data available at https://www.aoml.noaa.gov/phod/floridacurrent/data_access.php. (b) The monthly difference of Florida Strait transport between PERTURB and CONTROL experiments.

Turning to the subpolar North Atlantic, the prevailing cyclonic surface wind stress curl (Figure 4.22a) drives an Ekman divergence which leads to a bowl-shaped sea surface and a doming structure in the isopycnals. This, in turn, leads to a cyclonic subpolar gyre circulation. The strength of the subpolar gyre can be inferred from the sea surface height map observed by the satellite altimetry (*Häkkinen and Rhine, 2004; Hátún et al., 2005*) or from a more direct volume transport estimate. The strength of the subpolar gyre circulation here is defined in three different ways: the minimum barotropic streamfunction along the cross section in the Labrador Sea (*Holdsworth and Myers, 2015*), the minimum barotropic streamfunction along 60°N (*Marzocchi et al., 2015*) and the minimum barotropic streamfunction within the subpolar gyre region determined by the closed contour of sea surface height with the largest horizontal area (e.g. *Eden and Willebrand, 2001; Treguier et al., 2005; Lohmann et al., 2009*). Figure 4.20 shows that the subpolar gyre strength estimated by these three definitions shares similar interannual variability and the long-term trend with the mean

transport of 43.6 ± 7.6 Sv for CONTROL run and 45.1 ± 8.7 Sv for PERTURB averaged over three indices.

Turing to the AMOC, its strength is often defined as the maximum value of overturning streamfunction at various latitudes depending on the region of interest. In our experiments we define an AMOC index using the overturning streamfunction values at 26.5°N , which is at the same latitude of the RAPID-AMOC array (*Srokosz and Bryden, 2015*). The trends of AMOC index evolution in both CONTROL and PERTURB bear a similarity to the Florida Strait transport with a relative low time-mean transport over the first 10 years from 2000 to 2009 (CONTROL: 14.4 ± 2.8 Sv, PERTURB: 14.8 ± 3.3 Sv) and then undergo an increase from 2009 onwards (CONTROL: 18.7 ± 3.0 Sv, PERTURB: 18.7 ± 3.1 Sv) as shown by Figure 4.21a. A broad agreement is achieved between the CONTROL AMOC and RAPID-MOCHA-WBTS (Rapid-Meridional Overturning and Heatflux Array-Western Boundary Time Series) observation (*Smeed et al., 2019*) after 2009 with the CONTROL estimate slightly higher than the observation by 1.4 Sv. The increasing trend of modelled AMOC is similar to that observed in Florida Strait transport, and is likely to be attributed to the spin-up stage experienced by the model.

B. Differences between the twin experiments

The response of the ocean circulation systems is estimated as the difference between the PERTURB and the CONTROL diagnostics for each circulation system. Both gyre circulations and the AMOC transport have demonstrated a systematic response to the CA perturbations from 2000 to 2010, while changes in the circulation response emerge after 2010.

Overall the PERTURB Florida Strait transport shows a systematic intensification of 2.1 Sv compared to the CONTROL estimate (Figure 4.19b). The stronger Florida transport in the PERTURB run is associated with a more strongly tilted vertical thermocline structure (Figure 4.22c) across the Florida

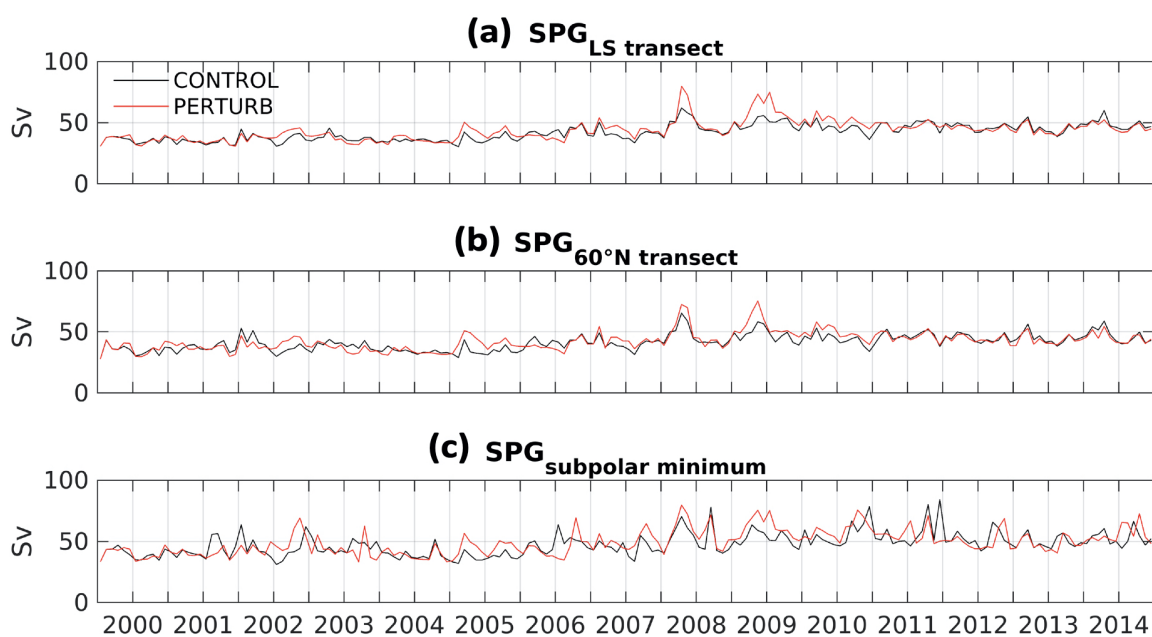


Figure 4.20: Time series of subpolar gyre indices based on the minimum barotropic streamfunction (a) along the cross section over the Labrador Sea, (b) along the 60°N and (c) from the closed SSH contour with largest area over subpolar latitudes. Note that the absolute values of the streamfunction are plotted and larger value denotes stronger subpolar gyre.

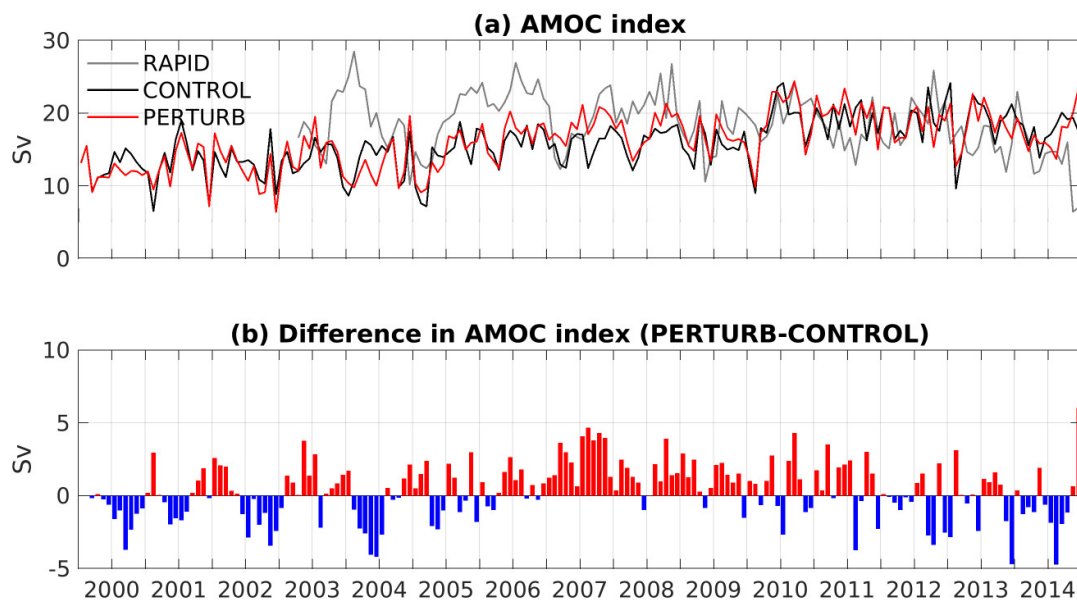


Figure 4.21: The time series of (a) AMOC indices defined as the maximum barotropic streamfunction at 26.5°N in CONTROL (black), PERTURB (red) experiments and RAPID observation (grey). (b) The difference (PERTURB-CONTROL) in (b) AMOC index, with the positive value indicating stronger AMOC in PERTURB run.

Strait that leads to a stronger northward geostrophic velocity. The strength of Florida Strait transport is generally related to the basin-wide wind stress curl (*Baringer and Larsen, 2001*). As shown in Figure 4.15c, the CA perturbation enhances wind stress more significantly in the low-latitude easterlies and mid-latitude westerlies. As a result, the anticyclonic basin-wide wind stress curl in the North Atlantic subtropical gyre is strengthened (Figure 4.22b), which, in turn, enhances the Ekman convergence, pushes the thermocline further down (Figure 4.22d), and this leads to a strengthened Florida Strait Transport. The difference in Florida Strait transport between CONTROL and PERTURB is statistically significant ($p < 0.01$) for 2000-2014 (and for the first eleven and last five year sub-periods) using a two-tailed t -test with the null hypothesis that the difference is indistinguishable from 0 (Table 4.3).

For the subpolar gyre circulation, it is found that all three indices show an overall strengthening in the subpolar gyre circulation modelled by PERTURB over the first 11 years (Figure 4.23a-c). This can be attributed to the stronger cyclonic wind stress curl (Figure 4.22b) and enhanced surface heat loss in the subpolar region (Figure 4.15b). The PERTURB subpolar gyre transport is about 2.2 Sv higher on average over the three gyre indices from 2000 to 2010. The difference in the subpolar gyre circulation strength between PERTURB and CONTROL over the first 11 years is statistically significant ($p < 0.05$, Table 4.3) in a t -test. Figure 4.21b also demonstrates an overall strengthening of PERTURB AMOC from 2000 to 2010 by 0.4 Sv compared to the CONTROL. The PERTURB AMOC strength during 2000-2010 is statistically different from the CONTROL examined by a two-tailed binomial test, but the time series are not distinguishable with a t -test (Table 4.3).

From 2009/2010 onwards, the differences in the subpolar gyre strength and AMOC transport between the twin experiments demonstrate qualitatively different behaviours than the first 10-year period. From 2010 to 2014, the subpolar gyre strength in the PERTURB is marginally weaker than that in the CONTROL experiment by about 0.7 Sv, which is statistically significant using a

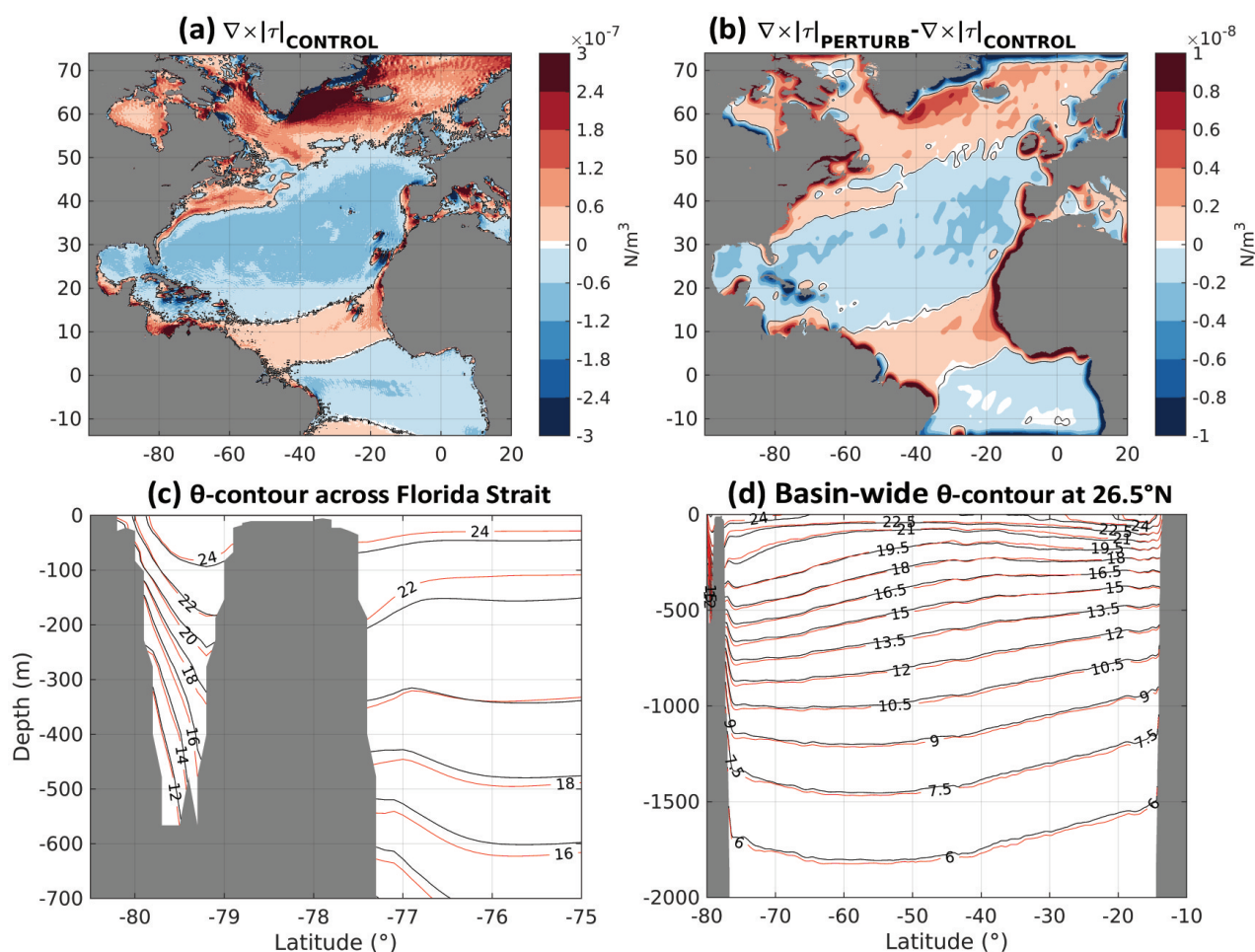


Figure 4.22: 15-year mean of (a) CONTROL wind stress curl, (b) the wind stress curl difference between PERTURB and CONTROL, smoothed by a $5^\circ \times 5^\circ$ 2D Gaussian filter. Positive value denotes the cyclonic wind stress curl. The spatial filter is applied to highlight the large-scale pattern in the wind stress curl anomaly. (c) The vertical thermocline structure averaged over 15 year period at 26.5°N , panel extends to the east of Grand Bahamas Island to illustrate the thermocline structure connection to the open ocean. (d) Basin-wide thermocline structure at 26.5°N .

binomial test, but not with a t-test (Table 4.3). This is partly because that year 2010 is a year when the PERTURB SPG is still stronger while after 2010, SPG strength in PERTURB is mostly weakened compared to CONTROL. A concurrent sign reversal is also found in the difference in the subpolar gyre ocean heat content (OHC) (Figure 4.23d) and the subpolar ML depth (Figure 4.23e) between CONTROL and PERTURB, while for the first ten years the SPG cools and has a deeper ML depth for the first ten years, before reversing to a warming with a shallower ML depth. Here the subpolar gyre OHC and ML

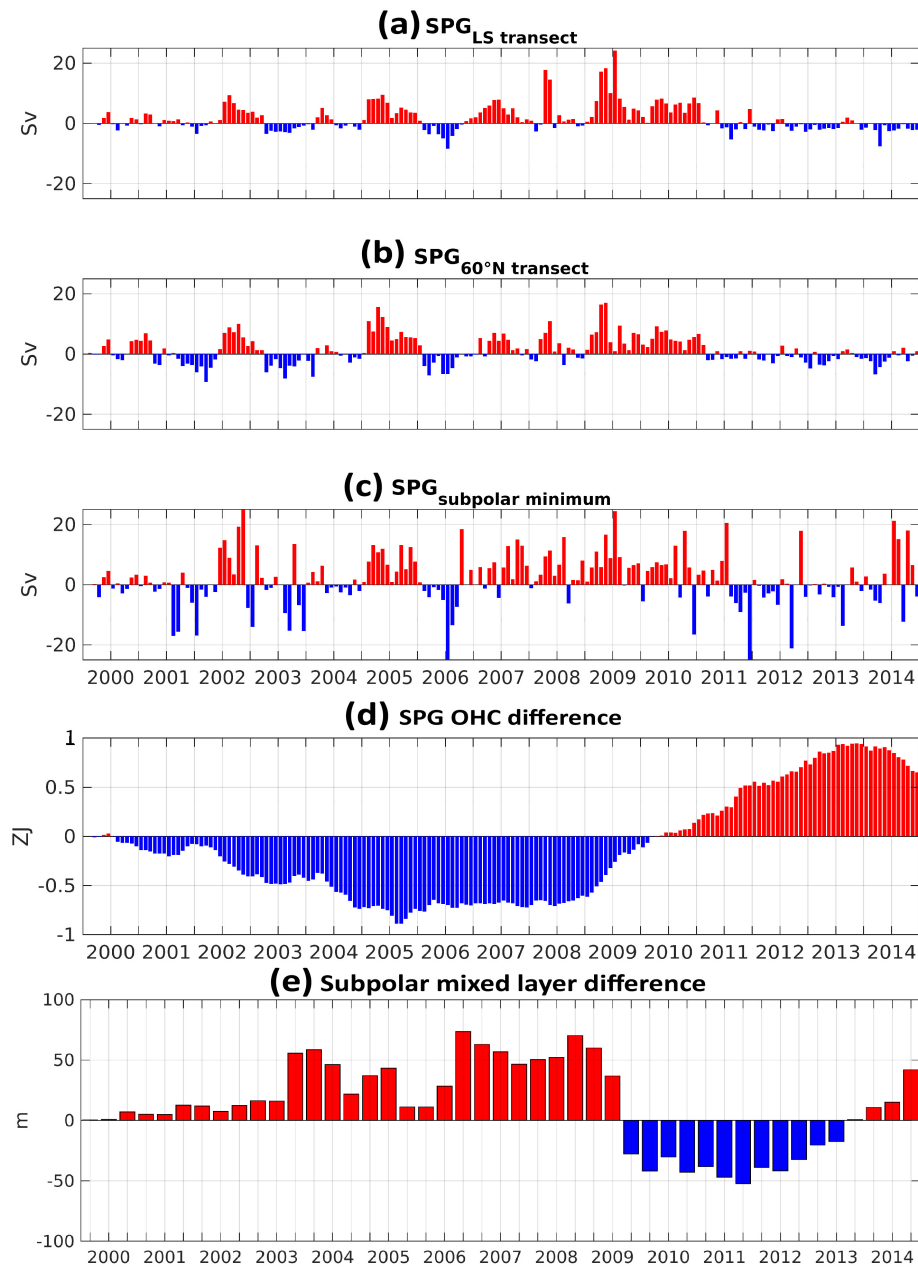


Figure 4.23: Time series of the difference in subpolar gyre indices (PERTURB-CONTROL) based on the minimum barotropic streamfunction (a) along the cross section over the Labrador Sea, (b) along the 60°N and (c) from the closed SSH contour with largest area over subpolar latitudes. The positive values (red bars) represent strengthened subpolar gyre in PERTURB experiment. (d) Difference of ocean heat content (OHC) ($1 \text{ ZJ} = 10^{21} \text{ J}$) in the subpolar box (40°N to 65°N , 60°W to 10°W) between PERTURB and CONTROL experiments, with positive values denoting ocean warming in PERTURB run. (e) Same as (d) but for the winter time (DJF) ML depth calculated in subpolar region, and positive values denote deeper ML in PERTURB run.

depth is calculated for the region between 40°N – 65°N and 60°W – 10°W .

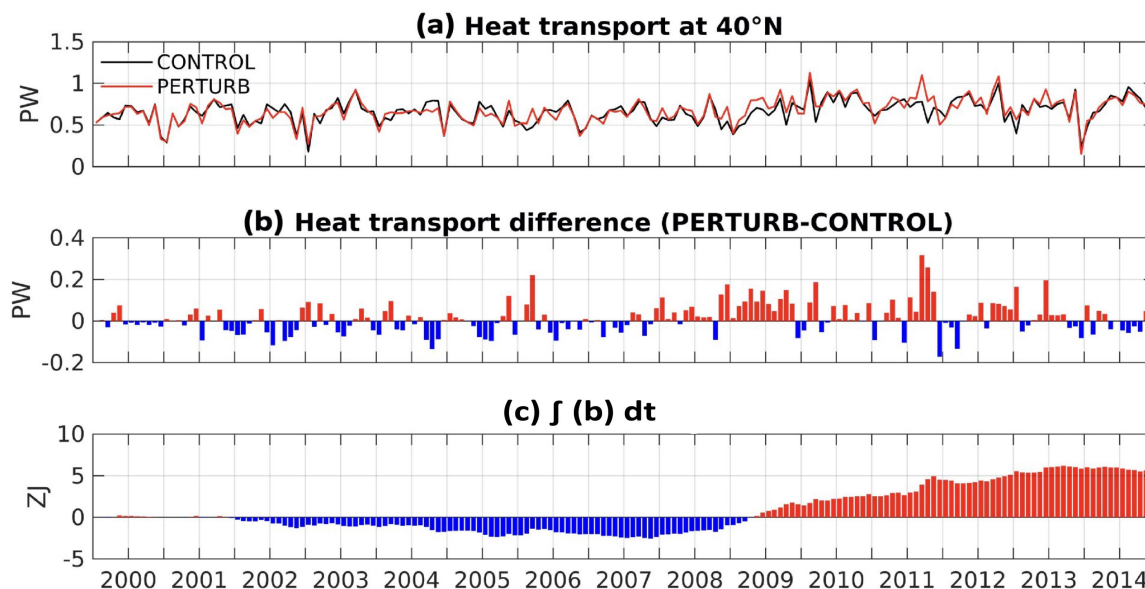


Figure 4.24: The time series of (a) the northward heat transport in CONTROL (black) and PERTURB (red) experiments, the difference (PERTURB-CONTROL) in (b) the northward heat transport and (b) accumulative heat transport at the gyre boundary at 40°N . An increased northward heat transport is found in winter 2008 and lead to an anomalous heat input into the subpolar region.

Interestingly, although the subpolar gyre loses more heat to the atmosphere in PERTURB (Figure 4.15b), the subpolar OHC in PERTURB becomes greater than CONTROL after 2010, indicating a stronger lateral heat transport from the subtropical to the subpolar region in PERTURB. The accumulative northward heat transport suggests that across the gyre boundary at 40°N , a strengthened northward heat transfer starts around year 2009 and monotonically increases from 2009 to 2014 (Figure 4.24c), even though the heat transport itself has demonstrated little intermittent difference (Figure 4.24a, b). The increased northward heat transport across the gyre boundary *lags* the strengthened Florida Strait transport by a few years (Figure 4.19b), while the accumulated anomalous heat transport across the gyre boundary *leads* changes in the subpolar OHC, the subpolar gyre strength and the AMOC transport by about one year. This heat transport difference then leads to a monotonically enhanced OHC gain and a persistently shallower wintertime subpolar ML depth in PERTURB compared to those in CONTROL from 2010 to 2014 (Figure 4.23e

and d), which acts to stratify the upper subpolar ocean, reduce the thermocline doming and lead to a weaker PERTURB subpolar gyre circulation (Figure 4.23). The timing of the AMOC difference between the twin experiments starting to reduce coincides with that of the changed difference in the subpolar gyre strength and the Florida Strait transport, which reflects the feedback of the subpolar gyre changes to the subtropical region. These results highlight the importance of ocean dynamics in generating a non-local ocean response to perturbations in atmospheric forcing.

	2000-2010			2010-2014		
	Δ	p-value	p-value	Δ	p-value	p-value
		(t-test)	(binomial test)		(t-test)	(binomial test)
FS	2.13 Sv	$p < 0.01$	$p < 0.01$	1.44 Sv	$p < 0.01$	$p < 0.01$
SPG ₁	2.47 Sv	$p < 0.01$	$p < 0.01$	-0.91 Sv	$p = 0.11$	$p < 0.01$
SPG ₂	1.86 Sv	$p = 0.02$	$p = 0.01$	-0.84 Sv	$p = 0.17$	$p = 0.01$
SPG ₃	2.38 Sv	$p = 0.03$	$p < 0.01$	-0.33 Sv	$p = 0.42$	$p = 0.31$
AMOC	0.47 Sv	$p = 0.13$	$p = 0.01$	-0.05 Sv	$p = 0.47$	$p = 1.00$

	2000-2014		
	Δ	p-value	p-value
		(t-test)	(binomial test)
FS	1.93 Sv	$p < 0.01$	$p < 0.01$
SPG ₁	1.57 Sv	$p = 0.02$	$p = 0.21$
SPG ₂	1.14 Sv	$p = 0.07$	$p = 0.41$
SPG ₃	1.65 Sv	$p = 0.06$	$p = 0.66$
AMOC	0.32 Sv	$p = 0.20$	$p = 0.04$

Table 4.3: A summary of the response of ocean circulation systems (Florida Strait transport, subpolar gyre, AMOC) and the northward heat transport at the boundary gyre ($\iint vTdx dz$) to the CA perturbation. Δ = difference calculated by PERTURB - CONTROL. The statistical significance of each result is shown by the p-values for both a two-tailed *t*-test and a two-tailed binomial test, where p-values < 0.05 (95%) are considered statistically significant, and are highlighted in red. Note that the difference in subpolar gyre strength is calculated using the absolute values of the streamfunction minimum, the same as in Figure 4.23.

4.6 Summary

In this chapter, we have evaluated the newly-released ERA5 reanalysis wind data in aspects of the representation of small-scale and high-frequency variance in reference to QuikScat scatterometer high-resolution wind measurements and in-situ sea surface wind time series recorded at 18 meteorology buoy stations. Spectral analysis of these dataset suggest that the ERA5 surface wind energy suffers from a deficit in small-scale and high-frequency energy due primarily to inadequate model representation of the sub-grid processes even though the observational data have been assimilated into the ERA5 reanalysis data.

Inspired by the principle of injecting energy into these smaller scales, we apply a stochastic wind perturbation scheme, introducing an interesting algorithm called Cellular Automata (CA), to mimic the evolution of small-scale motions. The probabilistic CA algorithm is found to be capable of generating random yet spatially coherent structures that continuously evolve over time. These structures are then used as the disturbance patterns to perturb ERA5 ocean winds. Results show that perturbed surface winds enjoy improvement of the energy spectra over length scales smaller than 400 km and over frequencies higher than 1 cycle per day. The CA-perturbed ERA5 winds that have been generated are tested and contain realistic amounts of kinetic energy.

A multi-column KPP (MC-KPP) ocean ML model is employed to investigate the one-dimensional thermal response of the upper ocean to the CA wind perturbations. The model results clearly demonstrate that the enhanced surface heat loss due to the CA perturbation forces a systematic sea surface cooling across the domain with a noticeable seasonal cycle in the enhanced SST cooling. The spatial distribution of the strong SST cooling is remarkably in phase with the seasonal variation of background ML depth and locally also correlated to the enhanced surface heat loss, especially at low-latitudes. The improved wind variability at small scales and high frequencies induced by the CA perturbation lowers the SST by $\sim 0.1^\circ\text{C}$ averaged over the basin and $\sim 1^\circ\text{C}$ locally over the

summer time in both hemispheres.

The ocean circulation response to the CA perturbation is investigated by conducting twin experiments (CONTROL and PERTURB) using the MITgcm for an extended period from 2000 to 2014 with a focus in the North Atlantic Ocean. The MITgcm results show a broad consistency with the MC-KPP results for the SST response to the CA perturbation, in terms of its seasonality and spatial distribution, especially over the open ocean. The response of the ocean circulation to the CA perturbation has demonstrated different behaviours between the subtropical and subpolar gyre circulations. From 2000 to 2010, both the subtropical and subpolar gyres are strengthened in PERTURB. This can be attributed to the anomalous anticyclonic surface wind stress curl at mid-latitudes and the anomalous cyclonic atmospheric circulation at high-latitudes of the North Atlantic respectively.

Changes in the circulation response are found after 2010. From 2010 to 2014, the subpolar gyre in the PERTURB experiment is weaker than the CONTROL gyre strength. This change is driven by an stronger northward heat transport across 40°N simulated in the PERTURB experiment, which is statistical significant using a binomial test. This stronger heat input from the subtropical to subpolar region in PERTURB elevates the subpolar OHC, flattening the domed structure of the thermocline which compensates the subpolar gyre response of the local buoyancy forcing and reverses the relative strength of the subpolar gyre between the PERTURB and CONTROL. The ML increases in response. Changes in the AMOC strength are linked to this inter-gyre interaction, demonstrating an evolution in phase with the subpolar gyre difference. These non-local responses of the ocean circulation represented by this gyre interaction offers an insightful perspective of understanding the cross-scale linkage between the low-frequency and large-scale ocean response modes to the highly-fluctuated anomalies in the atmospheric forcing represented here by the CA perturbation.

Based on the 2010-2014 period, the steady-state response to the CA perturbation is a stronger subtropic gyre, leading to enhanced northward heat transport from the subtropical gyre to the subpolar gyre. The steady-state response to this appears to be a slowing of the SPG transport, but this is not statistically significant in other the metrics. An extension of our model runs would shed light on the longer-term response. Nevertheless, our model results from MC-KPP and MITgcm have shown a qualitative difference in ocean behaviour with the addition of the realistic mesoscale (<400 km) and high-frequency (>1 cpd) weather systems in the atmospheric forcing, and we regard these effects are non-negligible and should be taken into account in the future global climate model studies.

CONCLUSIONS AND FUTURE WORK

This chapter summarizes the main findings of this PhD research, the outstanding questions, and the recommendations for future work.

5.1 Overview of key findings

High-frequency (sub-daily time scales) and mesoscale (<1000 km) atmospheric variabilities have been recognized as playing a role in regulating the longer-term and larger-scale atmosphere-ocean phenomena. In the last few decades, we have seen a significant improvement in the computer power which facilitates the simulation of numerical weather and climate prediction models with higher resolution and the inclusion of ever more physical processes and climate components such as the cryosphere and the biosphere (*Franzke et al., 2015*). Despite the increase in computer power, many important physical processes (e.g. tropical convections, gravity waves and mesoscale weather systems) are still not or only partially resolved and will not be explicitly resolved in the numerical weather and climate models in the foreseeable future (*Williams, 2005; Palmer and Williams, 2008*). Parameterizations are then needed to account for the collective effect of these high-frequency and mesoscale motions in the atmosphere on the larger-scale and longer-term systems which are not just of the great interest for scientific understanding but also help the society become more resilient to changes in extremes of weather and climate (*Palmer, 2019*). This

thesis presents a series of studies in that regard. Firstly, by understanding how the model performance is affected by both the observed and theoretically orchestrated high-frequency atmospheric variabilities, and secondly, by formulating and evaluating a parameterization method that represents the under-represented processes in a global reanalyses dataset using both the one-dimensional ocean ML models and a full three-dimensional ocean general circulation model to evaluate their impact on the ocean.

Starting with a case study, we conducted a set of sensitivity experiments using a mixed-layer model and carrying out simulations for the central Arabian Sea, where we have co-located observations of the atmosphere and ocean from a buoy and mooring. Here, a series of meteorological variables are measured in a high frequency of 7.5 minutes with the observing period lasting for a year and capturing a distinct full seasonal cycle of the local meteorological conditions that allows us to investigate the effect of high-frequency atmospheric variabilities under different seasonal background states. Control and sensitivity experiments are designed using a one-dimensional PWP ML model to determine the key elements from a suite of meteorological variables (i.e. sea surface wind, surface pressure, air temperature, air humidity and clouds) that regulate the evolution of the sea surface temperature and ML depth. The model is initialized with the observed temperature and salinity profiles. By forcing the model using atmospheric forcing with and without the sub-daily fluctuations, we find that including the high-frequency weather systems systematically lowers the daily-mean SST and damps the SST variability on daily-to-intraseasonal time scales whereas little systematic influence is found on the magnitude of the SST diurnal cycle. The high-frequency atmospheric forcing regulates the time-mean SST via the changes in the time-mean air-sea heat fluxes and wind stress with the magnitude and seasonality of the SST response strongly determined by the ML heat capacity, associated with the background ML depth. Furthermore, the key element standing out among these high-frequency meteorological variables that impacts the ocean the most is the near surface wind. Its high-frequency

fluctuation not only enhances the time-mean turbulent heat loss enhancement but also leads to strengthened wind-driven shear instability at the base of the ML depth via both the increased time-mean wind stress and the fluctuated wind direction.

A follow-on investigation on the high-frequency atmospheric forcing is inspired by the stochastic climate conceptual model proposed by *Hasselmann* (1976), where low-frequency variability of SST is conjectured to be induced by random variations in surface heat fluxes. This model is applied to understand the observed low-frequency SST variability such as the SST variability in the Pacific Ocean associated with the Pacific Decadal Oscillation (*Newman et al.*, 2003) and persistent SST decadal variability in the North Atlantic (*Deser et al.*, 2003; *de Coëtlogon and Frankignoul*, 2003). Based on our knowledge from previous studies and Chapter 2, the ML variation is important in regulating the SST response to the atmospheric forcing. It is then of our interest to extend Hasselmann's conceptual model by including the ML variation to examine its role in regulating the SST response. We first formulated the stochastic atmospheric forcing by generating a series of random anomalies and superimposed with time-mean radiative and turbulent heat fluxes. The time-mean net heat flux across the sea surface is zero. Both non-solar penetrative and a solar-penetrative schemes are applied in the PWP model to adjust response of the ML to the surface heat flux. The SST spectra derived from both PWP experiments are similar to that in *Hasselmann* (1976) suggesting that the ML variation does not excite any spectral peak at low-frequencies. However, we find that the ML variation induced by the solar penetration scheme produces a long-term warming rectification effect on the SST due to the asymmetric SST response to the surface heating and cooling. The dependence of the SST rectification on the model constraints such as the forcing amplitude and the initial condition is associated with the solar penetration depth with a shallower solar penetration depth produces a more pronounced warming rectification on SST.

Finally, we propose a stochastic parameterization approach to represent the

under-represented effect of the realistic mesoscale and high-frequency atmospheric variability on the wind kinetic energy spectra in ERA5 wind data set. This study is inspired by a well-known issue of the effective resolution in the numerical models, which is defined as the smallest length scale where model-derived kinetic energy spectrum departs from the observation (*Lean and Clark, 2003; Skamarock, 2004; Hamilton et al., 2008*). Our spectral analysis on the ERA5 wind data has shown that this reanalysis wind data suffers from energy deficiency at length scales smaller than 400-500 km and also at time scales shorter than 1 day when compared to the QuikScat and *in-situ* wind measurements. We demonstrate that with a set of properly tuned parameters, a cellular automata (CA) algorithm can generate spatially coherent patterns that continuously evolves over time and simultaneously improve the performance of the ERA5 wind wavenumber spectra and frequency spectra. One-dimensional modelling shows a systematic SST cooling in response to the enhanced turbulent heat loss and wind stress driven by the CA perturbation, characterized by a basin-averaged SST cooling of 0.1°C in the summer hemisphere and local instantaneous SST cooling up to 1°C . The distribution and seasonality of the SST response is largely confined by the background ML depth consistent with our knowledge from previous chapters. OGCM experiments show a large-scale oceanic circulation changes driven by the CA perturbation with a spin up of both the North Atlantic subtropical and subpolar gyres and a strengthening the AMOC in response to the enhanced subtropical anticyclonic wind stress curl, subpolar cyclonic wind stress curl and enhanced surface heat loss from 2000 to 2010. A steady-state response emerges from 2010 to 2014 characterized by a stronger northward heat transport at the boundary gyre associated with the stronger western boundary currents in the subtropic North Atlantic. The enhanced heat transport leads to a greater heat content in the subpolar gyre, which, in turn, compensates the local heat loss and reduces the doming structure of the thermocline in the subpolar region, resulting in a weaker subpolar gyre circulation. These results highlight the importance of the ocean dynamics in generating the non-local response of ocean circulations to realistic

high-frequency and mesoscale weather systems.

5.2 Connection to the motivative literatures

In summary, our results show that the ocean is sensitive to the high-frequency and small-scale atmospheric variabilities. The first two chapters investigate the rectification of SST in response to the high-frequency weather systems and stochastic air-sea heat fluxes which is largely motivated by the discrepancies between the statements in *Williams* (2012) and other study on the diurnal variation of SST. *Williams* (2012) reported a long-term SST cooling and ML deepening in response to the stochastic surface air-sea fluxes, and it is proposed that the surface cooling destabilizes the water column and deepens the ML whereas the surface heating simply stabilizes the water column but cannot undo what the cooling did on the ML depth. However, the studies on diurnal variation SST actually imply that the ML depth will shoal when the water column is stabilized and the cooling only removes the stratification build upon the background ML but rarely erodes the ML further. Therefore the diurnal variation SST rectifies the daily mean SST toward a warmer state. It seems that Chapter 2 clearly shows that even though with the diurnal cycle in SST, the time-mean SST can still be cooled in response to the high-frequency weather systems. While it is worth to note that this conclusion is drawn by comparing the modelled SST to the that forced by surface fluxes calculated from daily-averaged meteorological variables instead of the SST forced by averaged fluxes as in studies focusing on the SST diurnal cycle. In other words, Chapter 2 results demonstrate systematic impact from the high-frequency weather systems but does not fully reconcile the discrepancy aforementioned. In Chapter 3, the extreme case shows that warm rectification similar to the diurnal SST exists caused by the same mechanism where the SST increases more than SST decreases due to the ML variation. We did not find what *Williams* (2012) suggested, but we cannot completely overthrow the mechanism proposed

Williams (2012) because the models and experimental design used for their study is different from ours. The results in *Williams* (2012) emerges from their century-long coupled simulations and they did not explicitly disentangle the contribution of the advective processes to the observed ML deepening and SST cooling in their model results while Chapter 3 only produces 100 days of simulation with a one-dimensional ML model.

Chapter 4 work highlights broader impact of the stochastic wind variabilities on the regional ocean circulation and sea surface states, which the atmospheric circulations are sensitive to. For example, the strong signals of SST changes in response to the wind perturbation in the East tropical Atlantic can effectively alter the zonal sea surface temperature gradient that strongly coupled to the Walker circulation (e.g. *Bjerknes*, 1969; *Clement et al.*, 1996; *Xie et al.*, 2010). The changes in the strength in the circulation patterns in the Florida Strait current and the Gulf Stream can also induces more variabilities in the oceanic fronts position that alters the atmospheric storm tracks and influences the regional climate (e.g. *Small et al.*, 2014; *Kuwano-Yoshida and Minobe*, 2017). Recent atmospheric convection-permitting regional climate simulations (e.g. *Kolstad and Bracegirdle*, 2008; *Zahn and von Storch*, 2010) predict changes in the intensity and frequency of the mesoscale weather systems this century, it is of importance to estimate the impact induced by the discrepancies in the sea surface wind field within the mesoscale regimes between the observations and the reanalyses, with the latter tends to be extensively used in modelling work. As discussed in Chapter 4, the CA perturbation generates an isotropic perturbation pattern that fluctuates in space and time which can be regarded as the 'error' or 'uncertainty' that we estimated for ERA5 surface wind field in reference to the observation. It may not be the most accurate way to reproduce the discrepancies but it does reveal some promising aspects in the spectral analysis and wind speed PDF. The overall less -occurred high-wind events in the ERA5 wind field might induce bias in regional oceanic status such as overestimated SST (e.g. *Zhai*, 2013; *Zhou et al.*, 2018) or underestimated open

ocean convection events (e.g. *Pickart et al.*, 2003; *Condron and Renfrew*, 2013).

5.3 Future work

Several possible future steps are discussed in this section.

The first one is a cross-model comparison on the SST response to the stochastic surface heat fluxes in Chapter 3. In Chapter 3, a set of idealized ensemble simulations using PWP ML model are conducted to explore the role of ML variation in generating the SST rectification effect. The PWP model considers the ML to be vertically uniform in terms of the temperature, salinity and velocities and has provided a rather simple parameterization of ML dynamics to allow a straightforward interpretation of the ML variation and the SST response to the stochastic surface heat fluxes. Another category of ML model, the turbulence closure model, parameterizes the turbulent mixing via the eddy viscosity and eddy diffusivity based on the local stratification, vertical shear and surface fluxes to simulate the ML turbulent mixing (e.g. *Mellor and Yamada*, 1982; *Kantha and Clayson*, 1994; *Large et al.*, 1994). The ML depth modelled by the turbulence closure model is often diagnosed based on various criteria associated with the temperature, salinity and density, which is different than that in the PWP model. Owing to a higher complexity of the mixing parameterization, turbulence closure models are able to reproduce a more realistic upper-ocean thermocline structure and hence have a broader application of the in general ocean circulation models (e.g. MITgcm) and coupled weather and climate prediction models (e.g. *Takaya et al.*, 2010; *Hirons et al.*, 2015) than the PWP ML model.

It is found that under the surface cooling condition, the turbulence closure model tends to produce a stronger convective mixing than the PWP model (e.g. *Large et al.*, 1994; *Burchard and Bolding*, 2001; *Zhou et al.*, 2018) because the turbulence closure models parameterize active entrainment. The difference in the vertical

mixing schemes can be a source of uncertainty on the both the solar-penetrative (SP) and non-solar-penetrative (NSP) SST behaviour across the different models. Note that although the time-mean stochastic heat flux in Chapter 3 is zero at the sea surface, the ML itself experiences a time-mean cooling in SP scenario because that the solar radiation is partly absorbed within the ML depth while the heat loss is constantly applied at the surface. The random cooling events embedded in the stochastic fluctuations imposed on top of this mean surface heat flux are likely to excite a much stronger convective entrainment of the surface boundary layer than that in the experiment forced by the time-mean heat flux, which could partly or completely compensate the rapid warming of SST averaged over a long time period and lead to a possible cooling rectification effect on SST. Hence, it is worthwhile comparing the PWP model with one or two representative turbulence closure models to evaluate whether the sensitivity of SST rectification to the solar penetration scheme revealed by the PWP model is dependent on parameterization schemes of the vertical mixing or not.

The second potential future work is to further optimize the CA parameter selection in Chapter 4. We have shown that the CA perturbation effectively improves the spectral features in ERA5 reanalyses wind while the tuning of the parameters is not completed automatically. Key parameters that determine the spatial and temporal characteristics of the CA perturbation are N_L , ΔS_{CA} , the time step Δt_{CA} and α . N_L , ΔS_{CA} and Δt_{CA} are well defined (see Section 4.3.2). But the choice of α obeys some subjective choices, which requires iterative adjustments via the direct comparison between the observed and perturbed energy spectra in wavenumber and frequency domain for the optimal spectral match with observations. A further optimisation on the α selection can lead to a much efficient CA application and allow for more exploration of the CA perturbation scheme, such as incorporating a region-dependent α . The spatial map of α is able to redistribute energy input of the CA perturbation to obtain a more realistic perturbed wind field in regions lack of small-scale wind structure. For example, the strong small-scale wind shear observed tropical

Atlantic as shown in Figure 4.2 is poorly represented by ERA5 while the CA perturbation only elevates the overall small-scale variabilities, with less localized improvement in reproducing these events in the perturbed vorticity field (Figure 4.10b). This issue is likely to be (partly) addressed by the spatially-varying α .

Another standing out feature of the CA perturbation is that the generated 2D pattern is essentially an isotropic pattern which is not a completely realistic representation in certain mesoscale wind events such as the orographic tip jets, which is an elongated band of severe wind band. The QuikSCAT wind vorticity in Figure 4.2 in the tropical region also tends to be confined within limited meridional range. One improvement of CA perturbation would be incorporating the background information of the observed wind snapshot into the perturbation scheme. For example, a simple bulk relation between the wind speed and wind direction can be derived from the observation and ERA5 wind to constrain the perturbation scheme to yield the observed direction instead of applying same term on both wind components as we did in Chapter 4. 2D spatial background information can be derived from map of wind shear or local wind variabilities from the observation to locate 'hot bed' of wind discrepancies which is suggestive for designing weighting matrix for the CA perturbation.

The final potential future work is to extend the OGCM experiments to a global scale which allows more large-scale ocean circulation systems being examined and completing the picture of AMOC response and other potential inter-basin interactions driven by the localized CA wind perturbations. The final potential future work is to explore the impact of CA wind perturbation in an atmosphere-ocean coupled model. Our model analysis has shown a non-local ocean response to these localized coherent small-scale wind perturbations characterized by the basin-wide SST cooling, thermocline structure adjustment, intensified gyre circulations and gyre interactions. These changes in the ocean especially those in the upper ocean do not impose any feedbacks to the atmosphere in our model experiments for now. A coupled-model assessment will obtain a more comprehensive picture of the climatic response to these small-scale wind perturbations induced by the

CA algorithm.

Bibliography

- Alexander, M. A. and C. Deser, 1995: A mechanism for the recurrence of wintertime midlatitude SST anomalies. *J. Phys. Oceanogr.*, 25(1), 122-137.
- Alexander, M.A. and C. Penland, 1996: Variability in a Mixed Layer Ocean Model Driven by Stochastic Atmospheric Forcing. *J. Clim.*, 9(10), 2424-2442.
- Alexander, M.A. and C. Penland, 2000: Processes that influence sea surface temperature and ocean mixed layer depth variability in a coupled model. *J. Geophys. Res.*, 5(C7), 16823-16842.
- Ångström, A., 1915: A study of the radiation of the atmosphere, Smithsonian Miscellaneous Collection, 65, 182 pp.
- ASCE-EWRI, 2005: The ASCE Standardized Reference Evapotranspiration Equation, 173 pp.
- Baehr, J., A. Stroup and J. Marotzke, 2009: Testing concepts for continuous monitoring of the meridional overturning circulation in the South Atlantic. *Ocean Model.*, 29(2), 147-153.
- Balan Sarojini, B. and J. von Storch, 2009: Effects of fluctuating daily surface fluxes on the time-mean oceanic circulation. *Clim. Dynam.*, 33, 1-18.
- Baringer, M. O., and J. C. Larsen, 2001: Sixteen years of Florida Current transport at 27°N. *Geophys. Res. Lett.*, 34, L23615.
- Barsugli, J.J. and D.S. Battisti, 1998: The Basic Effects of Atmosphere-Ocean Thermal Coupling on Midlatitude Variability. *J. Atmos. Sci.*, 55, 477-493.

- Bender, M. a., Ginis, I., and Kurihara, Y., 1993: Numerical simulations of tropical cyclone-ocean interaction with a high-resolution coupled model. *J. Geophys. Res.*, 98(D12), 23245.
- Bengtsson, L., Steinheimer, M., Bechtold, P., Geleyn, J., 2013: A stochastic parameterization for deep convection using cellular automata. *Q. J. R. Meteorol. Soc.*, 139, 1533-1543.
- Berner, J., Doblas-Reyes, F. J., Palmer, T. N., Shutts, G. and Weisheimer, A., 2008: Impact of a quasi-stochastic cellular automata backscatter scheme on the systematic error and seasonal prediction skill of a global climate model. *Phil. Trans. R. Soc.*, 366, 2561-2579.
- Berner, J., G. Shutts, M. Leutbecher, T. N. Palmer, 2009: A spectral stochastic kinetic energy backscatter scheme and its impact on flow-dependent predictability in the ECMWF ensemble prediction system. *J. Atmos. Sci.*, 66(3), 603-626.
- Bernie, D. J., S. J. Woolnough, J. M. Sligo and E. Guilyardi, 2005: Modeling diurnal and intraseasonal variability of the ocean mixed layer. *J. Climate*, 18(8), 1190-1202.
- Bernie, D. J., E. Guilyardi, G. Madec, J. M. Slingo and S. J. Woolnough, 2007: Impact of resolving the diurnal cycle in an ocean-atmosphere GCM. Part 1: A diurnally forced OGCM. *Clim. Dynam.*, 29(6), 575-590.
- Bernie, D. J., E. Guilyardi, G. Madec, J. M. Slingo, S. J. Woolnough and J. Cole, 2008: Impact of resolving the diurnal cycle in an ocean-atmosphere GCM. Part 2: A diurnally coupled CGCM. *Clim. Dynam.*, 31(7-8), 909-925.
- Berloff, P. S., 2005: Random-forcing model of mesoscale eddies. *J. Fluid Mech.*, 529, 71-95.
- Biastoch, A., C. W. Böning, J. Getzlaff, J. M. Molines and G. Madec, 2008: Causes of interannual–decadal variability in the meridional overturning

- circulation of the midlatitude North Atlantic Ocean. *J. Climate*, 21(24), 6599-6615.
- Bingham, R. J., C. W. Hughes, V. Roussenov and R. G. Williams, 2007: Meridional coherence of the North Atlantic meridional overturning circulation. *Geophys. Res. Lett.*, 34(23).
- Bjerknes, J., 1969: Atmospheric teleconnections from the equatorial Pacific. *Mon. Wea. Rev.*, 97, 163–172.
- Blanke, B., J. D. Neelin, and D. Gutzler, 1997: Estimating the Effect of Stochastic Wind Stress Forcing on ENSO Irregularity. *J. Climate*, 10, 1473-1486.
- Brunt, D., 1932: Notes on radiation in the atmosphere. I. *Q. J. Roy. Meteor. Soc.*, 58(247), 389-420.
- Brutsaert, W., 1975: On a Derivable Formula for Long-Wave Radiation From Clear Skies. *Water Resour. Res.*, 11(5), 742-744.
- Burchard, H., and K. Bolding, 2001: Comparative analysis of four second-momentum turbulence closure models for the oceanic mixed layer. *J. Phys. Oceanogr.*, 31, 1943-1968.
- Cabanes, C., T. Lee, and L. L. Fu, 2009: Mechanisms of interannual variations of the meridional overturning circulation of the North Atlantic Ocean. *J. Phys. Oceanogr.*, 38(2), 467-480.
- Charney, J.G., 1971: Geostrophic turbulence. *J. Atmos. Sci.*, 28, 1087-1095.
- Chelton, D. B., Esbensen, S. K., Schlax, M. G., Thum, N., Freilich, M. H., Wentz, F. J., Gentemann, C. L., McPhaden, M. J. and Schopf, P. S., 2001: Observations of coupling between surface wind stress and sea surface temperature in the eastern tropical Pacific. *J. Clim.*, 14(7), 1479-1498.
- Chelton, D. B., Schlax, M. G., Freilich, M. H. and Milliff, R. F., 2004: Satellite measurements reveal persistent small-scale features in ocean winds. *Science*, 303(5660), pp.978-983.

- Chelton, D. B., Freilich M. H., Sienkiewicz J. M., and Von Ahn J. M., 2006: On the use of QuikSCAT scatterometer measurements of surface winds for marine weather prediction. *Mon. Wea. Rev.*, 134, 2055-2071.
- Chhak, K.C., A. M. Moore, R. F. Millif, G. Branstator and W. R. Holland, 2006: The North Atlantic Oscillation as a source of stochastic forcing of the wind-driven ocean circulation. Part I: A Diagnostic Analysis of the Ocean Response to Stochastic Forcing. *Dynam. Atmos. Oceans*, 43(3-4), 151-170.
- Cho, J. N. Y., Zhu Y., Newell, R. E., Anderson, B. E., Barrick J. D., Gregory, G. L. and Sachse, G. W., 1999a: Horizontal wavenumber spectra of winds, temperature, and trace gases during the Pacific Exploratory Missions: 1. Climatology. *J. Geophys. Res.*, 104(5), 5697-5716.
- Cho, J. N. Y., Zhu Y., Newell, R. E., Anderson, B. E., and Barrick J. D., 1999b: Horizontal wavenumber spectra of winds, temperature, and trace gases during the Pacific Exploratory Missions: 2. Gravity waves, quasi-two-dimensional turbulence, and vortical modes. *J. Geophys. Res.*, 104(13), 16297-16308.
- Clement, A. C., Seager, R., Cane, M. A., and Zebiak, S. E., 1996: An ocean dynamical thermostat. *J. Clim.*, 9, 2190–2196.
- Clement, A., K. Bellomo, L. N. Murphy, M. A. Cane, T. Mauritsen, G. Rädel, B. Stevens, 2016: The Atlantic Multidecadal Oscillation without a role of ocean circulation. *Science*, 350(6258), 320-324.
- Condron, A., Bigg, G. R. and Renfrew, I. A., 2008: Modeling the impact of polar mesocyclones on ocean circulation. *J. Geophys. Res. Oceans*, 113(C10).
- Condron, A. and I. A. Renfrew, 2013: The impact of polar mesoscale storms on northeast Atlantic Ocean circulation. *Nat. Geosci.*, 6(1), 34–37.
- Czaja, A. , Robertson, A. W. and Huck, T., 2003: The Role of Atlantic Ocean-Atmosphere Coupling in Affecting North Atlantic Oscillation Variability. In *The North Atlantic Oscillation: Climatic Significance and Environmental Impact* (eds J. W. Hurrell, Y. Kushnir, G. Ottersen and M. Visbeck).

- Danabasoglu, G., Large, W. G., Tribbia, J. J., Gent, P. R., Briegleb, B. P., and McWilliams, J. C., 2006: Diurnal coupling in the tropical oceans of CCSM3. *J. Clim.*, 19(11), 2347-2365.
- Dare, R. A., and McBride, J. L., 2011: Sea Surface Temperature Response to Tropical Cyclones. *Mon. Weather Rev.*, 139(12), 3798-3808.
- de Coëtlogon and C. Frankignoul, 2003: On the persistence of wind sea surface temperature in the North Atlantic. *J. Clim.*, 13, 1481-1495.
- Denis, B., Côte, J., and R. Laprise, 2002: Spectral decomposition of two-dimensional atmospheric field on limited-area domains using the discrete cosine transform (DCT). *Mon. Wea. Rev.*, 137(7), 1812-1829.
- Denman, K. L., 1973: A time-dependent model of the upper ocean. *J. Phys. Oceanogr.*, 3, 173-184.
- Deser, C. and M.L. Blackmon, 1993: Surface Climate Variations over the North Atlantic Ocean during Winter: 1900-1989. *J. Clim.*, 6, 1743-1753.
- Deser, C., M. A. Alexander and M. S. Timlin, 2003: Understanding the persistence of sea surface temperature anomalies in midlatitudes. *J. Clim.*, 16.
- Deser, C., M. A. Alexander, S.-P. Xie and A. S. Phillips, 2010: Sea Surface Temperature Variability: Patterns and Mechanisms. *Annu. Rev. Mar. Sci.*, 2, 115-143.
- Deshayes, J. and C. Frankignoul, 2005: Spectral characteristics of the response of the meridional overturning circulation to deep-water formation. *J. Phys. Oceanogr.*, 35(10), 1813-1825.
- Dewar, W. K., and G. R. Flierl, 1987: Some effects of the wind on rings. *J. Phys. Oceanogr.*, 17, 1653-1667.
- Dewan, E. M., 1979: Stratospheric spectra resembling turbulence. *Science*, 402, 832-835.

- Dilley, A. C., and O'Brien, D. M., 1997: Estimating downward clear sky long-wave irradiance at the surface from screen temperature and precipitable water. *Q. J. Roy. Meteor. Soc.*, 124(549), 1391-1401.
- Dima, M., N. Rimbu, S. Stefan, and I. Dima, 2001: Quasi-Decadal Variability in the Atlantic Basin Involving Tropics-Midlatitudes and Ocean-Atmosphere Interactions. *J. Clim.*, 14, 823-832.
- Dima, M. and G. Lohmann, 2007: A Hemispheric Mechanism for the Atlantic Multidecadal Oscillation. *J. Climate*, 20, 2706–2719.
- Dommenget, D., and M. Latif, 2002: Analysis of the observed and simulated SST spectra in the midlatitudes. *Clim. Dynam.*, 19, 277-288.
- Dommenget, D., and M. Latif, 2008: Generation of hyper climate modes. *Geophys. Res. Lett.*, 35, L02706.
- Eckermann, S. D., 2011: Explicitly Stochastic Parameterization of Nonorographic Gravity Wave Drag. *J. Atmos. Sci.*, 68(8), 1749-1765.
- Eden, C., and J. Willebrand, 2001: Mechanism of interannual to decadal variability of the North Atlantic circulation. *J. Clim.*, 14(10), 2266-2280.
- Errico, R. M., 1985: Spectra computed from a limited area grid. *Mon. We. Rev.*, 113, 1554-1562.
- Fairall, C. W., E. F. Bradley, J. E. Hare, A. A. Grachev and J. B. Edson, 2003: Bulk parameterisation of air-sea fluxes: Updates and verification for the COARE algorithm. *J. Clim.*, 16(4), 571-591.
- Feng, M., Duan, Y., Wijffels, S., Hsu, J., Li, C., Wang, H., Yang Y., Shen, H., Liu, J., Ning, C. and Yu, W., 2020: Tracking Air–Sea Exchange and Upper-Ocean Variability in the Indonesian–Australian Basin during the Onset of the 2018/19 Australian Summer Monsoon. *B. Am. Meteorol. Soc.*, 101(8), E1397–E1412.
- Ferrari, R. and C., Wunsch, 2009: Ocean circulation kinetic energy: reservoirs, sources and sinks. *Annu. Rev. Fluid Mech.*, 41, 253-282.

- Findlater, J., 1977: Observational aspects of the low-level cross-equatorial jet stream of the western Indian Ocean. *Pure Appl. Geophys.*, 115(5-6), 1251-1262.
- Fischer, A. S., 2000: The upper ocean response to the monsoon in the Arabian Sea. PhD Thesis, Massachusetts Institute of Technology and Woods Hole Oceanographic Institution, Woods Hole, Massachusetts, 220 pp.
- Fischer, A. S., Weller, R. A., Rudnick, D. L., Eriksen, C. C., Lee, C. M., Brink, K. H., Fox, C. A., and Leben, R. R., 2002: Mesoscale eddies, coastal upwelling, and the upper-ocean heat budget in the Arabian Sea. *Deep-Sea Res. PT. II*, 49(12), 2231-2264.
- Fox-Kemper, B. and Menemenlis, D., 2008: Ocean Modeling in an Eddying Regime: Can large eddy simulation techniques improve mesoscale rich ocean models? *Geophysical Monograph Series*, 177, 319-337.
- Fraedrich, K., U. Luksch and R. Bender, 2004: 1/f model for long-time memory of the ocean surface temperature. *Phys. Rev. E.*, 70.
- Frankignoul, C and K. Hasselmann, 1977: Stochastic climate models, Part II Application to sea-surface temperature anomalies and thermocline variability. *Tellus*, 29:4, 289-305.
- Frankignoul, C. and Müller, P., 1979: Quasi-geostrophic response of an infinite β -Plane ocean to stochastic forcing by the atmosphere. *J. Phys. Oceanogr.*, 9, 104-127.
- Frankignoul, C., A. 1985: Sea surface temperature anomalies, planetary waves and air-sea feedback in the mid-latitudes. *Rev. Geophys.*, 23(4), 357-390.
- Frankignoul, C., Müller, P. and Zorita, E., 1997: A simple model of the decadal response of the ocean to stochastic wind forcing. *J. Phys. Oceanogr.*, 27(8), pp.1533-1546.
- Frankignoul, C., A. Czaja, and B. L'Heveder, 1998: Air-Sea Feedback in the North Atlantic and Surface Boundary Conditions for Ocean Models. *J. Clim.*, 11, 2310-2324.

- Franzke, C. L. E, T. J. O’Kane, J. Berner, P. D. Williams and V. Lucarini, 2015: Stochastic climate theory and modelling. *Wiley Interdiscip. Rev.: Climate Change*, 6, 63-78.
- Fratantoni, D. M., W. E. Johns, T. L. Townsend and H. E. Hurlburt, 2000: Low-latitude circulation and mass transport pathways in a model of tropical Atlantic Ocean. *J. Phys. Oceanogr.*, 30(8), 1944-1966.
- Freilich, M.H., and Chelton D. B., 1986: Wavenumber spectra of pacific winds measured by the Seasat scatterometer. *J. Phys. Oceanogr.*, 16, 741-757.
- Gavrikov A., S. K. Gulev, M. Markina, N. Tilinina, P. Verezemskaya, B. Barnier, A. Dufour, O. Zolina, Y. Zyulyaeva, M. Krinitskiy, I. Okhlopkov and A. Sokov, 2020: RAS-NAAD: 40-yr high-resolution North Atlantic atmospheric hindcast for multipurpose applications (new dataset for the regional mesoscale studies in the atmosphere and the ocean). *J. Appl. Meteor. Climatol.*, 59(5), 793-817.
- Gage, K. S., 1979: Evidence for a $k^{-5/3}$ law inertial range in mesoscale two-dimensional turbulence. *J. Atmos. Sci.*, 36, 1950-1954.
- Gent, P. and J., McWilliams, 1990: Isopycnal mixing in ocean circulation models. *J. Phys. Oceanogr.*, 20, 150-155.
- Griffies, S. M., and R. W. Hallberg, 2000: Biharmonic friction with a Smagorinsky-like viscosity for use in large-scale eddy-permitting ocean models. *Mon. Wea. Rev.*, 47, 709-735.
- Guemas, V., D. Salas-Méla, M. Kageyama, H. Giordani and A. Voldoire: 2012, Impact of ocean mixed layer diurnal variation on the intraseasonal variability of sea surface temperature in the Atlantic Ocean. *J. Clim.*, 24(12).
- Gubler, S., Gruber, S., and Purves, R. S., 2012: Uncertainties of parameterised surface downward clear-sky shortwave and all-sky longwave radiation. *Atmos. Chem. Phys.*, 12(11), 5077-5098.
- Gulev, S. K., Zolina, O. and Grigoriev, S., 2001: Extratropical cyclone variability

- in the Northern Hemisphere winter from the NCEP/NCAR reanalysis data. *Clim. Dynam.*, 17(10), 795-809.
- Gulev, S. K., and Belyaev, K., 2012: Probability distribution characteristics for surface air-sea turbulent heat fluxes over the global ocean. *J. Clim.*, 25(1), 184-206.
- Häkkinen, S., and P. Rhines, 2004: Decline of subpolar North Atlantic during the 1990s. *Science*, 304,555-559.
- Ham, S., Hong, S. Y., and Park, S., 2014: A study on air-sea interaction on the simulated seasonal climate in an ocean-atmosphere coupled model. *Clim. Dynam.*, 42(5-6), 1175-1187.
- Hamilton, K., Y. O. Takahashi, and W. Ohfuchi, 2008: Mesoscale spectrum of atmospheric motions investigated in a very fine resolution global general circulation model. *J. Geophys. Res. Atmos.*, 113, D18110.
- Hasselmann, K., 1976: Stochastic climate models Part I. Theory, *Tellus*, 28(6), 473-485.
- Hátún, H., A. B. Sandø, H. Drange, B. Hansen and H. Valdimarsson, 2005: Influence of the Atlantic subpolar gyre on the thermohaline circulation. *Science*, 309, 1841-1844.
- Hoffmann, L., G. Günther, D. Li, O. Stein, X. Wu, S. Griessbach, Y. Heng, P. Konopka, R. Müller, B. Vogel and J. S. Wright, 2019: From ERA-Interim to ERA5: the considerable impact of ECMWF's next-generation reanalysis on Lagrangian transport simulation. *Atmos. Chem. Phys.*, 19, 3097-3124.
- Hirons, L. C., N. P. Klingaman and S. J. Woolnough, 2015: MetUM-GOML1: a near-globally coupled atmosphere-ocean-mixed-layer model. *Geosci. Model Dev.*, 8, 363-379.
- Hogg, A. M. C., Dewar, W. K., Berloff, P., Kravtsov, S. and Hutchinson, D. K., 2009. The effects of mesoscale ocean-atmosphere coupling on the large-scale ocean circulation. *J. Clim.*, 22(15), 4066-4082.

- Holdsworth, A. M. and P. G. Myers, 2015: The influence of high-frequency atmospheric forcing on the circulation and deep convection of the Labrador Sea. *J. Clim.*, 28(12), 4980-4996.
- Hosoda, S., M. Nonaka, T. Tomita, B. Taguchi, H. Tomita and N. Iwasaka, 2015: Impact of downward heat penetration below the shallow seasonal thermocline on the sea surface temperature. *J. Oceanogr.*, 75(5), 541-556.
- Howard, L. N. (1961). Note on a paper of John W. Miles. *J. Fluid Mech.*, 10(04), 509-512.
- Hu, A. and G. A. Meehl, 2009: Effects of the Atlantic hurricanes on the oceanic meridional overturning circulation and heat transport. *Geophys Res. Lett.*, 36, L03702.
- Hu, W., Duan, A., and Wu, G., 2015: Impact of subdaily air-sea interaction on simulating intraseasonal oscillations over the tropical Asian monsoon region. *J. Clim.*, 28(3), 1057-1073.
- Idso, S. B., and Jackson, R. D., 1969: Thermal Radiation from the Atmosphere. *J. Geophys. Res.*, 74(23), 5397.
- Idso, S. B., 1981: A Set of Equations for Full Spectrum and 8- to 14 micron and 10.5- to 12.5 micron Thermal Radiation From Cloudless Skies. *Water Resour. Res.*, 17(2), 295-304.
- Imkeller, P., and Monahan, A. H., 2002: Conceptual stochastic climate models. *Stoch. Dynam.*, 2(3), 311-326.
- Iziomon, M. G., Mayer, H., and Matzarakis, A., 2003: Downward atmospheric longwave irradiance under clear and cloudy skies: Measurement and parameterisation. *J. Atmos. Sol-Terr. Phys.*, 65(10), 1107-1116.
- Jerlov, N. G., 1976: Marine Optics. Elsevier, Amsterdam, 229 pp.
- Jung, T., S. Serrar and Q. Wang, 2014: The oceanic response to mesoscale atmospheric forcing. *Geophys. Res. Lett.*, 41(4), 1255-1260.

- Kalnay, E., M. Kanamitsu, R. Kistler, W. Collins, D. Deaven, L. Gandin, M. Iredell, S. Saha, G. White, J. Woollen, Y. Zhu, M. Chelliah, W. Ebisuzaki, W. Higgins, J. Janowiak, K. C. Mo, C. Ropelewski, J. Wang, A. Leetmaa, R. Reynolds, R. Jenne, and D. Joseph, 1996: The NCEP/NCAR 40-Year Reanalysis Project. *Bull. Amer. Meteor. Soc.*, 77, 437–471.
- Kantha, L. H., and Clayson, C. A., 1994: An improved ML model for geophysical applications. *J. Geophys. Res.*, 99(C12), 25235.
- Kawai, Y. and A. Wada, 2007: Diurnal sea surface temperature variation and its impact on the atmosphere and ocean: A review. *J. Oceanogr.*, 63, 721-744.
- Klingaman, N. P., S. J. Woolnough, H. Weller and J. M. Slingo, 2011: The impact of finer-resolution air-sea coupling on the intraseasonal oscillation of the Indian monsoon. *J. Clim.*, 24, 2451-2468.
- Kolstad, E. W. and Bracegirdle, T. J., 2008: Marine cold-air outbreaks in the future: An assessment of IPCC AR4 model results for the Northern Hemisphere. *Clim. Dynam.*, 30, 871–885.
- Konzelmann, T., van de Wal, R. S. W., Greuell, W., Bintanja, R., Henneken, E. A. C., and Abe-Ouchi, A., 1994: Parameterisation of global and longwave incoming radiation for the Greenland Ice Sheet. *Global Planet. Change*, 9(1-2), 143-164.
- Kraichnan, R. H., 1967: Inertial ranges in two-dimensional turbulence. *Phys. Fluids*, 10(7), 1417-1423.
- Kraus, E.B., 1972: Atmosphere-Ocean Interaction. Oxford University Press, New York, USA, 275 pp.
- Kuhlbrodt, T., Titz, S., Feudel, U. and Rahmstorf, S., 2001: A simple model of seasonal open ocean convection. Part II: Labrador Sea stability and stochastic forcing. *Ocean Dynam.*, 52(1), 36-49.
- Kuwano-Yoshida, A. and Minobe, S., 2017: Storm-Track response to SST fronts in the Northwestern Pacific Region in an AGCM. *J. Clim.*, 30(3), 1081-1102.

- Kwon, Y. O. and Frankignoul, C., 2012: Stochastically-driven multidecadal variability of the Atlantic meridional overturning circulation in CCSM3. *Clim. Dynam.*, 38(5-6), 859-876.
- Large, W. G., W. R. Holland, and J. C. Evans, 1991: Quasi-geostrophic ocean response to real wind forcing: the effects of temporal smoothing. *J. Phys. Oceanogr.*, 21, 998-1017.
- Large, W. G., J. C. McWilliams and S. C. Doney, 1994: Oceanic vertical mixing: A review and a model with a nonlocal boundary layer parameterization. *Rev. Geophys.*, 32(4), 303-403.
- Lazier, J., R. Hendry, A. Clarke, I. Yashayaev and P. Rhines, 2002: Convection and restratification in the Labrador Sea, 1990-2000. *Deep-Sea Res. Pt. I*, 49(10), 1819-1835.
- Lean, H. W., and P. Clark, 2003: The effects of changing resolution on mesoscale modelling of line convection and slantwise circulations in FASTEX IOP16. *Q. J. R. Meteorol. Soc.*, 129, 2255-2278.
- Lebeaupin Brossier, C., V. Ducrocq and H. Giordani, 2009: Effects of the air-sea coupling time frequency on the ocean response during Mediterranean intense events. *Ocean Dynam.*, 59(4), 539-549.
- Lewis, M. R., J. J. Cullen and T. Platt, 1983: Phytoplankton and thermal structure in the upper ocean: consequences of nonuniformity in chlorophyll profile. *J. Geophys. Res.*, 88, 2565-2570.
- Lindborg, E., 1999: Can the atmospheric kinetic energy spectrum be explained by two-dimensional turbulence? *J. Fluid Mech.*, 388, 259-288.
- Lohmann, K., H. Drange and M. Bentsen, 2009: A possible mechanism for the strong weakening of the North Atlantic subpolar gyre in the mid-1990s. *Geophys. Res. Lett.*, 36, L15602.
- Lozier, M. S., V. Roussenov, M. S. Reed and R. G. Williams, 2010: Opposing

- decadal changes for the North Atlantic meridional overturning circulation. *Nat. Geosci.*, 3(10), 728-734.
- Macdonald, A. M. and C. Wunsch, 1996: An estimate of global ocean circulation and heat fluxes. *Nature*, 382,436-439.
- Maykut, G. A. and Church, P. E., 1973: Radiation Climate of Barrow Alaska, 1962-66. *J. Appl. Meteor.*, 12, 620-628.
- Marshall, J., Hill, C., Perelman, L. and Adcroft, A., 1997: Hydrostatic, quasi-hydrostatic, and nonhydrostatic ocean modeling. *J. Geophys. Res. Oceans*, 102(C3), 5733-5752.
- Marshall, J., and F. Schott, 1999: Open-ocean convection: Observations, theory and models. *Rev. Geophys.*, 37(1), 1-64.
- Marshall, J. and R. A. Plumb, 2008: *Atmosphere, Ocean and Climate Dynamics: An introductory Text*. Elsevier Academic Press, Burlington, USA, 319 pp.
- Martin, G., 1970: Mathematical Games - The Fantastic Combinations of John Conway's Game 'Life'. *Scientific American*, 223, 120-123.
- Marzocchi, A., J. M. Hirschi, N. P. Holliday, S. A. Cunningham, A. T. Blaker and A. C. Coward, 2015: The North Atlantic subpolar circulation in an eddy-resolving global ocean model. *J. Marine Syst.*, 142, 126-143.
- McDougall, T. and P., McIntosh, 1996: The temporal-residual-mean velocity. Part I: Derivation and the scalar conservation equations. *J. Phys. Oceanogr.*, 26, 2653-2665.
- McPhaden, M. J., A. J. Busalacchi, R. Cheney, J. R. Donguy, K. S. Gage, D. Halpern, M. Ji, P. Julian, G. Meyers, G. T. Mitchum, P. P. Niiler, J. Picaut, R. W. Reynolds, N. Smith, and K. Takeuchi, 1998: The Tropical Ocean Global Atmosphere observing system: A decade of progress. *J. Geophys. Res.*, 103(C7), 14169-14240.

- Mellor, G. L., and T. Yamada, 1982: Development of a turbulence closure model for geophysical fluid problems. *Rev. Geophys.*, 20(4), 851-875.
- Miles, J. W., 1961: On the stability of heterogeneous shear flows. *J. Fluid Mech.*, 10(04), 496-508.
- Milliff, R. F., Large, W. G., Holland, W. R. and McWilliams, J. C., 1996: The general circulation responses of high-resolution North Atlantic Ocean models to synthetic scatterometer winds. *J. Phys. Oceanogr.*, 26(9), 1747-1768.
- Milliff, R. F., Large, W. G., Morzel, J., Danabasoglu, G. and Chin, T. M., 1998: Ocean general circulation model sensitivity to forcing from scatterometer winds. *J. Geophys. Res. Oceans*, 104(C5), 11337-11358.
- Mitchell, J., 1976: An Overview of Climatic Variability and its Causal Mechanisms. *Quaternary Res.*, 6(4), 481-493.
- Morel, A. and S. Maritorena, 2001: Bio-optical properties of oceanic waters: a reappraisal. *J. Geophys. Res.*, 106, 7163-7180.
- Müller, P., and C. Frankignoul, 1981: Direct atmospheric forcing of geostrophic eddies. *J. Phys. Oceanogr.*, 11, 287-308.
- Murtugudde, R. , J. Beauchamp, C. R. McClain, M. Lewis and A. J. Busalacchi, 2002: Effects of penetrative radiation on the upper tropical ocean circulation. *J. Clim.*, 15(5),470-486.
- Nastrom, G. D., and K. S. Gage, 1985: A climatology of atmospheric wavenumber spectra of wind and temperature observed by commercial aircraft. *J. Atmos. Sci.*, 42, 950-960.
- Newman, M., G. Compo, M. A. Alexander, 2003: ENSO-forced variability of the Pacific Decadal Oscillation. *J. Clim.*, 16, 3853-3857.
- Nicolis, C., 2004: Dynamics of model error: the role of unresolved scales revisited. *J. Atmos. Sci.*, 61, 1740-1753.

- O'Neill, L. W., Chelton, D. B. and Esbensen, S. K., 2003: Observations of SST-induced perturbations of the wind stress field over the Southern Ocean on seasonal timescales. *J. Clim.*, 16(14), 2340-2354.
- O'Neill, L. W., Chelton, D. B., Esbensen, S. K. and Wentz, F. J., 2005: High-resolution satellite measurements of the atmospheric boundary layer response to SST variations along the Agulhas Return Current. *J. Clim.*, 18(14), 2706-2723.
- Palmer, T. N., 1997: On parameterizing scales that are only somewhat smaller than the smallest resolved scales, with application to convection and orography. In Workshop on new insights and approaches to convective parameterization, 4-7 November 1996. European Centre for Medium-Range Weather Forecasts, Shinfield, Reading, UK.
- Palmer, T. N., 2001: A nonlinear dynamical perspective on model error: A proposal for non-local stochastic-dynamic parametrization in weather and climate prediction models. *Q. J. R. Meteorol. Soc.*, 127(572), 279-304.
- Palmer, T. N., G. J. Shutts, R. Hagedorn, F. J. Doblas-Reyes, T. Jung, and M. Leutbecher, 2005: Representing model uncertainty in weather and climate prediction. *Annu. Rev. Earth Planet. Sci.*, 33, 163-193.
- Palmer, T. N., and P. D. Williams, 2008: Introduction: Stochastic physics and climate modelling. *Phil. Trans. R. Soc. A.*, 366, 2421-2427.
- Palmer, T. N., 2019: Stochastic weather and climate models. *Nature Rev. Phys.*, 1(7), 463-471.
- Paulson, C. A. and J. J. Simpson, 1977: Irradiance measurements in the upper ocean. *J. Phys. Oceanogr.*, 7, 952-956.
- Penland, C. and Sardeshmukh, P. D., 1995: The optimal growth of tropical sea surface temperature anomalies. *J. Clim.*, 8(8), 1999-2024.
- Penland, C. and L. Hartten, 2014: Stochastic forcing of north tropical Atlantic sea surface temperatures by the North Atlantic Oscillation, *Geophys. Res. Lett.*, 41(6), 2126-2132.

- Perez, C. L., Moore, A. M., Zavala-Garay, J. and Kleeman, R., 2005: A comparison of the influence of additive and multiplicative stochastic forcing on a coupled model of ENSO. *J. Clim.*, 18(23), 5066-5085.
- Pickart, R. S., M. A. Spall, M. H. Ribergaard, G. W. K Moore and R. F. Milliff, 2003: Deep convection in the Irminger Sea forced by the Greenland tip jet. *Nature*, 424(6945), 152-156.
- Plant, R. S., and G. C. Craig, 2008: A Stochastic Parameterization for Deep Convection Based on Equilibrium Statistics. *J. Atmos. Sci.*, 65(1), 87-105.
- Polo, I., J. Robson, R. Sutton and M. A. Balmaseda, 2014: The importance of wind and buoyancy forcing for the boundary density variations and the geostrophic component of the AMOC at 26°N. *J. Phys. Oceanogr.*, 44, 2387-2408.
- Prata, A. J., 1996: A new long-wave formula for estimating downward clear-sky radiation at the surface. *Q. J. Roy. Meteor. Soc.*, 122(533), 1127-1151.
- Price, J. F., Mooers, C. N. and Van Leer, J. C., 1978: Observation and simulation of storm-induced mixed-layer deepening. *Journal of Physical Oceanography*, 8(4), 582-599.
- Price, J. F., Weller, R. A., and Pinkel, R., 1986: Diurnal Cyciling: Observation and models of the upper ocean response to diurnal heating, cooling and wind mixing. *J. Geophys. Res.*, 91, 8411-8427.
- Price, J. F., Morzel, J., and Niiler, P. P., 2008: Warming of SST in the cool wake of a moving hurricane. *J. Geophys. Res.-Oceans*, 113(7), 1-19.
- Qiu, B., S. Chen and P. Hacker, 2004: Synoptic-scale air-sea flux forcing in the western North Pacific: Observations and their impact on SST and the mixed layer. *J. Phys. Oceanogr.*, 34(10), 2148-2159.
- Rahmstorf, S., 2001: A simple model of seasonal open ocean convection. *Ocean Dynam.*, 52(1), 26-35.

- Rayner, D., J. J.-M Hirschi, T. Kanzow, W. E. Johns, P. G. Wright, E. Frajka-Williams, H. L. Bryden, C. S. Meine, M. O. Baringer, J. Marotzke, L. M. Beal, S. A. Cunningham, 2011: Monitoring the Atlantic meridional overturning circulation. *Deep-Sea Res. Pt. II*, 58(17-18), 1744-1753.
- Reed, R., 1977: On Estimating Insolation over the Ocean. *J. Phys. Oceanogr.*, 7, 482-485.
- Richardson, P. L., 2008: On the history of meridional overturning circulation schematic diagrams. *Prog. Oceanogr.*, 76(4), 466-486.
- Rochford, P. A., A. B. Kara, A. J. Wallcraft and R. A. Arnone, 2001: Importance of solar subsurface heating in ocean general circulation models. *J. Geophys. Res. Oceans*, 106, 30923-30938.
- Roberts, C. D., J. Waters, K. A. Peterson, M. D. Palmer, G. D. McCarthy, E. Frajka-Williams, K. Haines, D. J. Lea, M. J. Martin, D. Storkey, E. W. Blockley and H. Zuo, 2013: Atmosphere drives recent interannual variability of the Atlantic meridional overturning circulation at 26.5°N. *Geophys. Res. Lett.*, 40(19), 5164-5170.
- Sardeshmukh, P. D., C. Penland, and M. Newman, 2003: Drifts induced by multiplicative red noise with application to climate, *Europhys. Lett.*, 63(4).
- Satterlund, D. R., 1979: An improved equation for estimating long-wave radiation from the atmosphere. *Water Resour. Res.*, 15(6), 1649-1650.770 pp.
- Schiller, A. and J. S. Godfrey, 2003: Indian Ocean intraseasonal variability in an ocean general circulation model. *J. Climate*, 16(1), 21-39.
- Schott, F. A., R. Zantopp, L. Stramma, M. Dengler, J. Fischer and M. Wibaux, 2004: Circulation and deep-water export at the western exit of the subpolar North Atlantic. *J. Phys. Oceanogr.*, 34(4), 817-843.
- Seo, H., Jochum, M., Murtugudde, R., Miller, A. J. and Roads, J. O., 2007: Feedback of tropical instability-wave-induced atmospheric variability onto the ocean. *J. Clim.*, 20(23), 5842-5855.

- Shinoda, T. and H. H. Hendon, 1998: Mixed layer modeling of intraseasonal variability in the tropical western Pacific and Indian Oceans. *J. Climate*, 11(10).
- Shinoda, T., 2005: Impact of the diurnal cycle of solar radiation on intraseasonal SST variability in the western equatorial Pacific. *J. Climate*, 18(14), 2628-2636.
- Shutts, G. J., 2004: 'A stochastic kinetic energy backscatter algorithm for use in ensemble prediction systems', Technical Memorandum 449. ECMWF: Reading, UK.
- Shutts, G. J., 2005: A kinetic energy backscatter algorithm for use in ensemble prediction systems. *Q. J. R. Meteorol. Soc.*, 131, 3079-3102.
- Skamarock, W. C., 2004: Evaluating mesoscale NWP models using kinetic energy spectra. *Mon. Wea. Rev.*, 132, 3019-3032.
- Smagorinsky, J., 1963: General circulation experiments with the primitive equations: I. The basic experiment. *Mon. Wea. Rev.*, 91(3), 99-164.
- Small, R. D., S. P. deSzoeko, S. P. Xie, L. O'neill, H. Seo, Q. Song, P. Cornillon, M. Spall and S. Minobe, 2008: Air-sea interaction over ocean fronts and eddies. *Dyn. Atmos. Oceans*, 45(3-4), pp.274-319.
- Small, R.J., Tomas, R.A. and Bryan, F.O., 2013: Storm track response to ocean fronts in a global high-resolution climate model. *Clim Dyn*, 43, 805-828.
- Smeed, D., B. Moat, D. Rayner, W. E. Johns, M. O. Baringer, D. Volkov, E. Frajka-Williams, 2019: Atlantic meridional overturning circulation observed by RAPID-MOCHA-WBTS (Rapid-Meridional Overturning and Heatflux Array-Western Boundary Time Series) array at 26°N from 2004 to 2018. British Oceanographic Data Centre - Natural Environmental Research Council, UK.
- Soloviev, A. and R. Lukas, 1997: Observation of large diurnal warming events in the near-surface layer of the western equatorial Pacific warm pool. *Deep-Sea Res. Pt. I*, 44(6), 1055-1076.

- Spall, M. A., 2007: Effect of sea surface temperature–wind stress coupling on baroclinic instability in the ocean. *J. Phys. Oceanogr.*, 37(4), 1092-1097.
- Sproson, D. A. J., Renfrew, I. A., Heywood, K. J., 2010: A parameterization of Greenland’s tip jets suitable for ocean or coupled climate models. *J. Geophys. Res. Ocean*, 115(C8).
- Srokosz, M. A., and H. Bryden, 2015: Observing the Atlantic Meridional Overturning Circulation yields a decade of inevitable surprises. *Science*, 348(6241), 1255-1257.
- Stevens, B., S. Bony, H. Brogniez, L. Hentgen, C. Hohenegger, C. Kiemle, T. S. L’Ecuyer, A. K. Naumann, H. Schulz, P. A. Siebesma, J. Vial, D. M. Winker and P. Zuidema, 2020: Sugar, gravel, fish and flowers: Mesoscale cloud patterns in the trade winds. *Q. J. Roy. Meteor. Soc.*, 146(726), 141-152.
- Stommel, H., 1948: The western intensification of wind-driven ocean currents. *Trans. Amer. Geophys. Union*, 29, 202-206.
- Sura, P., Fraedrich, K., Lunkeit, F., 2001: Regime transitions in a stochastically forced double-gyre model. *J. Phys. Oceanogr.* 31, 411-426.
- Sura, P. and Penland, C., 2002: Sensitivity of a double-gyre ocean model to details of stochastic forcing. *Ocean Model.*, 4(3-4), 327-345.
- Sura, P., Newman, M. and Alexander, M. A., 2006: Daily to decadal sea surface temperature variability driven by state-dependent stochastic heat fluxes. *J. Phys. Oceanogr.*, 36(10), 1940-1958.
- Sui, C.-H., X. Li, K.-M. Lau and D. Adamec, 1997: Multiscale air-sea interactions during TOGA COARE. *Mon. Wea. Rev.*, 125, 448-462.
- Sweeney, C., A. Gnanadesikan, S. M. Griffies, M. J. Harrison, A. J. Rosati and B. L. Samuels, 2005: Impacts of shortwave penetration depth on large-scale ocean circulation and heat transport. *J. Phys. Oceanogr.*, 35, 1103-1119.

- Swinbank, W. C., 1963: Long-wave radiation from clear skies. *J. Appl. Meteor.*, 89(381), 339-348.
- Takaya, Y., F. Vitart, G. Balsamo, M. Balmaseda, M. Leutbecher and F. Molteni, 2010: Implementation of an ocean mixed layer model in IFS. Technical Memorandum 663. ECMWF: Reading, UK.
- Terray, P., Kamala, K., Masson, S., Madec, G., Sahai, A. K., Luo, J. J., and Yamagata, T., 2012: The role of the intra-daily SST variability in the Indian monsoon variability and monsoon-ENSO-IOD relationships in a global coupled model. *Clim. Dynam.*, 39(3), 729-754.
- Tian, F., von Storch, J., and Hertwig, E., 2016: Air-sea fluxes in a climate model using hourly coupling between the atmospheric and the oceanic components. *Clim. Dynam.*, 48, 2819-2836.
- Tian, F., von Storch, J., and Hertwig, E., 2018: Impact of SST diurnal cycle on ENSO asymmetry. *Clim. Dynam.*, 52, 2300-2411.
- Treguier, A. M., S. Theetten, E. P. Chassignet, T. Penduff, R. Smith, L. Talley, J. O. Beismann, C. Boning, 2005: The North Atlantic subpolar gyre in four high-resolution models. *J. Phys. Oceanogr.*, 35(5), 757-774.
- Våge, K., Pickart, R. S., Moore, G. W. K., and Ribergaard, M. H.. 2008: Winter mixed layer Development in the Central Irminger Sea: The Effect of Strong, Intermittent Wind Events. *J. Phys. Oceanogr.*, 38(3), 541-565.
- Vallis, G.K., 2006: Atmospheric and Oceanic Fluid Dynamics Fundamentals and Large-scale Circulation. Cambridge University Press, Cambridge, UK,
- VanZandt, T. E., 1982: A universal spectrum of buoyancy in the atmosphere. *Geophys. Res. Lett.*, 9, 575-578.
- Wang, X., P. H. Stone, and J. Marotzke, 1999: Global Thermohaline Circulation. Part I: Sensitivity to Atmospheric Moisture Transport. *J. Clim.*, 12, 71-82.

- Webster, P. J. and Lukas, R., 1992: TOGA COARE: The coupled ocean-atmosphere response experiment. *B. Am. Meteorol. Soc.*, 73(9), 1377-1416.
- Weller, R. A. and S. P. Anderson, 1996: Surface meteorology and air-sea fluxes in the western equatorial pacific warm pool during the TOGA coupled ocean-atmosphere response experiment. *J. Climate*, 9, 1959–1990.
- Weller, R. A., Baumgartner, M. F., Josey, S. A., Fischer, A. S., and Kindle, J. C., 1998: Atmospheric forcing in the Arabian Sea during 1994-1995: Observations and comparisons with climatology and models. *Deep-Sea Res. PT. II*, 45(10-11), 1961-1999.
- Weller, R. A., Fischer, A. S., Rudnick, D. L., Eriksen, C. C., Dickey, T. D., Marra, J., Fox, C. and Leben, R., 2002: Moored observations of upper-ocean response to the monsoons in the Arabian Sea during 1994-1995. *Deep-Sea Res. PT. II*, 49(12), 2195-2230.
- Willebrand, J., S. G. Philander, and R. C. Pacanowski, 1980: The oceanic response to large-scale atmospheric disturbances. *J. Phys. Oceanogr.*, 10, 411-429.
- Williams, P. D., 2005: Modelling climate change: the role of unresolved processes. *Phil. Trans. R. Soc. A*, 363, 2931-2946.
- Williams, P. D., 2012: Climatic impacts of stochastic fluctuations in air-sea fluxes. *Geophys. Res. Lett.*, 39(10), L10705.
- Wu, Y., X. Zhai and Z. Wang, 2016: Impact of synoptic atmospheric forcing on the mean ocean circulation. *J. Climate*, 29(16), 5709-5724.
- Xie, S., 2004: Satellite Observations of Cool Ocean-Atmosphere Interaction. *Bull. Amer. Meteor. Soc.*, 85, 195-208.
- Xie, S. P., Deser, C., Vecchi, G. A., Ma, J., Teng, H., and Wittenberg, A. T., 2010: Global warming pattern formation: Sea surface temperature and rainfall. *J. Clim.*, 23, 966–986.

- Xu, X., E. P. Chassignet, W. E. Johns, W. J. Schmitz and E. J. Metzger, 2014: Intraseasonal to interannual variability of the Atlantic meridional overturning circulation from eddy-resolving simulations and observations. *J. Geophys. Res. Oceans*, 119(8), 5140-5159.
- Zahn, M. and von Storch, H., 2010: Decreased frequency of North Atlantic polar lows associated with future climate warming. *Nature*, 467, 309–312.
- Zhai, X., H. L. Johnson, D. P. Marshall and C. Wunsch, 2012: On the Wind Power Input to the Ocean General Circulation. *J. Phys. Oceanogr.*, 42(8), 1357-1365.
- Zhai, X., and Marshall, D. P., 2013: Vertical eddy energy fluxes in the North Atlantic subtropical and subpolar gyres. *J. Phys. Oceanogr.*, 43(1), 95-103.
- Zhai, X., 2013: On the wind mechanical forcing of the ocean general circulation. *J. Geophys. Res. Oceans*, 118, 6561-6577.
- Zhai, X., and Wunsch, C., 2013: On the variability of wind power input to the oceans with a focus on the subpolar North Atlantic. *J. Clim.*, 26(11), 3892-3903.
- Zhai, X., H.L. Johnson, and D.P. Marshall, 2014: A Simple Model of the Response of the Atlantic to the North Atlantic Oscillation. *J. Climate*, 27, 4052-4069.
- Zhao, J., and W. Johns, 2014: Wind-forced interannual variability of the Atlantic meridional overturning circulation at 26.5°N. *J. Geophys. Res. Oceans*, 119, 2403-2419.
- Zhou, S., X. Zhai and I. A. Renfrew, 2018: The impact of high-frequency weather systems of SST and surface mixed layer in the Central Arabian Sea. *J. Geophys. Res. Oceans*, 123(2), 1091-1104.
- Zillman, J. W., 1972: A study of some aspects of the radiation and heat budgets of the Southern Hemisphere oceans. Meteorological Studies, 26, Bureau of Meteorology, Department of the Interior, Canberra, Australia, 562 pp.